Kinematics-Based Modelling of Deep Transfer Girders in Reinforced Concrete Frame Structures

A Thesis Submitted in Partial Fulfilment of the Requirements for the Degree of Doctor of Philosophy in

APPLIED SCIENCES

by

Jian Liu

accepted on proposal of the jury:

Miguel Fernández Ruiz	Senior Lecturer	École Polytechnique Fédérale de Lausanne
Yuguang Yang	Assistant Professor	Delft University of Technology
Jean-François Demonceau	Associate Professor	University of Liège
Vincent Denoël	Professor	University of Liège
Jean-Marc Franssen	Professor	University of Liège
Boyan Mihaylov	Assistant Professor	University of Liège (Supervisor)

Belgium
2019

Author's contact details

Jian Liu

Structural Concrete Laboratory, Urban and Environmental Engineering Research Unit, University of Liège

+1/419, B52 Quartier Polytech 1, Allée de la Découverte 9,
4000 Liège, Belgium

Email: j.liu@uliege.be, liujian0225@gmail.com

Acknowledgement

I would like to express my sincere gratitude to my supervisor, Prof. Boyan Mihaylov, for his patient guidance during my PhD research work. I am impressed by his great passion for concrete structures and I see him as a great example for me to follow.

I thank Prof. Serhan Guner at the University of Toledo for hosting me as an exchange student and sharing his knowledge on numerical computations with me.

I want to thank the many people that I have shared an office with over the past few years, especially Nikola Tatar, Renaud Franssen and Chathura Rajapakse.

Finally, I am thankful to Albert and my parents for their support during my entire PhD study.

Abstract

Reinforced concrete deep beams often carry heavy loads as transfer girders in high-rise buildings, pile caps in bridges or other important structural members. Due to their small slenderness, they exhibit shear failure with disturbed deformation patterns differently from slender beams. Many experiments have revealed the complexity of the shear mechanisms of deep beams, and a number of formulations and models have been proposed attempting to explain their behaviour. However, up to the present, the accurate prediction of the shear response of deep beams remains a challenge. Considering the importance of such kind of structural element, this thesis is dedicated to make a further investigation on the shear mechanisms and provide a useful tool to predict the entire shear response of deep beams.

More than seventy models for deep beams are firstly summarized and classified into different categories according to their main characteristics. Detailed evaluation is made on ten models among them, with the help of a database of 574 deep beam tests. It is found that a semi-empirical strut-and-tie model (STM) and a two-parameter kinematic theory (2PKT) for deep beams produce the least scattered predictions in terms of shear strength experimental-to-predicted ratio V_{exp}/V_{pred}. Further studies are conducted to explore the effect of various important parameters, e.g. shear-to-span-depth ratio (a/d), size effect, and other. While the 2PKT produces uniform V_{exp}/V_{pred} across the entire range of experimental data and captures well the effects of all studied parameters, the semi-empirical STM exhibits certain bias with respect to the beam slenderness and does not account for the important size effect in shear.

In order to evaluate the serviceability, safety and resilience of deep beams, the thesis continues with the development of a 1D macroelement based on a three-parameter kinematic theory (3PKT) which is an extension of the 2PKT method to continuous deep beams. This macroelement aims at capturing the entire response of deep beams including both the pre- and post-peak regimes. One macroelement represents a deep shear span by using only two nodes with two degrees of freedom per node. Both simply-supported and continuous deep beams are modelled with the proposed 1D macroelement. It is shown that the macroelement captures well the force redistribution between shear spans in continuous members, and in this way predicts their enhanced ductility as compared to simply supported deep beams. It is also shown that the model captures the opening of the critical shear cracks under increased loading. The crack predictions can be compared with field measurements to accurately evaluate the safety of the structure, and in this way to avoid potential costly strengthening measures. As a result of the compatibility between the proposed 1D macroelement and classical 1D slender beam elements, a mixed-type modelling framework is proposed to overcome the high cost of analysis on large frame structures including deep transfer girders modelled with 2D high-fidelity finite element procedures. The framework is implemented in an existing nonlinear analysis procedure and is used to model eighteen deep beam tests and a twenty-story frame. It is shown that the proposed framework provides similarly accurate predictions to 2D high-fidelity procedures but requires a fraction of the time for modelling and analysis. Furthermore, the macroelement improves the post-peak predictions, and therefore the proposed framework is suitable for evaluating the resilience of structures under extreme loading.

Although the full shear response of solid deep beams can be well captured with the proposed macroelements, it is still an open issue to understand the behaviour of deep beams with web openings. In practice, web openings are inevitably installed in deep transfer girders to allow for windows, doors and different conduits. They may disrupt the flow of forces from the loads to the supports and significantly reduce the shear strength of deep members. To address this issue, a new model for deep beams with

rectangular openings is proposed based on the 2PKT method for solid beams. It is established based on an analysis of the shear behaviour and failure modes of test specimens using nonlinear finite element and strut-and-tie models. In the new model, two sub deep beams form above and below the web opening. Each sub shear span is modelled with two kinematic parameters as in solid shear spans, and the deformation pattern of the entire shear span can be described by these four degrees of freedoms (DOFs). The model is validated with 27 tests from the literature showing adequate shear strength predictions. It is shown that shear strength of deep beams with web openings is more affected by the depth of the opening than by its horizontal dimension. Also, the transition from deep to slender beam behaviour in members with openings occurs at smaller aspect ratios than in solid members. These experimental observations are well captured by the 2PKT approach.

Table of Contents

Title i
Acknowledgement v
Abstract vii
Table of Contents ix
List of Figures xiii
List of Tables xvii
Symbols xix
1. Introduction 1
1.1. Deep beams in concrete structures 3
1.2. Motivation for research 5
1.3. Objectives 10
1.4. Mechanisms of shear resistance in deep beams 10
1.4.1. Dowel action 10
1.4.2. Aggregate interlock 12
1.4.3. Contribution of stirrups 14
1.4.4. Contribution of uncracked concrete 14
1.5. Thesis outline 16
2. Models for Shear Strength of Reinforced Concrete Deep Beams 17
2.1. Introduction 19
2.2. Models for shear strength of RC deep beams 19
2.2.1. Strut-and-tie models 20
2.2.2. Upper-bound plasticity models 23
2.2.3. Shear panel models 23
2.2.4. Other mechanical models 23
2.3. Comparison with experimental results 25
2.3.1. Database of deep beam tests 25
2.3.2. Shear strength predictions 27
2.4. Parametric study 29
2.4.1. Shear-span-to-depth-ratio a/d 29
2.4.2. Transverse reinforcement ratio ρ_v 29
2.4.3. Longitudinal reinforcement ratio ρ_l 31

2.4.4. Size effect in shear 32
2.5. Conclusions 33
3. Macroelement for Complete Shear Behavior of Continuous Deep Beams 35
3.1. Introduction 37
3.2. Kinematic model for deep beams 38
3.3. Macroelement for deep shear spans 40
3.4. Constitutive relationships of the springs 42
3.5. Overview of solution procedure 47
3.6. Comparisons with tests 48
3.7. Conclusions 54
4. Mixed-Type Modelling of Structures with Slender and Deep Beam Elements 57
4.1. Introduction 59
4.2. 1D macroelement for deep beams 60
4.3. Existing element for slender beams and columns 63
4.4. Mixed-type modelling framework 64
4.5. Evaluation and applications 67
4.5.1. Beams 67
4.5.2. Frame structure 74
4.5.3. Efficiency of studied modelling strategies 76
4.6. Conclusions 77
5. Shear Strength of RC Deep Beams with Web Openings 79
5.1. Introduction 81
5.2. Observed behaviour of deep beams with openings 82
5.3. Finite element analysis of deep beams with openings 84
5.4. Strut-and-tie model of deep beams with openings 86
5.5. Proposed model for deep beams with web openings 87
5.5.1. Summary of two-parameter kinematic theory 87
5.5.2. Account of external longitudinal forces 89
5.5.3. Kinematic model for deep beams with web openings 89
5.5.4. Failure load of deep beams with web openings 90
5.5.5. Calculation procedure 92
5.5.6. Limits of applicability 92
5.6. Comparison with tests 93

5.6.1. Effect of opening size m_1 and m_2 95
5.6.2. Effect of f_c 96
5.6.3. Effect of a/d ratio 97
5.7. Conclusions 98
6. Conclusions and outlook 99
6.1. Summary and conclusions 101
6.1.1. A comparative study for shear capacity of RC deep beams 101
6.1.2. Formulation and validation of a macroelement for RC deep beams 101
6.1.3. Mixed-type modelling for structures with both slender and deep beam elements 102
6.1.4. A kinematic model on shear capacity of simply-supported RC deep beams with web openings 103
6.2. Future work 105
References 107
Appendices 113
A. Database of simply supported deep beams 115
B. Additional equations for macroelement formulation 137
C. Database of deep beams with web openings 139

List of Figures

Fig. 1.1 A typical building elevation with deep transfer girders (adapted from Kong, 2006[1]) 3

Fig. 1.2 Deep transfer girders in the train station of Leuven, Belgium 4

Fig. 1.3 Deep transfer girders in Tour CBX in Paris, France (BESIX Group S.A.) 4

Fig. 1.4 Effect of member slenderness on the shear strength of beams – tests by Kani, 1979[2] 5

Fig. 1.5 A 4m-deep RC beam tested in the University of Toronto in 2015 (adapted from Collins et al.[11]) .. 6

Fig. 1.6 Predictions Participated in the Contest (adapted from Collins et al.[11]) 6

Fig. 1.7 Strut action disturbed by a web opening in a deep beam 7

Fig. 1.8 Shear failure of deep beam in a bus Terminal in the M5.5 earthquake of Popayan in Colombia on 31/03/1983 (https://www.eeri.org/1983/03/popayan/04-10/) 8

Fig. 1.9 Grand Chancellor Hotel damaged in the Mw6.2 earthquake of Christchurch in New Zealand on 22/02/2011[16] 9

Fig. 1.10 Calculated shear carried by each shear-transfer mechanism at peak load compared to the experimental shear strength V_{exp} (adapted from Cavagnis et al.[17]) 11

Fig. 1.11 Experiment to study dowel action in slender beams by Baumann and Rusch[5] (figure adapted from Huber et al.[4]) 11

Fig. 1.12 Model for dowel action in deep beams applied by Mihaylov et al.[6] 12

Fig. 1.13 Experimental study on aggregate interlock by Mansur et al.[20] 12

Fig. 1.14 Two-phase model for aggregate interlock by Walraven[21] 13

Fig. 1.15 Contact density model for aggregate interlock proposed by Li et al.[22] 13

Fig. 1.16 Contribution of stirrups (adapted from Huber et al.[17]) 14

Fig. 1.17 Contribution of uncracked concrete in slender and deep beams 15

Fig. 1.18 Modelling the uncracked concrete in deep beams 15

Fig. 1.19 Simply-supported deep beam under shear failure 15

Fig. 2.1 Models for shear capacity of RC deep beams published between 1987 and 2014. 20

Fig. 2.2 Mechanisms of shear resistance in strut-and-tie models 22

Fig. 2.3 Two-parameter kinematic theory (2PKT) for deep beams[19] 24

Fig. 2.4 Distribution of shear strength experimental-to-predicted ratios 26

Fig. 2.5 Distribution of shear strength experimental-to-predicted ratios against main test variables 28

Fig. 2.6 Effect of a/d ratio - tests by Clark[33] 30

Fig. 2.7 Effect of transverse reinforcement ratio - tests by Smith and Vantsiotis[34] 31

Fig. 2.8 Effect of ratio of tensile longitudinal reinforcement – tests by Mathey and Watstein[45] 32

Fig. 2.9 Size effect in shear – tests by Zhang and Tan[46] 33

Fig. 3.1 Typical crack patterns in deep bridge pier caps. 37

Fig. 3.2 Kinematic model for shear spans of deep beams under double curvature. 39
Fig. 3.3 Macroelement for deep shear spans. 42
Fig. 3.4 Behaviour of rotational springs 43
Fig. 3.5 Shear mechanisms in deep beams. 44
Fig. 3.6 Modelling of the critical loading zone (CLZ). 44
Fig. 3.7 Behaviour of shear springs. 46
Fig. 3.8 Solution procedure. 49
Fig. 3.9 Measured and predicted behaviour of beam S1M. 51
Fig. 3.10 Effect of a/d ratio and stirrup ratio (tests by Mihaylov et al.[49]) 51
Fig. 3.11 Measured and predicted behaviour of beam CB1[32]. 53
Fig. 3.12 Maximum width of diagonal cracks. 54
Fig. 4.1 Alternative models of a large 4-bay frame structure with both slender and deep beams. 60
Fig. 4.2 Macroelement for shear spans of deep beams. 61
Fig. 4.3 Load-deformation relationships of the springs of the macroelement. 62
Fig. 4.4 Existing element for slender beams. 64
Fig. 4.5 Unbalanced force approach (adapted from Guner and Vecchio[70]). 65
Fig. 4.6 Mixed-modelling framework. 66
Fig. 4.7 Modelling of simply supported deep beam 8[62]. 68
Fig. 4.8 Convergence during the analysis of beam 8. 69
Fig. 4.9 Modelling of simply supported deep beam 71
Fig. 4.10 Crack and deformation patterns of beams 1 and B-15 72
Fig. 4.11 Modelling of a continuous deep beam tested by Mihaylov et al.[41] 73
Fig. 4.12 Measured and predicted load-displacement response of a continuous deep beam. 73
Fig. 4.13 Two-story single-span frame. 74
Fig. 4.14 Modelling of a large frame. 75
Fig. 4.15 Results from frame analysis under applied vertical loads 76
Fig. 4.16 Results from frame analysis under applied vertical displacements. 77
Fig. 4.17 Efficiency of modelling strategies 77
Fig. 5.1 A 30-storey apartment having transfer girder with web openings 82
Fig. 5.2 Deep beams tested by El-Maaddawy and Sherif[71] 83
Fig. 5.3 Typical failure modes of deep beams with openings (adapted from El-Maaddawy and Sherif[80]) 84
Fig. 5.4 Deep beams with web openings studied by FEM 85
Fig. 5.5 Strut-and-tie model for deep beams with openings 87

Fig. 5.6 Two-parameter kinematic theory (2PKT) for deep beams 88
Fig. 5.7 Solution procedure under given Δ_c 88
Fig. 5.8 Other loading cases 89
Fig. 5.9 Kinematics of deep beams with openings 90
Fig. 5.10 Equilibrium of forces in deep beams with openings 92
Fig. 5.11 Calculation procedure 93
Fig. 5.12 A typical beam in this study 94
Fig. 5.13 Distribution of V_{exp}/V_{pred} with different parameters 94
Fig. 5.14 Effect of opening size on the shear strength – specimens NS-C[80] 95
Fig. 5.15 Effect of opening size on the shear strength – tests by Yang et al.[78]. 96
Fig. 5.16 Effect of concrete compressive strength on the shear strength – tests by Yang et al. [78] 97
Fig. 5.17 Effect of shear-span-to-depth ratio on the shear strength – tests by Yang et al. [78] 97

List of Tables

Table 2.1 Summary of ten models for shear capacity of deep beams 21
Table 3.1 Test specimens of deep beams 50
Table 4.1 Simply supported deep beam tests 68

Symbols

a: M/V	length of shear span measured from the centre of the support to the centre of the loading plate
$a_{b/t}$	length of bottom/top shear span in deep beams with web openings
a_g	maximum specified size of course aggregate
a_0	side length of square web openings in deep beams
a/d	shear-span-to-effective-depth ratio
A	gross cross-sectional area
$A_{c,eff}$	area of the concrete around the reinforcing bars responsible for the tension stiffening effect
A_g	gross area of cross section
A_s	area of longitudinal reinforcement
A_{s3}	area of vertical steel rebars crossing “section A” in deep beams with web openings
b	cross section width
CF	convergence factor
d	effective depth of section with respect to bottom reinforcement
d_b	diameter of bottom longitudinal bars
$d_{1/2}$	effective depth of section with respect to bottom/top reinforcement
d_3	effective depth of “Section A” in deep beams with web openings
E_c	modulus of elasticity of concrete
E_s	modulus of elasticity of steel
f_c	concrete cylinder strength at date of testing
f_y	yield strength of flexural tension reinforcement
$f_{y1/2}$	yield strength of bottom/top longitudinal reinforcement
f_{y3}	yield strength of vertical steel rebars crossing “Section A” in deep beams with web openings
f_{yv}	yield strength of stirrups
$\{F_a\}$	vector of applied loads
$\{F_N\}$	vector of nodal forces for all members from nonlinear procedures
$\{F_{Nd}\}$	vector of deep member end forces from nonlinear procedure
$\{F_{Ns}\}$	vector of slender member end forces from nonlinear procedure
$\{F_R\}$	vector of compatibility restoring forces
$\{F_U\}$	vector of unbalanced forces

G_c	shear modulus of concrete
h	member total depth
$h_{b/t}$	depth of bottom/top shear span in deep beams with web openings
I	moment of inertia of gross concrete section
[k]	secant stiffness matrix of macroelement
k_0	transverse spring stiffness when diagonal crack is fully formed
k_1	in Chapter 5, ratio between the shortest horizontal distance from the web opening to the centre of support and shear span for deep beams with web openings
$k_{1/2}$	in Chapter 3, stiffnesses of rotational spring 1/2
$k_{1/2,el}$	initial stiffnesses of rotational spring 1/2
k_2	in Chapter 5, ratio between the shortest vertical distance from the web opening to beam bottom and the beam height for deep beams with web openings
k_3	stiffnesses of the transverse spring
$k_{3,el}$	initial stiffnesses of the transverse spring
k_s	stiffness of rotational spring neglecting the concrete
l_0	length of heavily cracked zone at the bottom of the critical diagonal crack
l_3	the shortest horizontal distance between web opening and beam end for deep beams with web openings
$l_{b1/2}$	width of loading plate / support plate parallel to longitudinal axis of member
l_{b1e}	effective width of loading plate parallel to longitudinal axis of member
$l_{b1e,b/t}$	effective width of loading plate parallel to longitudinal axis of member in bottom/top shear span for deep beams with web openings
l_k	length of dowels provided by bottom longitudinal reinforcement
l_{t1}	length of the longitudinal reinforcement within the cracked portion of the shear span
L	beam length
L_f	distance between two loading points
L_n	clear span of beam
m_1	ratio between horizontal size of rectangular opening and shear span for deep beams with web openings
m_2	ratio between vertical size of rectangular opening and beam height for deep beams with web openings
M_0	bending moment beyond which the beam is fully cracked
$M_{1/2}$	absolute value of end moment causing tension in bottom /top reinforcement
M_{cr}	cracking moment

n_b	number of bottom longitudinal bars
$n_{s1/2}$	number of bottom/top longitudinal bars
N_t	tensile force generated in bottom longitudinal rebars by load transfer in top shear span in deep beams with web openings
$N_{1/2}$	axial force at end section 1/2
P	applied concentrated load for beams or total force applied to frame structure
{P}	vector of applied nodal forces
$P_{1/2}$	applied concentrated load or support reaction
P_{exp}	maximum load measured in experiment
P_{pred}	maximum predicted load
s	crack slip
s_{cr}	distance between radial cracks along bottom edge of member
s_v	horizontal spacing between stirrups
T	tension force in bottom reinforcement
[T]	transformation matrix relating the nodal displacements to internal DOFs of macroelement
$T_{1/2}$	tension force in bottom/ top longitudinal reinforcement
T_3	tensile force in vertical tie above support in deep beams with web openings
T_{cr}	force necessary to crack the effective tension area
$u_{1/2}$	axial displacement of end section 1/2
$v_{1/2}$	transverse displacement of end section 1/2
v_{ci}	the shear stress on the critical diagonal crack
V	shear force
$V_{b/t}$	shear force carried by bottom/top shear span in deep beams with web openings
V_c	shear resisted by diagonal strut
V_{ci}	shear resisted by aggregate interlock
V_{CLZ}	shear resisted by the CLZ
V_d	shear resisted by dowel action
V_{exp}	experimentally obtained shear strength
$V_{ext/int}$	shear force in the external/internal shear spans of continuous deep beams
V_{pred}	predicted shear strength
$V_{pred,1D}$	shear capacity predicted by 1D mixed-type model
$V_{pred,2D}$	shear capacity predicted by 2D high-fidelity FEM

V_s	shear resisted by stirrups
V_{sect}	sectional shear strength of slender beams acc. to AASHTO code
V_w	shear resistance provided by web reinforcement
$V_{1/2}$	shear force at end section 1/2
V_{2PKT}	shear strength of deep beams acc. to 2PKT approach
w	crack width
z	lever arm between T and C
α	angle of line extending from the inner edge of support plate to the far edge of the tributary area of the loading plate responsible for the shear force V
α_b	angle of line extending from the inner edge of support plate to the bottom inner corner of the web opening in deep beams with web openings
α_t	angle of line extending from the far edge of the loading plate to the top outer corner of the web opening in deep beams with web openings
α_1	angle of critical diagonal crack
β	angle of inclination of support reaction
δ_x	displacement along x axis
δ_z	displacement along z axis
θ	angle of shear cracks in a uniform stress field or angle of diagonal strut in STM
$\theta_{1/2}$	opening of fan 1/2
$\theta_{1p/2p}$	residual opening angle of fan 1/2
$\{\Delta\}$	vector of nodal displacements (from global frame analysis)
Δ_c	transverse displacement of CLZ
$\Delta_{c,b/t}$	vertical displacement in critical loading zone in bottom/top shear span in deep beams with web openings
Δ_{cp}	residual transverse displacement in CLZ
$\{\Delta_{el}\}$	vector of nodal displacements for each element
Δ_t	deflection due to elongation of bottom longitudinal reinforcement
$\varepsilon_{t(,b/t)}$	average strain along longitudinal reinforcement in (bottom/top) shear span in deep beams with web openings
$\varepsilon_{t,avg}$	average strain along bottom longitudinal reinforcement
$\varepsilon_{t1/2,avg}$	average strain along bottom/top longitudinal reinforcement
ε_v	transverse web strain
ε_1	principal tensile strain in critical loading zone
$\varepsilon_{1/2,avg}$	average strain along bottom/top longitudinal reinforcement

ρ_h	= ratio of longitudinal web reinforcement
$\rho_l=100A_s/(bd)$	= ratio of longitudinal reinforcement on flexural tension side of section
ρ_v	ratio of transverse reinforcement
$\varphi_{1/2}$	rotation of the end section 1/2
σ_v	stirrup stress

1. Introduction

1.1. Deep beams in concrete structures

Characterized by relatively small shear span-to-effective-depth ratios ($a/d \leq 2.5$), reinforced concrete deep beams are stiff and effective in resisting large shear forces. As a result, they are commonly used as transfer girders in high-rise buildings to create open, column-free spaces, or as foundation elements (e.g., spread footings, raft footings, and pile caps) in structures made of concrete, steel, or timber (see Fig. 1.1). Many buildings with deep beams play important roles in communities, such as the central station of Leuven in Belgium shown in Fig. 1.2, where deep beams are used to create passages for passengers and trains. Another example is Tour CBX located in the major business district of La Défense in Paris (see Fig. 1.3), which includes a deep transfer girder at the fifth floor to allow for a large space from the third to the fourth floor. As a large part of loads in the structure is transferred through deep beams, the performance of deep beams is often critical for the safety of the entire structure. The failure of deep beams in these structures may have catastrophic consequences such as partial or complete collapse of the structure.

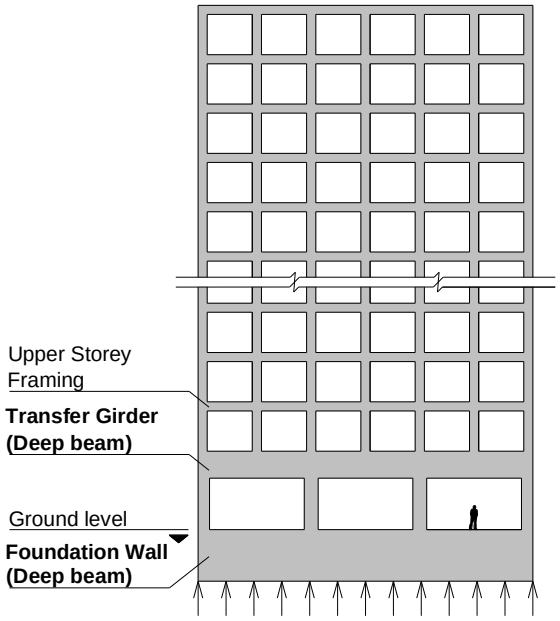

Fig. 1.1 A typical building elevation with deep transfer girders (adapted from Kong, 2006[1])

Different from slender beams, deep beams exhibit disturbed deformation patterns which do not obey the classic plane-sections-remain-plane hypothesis. The difference between these two types of beams is further demonstrated in Fig. 1.4 with experimental results of eleven RC beams tested by Kani et al.[2] (1979). With a constant section depth $d \approx 540$ *mm*, the tested beams had a/d ratios ranging from 1.0 to 6.8. The size of the loading and support plates was varied as well. All the beams failed in shear before the yielding of longitudinal reinforcement. It is found that the normalized shear capacity increases rapidly from 0.05 to 0.25 when the a/d ratio decreases from approx. 2.5 to 1.0, while only 25% decrease of shear capacity is observed as a/d increases from 2.5 to 6.8. These two different trends are dominated by two different shear resisting mechanisms: arch (or strut) action in deep beams and beam action in slender beams.

With beam action, slender beams carry shear forces through the uncracked concrete in the compression zone, by means of aggregate interlock along the shear cracks, as well as by dowel action of the longitudinal reinforcement. According to Yang[4], the failure of slender beams without stirrups originates from the unstable crack propagation along the longitudinal reinforcement which results in considerable opening of the major crack, and therefore loss of aggregate interlock action across the crack. In contrast to beam action, strut action relies on direct compression in the concrete from the loading point to the support, and due to the large compression capacity of concrete, deep beams can resist much higher shear forces than slender beams. To maintain equilibrium, the longitudinal reinforcement in deep beams works with a nearly constant tensile force along the shear span (tied arch).

Fig. 1.2 Deep transfer girders in the train station of Leuven, Belgium

(a) During Construction

(b) After Construction

Fig. 1.3 Deep transfer girders in Tour CBX in Paris, France (BESIX Group S.A.)

Recognizing the importance of strut action, deep beams are typically designed with strut-and-tie models as shown in Fig. 1.4. In these models the struts represent the compression in the concrete and the ties

represent the tension in the reinforcement. For deep beams with web reinforcement, the strut-and-tie model can be more complex incorporating additional horizontal or vertical ties. Strut-and-tie models can be either statically determinate or indeterminate, and in the latter case extra conditions are required, e.g. assuming the relative importance of each load path. Due to their simplicity and clear physical basis, strut-and-tie models have been widely adopted by researchers and engineers and have been included in different design standards[5-9] starting with the Canadian code of 1984[6]. In Fig. 1.4, the current strut-and-tie provisions of the Canadian code CSA A.23.3-04[7] were used to obtain the solid prediction curve which follows well the experimental points. This curve is combined with a curve based on the CSA shear sectional provisions for slender beams (dashed line) to cover the entire range of a/d ratios. Regardless of the accurate predictions in Fig. 1.4, it should be noted that strut-and-tie code provisions tend to significantly underestimate the shear capacity of deep beams when applied to a large number of tests with different variables[10].

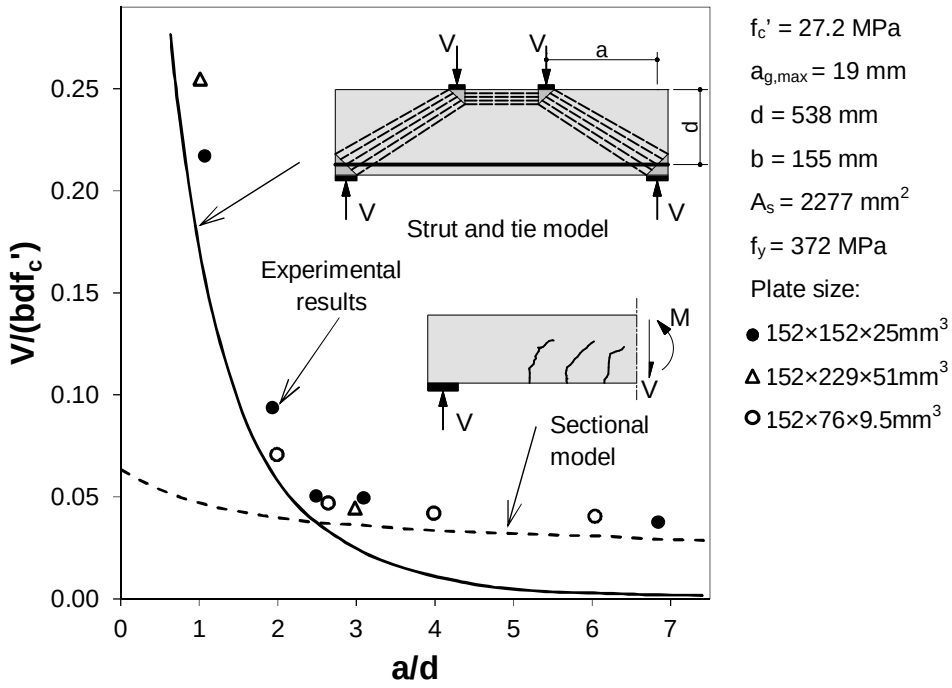

Fig. 1.4 Effect of member slenderness on the shear strength of beams – tests by Kani, 1979[2] (adapted from Collins and Mitchell, 1997[3])

1.2. Motivation for research

The ability of current codes and models to predict the shear capacity of deep beams was tested in 2015 when a large-scale test was performed at the University of Toronto[11]. The test consisted of loading to failure of a 4m-deep beam with one slender and one deep shear span. The deep shear span had an a/d ratio of 1.8 and failed along a critical diagonal crack as shown in Fig. 1.5. Before the test, 33 engineers and 33 researchers provided their predictions of shear strength obtained based on a variety of models. In the experiment, the deep shear span failed when the point load P reached 2162 kN, while the predictions varied from approx. 800 kN to 4000 kN. One quater of the predictions can be considered adequate with experimental-to-prediction ratios $P_{exp.}/P_{pred}$ between 1.0 and 1.2, while 35% of the participants provided

more conservative predictions. The most unconservative prediction overestimated the shear capacity of the beam by a factor of 1.85.

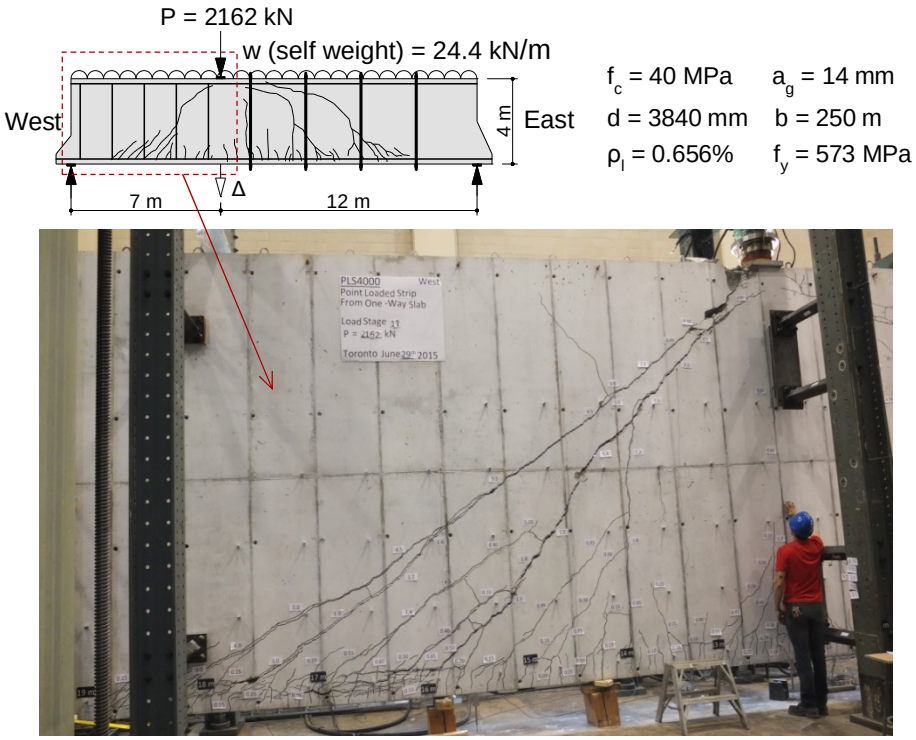

Fig. 1.5 A 4m-deep RC beam tested in the University of Toronto in 2015 (adapted from Collins et al.[11])

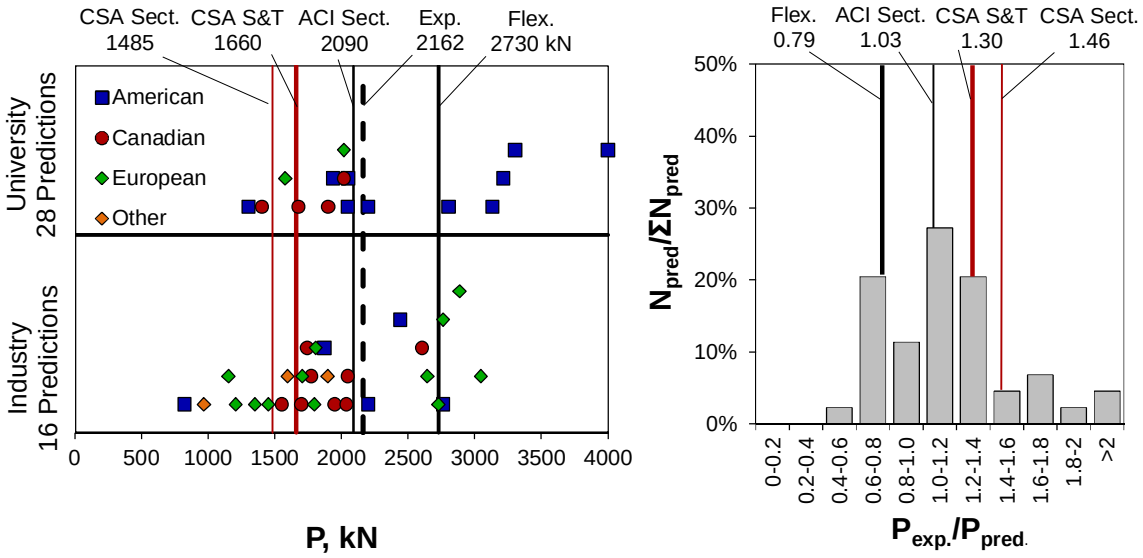

Fig. 1.6 Predictions participated in the contest (adapted from Collins et al.[11])

In terms of code provisions, the ACI sectional model produced an excellent prediction; however, the predictions based on either the strut-and-tie model or the sectional model in the Canadian standard were very conservative. These results show that, even though a large number of experiments were conducted and many models were proposed to investigate the shear behaviour of deep beams in the past sixty years, it is still a challenge to thoroughly understand the shear mechanisms in deep beams and to provide reliable predictions of the shear response. Nevertheless, as a number of models produced adequate predictions, there is a need for a more thorough evaluation and comparison of different modelling approaches by using the large number of tests available in the literature.

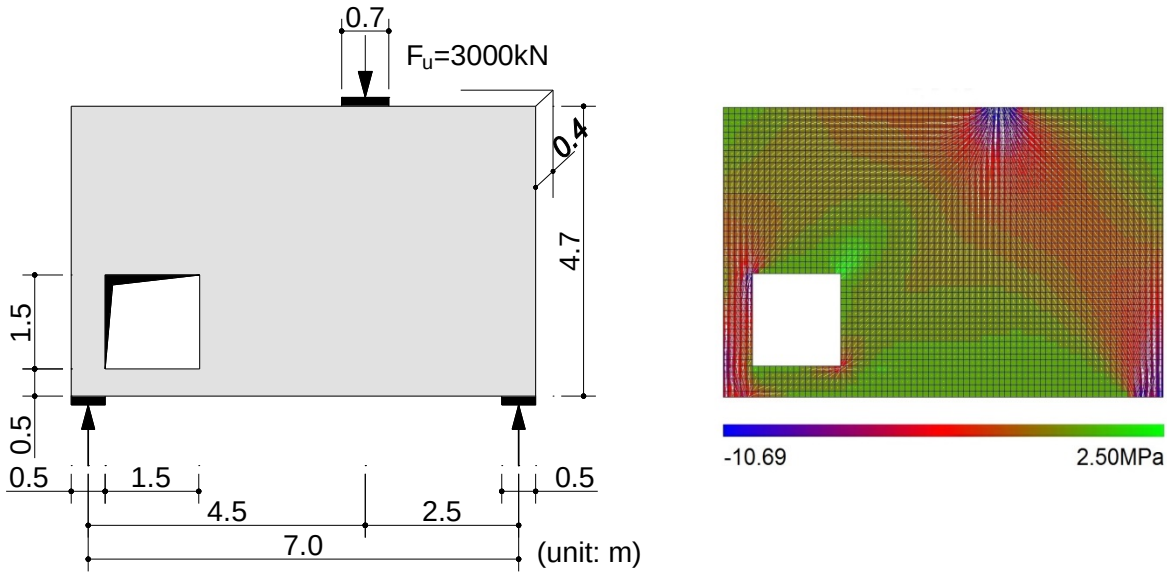

(a) Deep beam with web opening (adapted from Schlaich et al., 1987[12])

(b) Principal compressive stresses from linear elastic analysis with VecTor2[13]

Fig. 1.7 Strut action disturbed by a web opening in a deep beam

In addition to solid deep beams, it is also of interest to study the shear behaviour of deep beams with web openings. Fig. 1.7 shows an example of such a member together with the distribution of principal compressive stresses obtained from a linear elastic analysis. The stress distribution shows that in the shear span without an opening the load is transferred directly to the support through strut action, while in the shear span with an opening the compressive stress flow diverges into two load paths above and below the opening. The disturbance of the stress flow caused by the web opening must be investigated and understood, considering that in practice deep transfer girders often incorporate openings to accommodate windows, doors and various conduits. However, although great research efforts have been devoted to solid deep beams, few investigations have been carried out taking into account web openings.

Finally, deep transfer girders are typically part of complex structural systems in which force redistribution can occur under overloading. Fig. 1.8 shows that a deep beam in a bus terminal failed during the March 31, 1983 earthquake of Popayan in Colombia. However, the structure remained standing due to the redundancy of the structural system. The residual load-bearing capacity of the beam in combination with the capacity of the rest of the structure was sufficient to prevent a complete collapse. Similar cases were observed in the February 22, 2011 earthquake in New Zealand which devastated the city of Christchurch. Fig. 1.9 shows the 22-storey Grand Chancellor Hotel (GCH) at the city centre which was severely

damaged and had to be stabilized in the days after the earthquake. The lower 14-story car park structure comprised RC shear walls and cast-in-place flat slabs on columns, and the eastern bay was cantilevered using several deep transfer girders between levels 12 and 14. The upper 15-storey structure comprised of perimeter moment frames with a precast floor system, and the eastern bay was cantilevered by beams at each level and grid line. Although the magnitude of the earthquake was not exceptionally high, the epicenter was shallow and close to the city and the vertical ground accelerations reached unforeseen values of up to 1.8g. As a result, a shear wall located in the south-east corner of the building experienced brittle shear failure (see Fig. 1.9b-c), while at the same time this wall was responsible for roughly one-eighth of the structural mass. Following the failure of the shear wall, other significant damage was observed in the building, e.g. shear and axial failures of columns supporting the southern transfer girders (see see Fig. 1.9b-c). Finally, load redistribution occurred in the entire structure and the structure barely avoided a complete collapse and was demolished in the months after the earthquake.

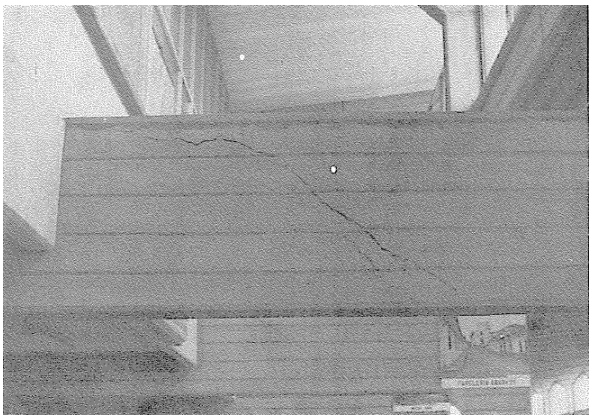

Fig. 1.8 Shear failure of deep beam in a bus terminal in the Mw5.5 earthquake of Popayan in Colombia on 31/03/1983 (https://www.eeri.org/1983/03/popayan/04-10/)

These examples demonstrate that, in order to evaluate the resilience of structures under extreme loading, it is necessary to model the entire structure with slender members and deep transfer girders. Furthermore, in order to capture the complex redistribution of forces in the structure, it is necessary to model accurately the complete behavior of the structural members, including the stages of large damage in the post-peak regime. There exist efficient 1D frame element formulations for slender beams and columns, but the only available modelling option for deep beams is high-fidelity 2D finite element formulations. While these formulations are suitable for modelling individual members, they require significant time for modelling and computations when embedded in models of entire complex structures. In addition, finite element formulations are not well suited for modelling the post-peak behavior of deep beams when large sliding deformations concentrate along diagonal cracks. Therefore, there is a need for different formulations that combine relative simplicity with adequate accuracy both in the pre- and post-peak regime of deep beams. These elements need to be integrated in a common modelling framework with existing elements for slender members which are equally as efficient and accurate.

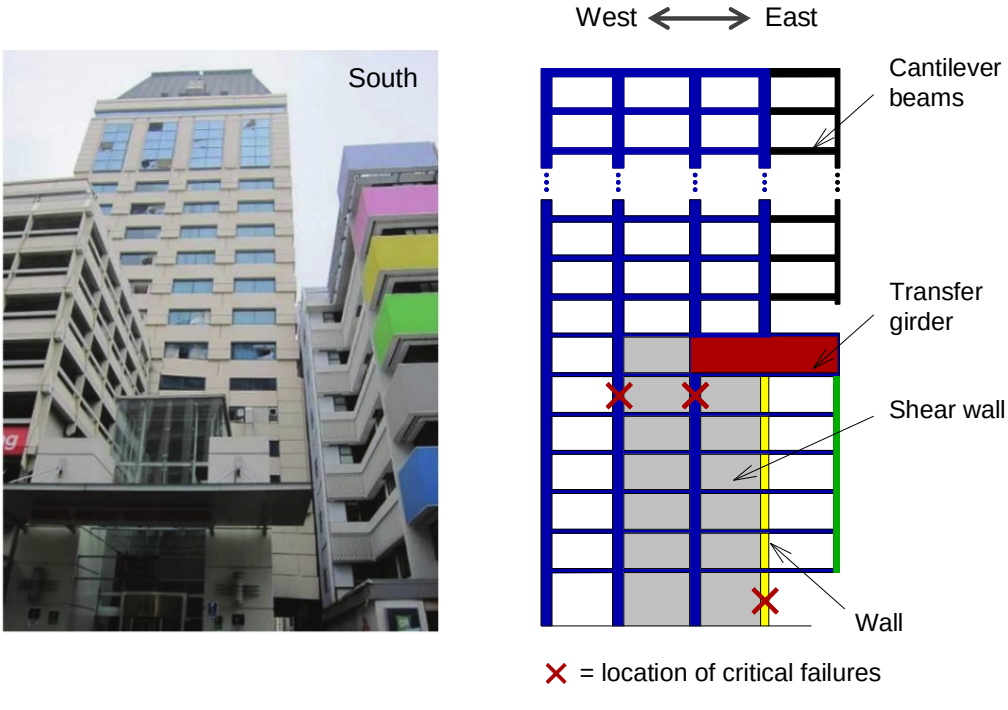

(a) The southern elevation

(b) Schematic elevation

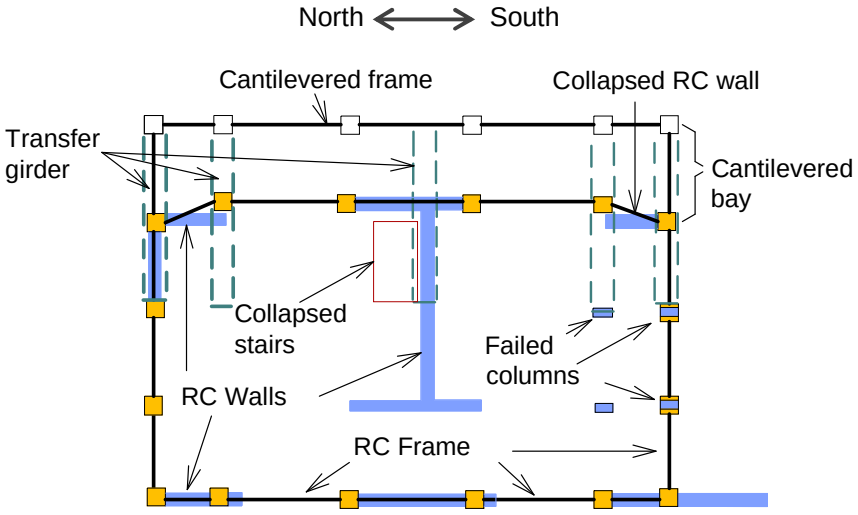

(c) Schematic plan

Fig. 1.9 Grand Chancellor Hotel damaged in the Mw6.2 earthquake of Christchurch in New Zealand on 22/02/2011[14]

1.3. Objectives

Based on the above, the main objectives of this thesis are four-fold:

1) To perform an extensive evaluation and comparison of existing models for shear resistance of deep beams by using a large database of laboratory tests;

2) To propose a 1D macroelement for deep beams based on an existing two-parameter kinematic theory[10];

3) To incorporate the proposed 1D deep beam element into a finite element program and to study the interaction between deep beams and the rest of the structure in large frame structures with deep transfer girders;

4) To propose a useful model to predict the shear capacity of RC deep beams with web openings.

All of the above objectives will be approached based on an existing two-parameter kinematic theory (2PKT)[10] proposed by Mihaylov et al. in 2013. This approach consists of three sets of fundamental equations – compatibility of deformations, equilibrium conditions and constitutive relationships for the mechanisms of shear resistance – which will be discussed in detail in Chapter 3.

1.4. Mechanisms of shear resistance in deep beams

In recent years, as the technology of digital image correlation (DIC) became available, more and more researchers use this optical method to measure the displacement and strain fields of structural members under loading[15,17]. Such measurements have been used in combination with local constitutive models for concrete, reinforcement and bond to evaluate the mechanics of shear resistance in reinforced concrete beams, and how much these mechanisms contribute to balance the applied load. For example, Fig. 1.10 shows the shear capacity predicted by Cavagnis et al.[15] based on the measured deformations of seven RC simply-supported beams with different a/d ratios (coloured bars). As the predicted capacity was compared to the measured applied load (horizontal black lines), a satisfactory agreement was achieved. The authors assumed that there were five shear mechanisms of shear resistance in RC beams without stirrups: dowel action of the bottom longitudinal rebars ($V_{D,tens}$); aggregate interlock along the shear crack (V_{Agg}); residual tensile strength of concrete (V_{RS}); dowel action of the top longitudinal rebars ($V_{D,compr.}$); and inclined compression in the uncracked concrete (V_C). It was found that, for beams with a/d ratio larger than 2.5, the contribution from the aggregate interlock and the residual tensile strength of concrete accounts for more than half of the shear resistance. As the a/d ratio decreases to 1.89, the residual strength of concrete becomes negligible, and at the same time the dowel action of the tensile longitudinal rebars and the aggregate interlock take up as few as 15% of the shear capacity. In all cases the dowel action of the top reinforcement was neglected. It is evident from these results that in deep beams ($a/d \leq 2.5$) the compression in the uncracked concrete dominates the shear resistance. Therefore, in the following, more information is provided on the mechanisms of shear resistance encountered in deep beams, including the contribution of the uncracked compression zone.

1.4.1. Dowel action

When longitudinal reinforcements cross a crack, the transversal displacement due to the opening and sliding of the crack generates shear force in the reinforcement, which is referred to as dowel action. Comprehensive experimental investigation into dowel action was performed as early as the 1970s by Baumann and Rusch[16] as shown in Fig. 1.11a, in which a wedge-shape concrete block contoured by

preformed cracks was introduced in the beam. The point load at the top of the block drove it downwards relatively to the rest of the beam, and transversal displacement δ across the longitudinal reinforcement caused dowel action. The concrete surrounding the longitudinal reinforcement was under tension as shown in Fig. 1.11b within a certain distance from the crack. As the tensile stress exceeded the tensile strength of the concrete, dowel cracks appeared along the longitudinal reinfocement (Fig. 1.11c). According to Baumann and Rusch, the shear contribution V_d remained approximately constant as the transverse displacement δ increased and the dowel crack propagated until a complete delamination of the concrete cover occurred as shown in in Fig. 1.11d.

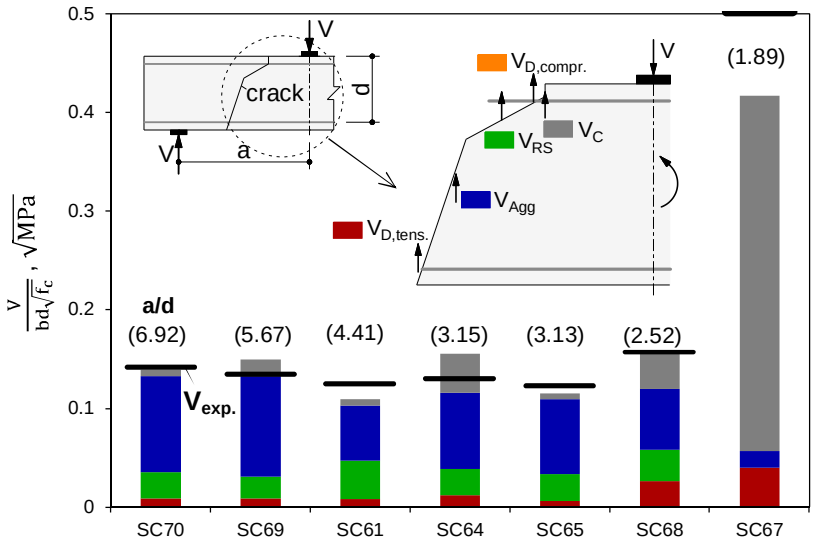

Fig. 1.10 Calculated shear carried by each shear-transfer mechanism at peak load compared to the experimental shear strength V_{exp} (adapted from Cavagnis et al.[15])

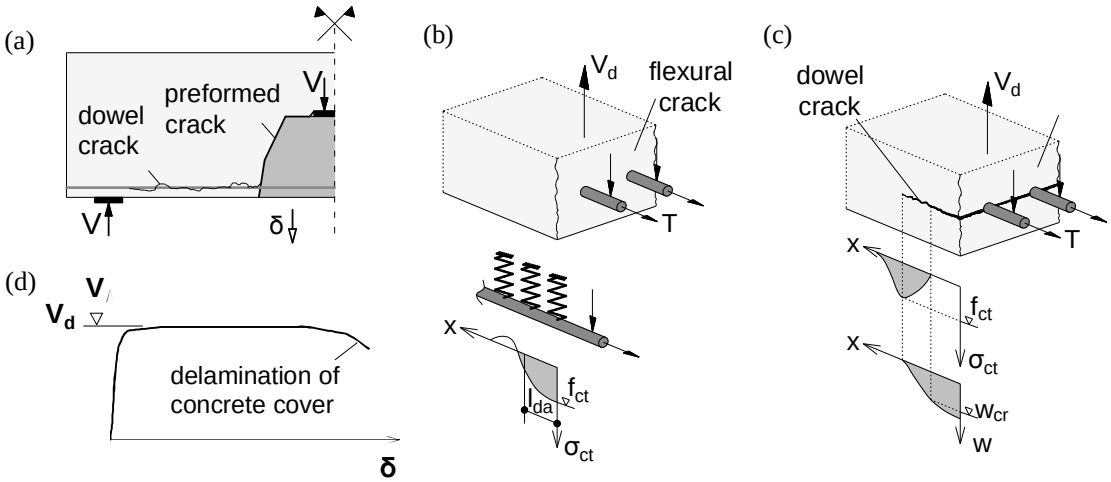

Fig. 1.11 Experiment to study dowel action in slender beams by Baumann and Rusch[16] (figure adapted from Huber et al.[17])

In deep beams, due to their short shear spans, dowel cracks do not propagate far and therefore the calculation of the shear contribution by dowel action V_d can be as simple as shown in Fig. 1.12. Mihaylov et al.[10] estimated the length of longitudinal reinforcement affected by dowel action, i.e. l_k (see Fig. 1.12a), and within this distance the rebars are considered as fixed-fixed steel beams (see Fig. 1.12b). The shear force V_d under a given transverse displacement Δ is calculated by assuming and elastic-plastic behaviour of the steel. The upper limit for V_d is reached when plastic hinges (see Fig. 1.12c) form at the two ends of the beam-dowel.

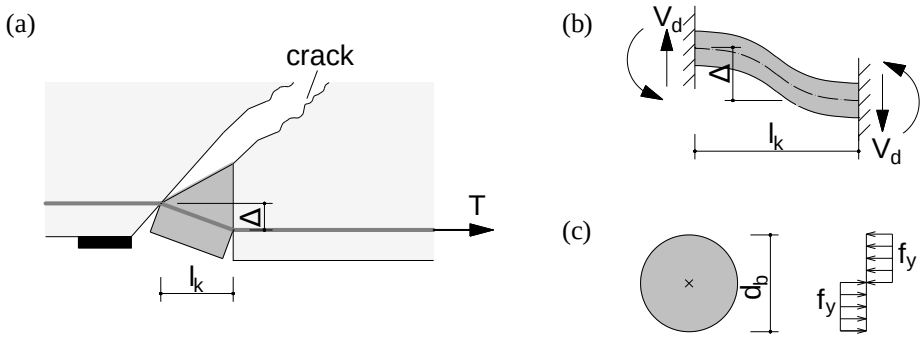

Fig. 1.12 Model for dowel action in deep beams applied by Mihaylov et al.[10]

1.4.2. Aggregate interlock

Aggregate interlock is a complex phenomenon occurring along cracks in concrete structures when the crack surfaces slide against each other as shown in Fig. 1.13a. The aggregates on one side of the crack interlock with the cement matrix on the opposite side, resulting in stress transfer along the crack including both shear and normal stresses. To study the shear transfer behaviour across cracks, Mansur et al.[18] performed push-off experiments to investigate 19 specimens as shown in Fig. 1.13b. The experimental results revealed five important stages during the monotonic loading (see Fig. 1.13c): 0-1 shear slip between the crack surfaces increases rapidly until the establishment of firm contact; 1-2 high stiffness is reached immediately after full contact between the two crack surfaces and it is found to benefit from high concrete strength and large amount of reinforcement; 2-3 the stiffness decreases and becomes independent of concrete strength and reinforcement ratio; 3-4 the reinforcement crossing the crack yields and the shear capacity of the specimens decreases rapidly; 4- after the loss of aggregate interlock the shear resistance decreases more gradually.

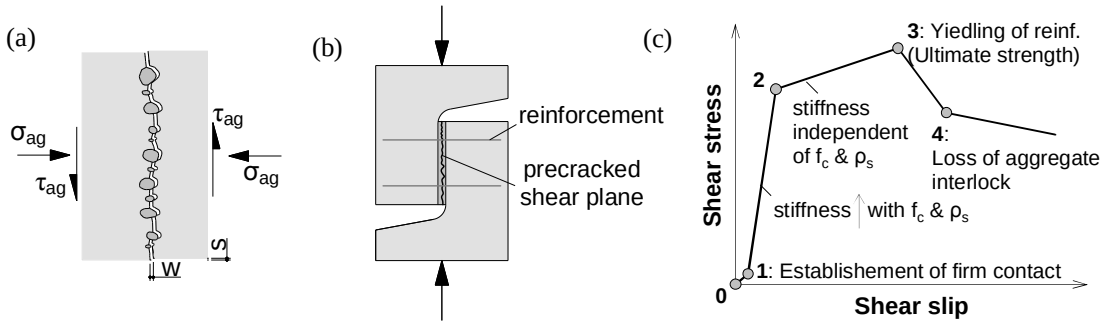

Fig. 1.13 Experimental study on aggregate interlock by Mansur et al.[18]

Several shear transfer models have been proposed by researchers to describe crack response to shear loading conditions. One of the most representative models is the two-phase model proposed Walraven[19] as shown in Fig. 1.14: the aggregate particles are idealized as rigid spheres (Fig. 1.14a), and the contact area between the aggregate and the cement matrix is determined by the crack opening and sliding as well as material properties, e.g. aggregate size etc. The cement matrix is assumed to behave in a rigid-plastic manner and the yield stress only depends on the concrete strength. Therefore, both of the shear and the normal stresses along the crack can be obtained based on equilibrium conditions shown in Fig. 1.14b.

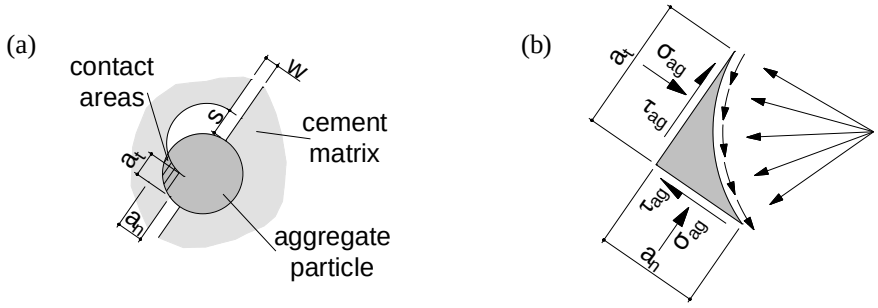

Fig. 1.14 Two-phase model for aggregate interlock by Walraven[19]

A Contact Density Model (CDM) proposed by Li et al.[20] is another widely used model, see Fig. 1.15. The crack surface is described with microscopic toughness of contact units and the direction of contact stress conicides with initial orientation of the contact units (see Fig. 1.15a). The contact behaviour on a contact unit is assumed elastic-perfectly-plastic as shown in Fig. 1.15b. The mortar around the contact area is elastically deformed until the relative displacement on the contact unit in the normal direction exceeds a predefined limit of 0.04 mm, and then under high confinement and frictional slip the motar behaves perfectly plastically. Through the effective ratio of contact area defined as a function of crack width, it is assumed that the contact is lost if the crack width exceeds one-half of the maximum aggregate size. Another important assumption of this theory is the idealization of the crack surface through a contact density function (see Fig. 1.15c). This function describes the distribution of crack contact units' orientations based on results from scanning of crack surfaces.

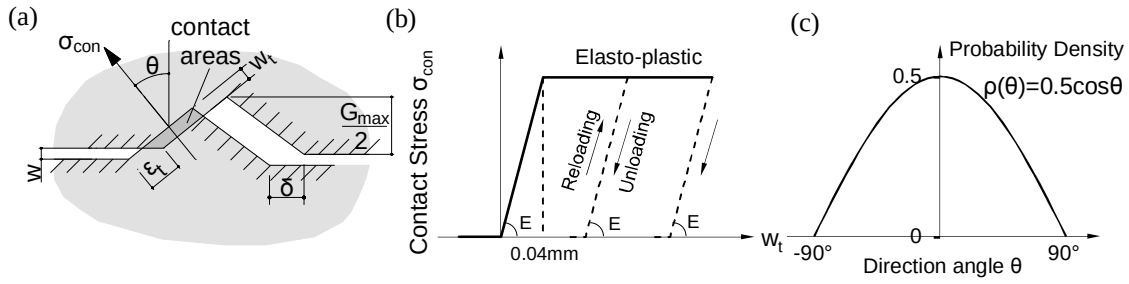

Fig. 1.15 Contact density model for aggregate interlock proposed by Li et al.[20]

1.4.3. Contribution of stirrups

Stirrups are effective in improving the shear resistance of RC beams through redistributing the tensile force along the shear crack to stirrups. Good bond condition between concrete and rebars brings the high tension in stirrups back to uncracked concrete as shown in Fig. 1.16a. To study this behaviour pull-out tests are performed (see Fig. 1.16b), and the bond stress-slip relationship is obtained based on experimental observations (see Fig. 1.16c). Several researchers made further investigation to correlate the shear slip to crack width and propose relationship between stirrup stress and crack width as shown in Fig. 1.16d. This method is based on comprehensive experimental work and solid physical background; however, the application is rather complex. Mihaylov et al.[10] considered this problem in a simpler manner: the tensile strain of the stirrup at crack is assumed to be double of the average strain along the entire length of the stirrup which is obtained based on the transverse expansion of the beam.

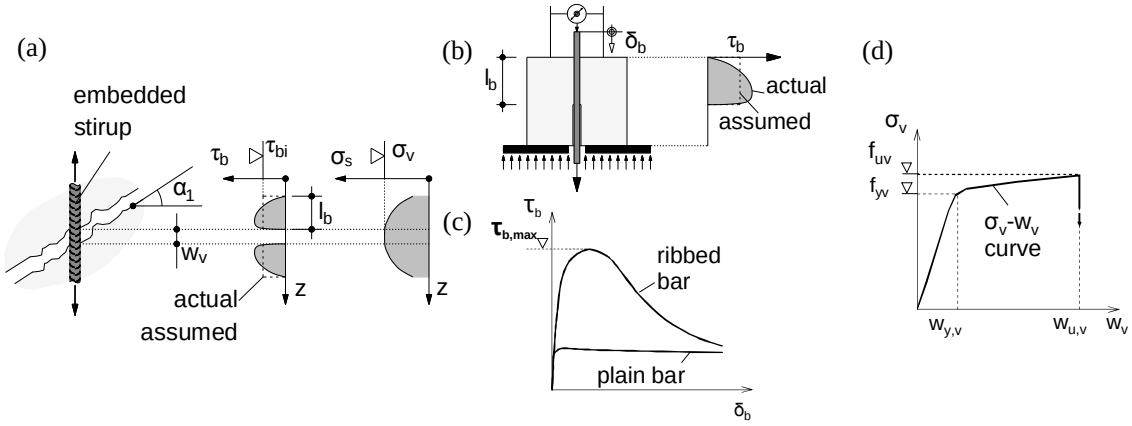

Fig. 1.16 Contribution of stirrups (adapted from Huber et al.[17])

1.4.4. Contribution of uncracked concrete

As mentioned earlier, a significant portion of the shear strength of deep beams is provided by the uncracked concrete above the critical shear crack. While in slender beams the critical crack has an S-shape and does not allow for direct compression to form between the load and support (Fig. 1.17a), in deep beams the crack is nearly straight and compressive stresses can "flow" parallel to the crack (Fig. 1.17b). This direct compression is often represented by a strut in strut-and-tie models as shown in Fig. 1.18a where the shear failure is usually dominated by crushing of the concrete in the strut. Bažant [21] included propagating crushing zone to the strut-and-tie model to take into account the localized fracture of the compression strut which was also observed in experimental studies. Fig. 1.19 shows a simply-supported deep beam tested by Mihaylov et al.[22] under cyclic loads. At shear failure the beam was separated into two parts by the diagonal crack, and it can be seen that above the critical crack localized concrete crushing occurred in a small zone near the loading plate. The spalled concrete and the orientation of the cracks in this zone indicated that it failed due to high diagonal compressive stresses. Mihaylov et al.[10] defined this zone as a "critical loding zone (CLZ)" and determined the approximate dimensions of the CLZ based on the size of the loading plate as shown in Fig. 1.18b. The zone of concrete above the critical diagonal crack is represented as a variable-depth elastic cantilever fixed at one end and loaded at the other. It is assumed that plane sections perpendicular to the bottom face of the cantilever remain plane and that the tip section is subjected to uniform compressive stress.

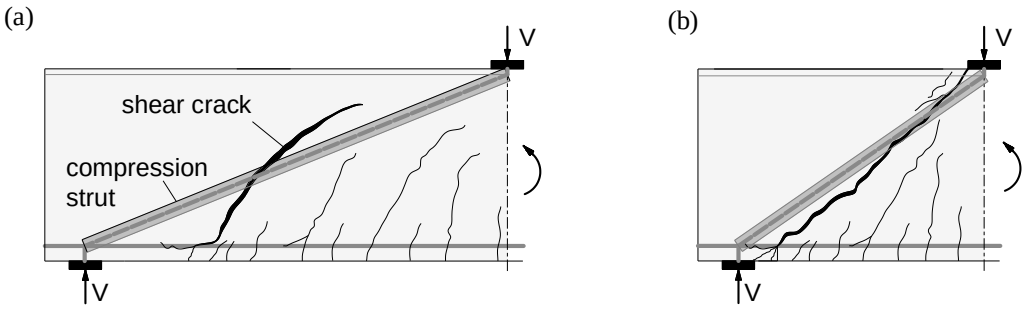

Fig. 1.17 Contribution of uncracked concrete in slender and deep beams

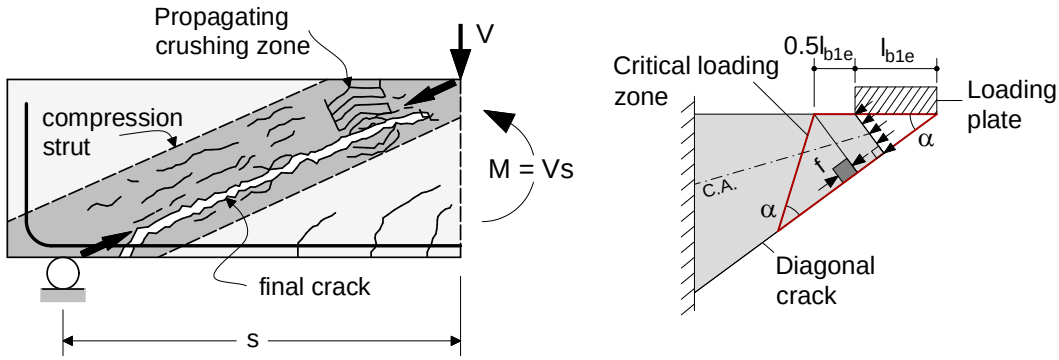

(a) Fracturing truss model proposed by Bažant[21] (b) Critical loading zone in 2PKT[10]

Fig. 1.18 Modelling the uncracked concrete in deep beams

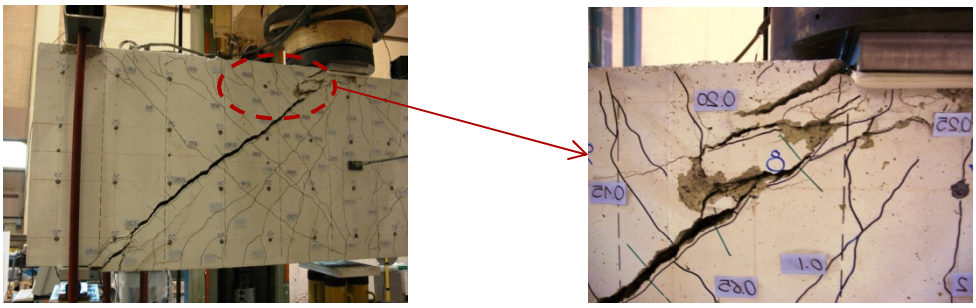

(a) Crack pattern of deep beam at shear failure (b) Concrete crushing near the loading plate

Fig. 1.19 Simply-supported deep beam under shear failure

1.5. Thesis outline

This thesis consists of 6 chapters and 3 appendixes.

Chapter 2 is a brief literature review listing different types of models to predict shear capacity of deep beams. Ten representative models are further studied in detail and applied to a large database of 574 tested simply-supported deep beams. Comparative studies are conducted for those selected models in terms of predicted shear capacity. Models with relatively better predictions are identified for further parametric studies, in which the effects of several key parameters, e.g. shear-span-depth ratio, longitudinal reinforcement ratio etc., are investigated. The purpose of this chapter is to provide an insight into the main characteristics of different types of models and to aid other researchers to select proper ones among a large number of models.

Chapter 3 firstly describes an existing kinematic model proposed by Mihaylov et al.[10], based on which a simple 1D macroelement composed of three springs (one transversal and two rotational) and two rigid bars is proposed to represent a shear span of continuous RC deep beams. The three springs are non-linear with constitutive relationships accounting for tension stiffening in the concrete around longitudinal reinforcement and different shear mechanisms along the critical shear crack. With few nodes and elements, the proposed new type of 1D deep beam element is used to predict the entire shear response of deep beam test specimens.

Chapter 4 proposes a framework to incorporate the new type of deep element into finite element programs for frame structures with slender elements. An existing programme named VecTor5 is selected as an example, in which the proposed new macroelement is added through a new subroutine without modifying the rest of the code. With the modified VecTor5 as a useful tool, a pushover analysis is conducted to a 20-storey frame with a large transfer girder designed based on ACI 318 code. The interaction between the deep girder and the rest of the structure is comprehensively studied.

Chapter 5 is devoted to proposing a model for the shear capacity of RC deep beams with web openings. Based on experimental studies of other researchers and finite element analyses, the load paths in deep beams with web openings are studied and a strut-and-tie model is proposed. The kinematic model proposed by Mihaylov et al.[10] is extended to account for the effect of web openings assuming the shear span is divided into two sub shear spans, one above and one below the opening. Together with other assumptions on the shear transfer path above the web opening, the extended kinematic model is applied to more than twenty deep beam test specimens with rectangular openings.

Chapter 6 presents a summary and conclusions from this study as well as suggestions for further research.

Appendix A contains a large database of 574 tested simply-supported deep beams, including all the important parameters regarding geometrical and material properties, as well as measured shear capacity and predicted shear capacity based on different models.

Appendix B presents the derivation of analytical expressions for the constitutive relationship of the three springs in the proposed 1D deep beam element in the initial stage of loading prior to the formation of critical shear cracks.

Finally, Appendix C contains a database of tested deep beams with rectangular web openings.

2.Models for Shear Strength of Reinforced Concrete Deep Beams

Abstract Since the 1960s, researchers have proposed different empirical formulas and analytical models for the shear strength of deep reinforced concrete beams. Some of these approaches have shown adequate accuracy when applied to small sets of beam tests, while their ability to predict the effect of a large range of test variables remains unknown. This paper presents a summary of models for deep beams from 73 publications, and focuses on a detailed evaluation of ten more recent models by using a database of 574 deep beam tests. It is found that a semi-empirical strut-and-tie model (STM) and a two-parameter kinematic theory (2PKT) for deep beams produce the least scattered predictions. The former model produced an average shear strength experimental-to-predicted ratio V_{exp}/V_{pred} of 1.00 with a coefficient of variation (COV) of 19.8%, while the latter resulted in an average of 1.08 with a COV of 15.4%. The two models are also compared by plotting the V_{exp}/V_{pred} ratios against different tests variables, and by performing parametric studies with individual test series. It is shown that the semi-empirical STM exhibits certain bias with respect to the shear-span-to-depth ratio, while the 2PKT produces uniform results across the entire range of experimental data. It is also noted that the semi-empirical STM requires somewhat less computational effort than the 2PKT approach.

Article Liu, J., and Mihaylov, B.I., "A comparative study of models for shear strength of reinforced concrete deep beams," *Engineering Structures*, V.112, April 2016, pp. 81-89. doi: 10.1016/j.engstruct.2016.01.012.

2.1. Introduction

The shear behaviour of deep reinforced concrete beams has been a subject of intensive experimental studies since the 1950s. It has long been recognized that, due to their small shear-span-to-depth ratios (a/d ≤ approx. 2.5), deep beams can carry significantly larger shear forces than slender beams. For this reason, deep beams are often used as transfer girders in buildings, cap beams in bridge bents, pile caps in foundations, and other heavily loaded structural members. From a modelling point of view, deep beams do not obey the classical plane-sections-remain-plane hypothesis, and therefore require different models than slender beams. Since the 1960s, researchers have proposed various empirical formulas and analytical models for evaluating the shear strength of deep beams[10, 23-32]. The most commonly used among these approaches is the strut-and-tie approach which is based on the main characteristic of deep beams, that is the direct transfer of forces from the loads to the supports by means of compressive stresses (strut action or arch action)[12]. This approach represents a simple and powerful tool for the design of structures, which typically provides conservative strength predictions. Other approaches have also shown adequate accuracy in predicting shear strengths when compared with small sets of experimental data[33], while their ability to capture the effects of a large range of test variables remains unknown. It is therefore the purpose of this paper to provide a more comprehensive evaluation and comparison of published models for shear strength of deep beams. The models will be compared by using a database of 574 tests of beams with a/d ≤ 3.0. The comparisons will be performed in terms of main physical assumptions, statistical performance, and the ability of the models to capture the effect of different experimental variables on the shear strength of deep beams.

2.2. Models for shear strength of RC deep beams

As part of this study, 73 papers on models for shear strength of deep beams published between 1987 and 2014 have been reviewed in detail. These models are applicable to beams subjected to single curvature bending under the action of point loads (typically one or two loads). Taking into account their main features, the models are divided into the following six categories: artificial intelligence models, numerical

models (i.e. finite element models, FEM, and discrete element models, DEM), strut-and-tie models, upper-bound plasticity models, shear panel models, and other mechanical models. As can be seen from Fig. 2.1, the majority of the 73 publications focus on strut-and-tie models, followed by numerical models, and artificial intelligence models. The smallest category is "other mechanical models" which includes a model proposed by Zararis[28] and a two-parameter kinematic theory (2PKT) proposed by Mihaylov et al.[10].

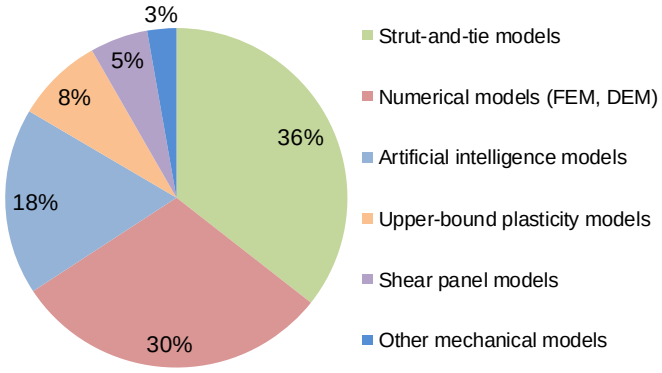

Fig. 2.1 Models for shear capacity of RC deep beams published between 1987 and 2014.

Out of all reviewed approaches, this study focuses on ten more recent models[10, 24-32] from four categories, excluding numerical approaches and artificial intelligence models. These models were adopted from a previous study by Senturk and Higgins[33] except for two models[10, 32] which were published after their study. The selected models are listed in Table 2.1 which also provides a summary of their main characteristics. Numerical models are excluded from the discussion because they are not developed specifically for deep beams and are significantly more complex than the rest of the approaches. Since one of the goals of this paper is to compare different physical assumptions for the modelling of deep beams, artificial intelligence models are also excluded from the discussion.

As can be seen from Table 2.1, the selected models are classified as either analytical or semi-empirical. By semi-empirical it is meant that the theoretical model includes factors, which are derived by fitting shear strengths obtained from deep beam tests. The physical assumptions and the range of test variables used in the development of the models impose limits on their applicability, as listed in the last column of Table 1. These limits, as reported in the original papers describing the models, are typically defined in terms of shear-span-to-effective-depth ratios (a/d) or shear-span-to-depth ratios (a/h). For example, limits $a/h \leq 2.0$ and $a/h \geq 0.23$ are meant to separate deep beams from slender beams and column-like members, respectively. The 2PKT[10] takes a different approach: the model has been developed to apply to members with short shear spans where the shear strength predicted by this model, V_{2PKT}, will exceed the shear strength predicted by sectional design procedures intended for longer spans, V_{sect}[5]. The following subsections provide a brief description of the ten selected models in their respective categories.

2.2.1. Strut-and-tie models

Strut-and-tie modelling is the most commonly used approach for deep beams as demonstrated by the fact that it has been part of design codes since 1984[6-9]. There are six strut-and-tie models included in this study, three of which semi-empirical and three analytical, see Table 1. In the general case, strut-and-tie models for deep beams include three mechanisms of shear resistance: a direct diagonal strut between the load and the support, a truss mechanism involving the vertical web reinforcement, and a truss mechanism-

Table 2.1 Summary of ten models for shear capacity of deep beams

Authors and year	Category	Type	Main failure mode	Size effect	Range of applicability
Mau and Hsu, 1989[24]	Shear panel	Semi-empirical	Web reinforcement yielding	No	$L_n/d \leq 3.3$ $\rho_h \leq 0.90\%$; $\rho_v \leq 2.45\%$
Ashour, 2000[25]	Upper bound plasticity	Analytical	Concrete crushing, reinforcement yielding along diagonal crack	No	$a/h \leq 2.5$
Hwang et al., 2000[26]	Strut-and-tie	Analytical	Concrete crushing in the vicinity of nodal zone	No	$a/d \leq 2.5$
Matamoros and Wong, 2003[27]	Strut-and-tie	Semi-empirical	Not explicitly defined	No	$a/d \leq 3.0$
Zararis, 2003[28]	Other mechanical	Analytical	Concrete crushing in compression zone	No	$1.0 \leq a/d \leq 2.5$
Tang and Tan, 2004[29]	Strut-and-tie	Analytical	Interaction between diagonal crushing and transverse splitting	Yes	$a/d \leq 2.7^*$
Russo et al., 2005[30]	Strut-and-tie	Semi-empirical	Not explicitly defined	No	$a/h \leq 2.0$ $L_n/h \leq 4$
Tan and Cheng, 2006[31]	Strut-and-tie	Analytical	Interaction between diagonal crushing and transverse splitting	Yes	$a/d \leq 3.38^*$
Yang and Ashour, 2011[32]	Strut-and-tie	Semi-empirical	Strut crushing	Yes	$a/h \leq 2.0^*$
Mihaylov et al., 2013[10]	Other mechanical	Analytical	Concrete crushing in critical loading zone	Yes	$V_{2PKT} \geq V_{sect}$

Notations: a = shear span from centre of support to centre of load; d = effective depth of section; h = total depth of section; L_n = clear span $\approx 2(a-l_{b2}/2)$; l_{b2} = width of support parallel to longitudinal axis of member; ρ_h = ratio of horizontal web reinforcement; ρ_v = ratio of transverse reinforcement ratio; V_{2PKT} = shear strength of deep beams acc. to 2PKT approach[10]; V_{sect} = sectional shear strength of slender beams acc. to AASHTO code[5].

* The papers describing the models do not explicitly specify a range of applicability. For this reason the limits on a/d and a/h adopted here correspond to the maximum values from test series used in the original papers for the validation of the models.

-involving the horizontal web reinforcement, see Fig. 2.2. The struts and ties join in nodal zones in the vicinity of the loading and support points. Hwang et al.[26] assumed that the proportion of shear carried by each of the three mechanisms can be determined based on the angle of the diagonal strut θ. Prior to yielding of the web reinforcement, the proportion of the shear carried by the vertical web reinforcement decreases with increasing θ, and that carried by the horizontal web reinforcement increases with θ. The proportion of shear resisted by the diagonal strut increases up to a strut angle of 45° and decreases for larger angles. Following the yielding of the web reinforcement, the shear increase is carried entirely by the diagonal strut up to the failure of the beam. The failure is assumed to occur due to crushing of the concrete in the vicinity of the nodal zones.

Matamoros and Wong[27] proposed a semi-empirical strut-and-tie model which includes factors for computing the strength of the three mechanisms in Fig. 2.2. The authors developed conservative expressions for these factors by fitting the model to a set of 175 deep beam tests. Russo et al.[30] followed a similar approach, but the coefficients were fitted with 240 tests aiming at an average experimental-to-predicted shear strength ratio of 1.0. In this model the shear strength is expressed with the following formula:

$$v = \frac{V}{bd} = v_c + v_w \tag{2.1}$$

Where v_c is the shear contribution provided by the diagonal strut and v_w is the contribution of the horizontal and vertical web reinforcements. Term v_c depends on the compressive strength of the concrete, the depth of the compression zone obtained from the classical beam theory, and the angle of the strut θ. Term v_w on the other hand depends on the ratios of the web reinforcements, the yield strength of the web reinforcements, the a/d ratio, and on angle θ.

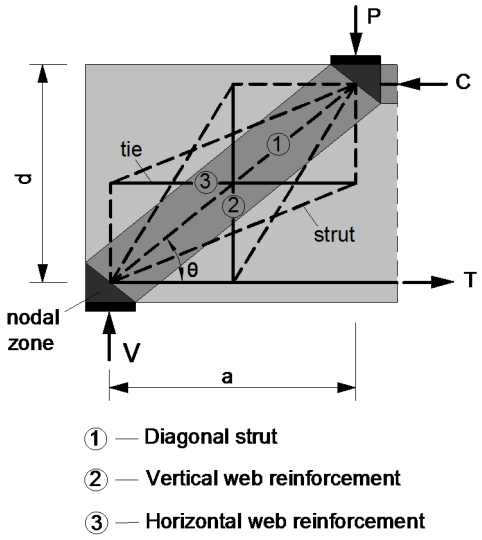

Fig. 2.2 Mechanisms of shear resistance in strut-and-tie models

Tang and Tan[29] proposed an interactive strut-and-tie model for shear strength of deep beams. In this model the failure of the beam is governed by the interaction of two failure modes: strut crushing and diagonal splitting. The interaction between the two modes is assumed to follow a linear relationship, in analogy to the classical Mohr-Coulomb failure criterion. Furthermore, the contributions to the splitting capacity provided by the concrete section, web reinforcement, and the flexural reinforcement are assumed to mobilize at the same rate. Tan and Cheng[31] proposed modifications to this model to better capture the size effect in shear. The modified model explains the size effect with the geometry of the struts, and the spacing and diameter of web reinforcement. Another strut-and-tie model which also accounts for the size effect in shear was proposed by Yang and Ashour[32] based on fracture mechanics. The authors introduced a crack band zone and a stress relief strip into the diagonal strut, and used energy equilibrium in the two zones. In this model the shear failure is governed by the crushing of the diagonal strut. Table 1 summarizes the main failure modes assumed in the ten models, and indicates which models account for the size effect in shear.

2.2.2. Upper-bound plasticity models

Ashour[25] proposed a model for the shear capacity of reinforced concrete deep beams based on the upper-bound theorem of the theory of plasticity. In this approach the concrete and steel are modelled as rigid - perfectly plastic materials. The model consists of two rigid blocks separated by a yield line (or failure zone) which extends from the inner edge of the support to the inner edge of the loading element, across the critical shear span of the beam. Two types of yield lines are proposed, namely a hyperbolic line and a line consisting of two straight segments. Due to the relative rotation between the two rigid blocks, energy is dissipated in both the concrete and steel along the yield line. The shear capacity of the beam is expressed as a function of the position of the centre of relative rotation between the blocks, and the solution of the model corresponds to the centre which produces a minimum shear capacity (upper-bound approach). In order to account for the fact that the concrete is not a perfectly plastic material, the concrete compressive strength is reduced by an effectiveness factor of ($0.8-f_c/200$), MPa. Other authors[34] have suggested that the effectiveness factors should be different for shear-critical beams with and without shear reinforcement.

2.2.3. Shear panel models

Mau and Hsu[35] have proposed a shear-panel model for deep beams which was later used by Bakir and Boduroğlu[36], Yu and Hwang[37], and other researchers. In this model the web of the beam is modelled as a reinforced concrete panel subjected to uniform shear stresses v and effective transverse compressive stresses p. The transverse stresses are due to the direct action of the point loads and support reactions on the horizontal top and bottom faces of the member. These stresses are sometimes referred to as clamping stresses, since they "clamp" the web in the vertical direction and in this way increase its shear resistance. The stress ratio p/v is assumed to remain constant throughout the loading history, and is determined based on the shear-span-to-depth ratio a/h. As the a/h ratio increases, the p/v ratio decreases because the clamping stresses diminish away from point loads and support reactions. The shear strength of the panel, and therefore the shear strength of the beam, is obtained by solving simultaneous equations for equilibrium, compatibility of deformations, and constitutive relationships for the concrete and reinforcement. Since the solution of these equations is relatively complex and inconvenient for design, Mau and Hsu have proposed a simplified version of the model[24] which is included in this study. The original model was simplified by deriving a formula containing four constants, and these constants were obtained by a calibration with experimental data. In their paper the authors state that the proposed formula gives accurate predictions in the range where the horizontal shear steel ratio is less than 0.9%, the web shear steel ratio is less than 2.45%, and the span-to-depth ratio is less than 3.3. These limits are therefore used to define the range of applicability of the model in Table 2.1.

2.2.4. Other mechanical models

In the mechanical model proposed by Zararis[28] the shear failure is assumed to occur along a critical diagonal crack with crushing of the concrete in the compression zone above this crack. As stated by the author, this zone acts as a "buffer" and prevents any meaningful slip displacements between the crack surfaces. In the absence of slip displacement, no aggregate interlock develops along the crack, and therefore the shear is carried entirely by the compression zone and the reinforcement crossing the crack. The resistance of the compression zone depends mainly on its depth above the critical crack, which can be significantly smaller than the depth of the compression zone above the flexural cracks. An expression is derived for the depth of the compression zone above the shear crack based on equilibrium conditions

and several simplifying assumptions. According to this expression, the ratio between the depth above the shear crack and that above the flexural cracks depends on the shear-span-to-depth ratio and the ρ_v/ρ_l ratio, where ρ_v is the ratio of transverse reinforcement and ρ_l the ratio of bottom longitudinal reinforcement. The classical beam theory is used to evaluate the depth of the compression zone above the flexural cracks. The shear resistance is obtained by considering the horizontal and moment equilibrium of the part of the beam above the critical crack. At failure the stresses in the compression zone reach the compressive strength of the concrete, and the stresses in the transverse reinforcement are assumed equal to the yield strength of the steel. It is stated that the assumption for yielding of the transverse reinforcement is not accurate for beams with $a/d < 1.0$, and therefore the model is applicable to beams with $1.0 \leq a/d \leq 2.5$. A similar approach is also followed to derive an expression for the shear strength of members with both transverse and horizontal web reinforcement.

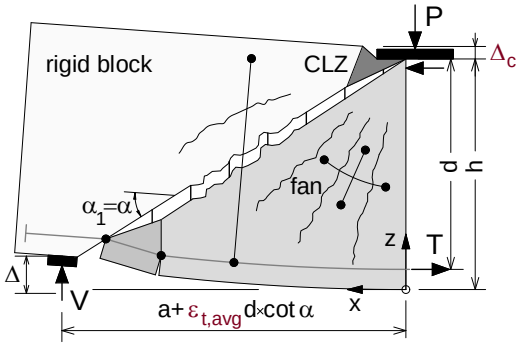

(a) Kinematics of deep beams

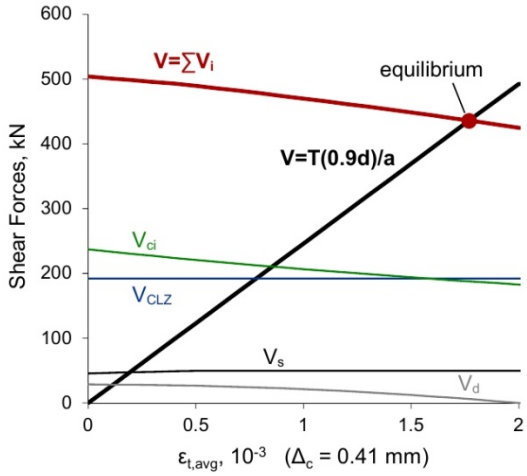

(Main properties of beam: a/d=1.0, d=500mm, ρ_l=1.2%, ρ_v=0.3%)

(b) Components of shear resistance and equilibrium at peak load

Fig. 2.3 Two-parameter kinematic theory (2PKT) for deep beams[10]

The two-parameter kinematic theory (2PKT) for shear behaviour of deep beams[10] is built on a kinematic description of the deformation patterns in deep beams. Similarly to the models by Ashour and Zararis, the shear failure is assumed to occur along a critical diagonal crack which divides the shear span into two parts as shown in Fig. 2.3a. The part below the crack is modelled by a fan of rigid radial struts while the

zone above the crack is represented by a rigid block. The deformation pattern of the shear span is described by two degrees of freedom (DOFs): the average strain along the bottom reinforcement $\varepsilon_{t,avg}$ and the vertical displacement in a critical loading zone (CLZ), Δ_c. The critical loading zone coincides with the compression zone above the critical diagonal crack discussed by Zararis. Degree of freedom $\varepsilon_{t,avg}$ causes widening of the critical crack while Δ_c is associated with both widening and slip in the crack. These deformations are exaggerated in Fig. 2.3a to better visualize the assumed kinematics at shear failure. In addition to the kinematic conditions, the 2PKT also includes equations for equilibrium and constitutive relationships for the mechanisms of shear resistance.

Degree of freedom Δ_c is obtained by assuming that the CLZ is at failure under diagonal compressive stresses, while DOF $\varepsilon_{t,avg}$ is obtained as illustrated in Fig. 2.3b. The thick black line in the plot shows the relationship between $\varepsilon_{t,avg}$ and the applied shear V, while the thick red line represents the shear resistance which decreases with increasing strains. This resistance consists of four components: shear carried in the CLZ, V_{CLZ}, aggregate interlock component V_{ci}, stirrups component V_s, and dowel action of the bottom reinforcement V_d. It can be seen that the reduction of shear resistance is caused by the weakening of shear components V_{ci} and V_d, while component V_{CLZ} is not influenced by DOF $\varepsilon_{t,avg}$. In this example component V_s is almost constant because DOF Δ_c=0.41 mm is sufficient to yield the stirrups even when $\varepsilon_{t,avg}$ is zero. The solution of the equations of the 2PKT corresponds to the intersection point of the black and red lines where the shear forces are in equilibrium. This graphical representation of the 2PKT is similar to that used by Muttoni in a critical shear crack theory for punching of slabs[38]. As the equations of the model are not suitable for a closed-form solution, the shear strength is found by an iterative solution procedure. With the predicted DOFs, the 2PKT can also be used to evaluate the deformation patterns of the beam near shear failure, including crack widths, deflections, and the complete displacement field of the beam. More recently this approach has been extended to capture the complete load-displacement response of simply supported deep beams[39] and the ultimate response of continuous deep beams[40]. It should be noted that in the 2PKT the flexural reinforcement is assumed to behave linearly, while yielding of the reinforcement can be taken into account by performing a flexural strength calculation based on code provisions. The final predicted failure load will be the minimum load obtained from a 2PKT shear calculation and a standard flexural strength calculation.

2.3. Comparison with experimental results

2.3.1. Database of deep beam tests

The ten models listed in Table 1 and summarized above are applied to a database of 574 tests of beams provided in an appendix. The tests in the database are selected based on the following criteria:

- Rectangular cross sections, no limits on member size;
- Three- or four- point bending without axial load or prestressing;
- Shear-span-to-effective-depth ratios $a/d \leq 3.0$;
- Steel reinforcement and normal weight concrete without limits on the yield strength of the steel and compressive strength of the concrete;
- Only beams with reported important test parameters are included (for example tests without reported loading and support plate widths are excluded);

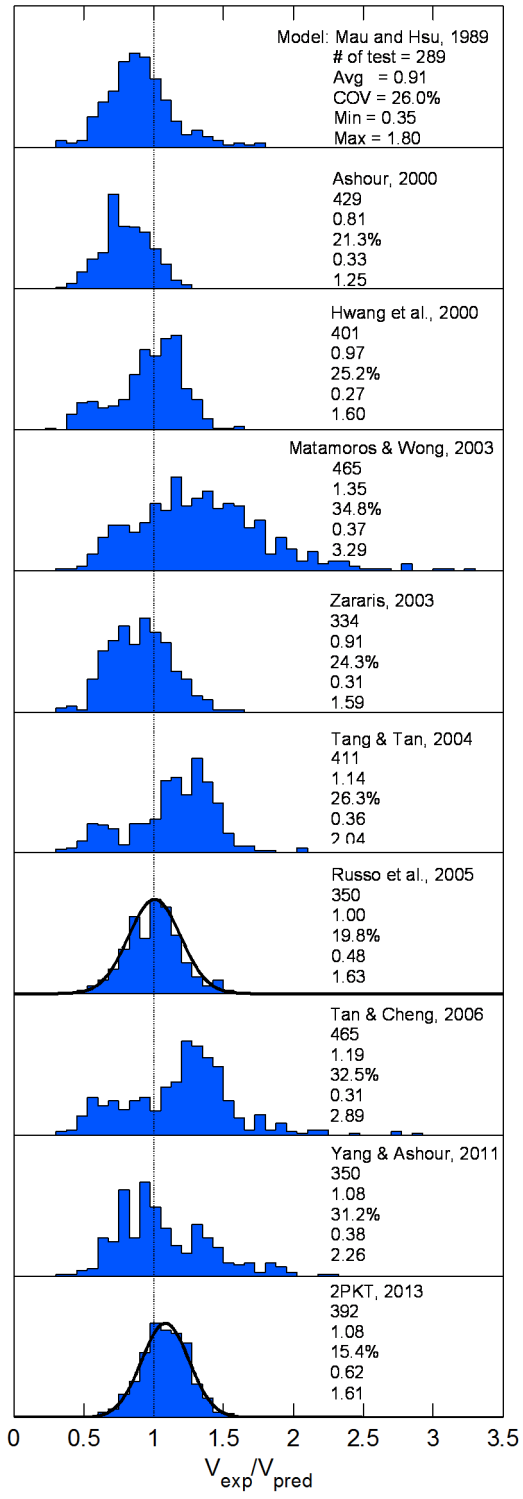

Fig. 2.4 Distribution of shear strength experimental-to-predicted ratios

- No bar cut-offs, no inclined web reinforcement, no fibres in the concrete;

- Beams supported directly on steel cylinders without steel plates between the cylinders and the specimen are excluded;

- No anchorage failures.

The shear-span-to-depth ratio of the beams in the database varies from 0.29 to 3.0, the effective depth from 160 mm to 2000 mm, the ratio of flexural reinforcement from 0.28% to 4.25%, the ratio of transverse reinforcement from 0% to 1.25%, the yield strength of the reinforcement from 267 MPa to 1330 MPa, and the concrete cylinder strength from 6.1 MPa to 120 MPa.

Out of the 574 beams in the database, 50 were reported to have failed in flexure and these are excluded from the comparisons. Furthermore, 59 beams which were reported to have failed in shear, but sustained maximum bending moments larger than 1.10 times the theoretical flexural capacity of the section are also excluded from the comparisons. The theoretical flexural capacity is calculated based on the ACI code provisions. By excluding these two groups of specimens, the number of tests is reduced to 465.

2.3.2. Shear strength predictions

The ten models included in this study were implemented in computer codes for calculating the shear strength of the test specimens from the database. In order to ensure that the implementation of the models was performed correctly, the results obtained in this study were compared with the results presented in the original papers describing the models. In all the cases it was found that the two sets of independent calculations produced almost identical shear-strength predictions. The results obtained for the entire database were then filtered according to the limits of applicability of each model (see the limits in Table 1). After this filtering, the number of tests varied from 289 for the model by Mau and Hsu[24] to 465 for the models by Matamoros and Wong[27], and Tan and Cheng[31].

The shear strength experimental-to-predicted ratios V_{exp}/V_{pred} obtained for the tests from the database are summarized in Fig. 2.4. The plots show the statistical distributions of these ratios produced by each of the ten models. The vertical axes of the plots are scaled such that the peak ordinates appear the same. The narrower is the distribution and the closer to the vertical line at $V_{exp}/V_{pred}=1$, the more accurate is the model. Based on these criteria it can be seen that the model by Russo et al.[30] and the 2PKT approach[10] produce most accurate shear-strength predictions. The Russo model produces a better average V_{exp}/V_{pred} (1.00 vs. 1.08), while the 2PKT results in a narrower distribution (coefficient of variation COV of 15.4% vs. 19.8%). The most unconservative predictions for the two models are respectively V_{exp}/V_{pred} of 0.48 and 0.62. In terms of range of applicability, the Russo model is applicable to 350 tests and the 2PKT approach to 392 tests. The smooth black lines in the plots show the theoretical Gaussian distributions for the two models. It can be seen that the results obtained with the 2PKT approach follow well the theoretical curve, indicating that this model is based on sound physical assumptions.

It is also of interest to examine whether the two models show any trends with respect to main test variables. Fig. 2.5 shows the V_{exp}/V_{pred} ratios plotted against the shear-span-to-depth ratio a/d, the ratio of transverse web reinforcement ρ_v, the ratio of flexural reinforcement ρ_l, and the effective depth d of the member. It can be seen that the 2PKT approach produces approximately constant average ratios and a uniform scatter across the entire range of the four variables, except for the beams with $\rho_v=0$. As observed in experimental studies, deep beams without shear reinforcement exhibit a larger experimental scatter, -

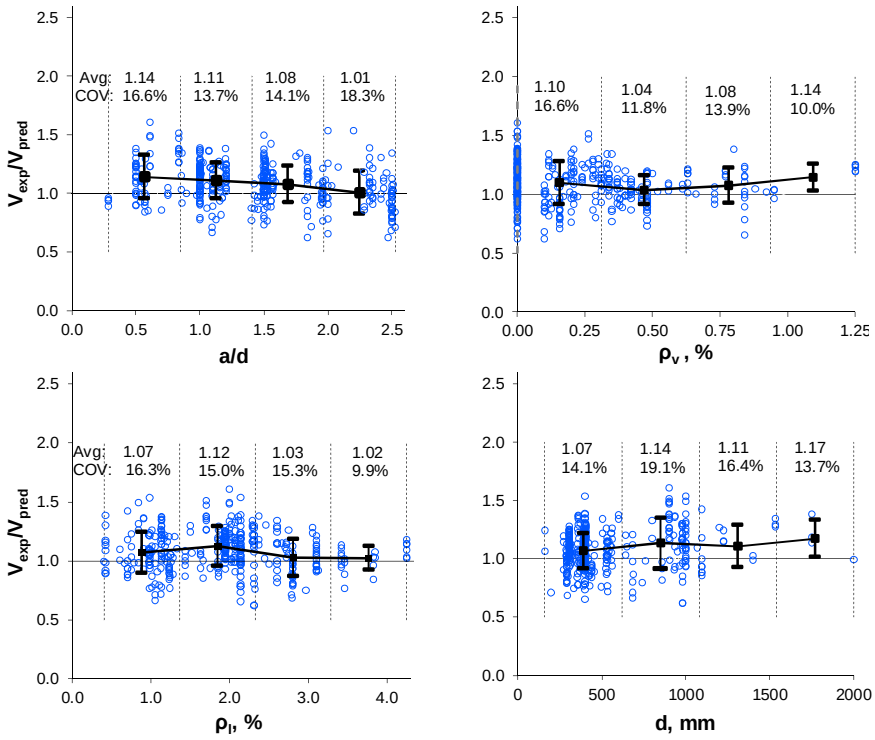

(a) Two-parameter kinematic theory (2PKT)[10] (Avg= 1.08, COV=15.4%)

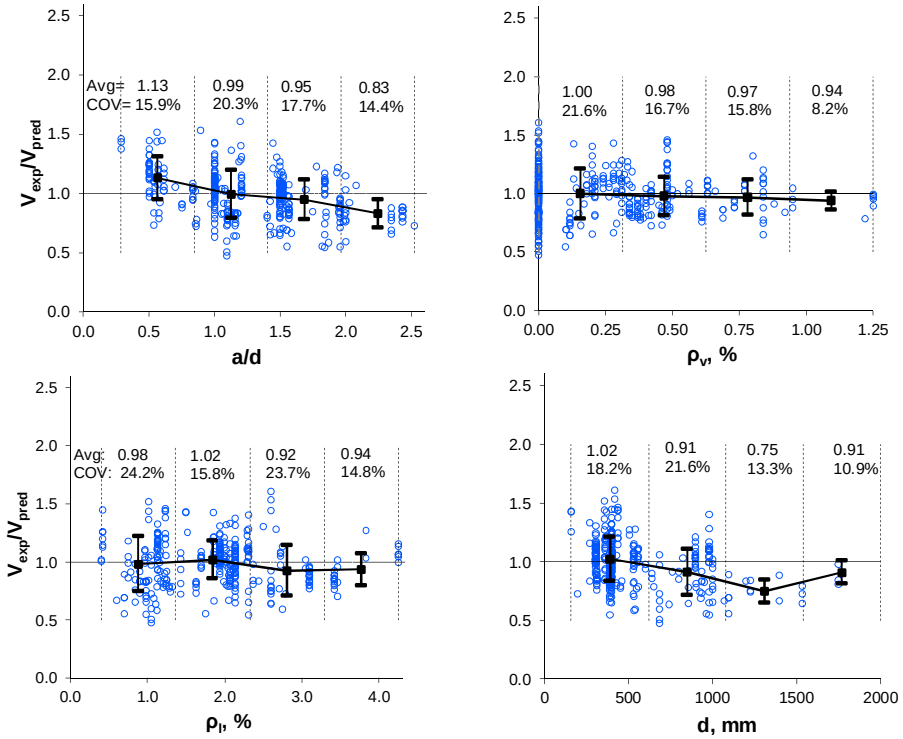

(b) Strut-and-tie model by Russo et al.[30] (Avg= 1.00, COV=19.8%)

Fig. 2.5 Distribution of shear strength experimental-to-predicted ratios against main test variables

- which is reflected in the larger scatter of the V_{exp}/V_{pred} ratios at ρ_v=0. The semi-empirical strut-and-tie model also produces uniform results with respect to variables ρ_v, ρ_l and d, while showing a certain bias - with respect to a/d. The model exhibits an almost linear trend of decreasing V_{exp}/V_{pred} ratios with increasing shear-span-to-depth ratio. It should be noted however that while the 2PKT produces less bias and less scattered predictions, it is more complex than the semi-empirical strut-and-tie model. As mentioned earlier, the model by Russo et al. uses a closed-form expression for the shear strength while the 2PKT approach requires an iterative solution procedure.

2.4. Parametric study

As concluded above, the strut-and-tie model proposed by Russo et al. and the 2PKT approach produced least scattered shear strength predictions. In the following sub-sections these two models are further evaluated in terms of their ability to capture the effect of different variables on the shear strength of individual sets of deep beams. Similarly to Fig. 2.5, the studied variables include the shear-span-to-ratio a/d, reinforcement ratios ρ_v and ρ_l, and the size of the member (size effect in shear).

2.4.1. Shear-span-to-depth-ratio a/d

Fig. 2.6 shows the effect of the a/d ratio on the shear strength of deep beams tested by Clark[41]. This effect is studied for four series of beams with different reinforcement ratios ρ_l from 0.98% to 3.05% and ρ_v from 0 to 1.22%. The experimentally obtained shear strengths are indicated with points, while the predictions of the 2PKT approach and the model by Russo et al. are depicted with continuous lines. Experimental points and prediction lines of the same colour correspond to the same test series. Both models predict that the shear strength decreases with increasing a/d from 1.0 to 2.5, and that the rate of decrease is reduced - or even diminished – by the addition of transverse reinforcement. The discontinuity in the black and green lines show that increased amounts of flexural reinforcement ρ_l results in increased shear strength predictions. These trends match the trends indicated by the experimental data, even though the two models differ slightly in terms of the absolute values of the predicted shear strengths. It can be seen that the model by Russo et al. overestimates the capacity of most of the test specimens while the 2PKT captures mostly the average experimental values. The shear strength of the only specimen with maximum amount of transverse reinforcement (ρ_v=1.22%) is overestimated by both models.

According to the 2PKT, the shear strength of beams without shear reinforcement decreases with increasing a/d due to the decrease of concrete shear components v_{CLZ} and v_{ci}. More slender beams are characterized by flatter diagonal cracks, which result in shallower CLZs with smaller shear resistance v_{CLZ} and larger displacement capacity Δ_c. The increased Δ_c in turn causes wider diagonal cracks with smaller aggregate interlock capacity v_{ci}. The sum of v_{CLZ} and v_{ci} in the 2PKT approach can be compared to the concrete shear strength contribution v_c in the model by Russo et al., see Eq.(2.1). This contribution is derived from the compression capacity of the diagonal strut, and decreases with increasing a/d due to the reduced angle of the strut θ. Both models predict that the contribution of the shear reinforcement increases with a/d, and that in beams with large amounts of stirrups this increase can compensate for the weakening of the concrete shear components ($v_{CLZ} + v_{ci}$) and v_c.

2.4.2. Transverse reinforcement ratio ρ_v

The effect of transverse reinforcement ratio ρ_v is studied with tests reported by Smith and Vantsiotis[42] (see Fig. 2.7). Three sets of beams with a/d ratios of 1.00, 1.50, and 2.08 were tested in this experimental-

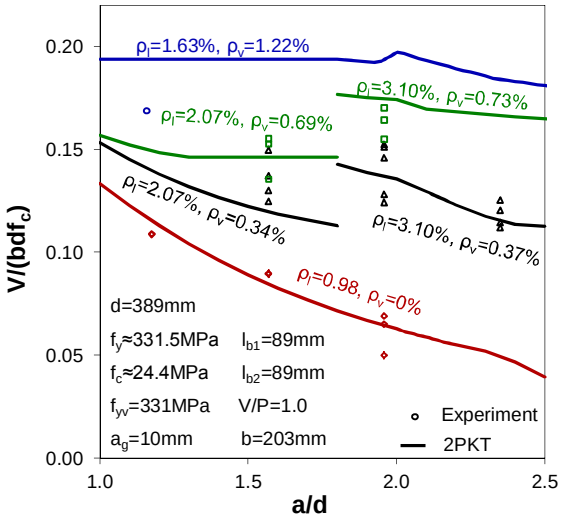

(a) Two-parameter kinematic theory (2PKT)[10]

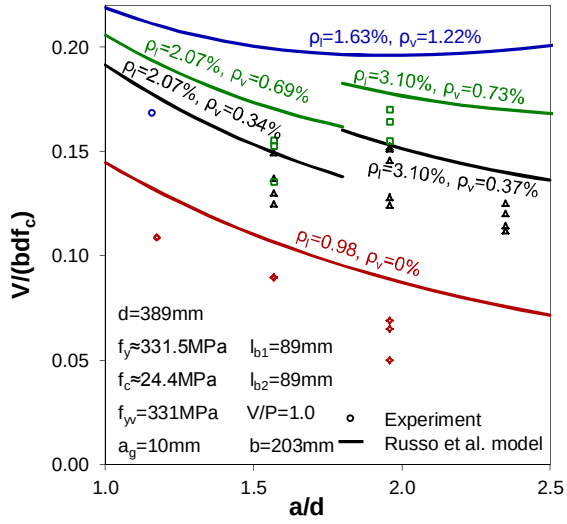

(b) Strut-and-tie model by Russo et al.[30]

Fig. 2.6 Effect of a/d ratio - tests by Clark[41]

-program. As evident from the plots, both models predict that the shear strength increases with ρ_v, and that the rate of increase is larger for beams with larger a/d ratios. This shows that transverse reinforcement is more effective in enhancing the shear capacity of more slender beams. A significant difference between the two approaches is that the strut-and-tie model predicts a linear relationship between v and ρ_v, while the 2PKT suggests that the effectiveness of stirrups diminishes beyond a certain value of ρ_v (ρ_v > approx. 0.7% for these tests). Beams with very large amounts of stirrups tend to fail along steep sections with crushing of the concrete across the entire section (sliding shear failures)[43]. These failures impose an upper limit on the shear strength which is evident from the red experimental points in Fig. 7 (beams with a/d=1.00). As it is well known, similar phenomenon occurs in slender beams where the shear strength provided by stirrups is limited by diagonal web crushing. Unfortunately, since ρ_v

of the specimens with a/d of 1.50 and 2.08 did not exceed 0.77%, these test series cannot be used to draw a stronger conclusion on the maximum shear strength of deep beams.

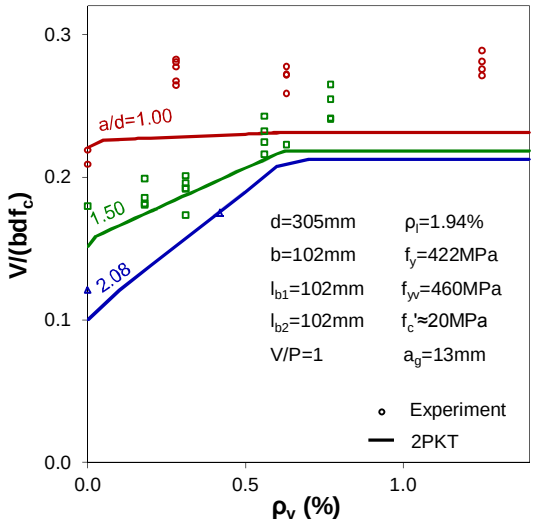

(a) Two-parameter kinematic theory (2PKT)[10]

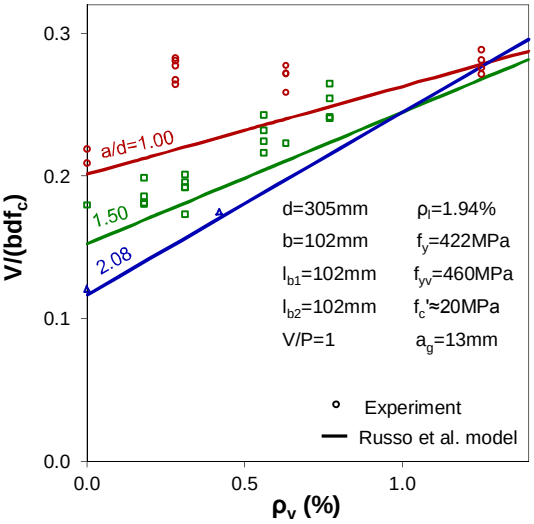

(b) Strut-and-tie model by Russo et al.[30]

Fig. 2.7 Effect of transverse reinforcement ratio - tests by Smith and Vantsiotis[42]

2.4.3. Longitudinal reinforcement ratio ρ_l

Fig. 2.8 shows the relationship between the longitudinal reinforcement ratio ρ_l and the shear capacity of deep beams tested by Mathey and Watstein[44]. When ρ_l was increased from 0.75% to 3.05%, the normalized shear stress V/bdf_c at shear failure increased from about 0.103 to about 3.05. In addition to ρ_l, the authors also varied the yield strength of the flexural reinforcement from 696 MPa for the beams with small reinforcement ratios to 267 MPa for the beams with large ρ_l. This variation followed approximately a linear relationship $f_y=-175\rho_l+845$ MPa, and this relationship was used to generate the prediction curves

in Fig. 8. It can be seen from the green prediction line that the model by Russo et al. captures very well the trend indicated by the experimental points. According to this model, larger amounts of flexural reinforcement result in deeper flexural compression zones, which in turn result in larger and stronger diagonal struts. The 2PKT approach also provides reasonable predictions, even though it slightly underestimates the shear capacity of the specimens with large reinforcement ratios and small yield strengths. In the 2PKT approach the effect of ρ_l and f_y is in part explained by the dowel action of the flexural reinforcement v_d which increases with these two variables. In addition, the model predicts that larger flexural reinforcement ratios result in narrower diagonal cracks with increased aggregate interlock resistance v_{ci}.

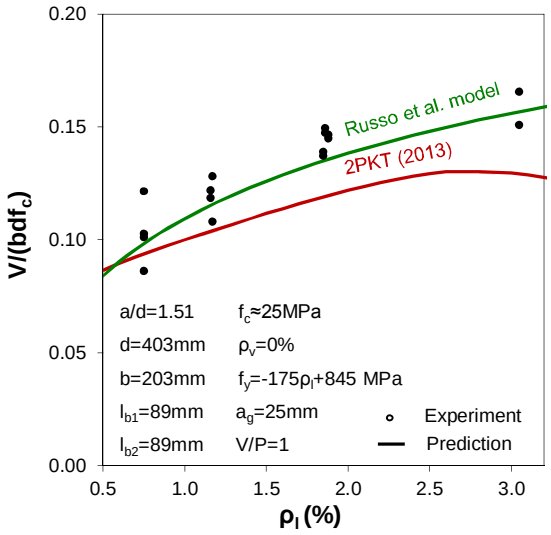

Fig. 2.8 Effect of ratio of tensile longitudinal reinforcement – tests by Mathey and Watstein[44]

2.4.4. Size effect in shear

The size effect in deep beams was investigated by Zhang and Tan[45] who tested series of geometrically similar beams with variable depth of the section, see Fig. 2.9. The experimental points in the plot show that when the effective depth of the section was increased from 313 mm to 904 mm, the shear stress at failure decreased by 18.1% and 13.9% for beams with and without stirrups, respectively. This size effect in shear can be important, since the depth of deep beams in buildings and bridges can be significantly larger than 904 mm, often reaching 3 to 6 m. As indicated in Table 1, four more recent models of the ten models discussed in this study account for the size effect in shear. The prediction lines in Fig. 2.9a show that the 2PKT approach captures well the decrease in shear strength observed in the tests. The model explains this decrease mainly with the weakening of the aggregate interlock mechanism. Larger beams have bigger critical loading zones with larger displacement capacities Δ_c. As mentioned earlier, larger Δ_c result in wider diagonal cracks and diminishing shear stresses transferred across the cracks. The 2PKT predicts that beams with transverse reinforcement will exhibit a slightly smaller size effect mainly due to the smaller proportion of shear resistance provided by the aggregate interlock mechanism. As evident from Fig. 2.9b, the strut-and-tie model does not account for the size effect in deep beams.

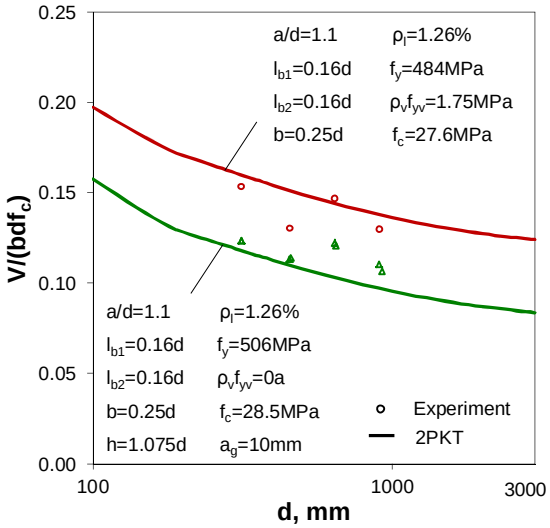

(a) Two-parameter kinematic theory (2PKT)[10]

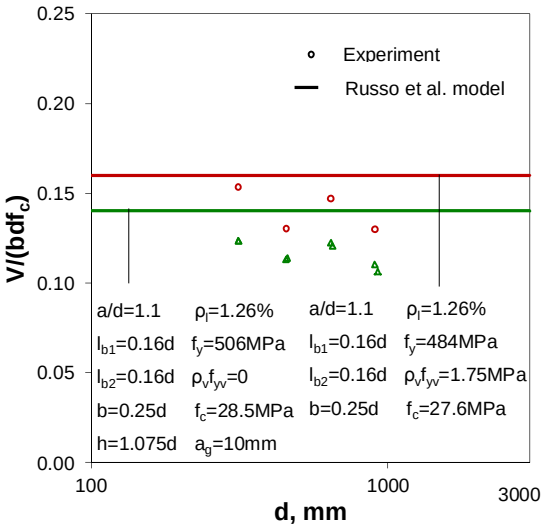

(b) Strut-and-tie model by Russo et al.[30]

Fig. 2.9 Size effect in shear – tests by Zhang and Tan[45]

2.5. Conclusions

In this study, models for shear strength of deep reinforced concrete beams from 73 publications were summarized and discussed. The models were divided into six categories based on their main features: strut-and-tie models, upper-bound plasticity models, shear panel models, other mechanical models, artificial intelligence models, and numerical models. Ten more recent models from the first four categories were evaluated by using a database of 574 published tests of beams with $a/d \leq 3.0$.

Based on the obtained shear strength experimental-to-predicted ratios V_{exp}/V_{pred} for the beams from the database, it was found that the semi-empirical strut-and-tie model proposed by Russo et al.[30] and the two-parameter kinematic theory (2PKT) by Mihaylov et al.[10] produced least scattered predictions. These

models resulted in average V_{exp}/V_{pred} ratios of 1.00 and 1.08 with coefficients of variation of 19.8% and 15.4%, respectively. The most unconservative predictions of the two models were respectively V_{exp}/V_{pred} of 0.48 and 0.62. When the V_{exp}/V_{pred} ratios were plotted against test variables a/d, ρ_v, ρ_l, and d, the 2PKT showed uniform results across the entire range of values. The strut-and-tie model also showed uniform results with respect to variables ρ_v, ρ_l, and d, while exhibiting a trend of decreasing V_{exp}/V_{pred} ratios with increasing a/d.

The ability of the two models to predict the effect of different variables was further evaluated by using individual series of deep beam tests. It was shown that both models capture well the trends in tests with variable a/d ratios, even though the strut-and-tie model produced somewhat unconservative predictions. In terms of the effect of flexural reinforcement ratio ρ_l, the model by Russo et al. exhibited excellent accuracy while the 2PKT was slightly conservative for beams with large ρ_l. It was found that the two models differ in predicting the effect of transverse reinforcement ratio ρ_v. While the strut-and-tie predicts a linear increase of shear strength with ρ_v, the 2PKT accounts for sliding shear failures which impose an upper limit on the shear capacity. The two models also differ in capturing the size effect in shear. The 2PKT predicted well this effect observed in two series of deep beam tests, while the model by Russo et al. does not capture the size effect in shear. Finally, it is noted that the 2PKT approach, which can be used to evaluate both shear strength and deformation patterns near failure, requires somewhat more computational effort than the semi-empirical strut-and-tie model which focuses on shear strength.

3. Macroelement for Complete Shear Behavior of Continuous Deep Beams

Abstract The evaluation of the serviceability, safety and resilience of deep girders in bridges and buildings requires accurate models for their pre- and post- peak shear behaviour. This paper purposes such a model formulated as a macroelement for deep shear spans under single and double curvature. The element has two nodes with two degrees of freedom per node (translation and rotation). The paper discusses the formulation of the macroelement based on a three-parameter kinematic theory and provides comparisons with tests. It is shown that the macroelement captures the redistribution of forces in continuous members, and in this way predicts their enhanced ductility as compared to simply supported beams. It is also shown that the model captures the opening of the critical shear cracks under loading. The crack predictions can be compared with field measurements to accurately evaluate the safety of the structure, and in this way to avoid potential costly strengthening measures.

Article Liu, J., and Mihaylov, B.I., "Macroelement for Complete Shear Behavior of Continuous Deep Beams," ACI Structural Journal, V.115, No.4, July 2018, pp. 1089-1099. doi: 10.14359/51702047.

3.1. Introduction

Deep beams with small shear-span-to-depth ratios (a/d ≤ approx. 2.5) possess large stiffness and can carry high shear forces by means of strut action. Owing to these properties, deep beams are used as transfer girders in high-rise buildings, pile caps in foundations, cap beams in bridge pier bents and other heavily-loaded members. In bridges, due to the significant increase of traffic intensity and truck loads in recent decades, cap beams have exhibited visible shear crack patterns as illustrated in Fig. 3.1. Diagonal crack widths of up to 0.9 mm have been observed in existing highway bridges[46] and have raised questions about the long-term serviceability and safety of such structures. While the safety of deep cap beams can be evaluated conservatively by using strut-and-tie models based one research studies[47-50] and design codes[5-9], more accurate models are needed in cases where this approach can result in costly and disruptive strengthening measures. In addition, in order to evaluate whether existing shear cracks represent danger for the structure, there is a need for models that can predict the opening of the cracks with increasing loads. As strut-and-tie models consider mainly the equilibrium of the beam near failure, they are not well suited for the evaluation of cracks.

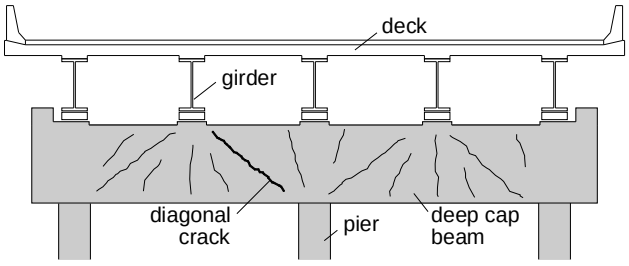

Fig. 3.1 Typical crack patterns in deep bridge pier caps.

Crack opening as well as the complete behaviour of deep beams can be evaluated by using 2D nonlinear finite element models (FEM) based on different constitutive relationships implemented in computer (VecTor2[13], ATENA[51], DIANA[52]). These models account for the complex behaviour of cracked reinforced concrete, and in this way can provide realistic predictions of the state of the structure. At the same time, FE models require significant time for modelling and computations, as well as a significant expertise to use safely. Therefore, there is a need for alternative approaches that are positioned between simple conservative strut-and-tie models and complex nonlinear FE models, combining relative simplicity

with high accuracy. Such models should be based on first principles and should use a straightforward input without open parameters. To address this necessity, this paper presents a macroelement for deep beams which uses only three degrees of freedom to describe the complete deformation patterns of deep shear spans. The macroelement is aimed at capturing the complete response of deep members, including the entire post-peak regime which is important for assessing the ability of the structure to redistribute forces and survive overloading. The formulation of the macroelement will be based on a three-parameter kinematic theory[40](3PKT) for the shear behaviour of deep beams proposed by Mihaylov et al. in 2015.

3.2. Kinematic model for deep beams

The three-parameter kinematic theory (3PKT)[40] is based on the premise that the apparently complex deformation patterns of deep beams subjected to double curvature can be described with a kinematic model with only three degrees of freedom (DOFs). The theory was developed to capture the peak shear resistance of deep beams as well as the deformations near failure. The three DOFs of the model are the average strains along the top and bottom longitudinal reinforcement, and the transverse displacement in the critical compression zones near point loads or support reactions. To predict the DOFs at shear failure, the 3PKT combines conditions for compatibility of deformations, equilibrium equations and constitutive relationships for the mechanisms of shear resistance [10, 39, 40].

The kinematic model and conditions for compatibility of deformations are summarized in Fig. 3.2. As illustrated in the figure, the 3PKT features a critical diagonal crack that divides the shear span into two parts, where each part is marked by radial cracks centred at the loading and support points. The shear failure of the member occurs with widening of the critical crack and crushing of the concrete in the vicinity of the load above the crack. This zone of crushed concrete is referred to as the critical loading zone (CLZ) and has been shown to trigger the shear failure of deep beams. The zones above and below the critical crack are represented by two fans of rigid radial struts pinned at the loading (support) point and connected to the bottom (top) longitudinal reinforcement. The fans open as the bottom and top reinforcement elongate with average strains $\varepsilon_{t1,avg}$ and $\varepsilon_{t2,avg}$, respectively. These strains are the first two DOFs of the kinematic model while the third DOF is the transverse displacement in the critical loading zone Δ_c. As shown in Fig. 3.2a, the complete deformation pattern of the shear span is obtained as a superposition of two simpler deformation patterns: one characterized by the opening of the two fans and the other by the transverse displacement in the critical diagonal crack. The former pattern can be associated with flexure while the latter with shear. The following is a brief summary of the kinematic model while the complete derivation of the model can be found elsewhere[40].

Fig. 3.2b summarizes the geometry of the kinematic model. The main geometrical properties of the model include the effective width of the loading plate l_{b1e}, the angle of the critical crack α_1, dowel length along the longitudinal reinforcement l_k, and the cracked length along the reinforcement l_{t1}. As it will be shown later, width l_{b1e} determines the size of the CLZ and has a significant influence on the behaviour of deep beams. The angle of the critical crack α_1 in deep beams is assumed to coincide with the angle of the diagonal of the shear span α. However, to ensure the transition from deep to slender beams, α_1 is limited to a minimum of θ, where θ is the angle of the cracks that develop away from concentrated loads. Having defined α_1, this angle is used to evaluate the dowel length l_k along the longitudinal reinforcement. This length corresponds to the zone at the bottom of the critical crack where the reinforcement is subjected to double curvature associated with DOF Δ_c. Eq. (3.3) for l_k takes into account the mean distance between the cracks along the bottom reinforcement s_{cr}. The last equation in Fig. 3.2b uses angle α_1 and length l_k to-

(a) Deformation patterns and DOFs

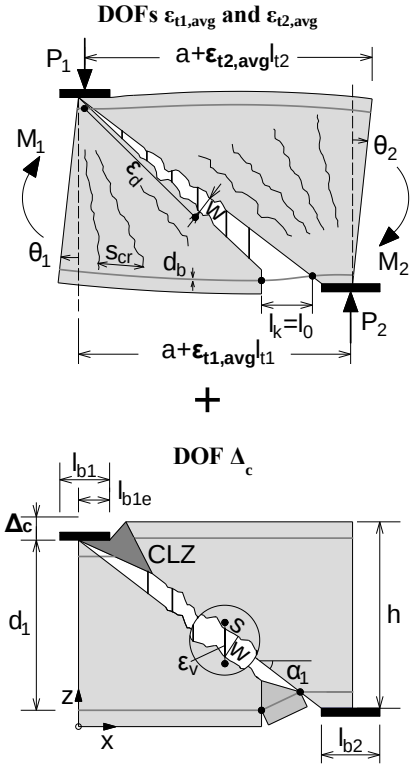

(b) Geometry

Effective width of loading plate

(3.1) $l_{b1e} = (V/P_1) l_{b1} \geq 3a_g$

Angle of critical crack

(3.2) $\alpha_1 = \alpha \geq \theta$

α - angle of line connecting inner end of l_{b2} and outer end of l_{b1e}

θ - based on sectional shear provisions of AASHTO[9] or 35°

Dowel length

(3.3) $l_k = l_0 + d_1(\cot\alpha - \cot\alpha_1)$

$$l_0 = 1.5(h - d_1)\cot\alpha_1 \geq s_{cr}$$

$$s_{cr} = \frac{0.28 d_b}{\rho_l} \frac{2.5(h - d_1)}{d_1}$$

Cracked length along longitudinal reinforcement

(3.4) $l_{t1} = d_1 \cot\alpha_1 + l_k - l_0$

(c) Deformations

Displacement field

- below critical crack

(3.5) $\delta_x = \varepsilon_{t1,avg} x$

(3.6) $\delta_z = \dfrac{\varepsilon_{t1,avg} x^2}{h - z}$

- above critical crack

(3.7) $\delta_x = \varepsilon_{t1,avg}(h - z)\cot\alpha + \varepsilon_{t2,avg}(x - a + z\cot\alpha)$

(3.8) $\delta_z = \varepsilon_{t1,avg} x \cot\alpha + \Delta_c + \varepsilon_{t2,avg} \dfrac{(x - a + z\cot\alpha)(a - x)}{z}$

Stirrup strain

(3.9) $\varepsilon_v = 2\dfrac{\Delta_c + 0.25\varepsilon_{t1,avg} d_1 \cot^2\alpha_1}{0.9 d_1}$

Crack width and slip

(3.10) $w = \dfrac{\varepsilon_{t1,avg} l_k}{2\sin\alpha_1} + \Delta_c \cos\alpha_1$

(3.11) $s = \Delta_c \sin\alpha_1 - \left|\varepsilon_d^*\right| \dfrac{d}{2\sin\alpha_1} \geq 0$

* The derivation of ε_d is listed in Appendix B.

Fig. 3.2 Kinematic model for shear spans of deep beams under double curvature.

- calculate the length of the longitudinal reinforcement l_{t1} within the cracked portion of the shear span. It is this length that is used to define the average strain $\varepsilon_{t1,avg}$ along the bottom reinforcement. A similar calculation can be performed to obtain the cracked length l_{t2} along the top reinforcement needed to define strain $\varepsilon_{t2,avg}$. Lengths l_{t1} and l_{t2} can be used together with DOFs $\varepsilon_{t1,avg}$ and $\varepsilon_{t2,avg}$ to express the opening of the fans of the kinematic model as follows, see Fig. 3.2a:

$$\theta_1 = \frac{\varepsilon_{t1,avg} l_{t1}}{d_1} \tag{3.12}$$

$$\theta_2 = \frac{\varepsilon_{t2,avg} l_{t2}}{d_2} \tag{3.13}$$

It will be shown later that rotations θ_1 and θ_2 are convenient for the formulation of a microelement for deep shear spans. In general, they can be used interchangeably with strains $\varepsilon_{t1,avg}$ and $\varepsilon_{t2,avg}$ as DOFs of the kinematic model.

Having defined the geometry of the kinematic model and its degrees of freedom, the deformations in the shear span are expressed based on small-displacements kinematics. These relationships are summarized in Fig. 3.2c and have meaning of conditions for compatibility of deformations. All deformations are expressed as functions of the three degrees of freedom of the kinematic model. Eq. (3.5) - (3.8) describe the complete displacement field of the shear span in an x-z coordinate system attached to the vertical section under the load P_1. These equations are used to derive Eq. (3.9) - (3.11) for the strain in the transverse reinforcement halfway along the critical crack ε_v as well as the relative displacements between the crack interfaces. In the macroelement, strain ε_v will be used to evaluate the shear resisted by the stirrups, while the crack width and crack slip will be used to evaluate the shear transferred across the crack by means of aggregate interlock. Note that DOF $\varepsilon_{t1,avg}$ causes opening of the critical crack, while DOF Δ_c causes both opening and slip. However, the slip on the crack caused by Δ_c is reduced by the shortening of the strut below the crack. This shortening is expressed with the strain in the strut ε_d (Fig. 3.2a) whose calculation is derived elsewhere[39] and summarized in Appendix B.

Finally, it should be noted that the formulation of the kinematic model leaves two open questions, namely how to determine the location and size of the critical loading zone. While the CLZ in Fig. 3.2 is located in the vicinity of load P_1, in reality it can also occur in the vicinity of the support reaction P_2. In the latter case the equations of the kinematic model remain the same, except that indexes 1 become 2. As with regards to the size of the CLZ, it depends on the shear-force-to-applied-load ratio $V/P_{1(2)}$ via the effective width of the loading plate $l_{b1(2)e}$. Because the $V/P_{1(2)}$ ratio can change during the loading of statically indeterminate beams, it is necessary to determine which value is the most appropriate. These questions will be addressed later in the formulation of the macroelement for deep shear spans.

3.3. Macroelement for deep shear spans

The deformation patterns described by the kinematic model in Fig. 3.2a point to a convenient formulation of a macroelement for deep shear spans. The top deformation pattern consists of the opening of the two fans of struts under the action of the bending moments M_1 and M_2 in the end sections of the shear span. As the opening is expressed with the end rotations θ_1 and θ_2, the behaviour of the fans can be modelled by two rotational springs with appropriate M-θ relationships. Similarly, the bottom deformation pattern consists of the vertical movement in the critical diagonal crack under the action of the shear force V. The behaviour across the critical crack can therefore be modelled with a vertical spring with an appropriate V-

Δ_c relationship. The deformations of the springs θ_1, θ_2, and Δ_c coincide with the three degrees of freedom of the kinematic model. If these DOFs are predicted throughout the loading history, they can be used to compute the evolution of the deformation patterns of the shear span.

This idea is implemented in the macroelement for deep shear spans shown in Fig. 3.3a. In this element the rotational springs are placed at the end sections while the transverse spring is in the middle of the shear span. The three springs are connected with rigid bars and the end sections are represented with two rigid blocks. As shown in the deformed configuration of the macroelement in Fig. 3.3, the end sections perform translations and rotations, and the rigid rods remain parallel to each other. The displacements of the end sections v_1, v_2, φ_1, and φ_2 represent the external degrees of freedom of the macroelement, while θ_1, θ_2, and Δ_c are the internal DOFs. The relationship between the two sets of DOFs depends on the stiffnesses of the three springs k_1, k_2, and k_3. As the springs are nonlinear, k_1-k_3 will represent the secant stiffnesses obtained by dividing the current force in the spring by the corresponding deformation in the spring. Based on this formulation, the relationship between the forces in the end sections and the displacements of these sections can be expressed as:

$$\begin{Bmatrix} M_1 \\ V \\ M_2 \\ -V \end{Bmatrix} = [k] \begin{Bmatrix} \varphi_1 \\ v_1 \\ \varphi_2 \\ v_2 \end{Bmatrix} \tag{3.14}$$

where [k] is the stiffness matrix of the element:

$$[k] = \frac{1}{k_1 + k_2 + k_3 a^2} \times \begin{bmatrix} k_1\left(k_2 + k_3 a^2\right) & -k_1 k_3 a & -k_1 k_2 & k_1 k_3 a \\ -k_1 k_3 a & k_3\left(k_1 + k_2\right) & -k_2 k_3 a & -k_3\left(k_1 + k_2\right) \\ -k_1 k_2 & -k_2 k_3 a & k_2\left(k_1 + k_3 a^2\right) & k_2 k_3 a \\ k_1 k_3 a & -k_3\left(k_1 + k_2\right) & k_2 k_3 a & k_3\left(k_1 + k_2\right) \end{bmatrix} \tag{3.15}$$

The relationship between the internal and external DOFs is:

$$\begin{Bmatrix} \theta_1 \\ \theta_2 \\ \Delta_c \end{Bmatrix} = [T] \begin{Bmatrix} \varphi_1 \\ v_1 \\ \varphi_2 \\ v_2 \end{Bmatrix} \tag{3.16}$$

where [T] is a transformation matrix:

$$[T] = \frac{1}{k_1 + k_2 + k_3 a^2} \times \begin{bmatrix} \left(k_2 + k_3 a^2\right) & -k_3 a & -k_2 & k_3 a \\ -k_1 & -k_3 a & \left(k_1 + k_3 a^2\right) & k_3 a \\ k_1 a & -\left(k_1 + k_2\right) & k_2 a & \left(k_1 + k_2\right) \end{bmatrix} \tag{3.17}$$

It is important to note that this formulation with only three internal DOFs is significantly simpler than complex finite element models of deep beams that use thousands of DOFs. Furthermore, the proposed element is compatible with elements for slender beams both in terms of simplicity and degrees of

freedom. Therefore, the macroelement can be easily connected to other elements to model continuous beams or complex structures. However, to complete the formulation of the macroelement, it is necessary to derive the constitutive relationships for the three nonlinear springs.

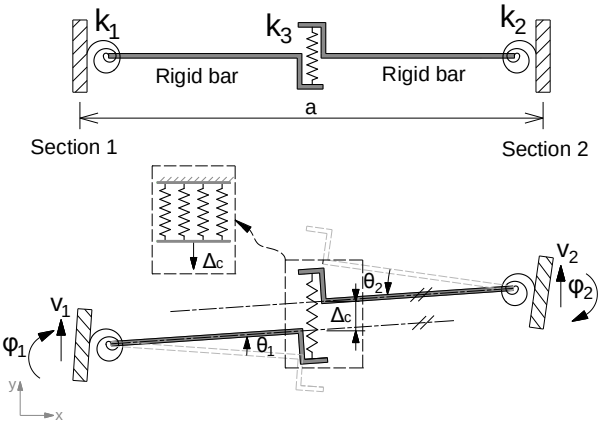

Fig. 3.3 Macroelement for deep shear spans.

3.4. Constitutive relationships of the springs

The constitutive relationships M-θ and V-Δ_c will be derived from first principles by using the equations of the kinematic model. To derive the relationships of the rotational springs, it is necessary to consider the compatibility conditions expressed by Eq. (3.12) - (3.13). For a given θ, these equations are used to calculate the average strain in the longitudinal reinforcement $\varepsilon_{t,avg}$ along the cracked length l_t. As deep beams develop arch action and work with nearly constant tension force along the longitudinal reinforcement, strain $\varepsilon_{t,avg}$ can be used to calculate the tension force in the section with maximum bending moment:

$$T = E_s A_s \varepsilon_{t,avg} + \frac{0.33\sqrt{f_c'}}{\sqrt{1+200\varepsilon_{t,avg}}} A_{c,eff} \le A_s f_y \tag{3.18}$$

where the first term of this expression models the behaviour of bare elastic reinforcement, the second term accounts for the tension stiffening effect of the concrete[53], and $A_s f_y$ is the yield force of the reinforcement. Quantity $A_{c,eff}$ is the area of the concrete around the reinforcing bars responsible for the tension stiffening effect. The width of this area is equal to the width of the section *b* while the depth is estimated as the minimum of 2.5(h-d) and h/2.[9] Assuming that the lever arm of the internal forces in the end sections of the shear span is approximately 0.9d, the bending moment in the section is calculated as M=T(0.9d).

The M-θ relationship obtained in this manner is valid when the shear span is fully cracked. However, at the early stages of loading when the cracks in the fans develop consecutively away from the end sections, the rotational springs must be stiffer. This effect is included in the plot in Fig. 3.4 which shows the complete M-θ relationship of the rotational springs. As evident from the plot, the initial behaviour is linear up until the first cracking in the end section at $M=M_{cr}$, followed by a transition curve that models the formation of flexure-shear cracks up until $M=M_0$. When the moment exceeds M_0, the fan is fully cracked and the response of the spring is governed by Eq. (3.18). To model the initial response prior to

cracking, the elastic stiffness of the spring is estimated according to the Timoshenko beam theory and the derivation is listed in Appendix B:

$$k_{1,el} = k_{2,el} = \frac{6kG_cAE_cI}{12E_cI + kG_cAa^2}\left(\frac{4E_cI}{kG_cAa} + \frac{a}{3}\right) \tag{3.19}$$

where A is the gross cross-sectional area of the section, I is the gross moment of inertia, E_c is the elastic modulus of the concrete, $G_c \approx 0.4E_c$ is the shear modulus, and k=1.2 for rectangular sections. The cracking moment M_{cr} is estimated as $T_{cr}(0.9d)$, where T_{cr} is the force necessary to crack the effective tension area $A_{c,eff}$:

$$T_{cr} = \left[A_{c,eff} + (E_s/E_c - 1)A_s\right]0.63\sqrt{f_c'} \tag{3.20}$$

Based on comparisons with tests and nonlinear finite element simulations, the bending moment M_0 is estimated at $2T_{cr}(0.9d)$. To approximate the response of the rotational springs in the range $M_{cr} \le M \le M_0$, it is proposed to use a parabolic curve determined by the coordinates of the initial and final points at $M=M_{cr}$ and $M=M_0$, as well as the slope at the first point. This slope is estimated as $k_s=E_sA_s(0.9d)d/l_t$ and equals the stiffness of the rotational spring obtained by assuming bare reinforcement. All equations describing the backbone curve in Fig. 3.4 are summarized in Appendix B.

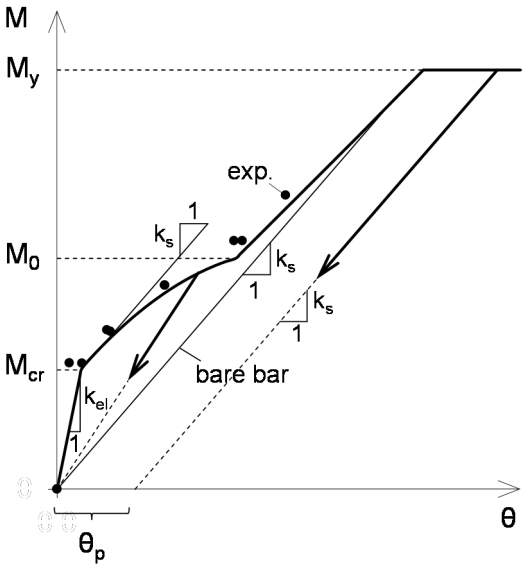

Fig. 3.4 Behaviour of rotational springs.

To complete the M-θ relationship, in addition to the backbone curve, it is also necessary to define the unloading of the rotational springs. This is important for studying the post-peak behaviour of shear critical members and the redistribution of forces in continuous deep beams. As indicated in Fig. 3.4, prior to the yielding of the reinforcement the unloading branch is assumed linear without residual rotations to keep the formulation as simple as possible. If the reinforcement yields, the unloading stiffness is estimated as equal to k_s.

The transverse spring of the macroelement models the mechanisms of shear resistance across the critical diagonal crack. The 3PKT method accounts for four shear contributions shown in Fig. 3.5: shear carried in the critical loading zone V_{CLZ}, aggregate interlock shear along the critical crack V_{ci}, shear carried by the stirrups V_s, and shear resisted by the dowel action of the flexural reinforcement V_d. Therefore, as indicated in Fig. 3.3, the transverse spring can be viewed as consisting of four parallel springs. The constitutive relationship of each of these springs is derived separately, and the results are combined to obtain the complete V-Δ_c relationship.

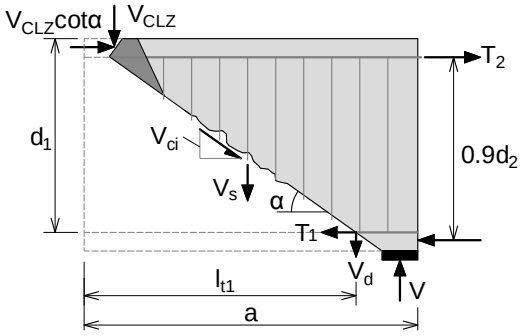

Fig. 3.5 Shear mechanisms in deep beams.

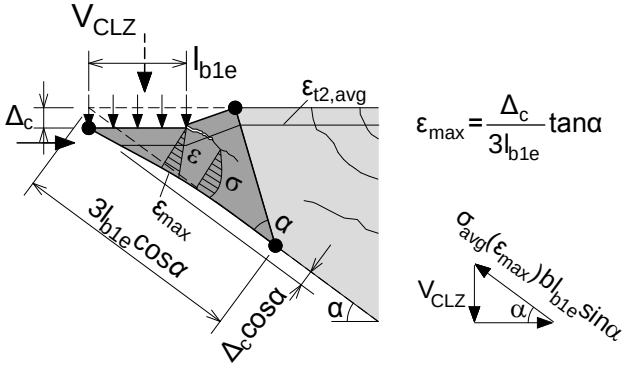

Fig. 3.6 Modelling of the critical loading zone (CLZ).

A major contribution to the shear resistance of deep beams is provided by the critical loading zone. The modelling of this zone is illustrated in Fig. 3.6[39]. The CLZ has a triangular shape that depends on the effective width of the loading plate l_{b1e} and the angle of the critical crack in the vicinity of the load approximated with the angle α. The concrete in the CLZ is subjected to diagonal compressive stresses σ and strains ε. The strains are assumed to vary linearly from zero at the free edge of the beam to ε_{max} along the bottom face of the CLZ. Taking into account the deformed configuration of the CLZ, strain ε_{max} is expressed as a function of DOF Δ_c as shown in Fig. 3.6. The diagonal compressive stresses σ are calculated from the strains ε by using an appropriate stress-strain relationship for the concrete under uniaxial compression[54]. In order to evaluate the diagonal compressive force in the CLZ, the average stress in the concrete σ_{avg} is multiplied by the area of the section passing through the edge of the loading plate and perpendicular to the bottom face of the CLZ. This diagonal force is shown in the triangle of forces in Fig. 3.6 based on which the shear carried in the critical loading zone V_{CLZ} is expressed:

$$V_{CLZ} = k_c \sigma_{avg} \left[\varepsilon_{\max} \left(\Delta_c \right) \right] b l_{b1e} \sin^2 \alpha \tag{3.21}$$

The additional coefficient k_c in this expression accounts for the tensile strains in the longitudinal reinforcement crossing the CLZ. These strains damage the concrete and reduce its resistance to diagonal compression. This compression softening effect is modelled according to the modified compression field theory[53]:

$$k_c = 1 / \left(0.9 + 170 \varepsilon_1 \right) \leq 1 \tag{3.22}$$

where ε_1 is the principal tensile strain in the CLZ estimated as

$$\varepsilon_1 = \left(1 + \cot^2 \alpha \right) \varepsilon_{t2,avg} \geq 0 \tag{3.23}$$

The V_{CLZ}-Δ_c relationship is plotted in Fig. 3.7a for a sample deep beam. It can be seen that the response of the CLZ resembles that of concrete in compression, except that it is more ductile due to the averaging of the compressive stresses in the vicinity of the load. It can also be seen that a strain $\varepsilon_{t2,avg}=1x10^{-3}$ results in a significant compression softening effect.

Fig. 3.7b shows the constitutive relationship of the aggregate interlock spring V_{ci}-Δ_c. As proposed by Mihaylov[39], this relationship is expressed as

$$V_{ci} = 0.18 v_{ci} \left(w, s \right) b d \tag{3.24}$$

based on a contact density model[20] (CDM) proposed by Li et al. This model is used to evaluate the shear stress v_{ci} on the critical diagonal crack as a function of the width of the crack *w* and the slip on the crack *s*. The equations for computing $v_{ci}(w,s)$ are provided in the appendix of the paper. In the original CDM v_{ci} vanishes when the w exceeds one-half of the maximum aggregate size a_g, while in the macroelement this limit is increased to a_g to account approximately for the global roughness of the critical crack (see Appendix B). The relative displacements between the crack faces are calculated from Eq. (3.10) – Eq. (3.11) of the kinematic model as functions of DOFs $\varepsilon_{t1,avg}$ and Δ_c. As can be seen from the solid line in Fig. 3.7b, Δ_c alone causes an approximately parabolic V_{ci}-Δ_c behaviour with pre- and post- peak regimes. When $\varepsilon_{t1,avg}>0$, the crack is open even when $\Delta_c=0$, and the crack faces require a certain slip displacement before they come in contact and begin to transfer shear.

The third mechanism of shear resistance plotted in Fig. 3.7 is the tension in the transverse reinforcement crossing the critical diagonal crack. This V_s-Δ_c curve is obtained from:

$$V_s = \sigma_v \rho_v b \left(d \cot \alpha_1 - l_0 - 1.5 l_{b1e} \right) \tag{3.25}$$

where σ_v is the stress in the stirrups and $\rho_v \leq 0.15 f_c' / f_{yv}$ is the stirrup ratio. Stress σ_v is calculated from the strain of the stirrups ε_v by using an elastic – perfectly plastic stress-strain relationship for the steel. As before with regards to *w* and *s*, strain ε_v is calculated from the kinematic model as a function its DOFs (Eq. (3.9). The expression in the brackets of Eq. (3.25) is the portion of the horizontal projection of the critical crack along which the stirrups are considered sufficiently strained to contribute to the shear resistance. This projection should not be taken smaller than $0.5d\cot\alpha_1$.

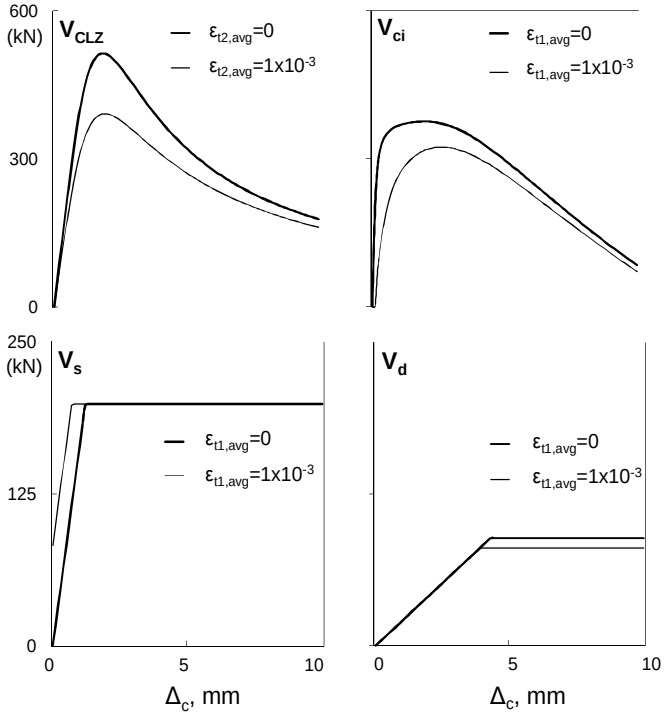

(a) Individual shear mechanisms

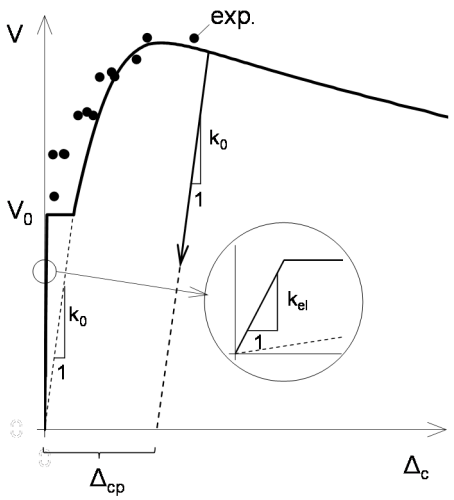

(b) Total response

Fig. 3.7 Behaviour of shear springs.

The last mechanism of shear resistance included in the macroelement is the dowel action of the longitudinal reinforcement, see Fig. 3.8d. The dowel action develops over the length l_k where the reinforcement is subjected to double curvature (Fig. 3.2). To model this action, the reinforcement within l_k is modelled as a fixed-fixed steel beam subjected to transverse displacement Δ_c and axial strain $\varepsilon_{t1,avg}$:

$$V_d = n_b \frac{12 E_s \pi d_b^4}{64 l_k^3} \Delta_c \le n_b f_y \frac{d_b^3}{3 l_k} \left[1 - \left(\frac{T}{A_s f_y} \right)^2 \right] \tag{3.26}$$

where n_b is the number of bars (dowels) and d_b is the bar diameter. The first part of this equation models the elastic behaviour of the dowels while the second part corresponds to the formation of plastic hinges at the ends of the dowels. The expression in the square brackets captures the reduced moment capacity of the plastic hinges due to the tension in the bars $T(\varepsilon_{t1,avg})$. This reduction of dowel capacity is evident in Fig. 3.7d where the top curve is generated with $\varepsilon_{t1,avg}=0$ and the bottom curve with $\varepsilon_{t1,avg}=1x10^{-3}$.

Finally, as with the rotational springs, the transverse springs should also model a possible unloading behaviour. To keep the formulation simple, the unloading branch is assumed linear and parallel to the initial stiffness of each of the four springs.

When the four shear contributions in Fig. 3.7 are added up, they produce the complete V-Δ_c response of the transverse spring shown in Fig. 3.7e. It is important to note however that this response is valid only if the critical diagonal crack has formed, i.e. if the bending moment at either end of the shear span exceeds M_0. Therefore, when $M \le M_0$, the stiffness k_3 is estimated based on the Timoshenko beam theory and the derivation is listed in Appendix B:

$$k_{3,el} = \frac{6 k G_c A E_c I}{12 E_c I + k G_c A a^2} \left(\frac{2}{a} + \frac{3 k G_c A a}{6 E_c I - k G_c A a^2} \right) \tag{3.27}$$

Once M exceeds M_0 in either of the two rotational springs, the response becomes nonlinear. The first rotational spring that reaches M_0 determines the location of the CLZ. According to Fig. 3.2a, if the cracking occurs in the left fan (spring), the CLZ will be in the vicinity of load P_1, and if M_0 is reached first in the right rotational spring, the CLZ will be in the vicinity of P_2. It is therefore at this load level that the geometry of the critical crack is fixed, and the $V/P_{1(2)}$ ratio in Eq. (3.1) is determined.

Finally, as with the rotational springs, the transverse spring should also model a possible unloading behaviour. To keep the formulation simple, the unloading branch is assumed linear and parallel to the initial stiffness k_0.

3.5. Overview of solution procedure

The solution procedure for the analysis of deep beams using macroelements will be summarized with the help of the continuous beam and flowchart in Fig. 3.8. The continuous beam is subjected to point loads and each of its shear spans is modelled with a single macroelement. The solution procedure is based on the secant stiffness approach which provides excellent convergence properties. Each of the shear spans of the beam is modelled with a single element which can capture double-curvature or single-curvature bending. The solution procedure at a given load level begins by assembling the local stiffness matrix of each macroelement (Eq. (3.15)) and the global stiffness matrix of the structure. For the first iteration it is recommended to use the secant stiffnesses of the springs k_1-k_3 of each element from the previous converged load stage. The global stiffness matrix is used to formulate the simultaneous equilibrium equations of the method of displacements

$$\{P\} = [K]\{\Delta\} \tag{3.28}$$

where {P} is the vector of applied nodal forces, [K] is the global stiffness matrix, and {Δ} is the vector of nodal displacements. The support conditions are introduced by eliminating the rows and columns in the simultaneous equations corresponding to the restrained DOFs, and the remaining equations are solved to obtain the unknown nodal displacements {Δ}. Once calculated, these displacements are imposed on the individual macroelements to calculate the internal degrees of freedom θ_1, θ_2, and Δ_c by using Eq. (3.16)-(3.17). The internal DOFs are in turn used to calculate the forces in the springs M_1, M_2, and V via the constitutive relationships defined in the previous section. With the updated spring forces, the secant stiffnesses are calculated as $k_1=M_1/\theta_1$, $k_2=M_2/\theta_2$, and $k_3=V/\Delta_c$. Due to the nonlinearity of the springs, these stiffnesses will differ from the initially assumed values. It is therefore necessary to use the updated stiffnesses to recalculate the internal DOFs θ_1, θ_2, and Δ_c. These iterations continue within each macroelement until the spring stiffnesses converge to constant values. With these new values, the nodal displacements {Δ} are recalculated from the global equilibrium equation Eq. (3.28), and these displacements are again imposed on the individual macroelements. Therefore, as illustrated in the flowchart in Fig. 3.8, the iterations at a given load level {P} are performed in two loops: an outer loop based on Eq. (3.28) (structural level) and an inner loop based on Eq. (3.14) (element level). The calculations are completed when the secant stiffnesses of the springs converge to constant values in both loops.

This solution procedure applies when the nonlinear springs do not exhibit unloading. To take unloading into account, the procedure requires certain modifications related to the residual deformations θ_{1p}, θ_{2p}, and Δ_{cp} in the springs. These deformations are updated at each load stage based on the assumed linear unloading paths of the springs. In the linear equation Eq. (3.14) they are treated as prestrains according to the approach proposed by Vecchio[55], and the secant stiffness are calculated as $k_1=M_1/(\theta_1-\theta_{1p})$, $k_2=M_2/(\theta_2-\theta_{2p})$, and $k_3=V/(\Delta_c-\Delta_{cp})$.

While the flowchart in Fig. 3.8 is prepared for analyses under increasing load (force control), it can be easily modified to compute the behaviour of deep beams under applied displacements and/or support settlements. It should be noted however that the current formulation of the macroelement does not allow for the modelling of shear spans in which the end bending moments M_1 and M_2 have the same sign, or in cases where the shear force reverses during the analysis.

3.6. Comparisons with tests

To demonstrate the capabilities of the proposed macroelement, it is first applied to a simply supported deep beam tested to failure under symmetrical three-point bending (specimen S1M[22]). The beam had a 400 mm by 1200 mm rectangular section and a shear-span-to-depth ratio a/d of 1.55. The longitudinal reinforcement of the beam had a ratio ρ_l=0.70% while the stirrup ratio was ρ_v=0.10%. All other properties of the test specimen are provided in Table 3.1. The beam was loaded monotonically until one of the shear spans failed in a brittle manner along a critical diagonal crack.

The crack pattern of the specimen after failure is shown in Fig. 3.9a together with the macroelement model of the beam. As evident from the photograph, each of the two shear spans developed a fan of radial cracks and a major diagonal crack. The right-hand diagonal crack was critical as it opened at failure simultaneously with the crushing of the concrete in the critical loading zone. In the model the two fans are represented by the inner rotational springs of the macroelements while the behaviour across the diagonal

cracks is modelled by the transverse springs. As the moment at the supports is zero, the support springs do not open, and therefore the concrete blocks above the diagonal cracks remain undeformed.

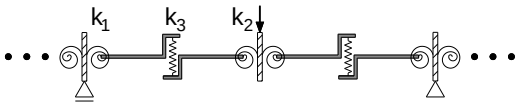

(a) Macroelement model of a continuous deep beam under point loads

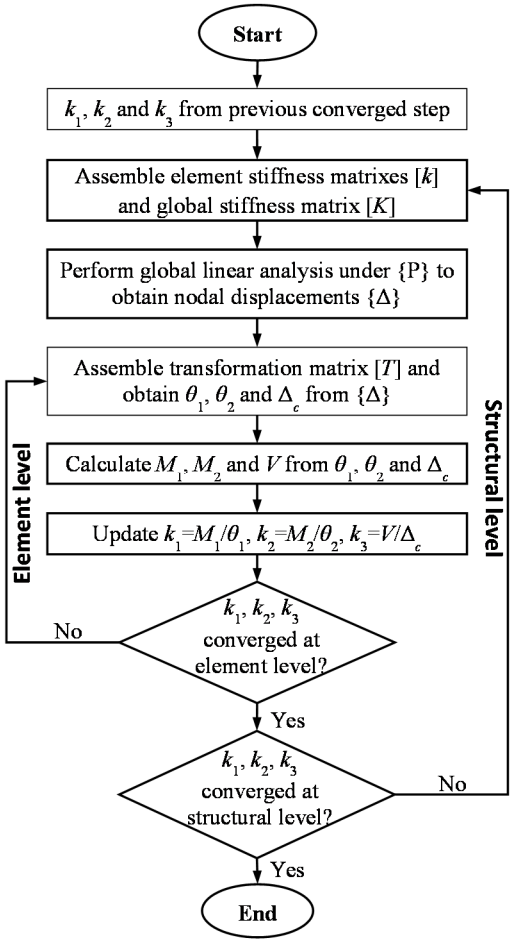

(b) Solution procedure for one load step

Fig. 3.8 Solution procedure.

Fig. 3.9b compares the measured and predicted load-displacement responses of beam S1M. It can be seen that the macroelement model captures adequately the entire measured response, including the initial regime of crack formation, the following pre-peak response as well as the steep post-peak behaviour. These excellent results are achieved with an almost instantaneous analysis based on a straightforward input without open parameters.

To better understand the shear behaviour of beam S1M, Fig. 3.9c shows the V-Δ_c response of the two transverse springs of the model. It can be seen that both springs remained nearly undeformed until the

propagation of the diagonal cracks. Immediately after the crack propagation, the cracks undergo slip displacements necessary to achieve new equilibrium between the applied shear and the internal shear forces. This sudden increase of Δ_c results in a short horizontal branch in the V-Δ response which was also observed in the test. Following the propagation of the diagonal cracks, the shear across the cracks is resisted by the four mechanisms plotted with thin lines. It can be seen that the dominant mechanism is the diagonal compression in the critical loading zone (component V_{CLZ}), and it is the failure of this mechanism that triggered the failure of the critical shear span. In the post-peak regime, the deformations of the failed spring continue to increase while the other transverse spring unloads. The bottom longitudinal reinforcement remained elastic and the rotational springs unloaded as well. The results from the same analysis were used also to generate the M-θ and V-Δ_c plots in Fig. 3.4 and Fig. 3.7. The experimental points in these two plots confirm the appropriateness of the constitutive relationships of the springs.

Table 3.1 Test specimens of deep beams

Beam	a/d	l_{b1}	l_{b2}	b	d_1	d_2	ρ_{l1}	ρ_{l2}	f_y	a	h	a_g	f_c'	ρ_v	f_{yv}	P_{exp}	P_{pred}	$\frac{P_{exp}}{P_{pred}}$
		(mm)	(mm)	(mm)	(mm)	(mm)	(%)	(%)	(MPa)	(mm)	(mm)	(mm)	(MPa)	(%)	(MPa)	(kN)	(kN)	
S0M	1.55	300	150	400	1095	1095	0.70	0.70	652	1700	1200	20	34.2	0.00	-	1442	1581	0.91
S1M	1.55	300	150	400	1095	1095	0.70	0.70	652	1700	1200	20	33.0	0.10	490	1882	1864	1.01
S1C	1.55	300	150	400	1095	1095	0.70	0.70	652	1700	1200	20	33.0	0.10	490	1886	1864	1.01
L0M	2.28	300	150	400	1095	1095	0.70	0.70	652	2500	1200	20	29.1	0.00	-	832	832	1.00
L0C	2.28	300	150	400	1095	1095	0.70	0.70	652	2500	1200	20	29.1	0.00	-	984	832	1.18
L1M	2.28	300	150	400	1095	1095	0.70	0.70	652	2500	1200	20	37.8	0.10	490	1326	1325	1.00
L1C	2.28	300	150	400	1095	1095	0.70	0.70	652	2500	1200	20	37.8	0.10	490	1284	1325	0.97
CB1*	1.55	300	300	300	1094	1094	0.91	0.91	422	1700	1200	20	29.7	0.20	490	1364	1446	0.94
	1.62	300	300	300	1094	1094	0.91	0.91	422	1775	1200	20	29.7	0.20	490			

* CB1 is a two span symmetrical continuous deep beam loaded with a point load in each span, and therefore there are two rows corresponding to the external shear spans with a/d=1.55 and the internal shear spans with a/d=1.62.

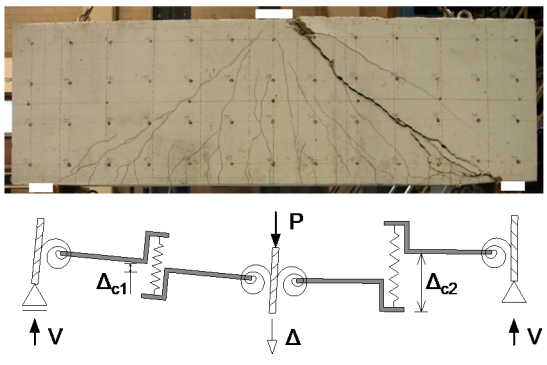

(a) Crack pattern and macroelement model

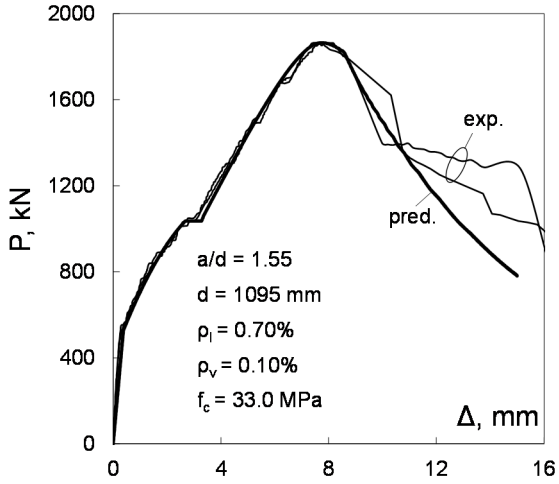

(b) Measured and predicted response

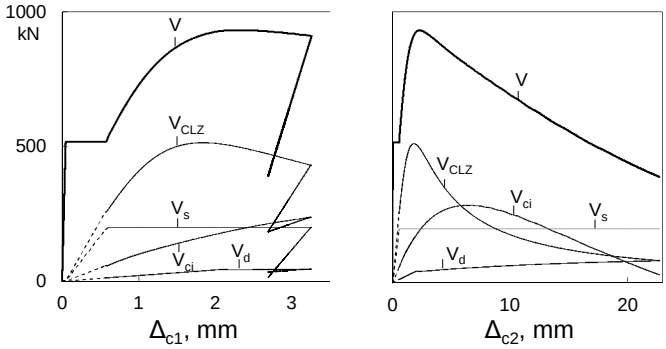

(c) Shear response of the non-critical (left) and critical (right) shear spans

Fig. 3.9 Measured and predicted behaviour of beam S1M.

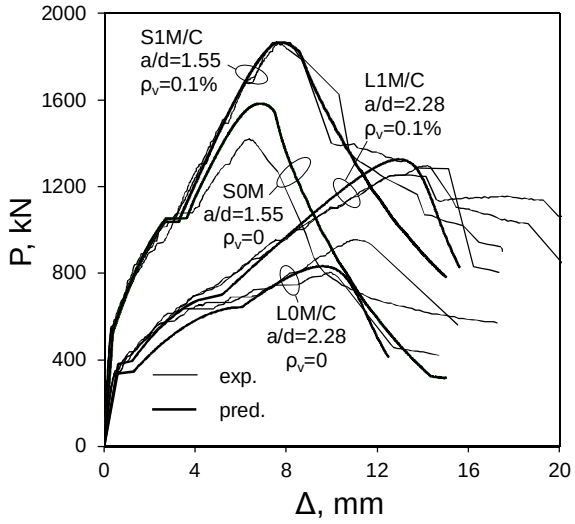

Fig. 3.10 Effect of a/d ratio and stirrup ratio (tests by Mihaylov et al.[22]).

Similar analyses were also performed for other six tests from the same experimental program; see beams S0M, L0M/C and L1M/C in Table 1. The specimens differed in terms of a/d ratio (1.55 vs. 2.28) and stirrup ratio (0.10% vs. no stirrups). Also, letter M stands for monotonic and letter C for cyclic loading. The measured and predicted behaviour of the specimens is shown in Fig. 3.10. It can be seen that the shorter beams S0M and S1M/C were significantly stiffer and stronger than the longer beams L0M/C and L1M/C. The stirrups of 0.10% had no effect prior to the development of the diagonal cracks, and increased the stiffness and shear strength of the beams after the crack propagation. As evident from the plot, the macroelement model captured well these trends, including the post-peak behaviour of the beams.

It is also of interest to apply the macroelement approach to a more complex continuous deep beam similar to the continuous cap beam shown in Fig. 3.1. Such member was tested by Mihaylov et al. [40] and featured two symmetrical spans of 3475 mm with a constant 1200 mm by 300 mm rectangular section (specimen CB1 in Table 3.1). The beam had symmetrical top and bottom longitudinal reinforcement with a ratio of 0.91% as well as stirrups with a ratio of 0.20%. The two spans were loaded by equal point loads applied approximately halfway between the supports via short columns. The loads were increased monotonically until one of the spans failed in shear.

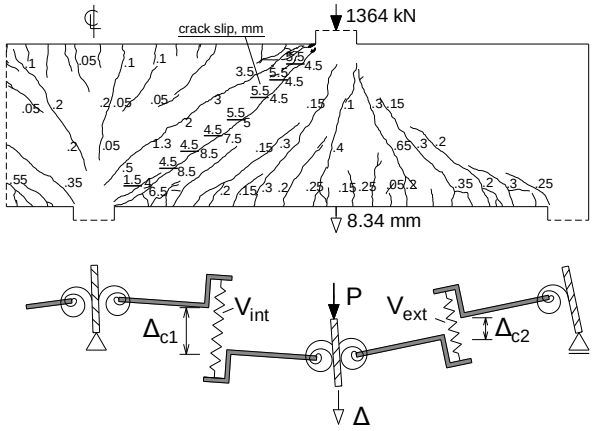

(a) Crack pattern at failure and macroelement model

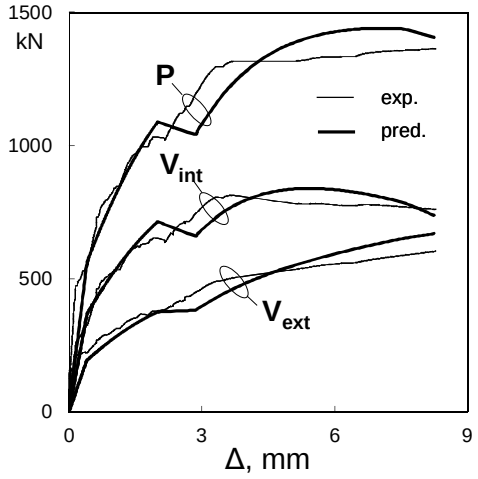

(b) Measured and predicted response

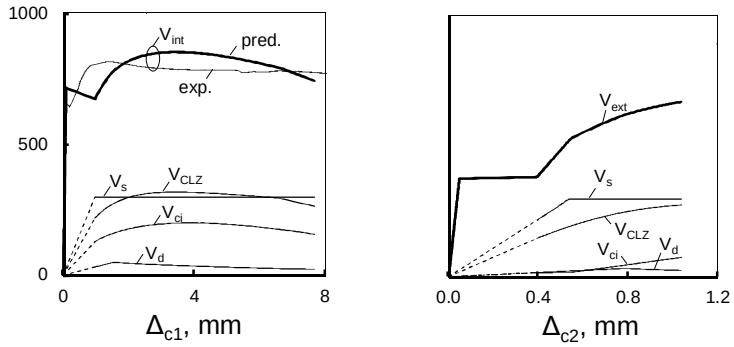

(c) Shear response of the internal (left) and external (right) shear spans

Fig. 3.11 Measured and predicted behaviour of beam CB1[40].

Fig. 3.11 shows the crack diagram of the failed span together with the measured and predicted load-displacement responses. The failure occurred along a diagonal crack in the inner shear span where the shear force was maximum. However, as compared to the brittle shear failures of simply supported deep beams, the continuous deep beam behaved in a more ductile manner. As evident from the P-Δ plot, the beam was able to maintain an approximately constant load for deflections ranging from 3.6 mm to 8.3 mm until the test was terminated.

This behaviour can be explained with the help of the macroelement model which, as evident from Fig. 3.11b, captures well the ductile load-displacement response of the specimen. In addition to the P-Δ response, the plot also shows the evolution of the shear forces V_{int} and V_{ext} in the internal and external shear spans. It can be seen that while in the range Δ=3.6-8.3 mm the applied load P increases slightly, the shear force V_{int} decreases. Because equilibrium dictates that V_{ext}=P-V_{int}, the shear force in the external shear span increases to compensate for the decrease of V_{int}. This can be seen more clearly in Fig. 3.11c which compares the V-Δ_c behaviour of the external and internal transverse springs of the macroelement model. It is evident that when the beam reached peak load, the critical shear span was in the post-peak regime and the external shear span was approaching failure. This shows that to predict the ductility of continuous deep beams, it is necessary to use models that capture the brittle post-peak behaviour of the individual shear spans.

Finally, because the macroelement predicts DOFs $\varepsilon_{t1,avg}$, $\varepsilon_{t2,avg}$ and Δ_c, these DOFs can be used to evaluate the width of the critical diagonal cracks at different load levels via Eq.(3.10). The evolution of the crack widths in test specimens S1M/C, L1M/C and CB1 are shown in Fig. 3.12. As evident from the plots, the macroelement predicts a sudden increase of *w* after the crack propagation. When the load is increased further, the predictions for the simply supported beams S1M/C and L1M/C follow an approximately parabolic trend with faster opening of the cracks near failure. It can be seen from Fig. 3.12a that these predictions agree well with the measured crack widths which reached 4.2 mm at peak load. Significantly wider diagonal cracks of up to 8.5 mm were measured in the continuous beam CB1 in which the critical shear span was in the post-peak regime when the member reached the peak load. This resulted in a flat P-w response which is well captured by the macroelement model. These results indicate that the proposed model is a valuable tool for the evaluation of existing deep beams in bridges and other structures. If the width of the diagonal cracks is measured on site, the model can be used to estimate the load on the girder as well as how close this load is to the peak resistance of the member. Because the macroelement approach captures the beneficial redistribution of forces in statically indeterminate girders, it can help

avoiding costly and disruptive repairs when they are not absolutely necessary. However, as the tests specimens used in this study had a relatively small amount of transverse reinforcement (ρ_v=0-0.2%), further research is needed to ensure the reliability of the crack width predictions for more heavily reinforced members with better crack control.

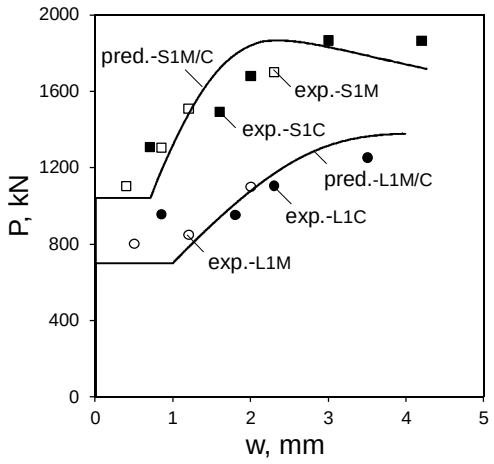

(a) Simply supported beams (tests by Mihaylov et al.[22])

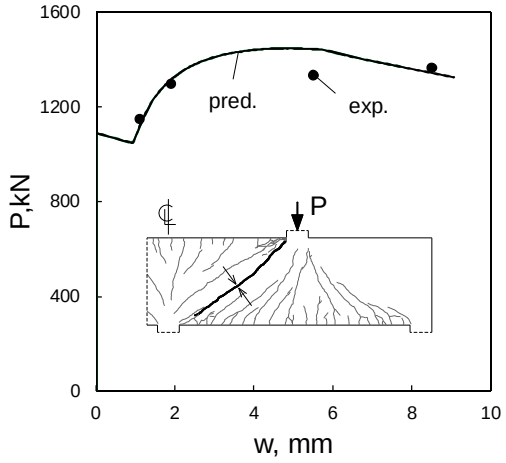

(b) Continuous beam CB1 (test by Mihaylov et al.[40])

Fig. 3.12 Maximum width of diagonal cracks.

3.7. Conclusions

This paper presented the formulation and validation of a macroelement for deep beams based on a three-parameter kinematic theory. The main conclusions of the study can be summarized as follows:

1) The macroelement provides accurate predictions of the complete pre- and post- peak shear response of simply supported and continuous deep beams. This is achieved with a straightforward input without open parameters.

2) The macroelement improves the strength predictions of simpler but conservative strut-and-tie models, while at the same time maintains simplicity and computational efficiency as compared to complex nonlinear finite element models.

3) Continuous deep beams can redistribute shear forces from the critical shear spans to adjacent spans resulting in a ductile behaviour. This favourable effect observed in experiments is captured well by the macroelement model.

4) As the macroelement is based on kinematics, the width of the critical diagonal cracks is expressed with the DOFs of the model which are predicted at each load step. Comparisons with tests showed that the predicted crack widths approximate well experimental results from simply supported and continuous deep beams up to the failure of the member.

5) The macroelement can be used for the evaluation of existing deep beams in bridges and buildings for which measurements of crack widths and deflections are available. These measurements can be used together with the predicted load-deformation curves to evaluate the state and safety of the structure.

4. Mixed-Type Modelling of Structures with Slender and Deep Beam Elements

Abstract The nonlinear analysis of reinforced concrete frame structures with slender members can be performed accurately and efficiently with 1D elements based on the plane-sections-remain-plane hypothesis. However, if the frame also includes deep beams which require 2D high-fidelity finite element procedures, the analysis of large structures can become very costly. To address this challenge, this paper proposes a mixed-type modelling framework which integrates 1D slender beam elements with a novel 1D macroelement for deep beams. The framework is implemented in an existing nonlinear analysis procedure and is used to model 18 deep beam tests and a 20-story frame. It is shown that the proposed modelling framework provides similarly accurate predictions to the 2D high-fidelity procedures but requires a fraction of the time for modelling and analysis. Furthermore, the macroelement improves the post-peak predictions, and therefore the framework is suitable for evaluating the resilience of structures under extreme loading.

Article Liu, J., Guner, S., and Mihaylov, B.I., "Mixed-Type Modelling of Structures with Slender and Deep Beam Elements," Accepted by *ACI Structural Journal.*

4.1. Introduction

Deep beams are characterized by small shear-span-to-depth ratios and carry shear by direct compression between the loading and support points (known as the strut or arch action). As concrete is very efficient in resisting compression, such members possess high stiffness and shear strengths as compared to slender beams. Owing to these properties, deep beams are typically used as transfer girders above large open spaces in the bottom floors of important concrete buildings such as government centres, hospitals and high-rise buildings (Fig. 4.1). The load-bearing characteristics of deep beams are also encountered in other members such as spread footings and pile caps. Due to their important functions, deep beams may often dictate the resilience of the entire structure when overloading occurs in rare events. The 2011 Christchurch earthquake, for example, produced unforeseen vertical ground accelerations (up to 1.8g) and caused the shear failures of several deep transfer girders. As a result, a number of buildings were on the verge of collapse and had to be demolished in the months after the earthquake [14, 56, 57, 58].

To design structures for resilience to extreme loading events, it is often necessary to perform a nonlinear pushover analysis, with the entire structure subjected to, for example, an earthquake or a column removal scenario representing a blast or impact loading[59]. Two approaches are commonly used for modelling buildings which incorporate deep transfer girders. The most common strategy, shown on the left in Fig. 4.1, is to model all members with one-dimensional (1D) slender elements based on the classical plane-sections-remain-plane hypothesis (fibre-based elements or lumped plasticity elements). This approach neglects the complex behavioural mechanisms associated with deep beams and cannot capture the interaction and redistribution of internal forces between the deep and slender members. While incorrect, this strategy is still commonly used due to its relatively simple and computationally efficient nature. The second approach is to use 2D nonlinear finite element methods (FEMs) which incorporate appropriate constitutive models for cracked reinforced concrete under plane stresses[60]. When used correctly, this approach captures the strut action of deep beams, the interaction between deep and slender elements, and the force redistribution in the post-peak stages. The disadvantage of 2D FEMs is that they require significant knowledge and experience from the user and demand significant time for the model development and analysis execution. Consequently, they are feasible only when modelling critical parts of structures as opposed to an entire building. A few other modelling frameworks, e.g. hybrid modeling[61], are also available, which combines these two modelling approaches.

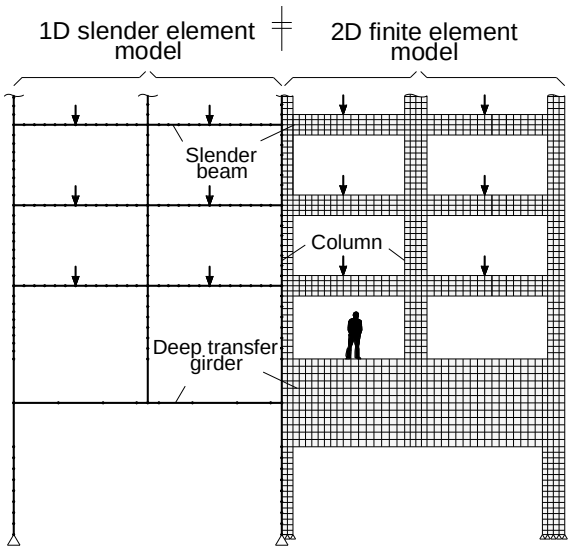

Fig. 4.1 Alternative models of a large 4-bay frame structure with both slender and deep beams.

This paper proposes a mixed-type modelling framework which aims to combine the accuracy of 2D FEMs with the speed and simplicity of 1D slender elements. The framework integrates 1D slender beam elements with equally simple 1D deep beam elements that can account for the strut action. The deep beam element incorporated in this study was recently formulated by Liu and Mihaylov[62] based on a three-parameter kinematic theory[40] for continuous deep beams. This element can capture the entire nonlinear shear response of deep shear spans, from initial high stiffnesses to the post-peak response which provides the structure with the ability to redistribute forces and survive overloading. The paper discusses the formulation of the proposed mixed-type modelling framework, provides comparisons with experimental tests, and presents a sample analysis of an entire 20-story frame with deep transfer girders.

4.2. 1D macroelement for deep beams

The efficient modelling of slender beams can be accomplished based on the plane-sections-remain-plane hypothesis which greatly simplifies the deformation patterns without compromising accuracy. To model deep beams in a similar fashion, it is necessary to describe their apparently complex deformation patterns in a simple and sufficiently accurate manner.

Fig. 4.2a shows such a model for deep beams under double curvature proposed by Mihaylov et al.[40]. In this model, a shear span of a deep beam is divided into two parts by a critical diagonal crack. Each of the parts is modelled as a "fan" of rigid struts outlined by radial cracks. The struts are pinned at points P_1 and P_2 and are connected to the bottom/top flexural reinforcement, respectively. As the flexural reinforcement develops average tensile strains $\varepsilon_{t1,avg}$ and $\varepsilon_{t2,avg}$ along the shear span a, the fans "open" by angles θ_1 and θ_2. While these deformations can be associated with flexure, the shear force causes the two fans to translate vertically with respect to each other due to the opening of the critical diagonal crack. The vertical displacement Δ_c in the crack is associated with diagonal crushing of the concrete in the critical loading zone (CLZ). Based on these kinematic assumptions, the complete displacement field of the shear span can be expressed as a function of only three degrees of freedom: $\varepsilon_{t1,avg}$, $\varepsilon_{t2,avg}$, and Δ_c, or eventually θ_1, θ_2, and Δ_c.

This three-parameter kinematic model forms the basis of the macroelement for deep beams proposed by Liu and Mihaylov[62] (Fig. 4.2b). In this element, the behaviour of the two fans is modelled by rotational springs, while the shear behaviour across the critical diagonal crack is represented by a transverse spring. The rotational springs are attached to end sections/nodes with two translational and one rotational degrees of freedom per node (u, v, φ). Inside the element, the three springs are connected by bars which are rigid in flexure and remain parallel to each other as the element deforms.

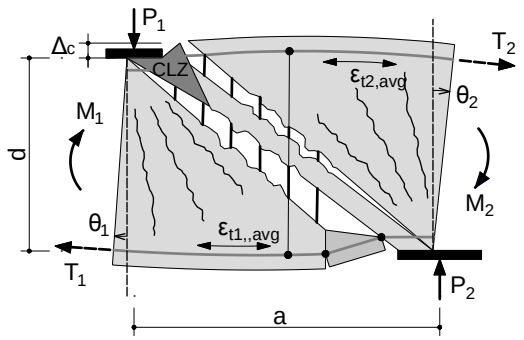

a) Three-parameter kinematic model

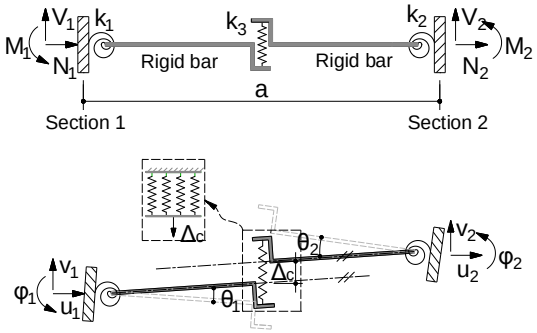

b) Components and deformed shape of macroelement

Fig. 4.2 Macroelement for shear spans of deep beams.

The nonlinear load-deformation relationships $M_i(\theta_i)$ and $V(\Delta_c,\theta_i)$ of the springs of the macroelement are developed from first principles: compatibility of deformations, stress-strain relationships and equilibrium. For a given degree of freedom (DOF) θ_1, the average strain in the bottom longitudinal reinforcement $\varepsilon_{t1,avg}$ is determined from compatibility. Using this strain, the tensile force in the reinforcement T_1 is determined by assuming an elastic-perfectly-plastic stress-strain relationship for the reinforcement, and also adding the tension stiffening effect of the concrete around the reinforcement. The bending moment M_1 is then obtained from equilibrium as $T_1(0.9d)$, where d is the effective depth of the section and 0.9d is the estimated lever arm of the internal longitudinal forces. A schematic representation of the $M_i(\theta_i)$ relationship obtained in this manner is shown in Fig. 4.3a[62].

The $V(\Delta_c,\theta_i)$ relationship of the transverse spring is somewhat more complex due to the complex manner in which deep beams resist shear. The macroelement accounts for four mechanisms of shear resistance across the critical diagonal crack: 1) shear carried in the critical loading zone, V_{CLZ}, 2) tension in the transverse reinforcement, V_s, 3) aggregate interlock shear, V_{ci}, and 4) dowel action of the longitudinal

reinforcement, V_d. Therefore, the transverse spring can be visualized as consisting of four parallel springs, where the strut action is associated mainly with spring V_{CLZ}.

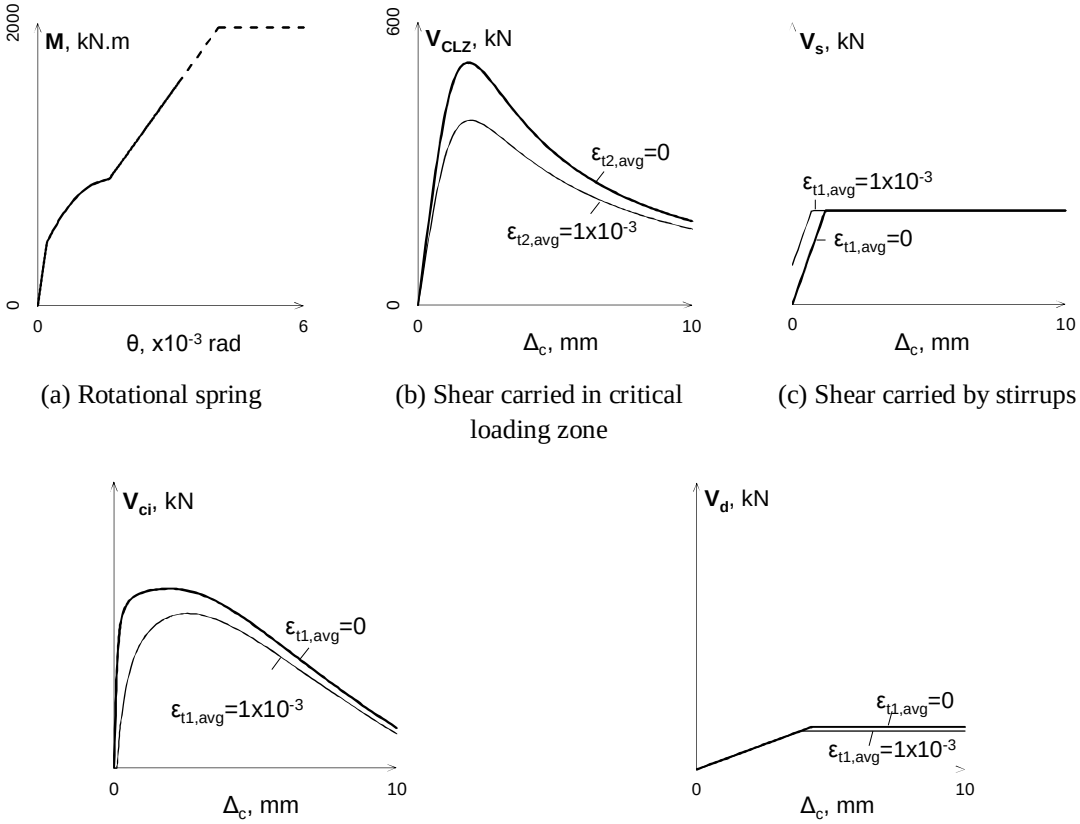

(a) Rotational spring

(b) Shear carried in critical loading zone

(c) Shear carried by stirrups

(d) Shear carried by aggregate interlock

(e) Shear carried by dowel action

Note: The plots are prepared based on beam S1M by Mihaylov et al. [22] with a/d=1.55, d=1095mm, b=400mm, l_{b1}=300mm, ρ_l=0.70%, ρ_v=0.10%, f_c'=33.0MPa.

Fig. 4.3 Load-deformation relationships of the springs of the macroelement.

The constitutive relationships of the four springs are presented schematically in Fig. 4.3b-e. As evident from the plots, the behaviour of the CLZ resembles that of concrete in compression, while the behaviour of the stirrups is similar to the tensile behaviour of steel. To model the aggregate interlock spring, it is necessary to use DOFs Δ_c and θ_1 (or $\varepsilon_{t1,avg}$) as they both contribute to the relative displacements between the crack faces. For given values of these DOFs, the average width of the critical crack *w* and the slip displacement *s* are expressed using the kinematic model. DOF θ_1 results in the widening of the critical crack while Δ_c causes both widening and slip. Displacements *w* and *s* are used to calculate the aggregate interlock stress on the crack $v_{ci}(w, s)$ based on a contact density model by Li et al.[20], and v_{ci} is integrated along the critical crack to obtain the shear force V_{ci}. As can be seen from Fig. 4.3d, V_{ci} increases with increasing Δ_c and eventually diminishes as the critical crack becomes very wide. At the bottom of the crack, the longitudinal reinforcement works in double curvature associated with DOF Δ_c, and therefore resists shear by dowel action. By modelling the bars in this zone as fixed-fixed steel beams, the dowel action relationship in Fig. 4.3e has been obtained. The dowel action is diminished by the tensile strain in the reinforcement $\varepsilon_{t1,avg}$.

To solve the nonlinear equations of the macroelement, a secant stiffness approach is employed, which will provide compatibility with the existing 1D slender beam elements. Therefore, the stiffnesses of the three springs of the element are obtained as $k_1=M_1/\theta_1$, $k_2=M_2/\theta_2$ and $k_3=V/\Delta_c$, and the secant stiffness matrix is formulated as:

$$\begin{Bmatrix} N_1 \\ V_1 \\ M_1 \\ N_2 \\ V_2 \\ M_2 \end{Bmatrix} = [k] \begin{Bmatrix} u_1 \\ v_1 \\ \varphi_1 \\ u_2 \\ v_2 \\ \varphi_2 \end{Bmatrix} \tag{4.1}$$

$$[k] = \frac{1}{C} \times \begin{bmatrix} CE_cA_g/a & 0 & 0 & -CE_cA_g/a & 0 & 0 \\ 0 & k_3(k_1+k_2) & k_1k_3a & 0 & -k_3(k_1+k_2) & k_2k_3a \\ 0 & k_1k_3a & k_1(k_2+k_3a^2) & 0 & -k_1k_3a & -k_1k_2 \\ -CE_cA_g/a & 0 & 0 & CE_cA_g/a & 0 & 0 \\ 0 & -k_3(k_1+k_2) & -k_1k_3a & 0 & k_3(k_1+k_2) & -k_2k_3a \\ 0 & k_2k_3a & -k_1k_2 & 0 & -k_2k_3a & k_2(k_1+k_3a^2) \end{bmatrix} \tag{4.2}$$

where $C=k_1+k_2+k_3a^2$, a is the shear span, E_c is the modulus of elasticity of the concrete, and A_g is the gross area of the concrete section. This matrix is an extension of the formulation presented in Liu and Mihaylov[62] which did not account for the axial degrees of freedom u_1 and u_2. As evident from the E_cA_g terms in the stiffness matrix, the axial behaviour of the beam is assumed linear-elastic for simplicity.

4.3. Existing element for slender beams and columns

One-dimensional (1D) nonlinear elements for slender beams are employed by many nonlinear frame analysis platforms such as OpenSees[63], SAP2000[64], RUAUMOKO[65], VecTor5[66] and others. As shown in Fig. 4.4a, beams and columns are discretized into several elements, and one element usually has two end nodes with three degrees of freedom per node (u, v, φ) as in the 1D macroelement for deep beams discussed above (Fig. 4.4b).

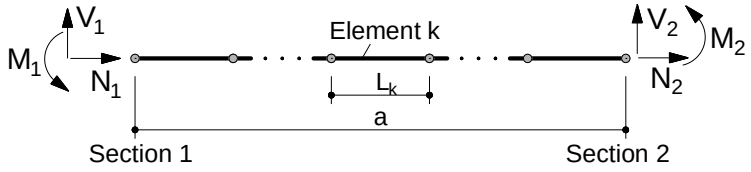

(a) Beam modelling with slender elements

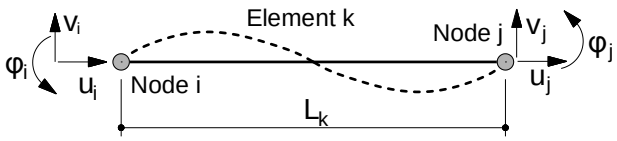

(b) Degrees of freedom

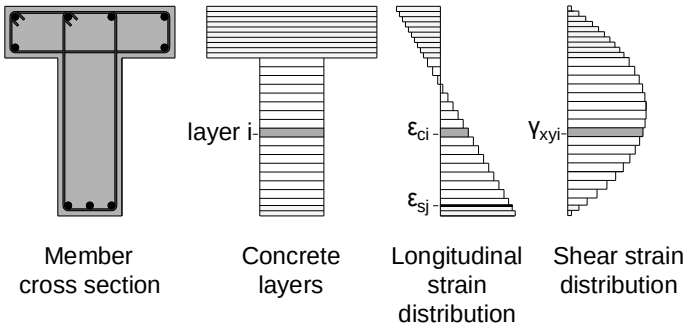

(c) Fibber-based sectional idealization

Fig. 4.4 Existing element for slender beams.

To model the nonlinear behaviour of slender beams, this study focuses on the distributed plasticity approach. In this approach the beam section is divided into a number of concrete and steel layers as shown in Fig. 4.4 b, and the longitudinal strains in the layers vary linearly across the section. The stresses in the layers are obtained from the strains based on material constitutive laws for uniaxial tension and compression. This is a universally-accepted way of modelling flexural behaviour, while the approaches for predicting the shear behaviour vary significantly. For example, SAP2000[64] and RUAUMOKO[65] employ a lumped-plasticity approach where the locations and behaviour of shear hinges is commonly defined by the user. However, expert knowledge on the shear behaviour of concrete is required to define these shear hinges. In addition, the changing shear behaviour as the elements sustain damage or axial force levels change cannot be captured. These severely limit the use of lumped-plasticity procedures for modelling shear effects in practice.

Shear behaviour can also be modelled using a distributed plasticity approach, where the concrete layers do not work in uniaxial tension/compression, but under a 2D state of stresses. This approach is more computationally demanding but removes the complex task of determining the shear hinge behaviour form the user. VecTor5[66] is one procedure based on a distributed plasticity approach and is adopted in this study. To simplify the problem, the pattern of distribution of the shear strains across the section is assumed either constant (not shown) or parabolic (shown in Fig. 4.4c). Knowing the longitudinal and shear strain distributions, each concrete and steel layer is analysed individually based on the Distributed Stress Field Model (DSFM, Vecchio 2000[67]). The DSFM is a smeared, hybrid crack model (i.e. between a fully-rotating and a fixed-crack model) and accounts for phenomena such as aggregate interlock, tension stiffening and softening, compression softening and confinement of the concrete, and yielding, strain hardening, buckling and dowel action of the reinforcement. This approach has been evaluated with a large number of experiments showing adequate predictions as well as excellent convergence properties[68].

4.4. Mixed-type modelling framework

The primary objective of this study is to propose an analysis framework which integrates 1D slender beam elements with a new 1D macroelement for deep beams. A key advantage of the macroelement, which will permit achieving this objective, is that it uses the same nodal degrees of freedom as the 1D slender elements.

The approach taken in this study is to avoid making major changes to the solution algorithm of the existing global analysis procedure of VecTor5. This is achieved by developing a new subroutine for the deep macroelement which performs the calculations discussed above and returns the results of deep members to the global VecTor5 solution procedure. The unbalanced force approach used in VecTor5 (to be discussed below) ensures the compatibility of these results with those calculated for the slender elements. A major advantage of this approach is that no other changes (such as a new finite element development, solution algorithm changes, or degree of freedom modifications) are required for the global analysis procedure. Even though the proposed formulations are implemented in VecTor5 due to its robust shear behaviour modelling, they are equally as applicable to other existing platforms for nonlinear analysis.

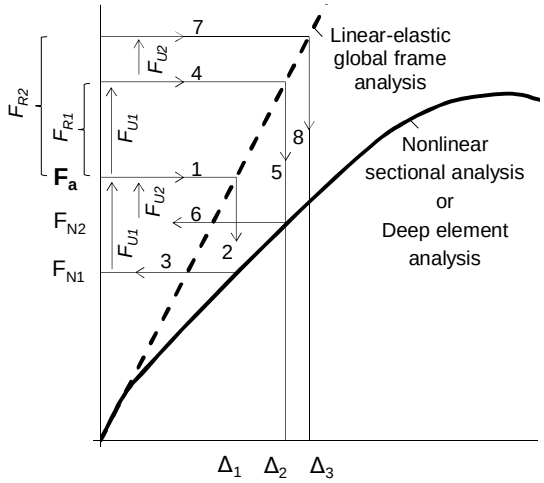

Fig. 4.5 Unbalanced force approach (adapted from Guner and Vecchio[69]).

The unbalanced force method[69] employed by VecTor5 is illustrated schematically in Fig. 4.5. The first step is to perform a global frame analysis with a constant stiffness under the applied loads $\{F_a\}$ to compute the nodal displacements Δ_1 (see path 1→2). These displacements are used to calculate the curvature and strain values for each element. The nonlinear sectional calculations are then performed, using the strain values, to obtain the end forces of the elements and the corresponding nodal forces for the entire structure F_{N1} (path 2→3). The difference between the applied forces and the nodal forces calculated by the sectional procedures are termed unbalanced forces $F_{Ui}=F_a-F_{Ni}$, which are used to establish a vector of the compatibility restoring forces $\{F_R\}$. These forces are applied in addition to the externally applied forces to increase the displacements and get closer to the true nonlinear response. Following this step, new unbalanced forces are calculated and added to $\{F_R\}$, and the iterations continue until all unbalanced forces converge to zero. This method is employed in VecTor5 for static analyses (such as monotonic and cyclic) as well as dynamic analyses (such as seismic, impact or blast). This study focuses on the static monotonic (or pushover) analysis only.

The proposed mixed-type modelling framework based on the unbalanced force method is outlined in Fig. 4.6. In this flowchart, the steps related to the newly added subroutines for deep beam elements are shaded in grey. The subroutine for slender elements is presented very briefly within the existing VecTor5 procedure and is also shaded in grey. From the displacement vector $\{\Delta\}$, a subroutine exacts the nodal displacements of each element $\{\Delta_{el}\}$ and supplies them to the subroutines for either deep or slender elements. These subroutines perform nonlinear calculations under imposed $\{\Delta_{el}\}$ and return the member

end forces $\{F_{Nd}\}$ and $\{F_{Ns}\}$. When assembled for the entire structure, $\{F_{Nd}\}$ and $\{F_{Ns}\}$ form the global vector of nodal forces which is used by the unbalanced force method.

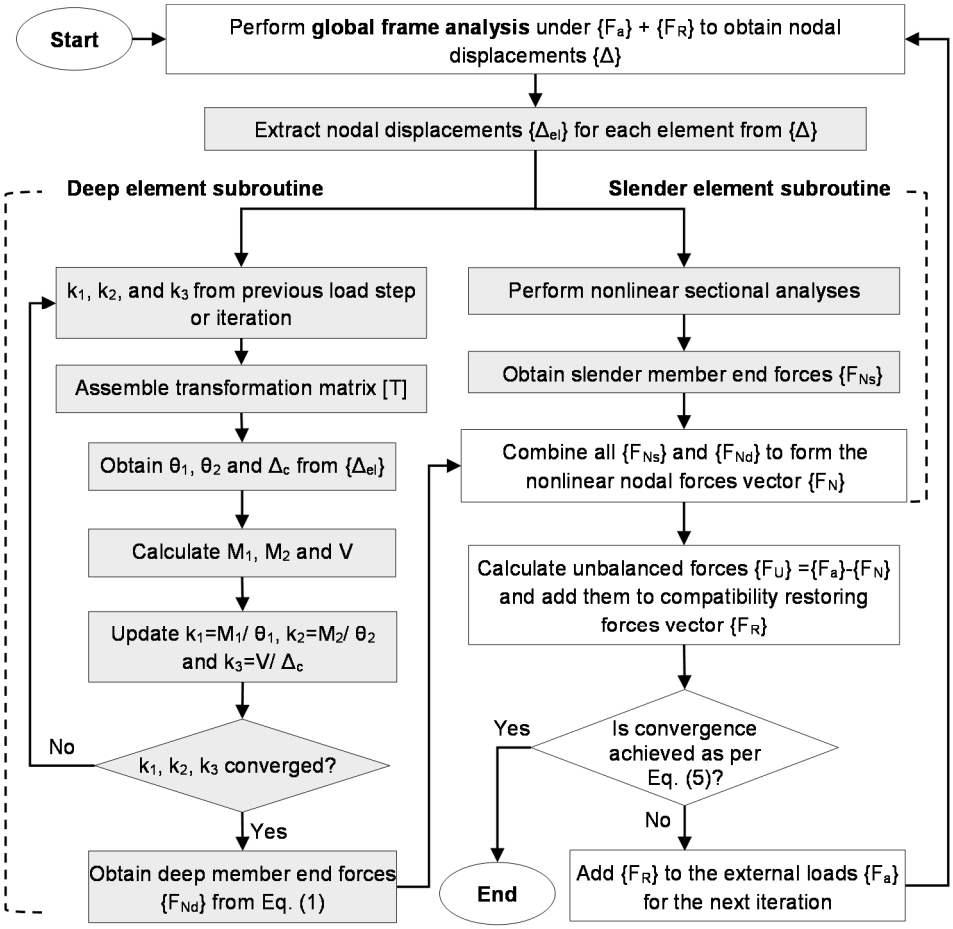

Fig. 4.6 Mixed-modelling framework.

As illustrated in Fig. 4.6, the new subroutine for deep elements consists of six main steps. The calculations begin by obtaining the secant stiffnesses k_1 to k_3 of the three springs of the macroelement from the previous iteration. The internal degrees of freedom of the macroelement θ_1, θ_2 and Δ_c are then calculated under the imposed nodal DOFs $\{\Delta_{el}\}$. This is achieved through the use of a transformation matrix [T] as follows:

$$\begin{bmatrix} \theta_1 \\ \theta_2 \\ \Delta_c \end{bmatrix} = [T]\{\Delta\} = [T] \begin{bmatrix} u_1 \\ v_1 \\ \varphi_1 \\ u_2 \\ v_2 \\ \varphi_2 \end{bmatrix} \tag{4.3}$$

$$[T] = \frac{1}{k_1 + k_2 + k_3 a^2} \times \begin{bmatrix} 0 & -k_3 a & k_2 + k_3 a^2 & 0 & k_3 a & -k_2 \\ 0 & -k_3 a & -k_1 & 0 & k_3 a & k_1 + k_3 a^2 \\ 0 & k_1 + k_2 & -k_1 a & 0 & -(k_1 + k_2) & -k_2 a \end{bmatrix} \quad (4.4)$$

DOFs θ_1, θ_2 and Δ_c are used together with the nonlinear constitutive relationships of the springs (shown in Fig. 4.3) to obtain the end moments M_1 and M_2 as well as the shear V. As k_1 to k_3 are secant stiffnesses, they are recalculated as $k_1=M_1/\theta_1$, $k_2=M_2/\theta_2$ and $k_3=V/\Delta_c$. The secant stiffness formulation always provides positive stiffness values and results in excellent convergence characteristics. The calculations are repeated until the initial and calculated stiffness values converge. The member end forces $\{F_{Nd}\}$ are then obtained from Eq. (4.1) .

As mentioned previously, the obtained reaction forces $\{F_{Nd}\}$ and $\{F_{Ns}\}$ are assembled to form the global vector of nodal forces $\{F_N\}$. If forces $\{F_N\}$ are not equal to the applied forces $\{F_a\}$, unbalanced force will be calculated. The solution at a given load step is considered converged when the unbalanced forces are close to zero; otherwise these forces are added to the vector of compatibility restoring forces $\{F_R\}$ from the previous iteration, and the entire procedure is repeated with the updated load $\{F_a\}+\{F_R\}$.

4.5. Evaluation and applications

4.5.1. Beams

To evaluate the new mixed-type modelling framework with experimental results, seventeen simply supported deep beams, one continuous deep beam, and one large frame structure are analysed. All beams were shear-critical and modelled with both the proposed 1D mixed-type modelling approach and a 2D high-fidelity finite element model (FEM). The 2D FEM analyses are performed with program VecTor2[13] based on the same theory (i.e., the DSFM[67]) as in VecTor5 to avoid discrepancies related to the theories used in the global analyses. The two modelling approaches are compared in terms of accuracy and computational efficiency.

4.5.1.1. Simply supported deep beams

The simply supported deep beams considered in this study were tested to failure by Tanimura and Sato[70](12 beams) and Salamy et al.[71] (5 beams). All beams were subjected to symmetrical four-point bending and featured different geometry and material properties as listed in Table 4.1. The shear-span-to-depth-ratio a/d varied from 0.5 to 1.5, the effective depth from 400 mm to 1400 mm, the longitudinal reinforcement ratio from 1.99% to 2.14%, the stirrup ratio from 0 to 0.84%, and the concrete compressive strength from 22.5 MPa to 29.3 MPa.

A representative sample beam (e.g., beam 8 in Table 4.1) and the two models created for this beam are shown in Fig. 4.7. The FEM consists of quadrilateral elements for the concrete and discrete truss elements for the longitudinal reinforcement. As the stirrups are typically uniformly spaced, they are modelled with smeared reinforcement as a part of the concrete elements. To allow the analyses to be easily repeated by others, the default constitutive models of VecTor2 were used with no tuning of any input parameters. The only exception is the compression stress-strain curve of the concrete for which the Popovics[54] model was preferred over the default simple parabola. The beams are analysed under imposed increasing displacements applied at the loading points.

Table 4.1 Simply supported deep beam tests

Authors &Year	Beam	a/d	b, mm	d, mm	h, mm	a, mm	L_f, mm	L mm	l_{b1}, mm	l_{b2}, mm	f'_c, MPa	ρ_l, %	f_y, MPa	ρ_v, %	f_{yv}, MPa	V_{exp}, kN	$V_{exp}/V_{pred,2D}$	$V_{exp}/V_{pred,1D}$
Tanimura and Sato, 2005[70]	1	0.5	300	400	450	200	400	1400	100	100	23.2	2.14	458	0.00	-	853	1.08	1.06
	2	0.5	300	400	450	200	400	1400	100	100	23.2	2.14	458	0.21	370	821	1.08	1.00
	3	0.5	300	400	450	200	400	1400	100	100	23.2	2.14	458	0.48	388	833	1.09	1.02
	4	0.5	300	400	450	200	400	1400	100	100	23.2	2.14	458	0.84	368	869	1.15	1.07
	5	1.0	300	400	450	400	400	1800	100	100	29.0	2.14	458	0.00	-	632	0.94	1.14
	6	1.0	300	400	450	400	400	1800	100	100	29.1	2.14	458	0.21	370	731	1.00	1.23
	7	1.0	300	400	450	400	400	1800	100	100	29.2	2.14	458	0.48	388	750	0.97	1.20
	8	1.0	300	400	450	400	400	1800	100	100	29.3	2.14	458	0.84	368	804	0.91	1.23
	9	1.5	300	400	450	600	400	2200	100	100	22.9	2.14	458	0.00	-	284	0.78	0.80
	10	1.5	300	400	450	600	400	2200	100	100	22.5	2.14	458	0.21	370	464	0.94	1.13
	11	1.5	300	400	450	600	400	2200	100	100	23.0	2.14	458	0.48	388	491	0.84	0.99
	12	1.5	300	400	450	600	400	2200	100	100	23.5	2.14	458	0.84	368	570	0.92	0.99
Salamy et al., 2005[71]	B-10-2	1.5	240	400	475	600	300	1900	100	100	23.0	2.02	376	0.00	-	357	1.08	1.41
	B-13-2	1.5	480	800	905	1200	600	3800	200	200	24.0	2.07	398	0.00	-	1128	1.00	1.10
	B17	1.5	600	1000	1105	1500	750	4750	250	250	28.7	2.04	398	0.40	398	2607	0.98	1.09
	B15	1.5	720	1200	1305	1800	900	5700	300		27.0	1.99	402	0.00	-	2695	1.06	1.16
	B18	1.5	840	1400	1505	2100	1050	6650	350		23.5	2.05	398	0.40	398	4198	0.89	0.95
																Avg =	0.98	1.09
																COV =	10.1%	12.6%

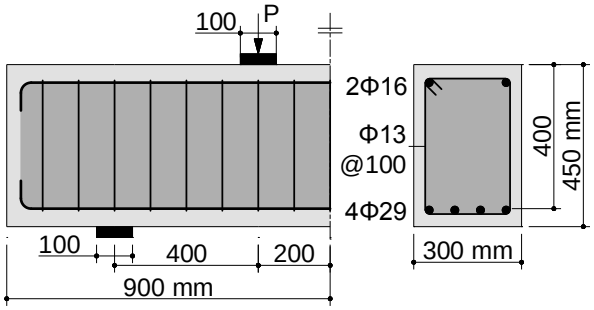

a) Deep beam under symmetrical 4-point bending

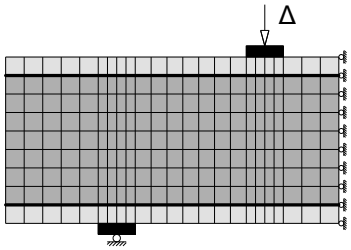

b) 2D finite element model

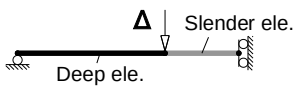

c) 1D mixed-type model

Fig. 4.7 Modelling of simply supported deep beam 8[70].

In contrast to the 2D FEM that uses 261 elements for beam 8, it can be seen in Fig. 4.7c that the proposed 1D mixed-type modelling approach uses only two elements for the same beam. A slender element is used for the pure bending region while a deep macroelement is used for the shear span to show the compatibility of the two elements in the same structure. Again, the default constitutive models of VecTor5 were used (except for the compression stress-strain curve of the concrete), which are the same as those contained in VecTor2, to achieve a more consistent comparison.

In order to verify the proposed modelling approach, it is first necessary to examine its convergence properties. For this study, an unbalanced-force-based-convergence criterion is used as follows:

$$CF = 1 + \sqrt{\frac{1}{3 \times n} \times \sum_{i=1}^{n} \left(\left(\frac{N_{ui}}{N_i} \right)^2 + \left(\frac{V_{ui}}{V_i} \right)^2 + \left(\frac{M_{ui}}{M_i} \right)^2 \right)} \tag{4.5}$$

where n is the total number of elements, N_{ui}, V_{ui} and M_{ui} are the unbalanced end forces for each element, and N_i, V_i and M_i are the end element forces calculated by the global frame analysis. The convergence factors *CF* and the number of iterations from the analysis of beam 8 are plotted in Fig. 4.8 as functions of the load step number, where the peak resistance of the beam was reached at load step 19. It can be seen that the solution reached convergence at all load steps, including in the post-peak regime of the beam. This was achieved even without reaching the maximum number of iterations (i.e., 100). Similar observations were made for the rest of the beams modelled in this study.

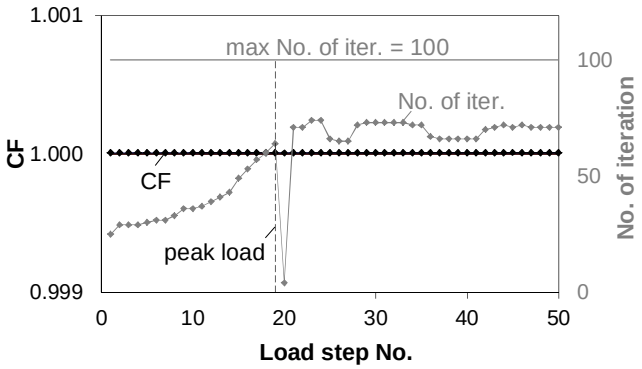

Fig. 4.8 Convergence during the analysis of beam 8.

The complete pre- and post-peak load-deflection responses of the seventeen simply supported deep beams in Table 4.1 are shown in Fig. 4.9. The plots compare the experimentally-obtained responses to the predictions from the 1D (proposed) and 2D models. Overall, both approaches capture the pre-peak response and produce satisfactory strength predictions within ±10% - well inside the margins of error expected when analysing shear-critical reinforced concrete members. As shown in Table 4.1, the average shear strength experimental-to-predicted ratio obtained with the 2D FEM is 0.98 and the coefficient of variation (COV) is 10.1%. For the proposed 1D mixed-type modelling approach these numbers are respectively 1.09 and 12.6%, which indicates that the new approach is slightly more conservative than the 2D FEM. It can also be observed in Fig. 4.9 that the 1D model produced better results in the post-peak regime, which becomes very important when evaluating the resilience of structures under extreme loads. While the 2D FEM predicts very brittle failures, the proposed 1D model accounts for the available residual capacity. Therefore, the new -modelling framework will be able to properly account for the redistribution of forces in complex statically-indeterminate structures incorporating deep beams.

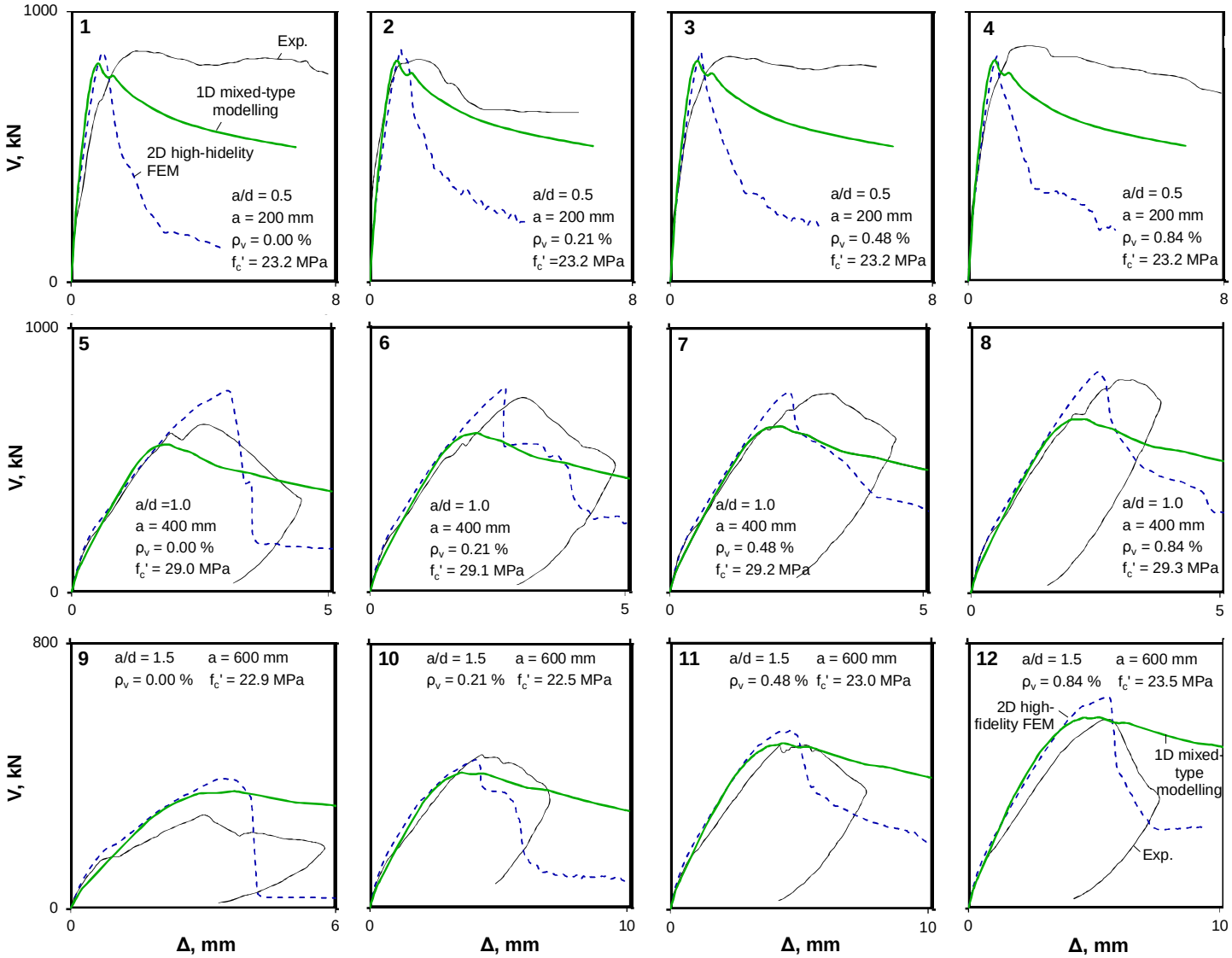
1
Exp.
1D mixed-type modelling
2D high-hidelity FEM
a/d = 0.5
a = 200 mm
ρv = 0.00 %
fc' = 23.2 MPa
2
a/d = 0.5
a = 200 mm
ρv = 0.21 %
fc' =23.2 MPa
3
a/d = 0.5
a = 200 mm
ρv = 0.48 %
fc' = 23.2 MPa
4
a/d = 0.5
a = 200 mm
ρv = 0.84 %
fc' = 23.2 MPa
5
a/d =1.0
a = 400 mm
ρv = 0.00 %
fc' = 29.0 MPa
6
a/d = 1.0
a = 400 mm
ρv = 0.21 %
fc' = 29.1 MPa
7
a/d = 1.0
a = 400 mm
ρv = 0.48 %
fc' = 29.2 MPa
8
a/d = 1.0
a = 400 mm
ρv = 0.84 %
fc' = 29.3 MPa
9
a/d = 1.5 a = 600 mm
ρv = 0.00 % fc' = 22.9 MPa
10
a/d = 1.5 a = 600 mm
ρv = 0.21 % fc' = 22.5 MPa
11
a/d = 1.5 a = 600 mm
ρv = 0.48 % fc' = 23.0 MPa
12
a/d = 1.5 a = 600 mm
ρv = 0.84 % fc' = 23.5 MPa
2D high-fidelity FEM
1D mixed-type modelling
Exp.
V, kN
Δ, mm
1000
800
0
8
5
6
10

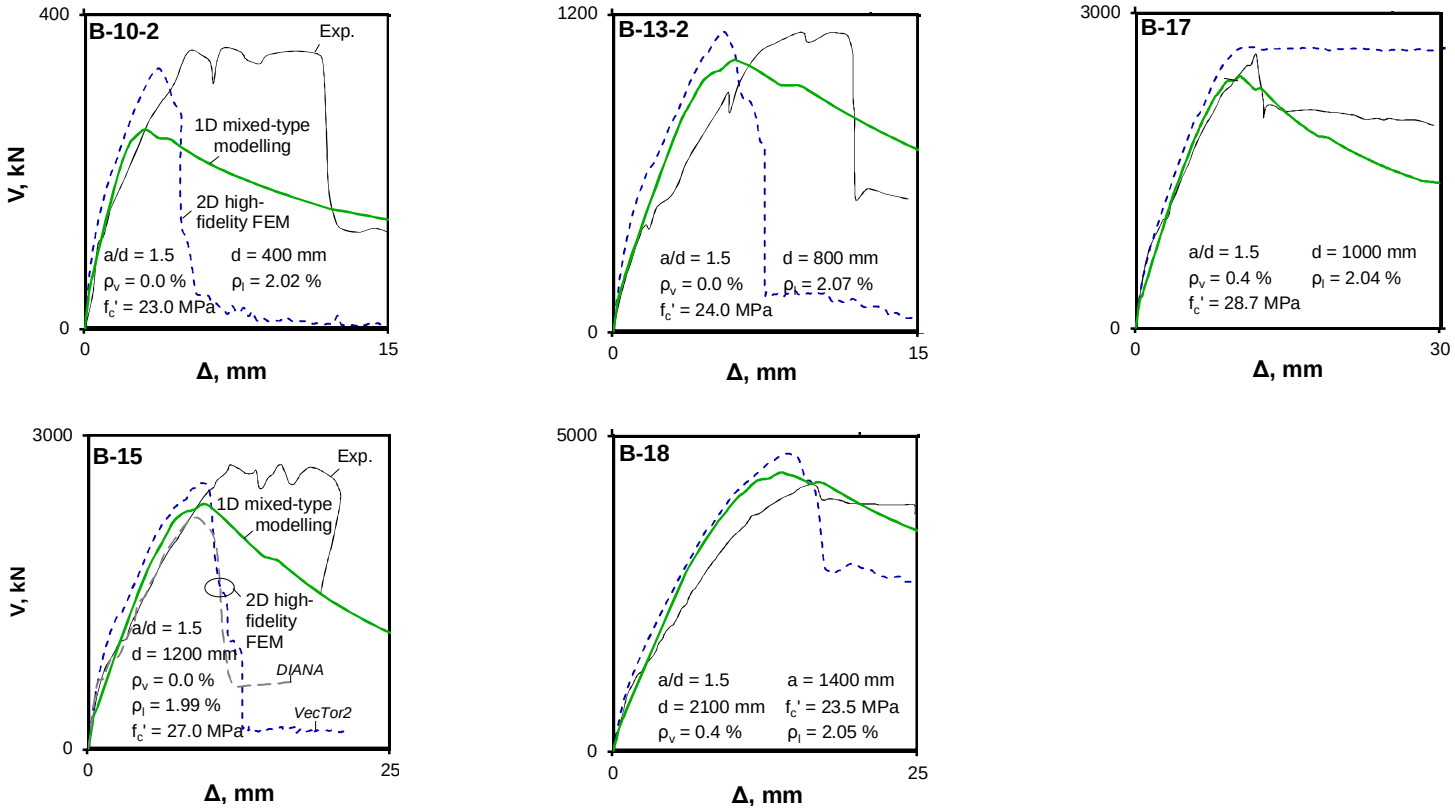

Fig. 4.9 Modelling of simply supported deep beam.

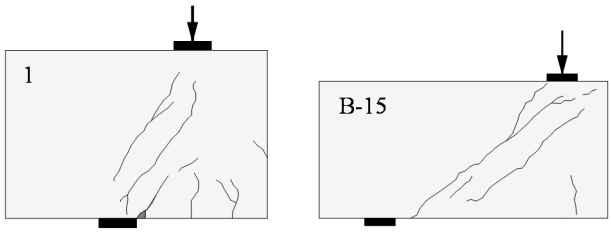

(a) Observed cracks at failure

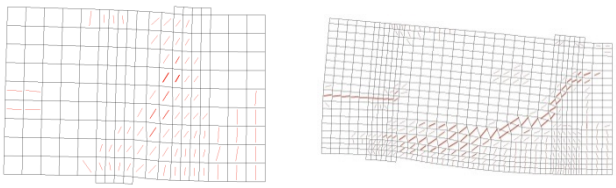

(b) 2D FEM predictions at failure (displacements×20)

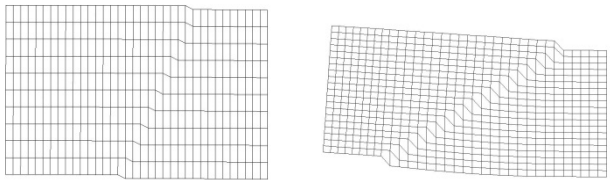

(c) 1D mixed-type model predictions at failure (×20)

Fig. 4.10 Crack and deformation patterns of beams 1 and B-15.

To better understand the modelling of the peak and post-peak behaviour, Fig. 4.10 compares measured and predicted crack and deformation patterns of two specimens. In Beams 1 and B-15 with a/d ratios of 0.5 and 1.5, respectively, the critical shear cracks developed diagonally across the shear span. For the shorter beam (i.e. Beam 1), the 1D and 2D models produce very similar deformation patterns at failure. For the longer beam (i.e. Beam B-15), the 1D model uses a straight diagonal crack while the 2D model predicts a steeper critical crack that extends along the bottom reinforcement. To generate these patterns, the 1D model uses DOFs θ_1 and Δ_c (θ_2=0 as the shear span is under single curvature bending), while the 2D model uses several hundreds of DOFs. Furthermore, as the proposed simpler approach models a discrete critical crack, it can accurately capture the ductility of the member when large sliding displacements occur along the crack in the post-peak regime. In contrast, the 2D smeared crack formulation results in a large concentration of principal tensile strains in a narrow band of finite elements. These strains in turn result in unrealistically high compression softening of the concrete and a rapid loss of post-peak resistance. Similar observations have been made with other 2D smeared crack formulations as they all result in strain concentrations (see for example the predictions of platform DIANA for beam B-15 in Fig. 4.9 reported by Salamy et al.[71]).

It is also of interest to compare the analysis time required by the 1D and 2D models. On the same PC with a 3.4 GHz quad-core processor and 16 GB of RAM, the 1D model required an average analysis time (considering all seventeen beams) of about 5s, while the 2D model required about 50s. While both times are short, the difference between the two models becomes important when large structures are analysed as

it will be demonstrated later. In addition, the time for modelling with the 1D approach is significantly shorter due to the straightforward input and small number of elements required.

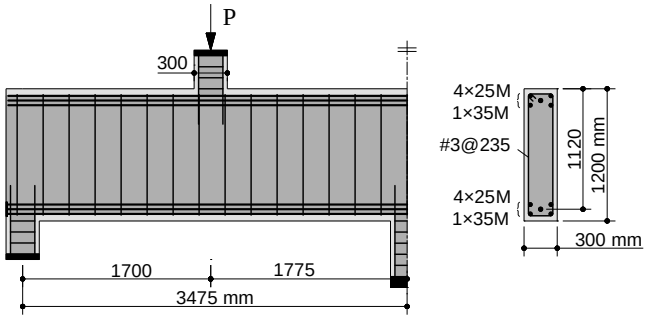

(a) Continuous deep beam specimen

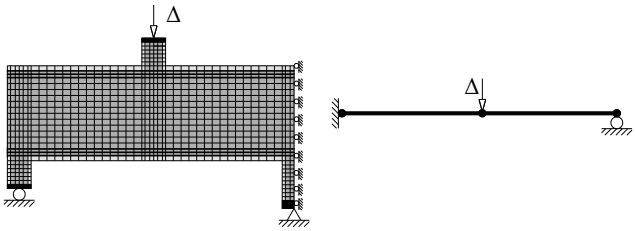

(b) 2D FE model c) 1D mixed-type model

Fig. 4.11 Modelling of a continuous deep beam tested by Mihaylov et al.[40]

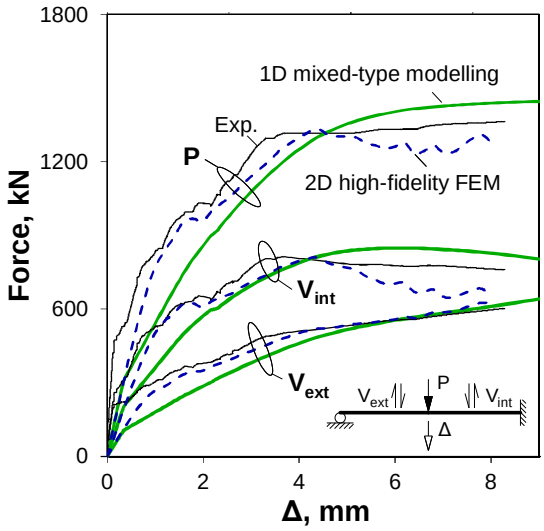

Fig. 4.12 Measured and predicted load-displacement response of a continuous deep beam.

4.5.1.2. Continuous deep beams

A continuous deep beam with two symmetrical spans was tested under two symmetrical concentrated loads by Mihaylov et al.[40] (see Fig. 4.11). The beam had a symmetrical top and bottom longitudinal reinforcement with a ratio of 0.91%, as well as stirrups with a ratio of 0.20%. As shown in Fig. 4.11b and c, only one half of the beam was modelled due to the symmetry. The 2D FEM uses 1179 elements while

the proposed 1D model uses only two macroelements. The two macroelements model the two shear spans, where the external shear span is under single curvature and the internal one is under double curvature. As with the simply supported beams, significantly less time was needed to generate the 1D model as compared to the 2D FEM. In terms of analysis time, the 2D model required about 145s while the 1D model took about 3s to complete the calculations.

4.5.2. Frame structure

Finally, it is of interest to compare the different modelling approaches when analysing large frame structure containing both slender and deep members. As laboratory tests of such structures are not available even in small scales, a sample 20-story frame was designed based on the ACI 318 provisions[8]. Fig. 4.13 shows the bottom two stories of the frame where a deep transfer girder is used to support a column from the floors above. The depth of the girder is chosen as 1.8 m, resulting in an a/d ratio of 1.63.

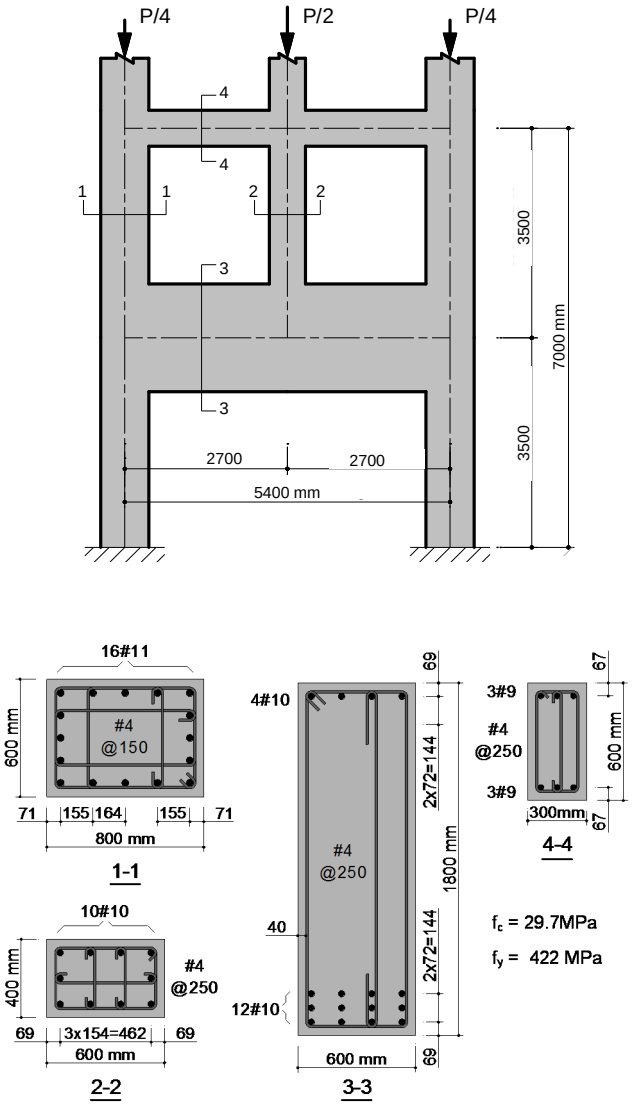

Fig. 4.13 Two-story single-span frame.

The lowermost two floors were modelled based on two strategies: 2D FEM and proposed 1D mixed-type modelling approach (Fig. 4.14a and b). The latter approach was also used to model the entire 20-story frame (Fig. 4.14c). For simplicity, only three point loads were applied at the top beam-column joints in the two-story models. The loads were increased monotonically until the transfer girder failed in shear along diagonal cracks.

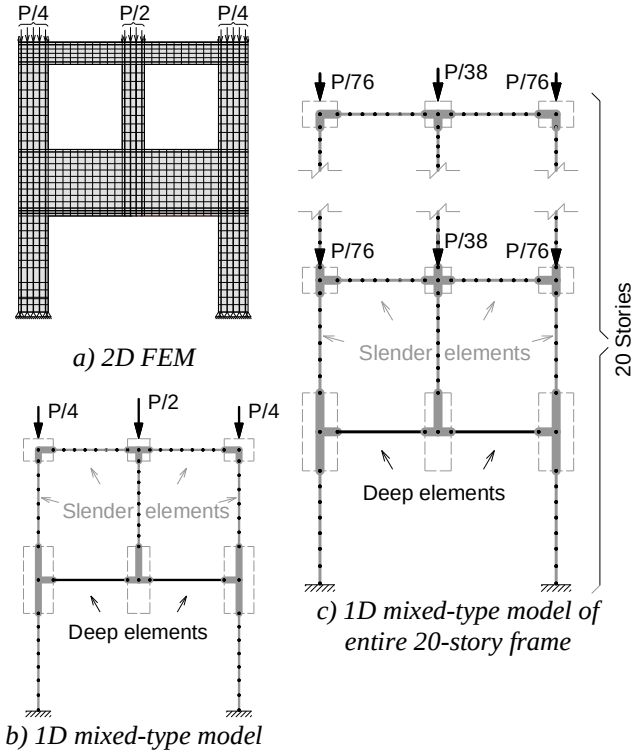

Fig. 4.14 Modelling of a large frame.

The total applied load on the frame is plotted in Fig. 4.15 as a function of the deflection of the deep transfer girder. As evident from the plot, the 2D FEM and the 1D mixed-type modelling approach produced very similar results, including an almost identical peak load. The plot also shows the results from the complete analysis of the 20-story frame performed with the 1D model in Fig. 4.14c. The forces P/2 and P/4 applied in the two-story model were distributed as P/38 and P/76 along the height of the 20-story model. Therefore, the load P in Fig. 4.15 remains the total load on the frame. In this regard, it is of interest to note that the 20-story building carried nearly two times larger total load than the 2-story frame. This increased resistance is due to the slender beams in the above floors which, though significantly less stiff than the transfer girder, provide a certain resistance as the girder deforms and fails in shear. Therefore, focusing the analysis on the bottom two floors and neglecting the interaction with the slender beams in the higher floors proves to be very conservative in this case.

To further study the redistribution of forces between deep and slender beams, an additional analysis of the 20-story frame is performed under imposed displacements. As shown in the inset of Fig. 16, equal vertical displacements were applied at the internal beam-column joints to obtain the post-peak behaviour of the frame. The plot shows the accumulative vertical force resulting from the shear forces in each beam. It can be seen that at the peak load the transfer girder carries approximately 40% of the total load. In the post-

peak regime, the deep girder fails almost completely when the deflection reaches approximately 18 mm, followed by the consecutive shear failures of the slender beams in the 2nd, 3rd and 4th floors. All failures occur in the same bay and the frames displaces laterally. Regardless of these failures, the structure continues to support a significant portion of the peak load due to the redistribution of the forces among the beams.

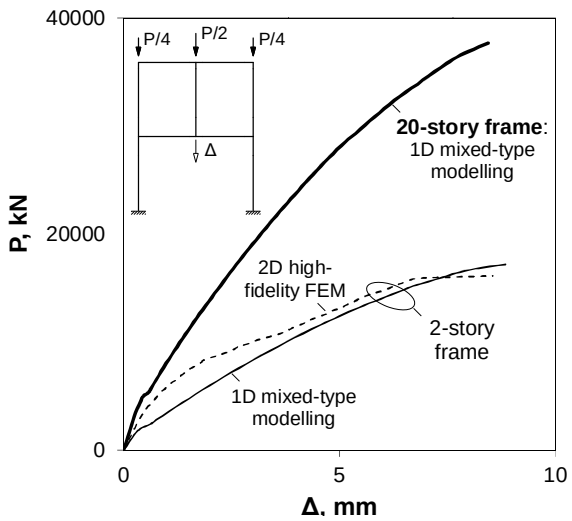

Fig. 4.15 Results from frame analysis under applied vertical loads.

A final analysis shows that the ductility of the frame can be further improved if it is part of a structure with stiff shear walls. The walls will limit the lateral displacements of the frame in the post-peak regime and will force more symmetrical shear failures in the two bays. The dashed line in Fig. 4.16 shows the behaviour of the frame when the lateral displacements are fully-restrained. It can be seen that, while the pre-peak response remains unchanged, the post-peak resistance is significantly higher, and therefore the structure is more resilient to overloading. This highlights the need for efficient 1D models for slender and deep beams that allow to capture the favourable effects that develop at the global structural level.

4.5.3. Efficiency of studied modelling strategies

Finally, the efficiency of the proposed 1D mixed-type modelling framework is examined and graphically illustrated in Fig. 4.17. The plot shows that for the structures modelled in this study, the proposed 1D model required significantly less degrees of freedom and computational time than the 2D FEM. The largest model (i.e. the 20-story frame under imposed displacements) required slightly less than 6 hours with 40 load steps. While not attempted, the analysis of this frame with the 2D FEM would require many days to run. In addition, creating a finite element mesh would require significant time and experience. This advantage of the proposed 1D mixed-type modelling will be even more pronounced in the analysis of larger multi-bay multi-story structures.

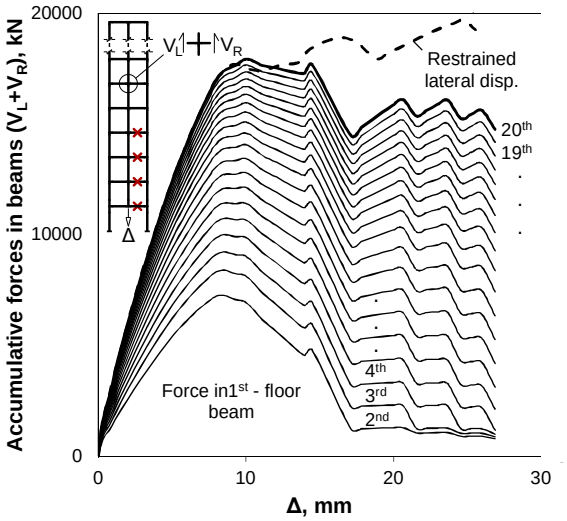

Fig. 4.16 Results from frame analysis under applied vertical displacements.

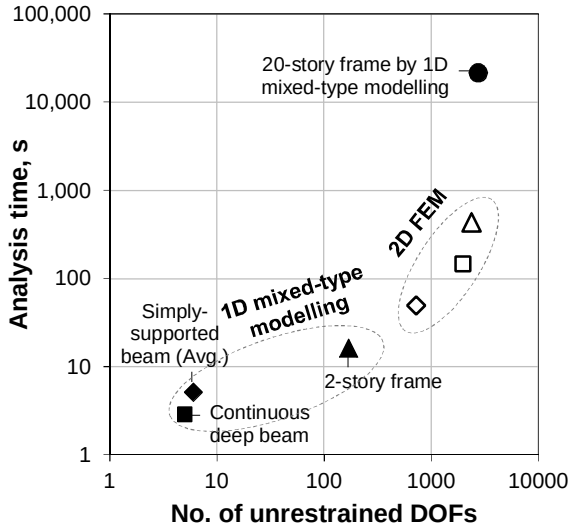

Fig. 4.17 Efficiency of modelling strategies.

4.6. Conclusions

This paper proposed a mixed-type modelling framework for large structures containing both slender and deep members. The framework integrates existing 1D beam elements for slender members with a novel 1D macroelement for shear spans of deep beams. It was implemented in an existing computer program VecTor5 for monotonic loading conditions, and evaluated with 18 deep beams and a 20-story frame. The performed studies led to the following conclusions:

The 1D macroelement for deep shear spans provides a full compatibility with fibre-based 1D beam elements for slender members as it uses the same nodal DOFs.

When applied to simply supported deep beams, the proposed framework produces similarly adequate results as those obtained with 2D high-fidelity FEM, and even improves the post-peak predictions.

The proposed 1D macroelement captures the increased ductility of shear-critical continuous deep beams resulting from force redistribution.

The proposed mixed-type modelling framework uses straightforward input and requires significantly less time for modelling and computation than 2D FEM.

As the new framework is computationally efficient and captures well the complete pre- and post-peak behaviour of frames with slender and deep members, it represents a valuable tool for the analysis of complex structures under extreme loading.

5. Shear Strength of RC Deep Beams with Web Openings

Abstract Deep concrete beams often feature web openings that disrupt the flow of forces from the loads to the supports and reduce the shear strength of the member. While such openings can significantly impact the safety level of the structure, the research on deep beams has been focused mostly on the shear behaviour of solid members. To address this issue, this paper proposes a new model for deep beams with rectangular openings that stems from a two-parameter kinematic theory (2PKT) for solid beams. The model is established based on an analysis of the shear behaviour and failure modes of test specimens using nonlinear finite element and strut-and-tie models. In the new model, a deep shear span with an opening is represented with two solid shear spans, one above and one below the opening. By linking the two sub-models, the proposed kinematics-based approach describes the complete deformed shape of the shear span with four degrees of freedom (DOFs). These DOFs are predicted by combining the kinematic conditions with equilibrium conditions and constitutive relationships for the mechanisms of shear resistance across the critical shear cracks. The model is validated with 27 tests from the literature showing adequate shear strength predictions.

Article Liu, J., and Mihaylov, B.I., "Shear strength of RC deep beams with web openings based on two-parameter kinematic theory," submitted to *Structural Concrete.*

5.1. Introduction

Deep beams are widely used as transfer girders in high-rise buildings, cap beams in bridges, pile caps in foundations and other important structural members. Due to their small shear-span-to-depth ratios ($a/h \leq$ approx. 2.5), deep beams carry heavy shear forces and develop more complex deformation patterns than slender beams. Since the 1950s, researchers have carried out a large number of experiments [41, 22,72-75] and have proposed different types of models[24,25,30,32,49] in order to understand the shear behaviour and provide reliable predictions of the shear capacity of deep beams. However, the majority of these studies have been focused on members without web openings, while in practice openings are frequently installed in deep beams to accommodate doors, windows, various conduits and communications as shown in Fig. 5.1. The presence of such openings can significantly reduce the shear capacity of deep beams, particularly if they interrupt the direct flow of compressive stresses from the loading points to the supports (strut or arch action).

To study these effects, some of the early experimental studies were performed by Kong and co-workers in the 1970s[76]. More recently, Yang et al.[77] performed shear tests of thirty two simply-supported deep beams with rectangular openings and studied the effects of the opening size and position, as well as the strength of the concrete. It was concluded that the shear strength strongly depended on the angle of the inclined plane joining the support and the closest corner of the web opening. Furthermore, the concrete strength appeared to play a more significant role in deep beams with web openings than in solid deep beams. Yang and Ashour[78] extended their interest to continuous deep beams with openings, and twenty-two specimens were tested to investigate the effect of the configuration of web reinforcement around openings, location of openings, and a/d ratio. It was found that the shear capacity was significantly affected by the openings within interior shear spans rather than exterior shear spans, and inclined web reinforcement was the most effective type for controlling diagonal crack width and increasing load capacity. Campione and Minafo[79] carried out experimental investigations on deep beams with circular web openings, and found that an opening that occupies 21% of the section depth can reduce the shear capacity of deep beams by up to 30%. Sahoo et al.[80] designed two RC deep beams with large openings based on strut-and-tie models (STMs) based on which complicated reinforcement detailing was required around the web openings. It was found that the STMs significantly underestimated the shear capacity of the tested specimens and failed to predict

some severe local failures. By testing two companion beams reinforced by steel fibres, the authors suggested replacing the conventional reinforcing bars with de-formed steel fibres at a certain volume to benefit from the duc-tile plastic mechanism and avoid complicated detailing of rein-forcements. Considering that deep beams in existing structures are often strengthened after the drilling of web openings, El-Maaddawy and Sherif[81], Hawileh et al.[82], Hussain and Pimanmas[83], and Lu et al.[84] studied the effect of different strengthening systems on the shear behaviour of such members. In order to account for the effect of openings on the shear capacity, Tan et al.[85] proposed a strut-and-tie model that includes load paths above and below the opening following earlier research by Kong and Sharp[86]. Using this statically indeterminate model, Tseng et al.[87] distributed the shear force to the two load paths according to their relative stiffness and calculated the shear capacity of each load path as for deep beams without openings. For 26 tests specimens without horizontal reinforcement above the opening, the proposed model resulted in an average shear strength experimental-to-predicted ratio of 1.34 and a coefficient of variation (COV) of 18%. The same tests were also analysed with the strut-and-tie models proposed in [85,86] resulting in average ratios of 1.0 (1.01) and COV of 23%(28%).

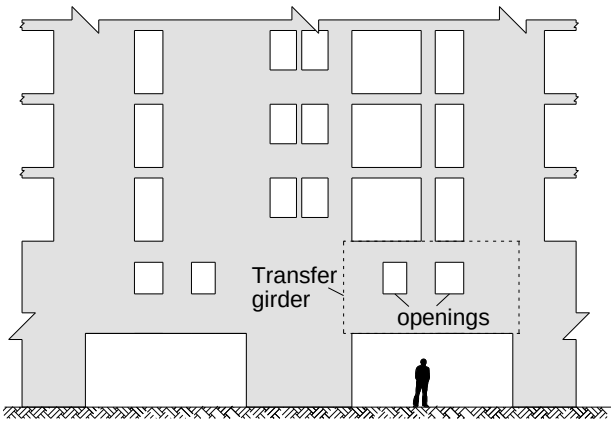

Fig. 5.1 A 30-storey apartment having transfer girder with web openings

This paper proposes a different approach for evaluating the capacity of the load paths in deep beams with rectangular openings. The critical regions below and above the opening will be modelled based on a two-parameter kinematic theory (2PKT)[10] for solid deep beams, and the interactions between the regions will be taken into account by considering the equilibrium of the internal forces. The 2PKT is based on a simple two-degree-of-freedom description of the deformation patterns of short shear spans, and also includes equilibrium conditions and constitutive relationships for the mechanisms of shear resistance. Using a database of 434 tests of solid deep beam, Liu and Mihaylov[47] have shown that the 2PKT provides the most reliable and accurate predictions of shear strength as compared to existing strut-and-tie models, upper-bound plasticity and other models. In addition to shear strength, the 2PKT also predicts the deformation patterns of the beam at failure, and this will be extended to model the kinematics of deep beams with web openings.

5.2. Observed behaviour of deep beams with openings

The behaviour of deep beams with web openings will first be discussed with the help of lab tests performed by El-Maaddawy and Sherif[81]. The test programme involved nine deep beam specimens with web openings loaded to failure under symmetrical four-point bending (Fig. 5.2). The beams had an 80

mm by 500 mm rectangular section and a shear span of 400 mm. A square opening was placed in each shear span symmetrically about the mid-span section of the beam. According to the position of the opening, the nine beams were classified into three groups, i.e. an opening at the centre, bottom and top part of the shear span. In each group, the opening size a_0 was either 150 mm, 200 mm or 250 mm. The 28-day compressive strength of the concrete was 21.0 MPa while the yield strength of the longitudinal and web reinforcement was 420 MPa and 300 MPa, respectively. To reproduce cases of drilling or enlarging an opening in existing beams, the web steel reinforcement intercepted by the opening was cut at its contour.

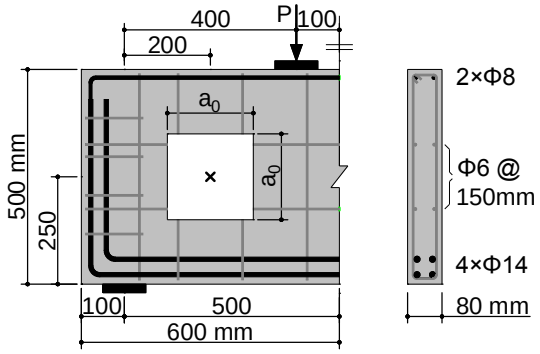

(a) Opening at centre

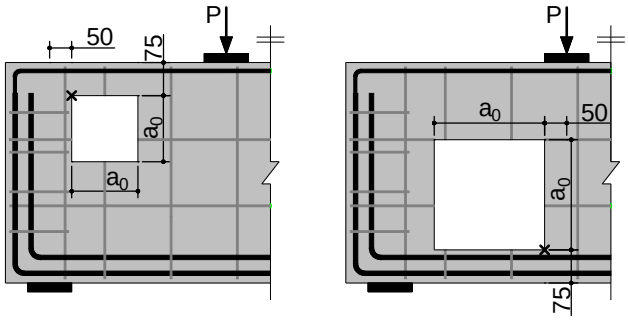

(b) Opening at top (c) Opening at bottom

Fig. 5.2 Deep beams tested by El-Maaddawy and Sherif[81]

Fig. 5.3 compares the crack patterns of test specimens NS-150-C and NS-250-C after failure. The two beams differed only in terms of the size of the web openings which were centred at mid-depth of the section (a_0=150 mm vs. 250 mm). In both beams the cracking began at the two opposite corners of the opening along the line connecting the loading and support points. These cracks propagated away from the opening and were not well controlled by web reinforcement as evident from the reinforcement layout in Fig. 5.2a. However, as the load was increased, new inclined cracks formed in the shear span, and the crack patterns of the two specimens diverged. According to the authors of the tests, this resulted in two typical failure modes depending on the opening size. The first failure mode was observed when the opening size was 150 mm or 200 mm, while the second occurred in the specimens with the largest openings (250 mm). In the former cases, the beam failed suddenly along inclined cracks in the regions below and above the opening. As the inclined cracks opened, the shear span split into two relatively intact segments ① and ② as indicated in Fig. 5.3a. In contrast, the specimens with the largest openings exhibited a more gradual failure along three sets of cracks (Fig. 5.3b). In these cases, segments ①, ②

and ③ performed relative rotations simultaneously with the widening of the cracks. In terms of shear capacity of the beams in Fig. 5.3, specimen NS-150-C with an opening of 150 mm was about two times stronger than NS-250-C with a_0=250 mm (103 kN vs. 53 kN).

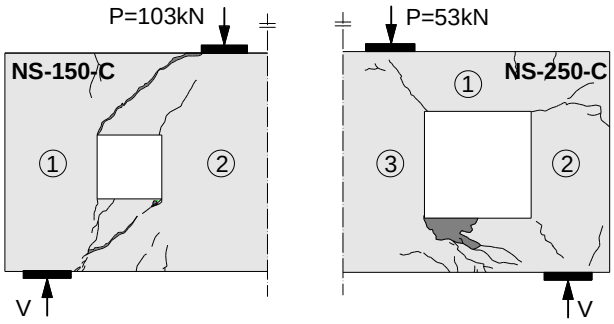

(a) Failure mode A (b) Failure mode B

Fig. 5.3 Typical failure modes of deep beams with openings (adapted from El-Maaddawy and Sherif[81])

5.3. Finite element analysis of deep beams with openings

To gain further insight into the shear behaviour of deep beams with web openings, the behaviour of selected test specimens is simulated with a nonlinear finite element model (FEM). The analyses were performed based on the Distributed Stress Filed Model for reinforced concrete (DSFM)[67] implemented in program VecTor2[13]. The DSFM is smeared rotating crack model that originates from the modified compression field theory for reinforced concrete elements subjected to shear (Vecchio and Collins, 1986)[53]. In the DSFM, the cracks are assumed parallel to the principal compressive stress directions in the concrete, while the principal strain directions deviate from the stress directions due to slip displacements in the cracks. The slip displacements and crack widths are used to calculate aggregate interlock stresses transferred across the cracks. In addition to aggregate interlock, the DSFM also accounts for the tension stiffening and softening of the concrete, compression softening and confinement of the concrete, as well as the yielding of the reinforcement. To ensure that the analyses can be easily reproduced, these effects were modelled based on the default constitutive relationships implemented in program VecTor2. The only exception is the compression behaviour of the concrete for which the Popvics' model[54] for normal strength concrete was preferred.

Fig. 5.4a shows a typical finite element model of a deep beam with openings (specimen NS-150-C). The model consists of quadrilateral plane-stress elements for the concrete and truss elements for the reinforcement. Due to the symmetry, only one-half of the beam was modelled with the mid-span section of the beam restrained by horizontal supports. The applied load and support reaction were distributed uniformly along the loading plate and the support plate. The forces were increased monotonically to study the behaviour of the beam up to failure.

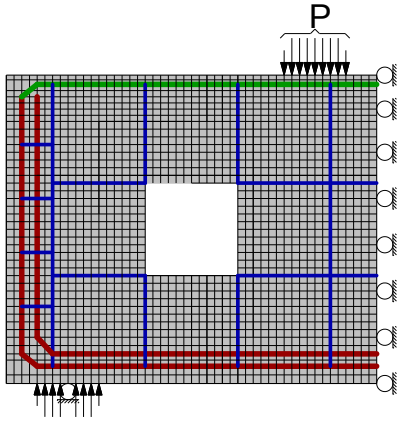

(a) FEM model of beam NS-150-C

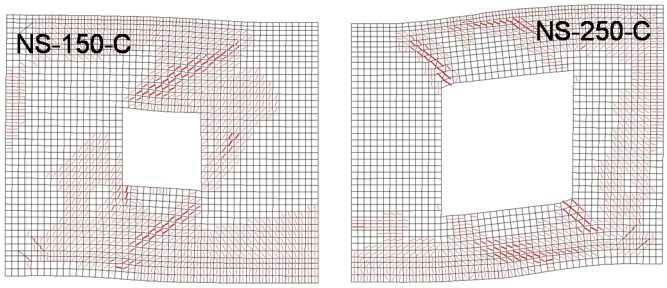

(b) Deformation (×10) and crack pattern

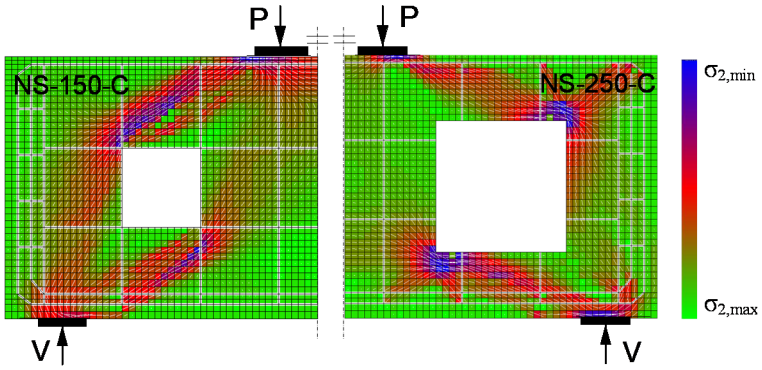

(c) Principle compressive stress

Fig. 5.4 Deep beams with web openings studied by FEM

Based on these analyses, Fig. 5.4b shows the predicted deformed shapes and crack patterns of beams NS-150-C and NS-250-C at peak load. It can been seen that the specimen with the smaller opening failed along shear cracks in the regions below and above the openings, while the companion beam exhibited opening of the initial cracks in the corners of the openings. These results, as well as the magnified deformed shapes in Fig. 5.4b, agree well with the tests observations. In addition, the FEM was also able to capture well the shear strength of the beams: 99.2kN for NS-150-C (4% less than the test) and 48.0 kN for NS-250-C (10% less than the test).

Considering these adequate predictions, it is of interest to use the FEM to gain insight into the load paths that developed in the two beams. Fig. 5.4c shows the predicted distribution of the principle compressive stresses in specimens NS-150-C and NS-250-C at failure. It is evident from these diagrams that the beams developed simultaneous load paths above and below the openings consistent with earlier findings[85]. It can also be seen that when the opening size is small (38% of the shear span in the case of NS-150-C), the force is transferred from the loading point to the support directly around the corners of the opening. On the other hand, as the opening size is increased to 63% of the shear span in NS-250-C, the compressive stresses on the left and right sides of the opening appear to be relatively low, while high compression develops between the top corner of the beam and the closest corner of the web opening.

5.4. Strut-and-tie model of deep beams with openings

The stress trajectories in Fig. 5.4c are used to establish an appropriate strut-and-tie model for deep beams with web openings, see Fig. 5.5a. This model details the load paths above and below the opening by using struts for the compression flow in the concrete and ties for the tension in the reinforcement. The main components of both load paths are pairs of struts that connect the loading and support points by deviating around the corners of the opening. To ensure the equilibrium of the forces at the upper corner, the top mechanism includes a system of two ties (T_2 and T_3) and an additional strut. On the other hand, the equilibrium at the bottom corner is provided without tension by a horizontal strut. The shear resistance of the member is expressed as the sum of the shear carried by the top and bottom inclined struts V_t and V_b, respectively. It is immediately evident from the model that the top strut may not reach its full capacity due to early yielding of tie T_2 or T_3.

It should be noted this model does not account for reinforcement (ties) around the opening, and therefore it is well suited for the cases when the opening is made in an existing girder as simulated in the tests by El-Maaddawy and Sherif[81]. If however the opening is previewed in the design process, it is common to provide such reinforcement in order to control the cracking at the corners of the opening. Furthermore, this reinforcement results in an additional load path as illustrated with the strut-and-tie model in Fig. 5.5b, and therefore can increase the load-bearing capacity of the beam. In the following, the relative importance and capacity of the load paths above and below the opening in Fig. 5.5a will be evaluated based on the two-parameter kinematic theory. For simplicity and on the conservative side, the additional load-bearing mechanisms provided by reinforcement around the opening will be neglected.

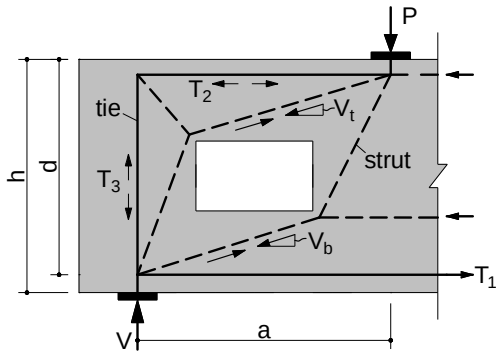

(a) Without reinfocement around web opening

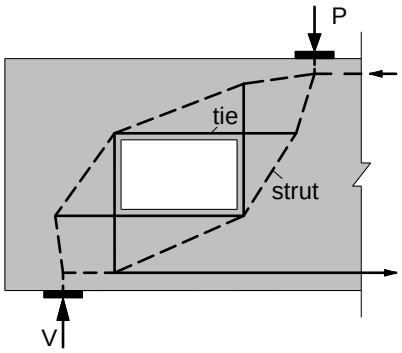

(b) With reinfocement around web opening

Fig. 5.5 Strut-and-tie model for deep beams with openings

5.5. Proposed model for deep beams with web openings

5.5.1. Summary of two-parameter kinematic theory

The two-parameter kinematic theory (2PKT)[10] for shear behaviour of deep beams is built on a kinematic description of the deformation patterns of short shear spans without openings. The shear failure is assumed to occur along a diagonal crack which divides the shear span into two parts as illustrated in Fig. 5.6a. The part below the crack is modelled as a fan of rigid struts while the zone above the crack is represented by a rigid block. The deformation pattern of the shear span is described with two degrees of freedom (DOFs): the average strain along the bottom reinforcement ε_t and the vertical displacement in the critical loading zone (CLZ) Δ_c. The CLZ represents the concrete under high diagonal compression above the tip of the critical crack where crushing typically occurs at failure. DOF ε_t is associated with widening of the critical crack while Δ_c with both widening and slip displacements. These crack displacements are used to evaluate the shear mechanisms across the crack by using appropriate constitutive relationships, and the shear resistance is expressed as:

$$V = \Sigma V_i = V_{CLZ} + V_s + V_{ci} + V_d \tag{5.1}$$

where V_{CLZ} is the shear carried by critical loading zone, V_s by the stirrups, V_{ci} by aggregate interlock, and V_d by dowel action of the flexural reinforcement (Fig. 5.6b). DOF Δ_c is evaluated based on the assumption that the CLZ crushes at failure, while ε_t is obtained by considering the equilibrium of the shear forces.

The solution procedure of the 2PKT approach is illustrated graphically in Fig. 5.7. The solution is obtained by intersecting a shear capacity curve given by Eq. (5.1) with a shear "demand" curve derived from the rotational equilibrium of the shear span:

$$V = T\, z/a \tag{5.2}$$

where $T(\varepsilon_t)$ is the tension force in the flexural reinforcement and $z \approx 0.9d$ is the lever arm of the longitudinal forces in the midspan section. Force T is obtained from strain ε_t by considering an elastic-perfectly-plastic behaviour of the bare reinforcement as well as the tension stiffening effect of the concrete. Further details about the 2PKT approach are available elsewhere [10,39].

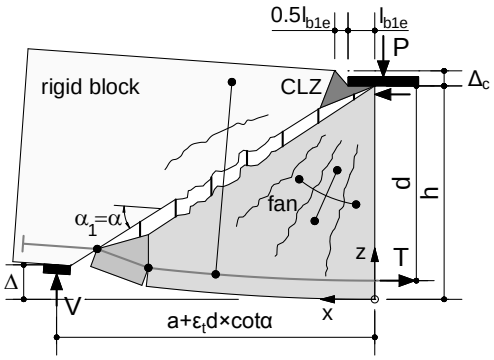

(a) Deformation pattern

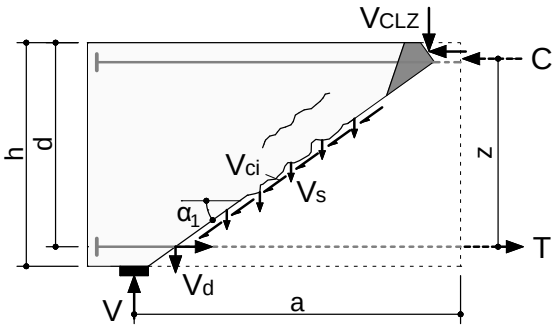

(b) Shear components along the diagonal crack

Fig. 5.6 Two-parameter kinematic theory (2PKT) for deep beams

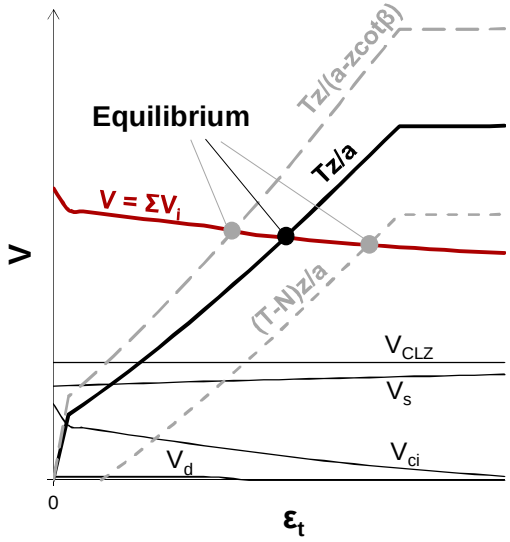

Fig. 5.7 Solution procedure under given Δ_c

5.5.2. Account of external longitudinal forces

As it will be illustrated later, the modelling of deep beams with opening requires a modification of the original 2PKT approach to take into account the effect of longitudinal forces. More precisely, a compression or tension force will be applied at the supports as illustrated in Fig. 5.8. The compression force is expressed as being proportional to the shear force N=V.cotβ, while the tension force is considered with a constant value N. To incorporate these forces in the 2PKT approach, it is needed to modify the shear demand Eq. (5.2) as follows:

$$V = Tz/\left(a - z\cot\beta\right) \tag{5.3}$$

for compression and

$$V = \left(T - N\right)z/a \tag{5.4}$$

for tension. These relationships are plotted with dashed lines in Fig. 5.7 on both sides of the original Eq. (5.2). It can be seen that compression will increase the shear strength prediction while tension will result in a weaker ultimate response. This effect is explained mainly with the aggregate interlock component of shear resistance V_{ci}: tension forces result in wider diagonal cracks and therefore less aggregate interlock across the crack. Inversely, compression forces clamp the cracks and increase their ability to transfer shear by interlocking.

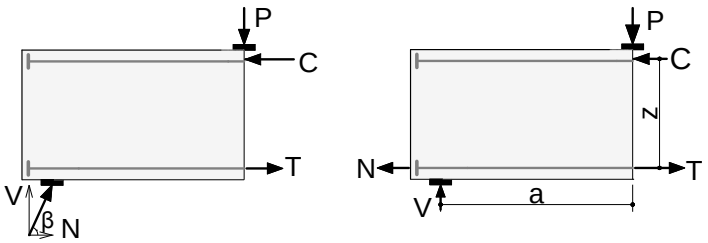

(a) Inclined support reaction (b) Tensile force at beam end

Fig. 5.8 Other loading cases

5.5.3. Kinematic model for deep beams with web openings

The crack patterns observed in Fig. 5.3 are used to propose a kinematic model for deep beams with openings that combines two solid deep beams, see Fig. 5.9a. The model includes three sets of major cracks: critical shear cracks above and below the opening, cracks connecting the corners of the opening to the loading and support points, and a horizontal crack that propagates from the side edge of the beam to the opening. Each of the two critical shear cracks occurs between a rigid block and a fan of struts as in the original 2PKT approach for solid beams. The fans are associated with the tensile strains in the top and bottom longitudinal reinforcement consistent with the strut-and-tie model in Fig. 5.5a. Therefore, the kinematics of the 2PKT will be applied to the zones above and below the opening. The bottom zone extends from the centre of the support to the far lower corner of the opening. Similarly, the top zone extends from the loading point to the far top corner of the opening. As evident from the figure, the critical loading zones develop at those two opposite corners of the opening where the concrete is under high compression according to the strut-and-tie model. As each of the solid deep beams above and below the openings features two degrees of freedom, the complete kinematic model uses four DOFs. In Fig. 5.9b

these DOFs are grouped two by two: average strains in the top and bottom longitudinal reinforcement ε_{tt} and ε_{tb} as well as transverse displacements Δ_{ct} and Δ_{cb} in the critical loading zones. In the general case, all DOFs are associated with opening of the five cracks assumed in the model, while DOFs Δ_{ct} and Δ_{cb} cause slip displacements in the critical shear cracks.

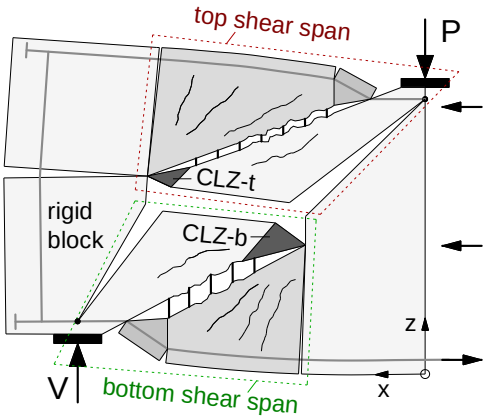

(a) Details of kinematic model

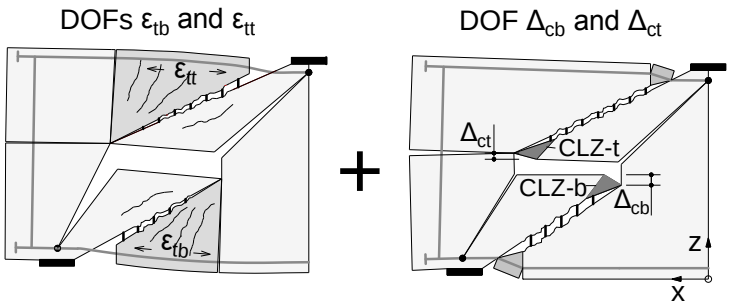

(b) Degrees of freedom of kinematic model

Fig. 5.9 Kinematics of deep beams with openings

5.5.4. Failure load of deep beams with web openings

To calculate the shear carried above and below the opening in deep shear spans, it is necessary to consider the free-body diagrams depicted in Fig. 5.10. In this figure the shear span is divided into two parts along the cracks propagating from the opening towards the loading and support points. Assuming that these cracks are approximately free of stresses, the L-shaped portion of the beam above the cracks is subjected to diagonal compression through the loading and support points. The thrust line in this block of concrete is shown with a dashed line inclined at angle β which is directly linked to the aspect ratio of the shear span. This illustrates that the deep beam above the opening with a shear span at works under the same loading conditions as the beam in Fig. 5.8a: shear V_t and a longitudinal compression force at the level of the flexural reinforcement $N_t=V_t.\cot\beta$. Therefore, the shear resistance V_t can be determined by using the 2PKT with Eq. (5.3) as illustrated in Fig. 5.7.

In addition to the shear calculation for the L-shaped portion of the shear span, it is also necessary to check the resistance of section “A” containing the horizontal crack. This section can fail under the combination

of bending and axial compression as indicated in the small free-body diagram in Fig. 5.10a. The compression force on the section is V_t while the bending moment is $V_t e$, where the eccentricity e is the horizontal distance from the centre of the section to the thrust line at angle β. The strength calculation can be performed based on the classical theory for flexure using a rectangular stress block in the compression zone. As a result, if V_t associated with failure of section A is smaller than the shear resistance of the region above the opening, it will govern the strength prediction for the L-shaped portion of the beam. Similarly to the strut-and-tie model, this illustrates the importance of the reinforcement along the vertical edge of the beam. If this reinforcement is small or completely omitted, this will greatly reduce or eliminate the capacity of the load path above the opening. Furthermore, this capacity can also be limited by a shear failure below section A which is rare but needs to be checked as well. As evident from the free-body diagram, the region below section A is subjected to shear N_t and compression V_t.

Once the calculation of the L-shaped block is completed and the forces V_t and N_t are known, it is necessary to study the equilibrium of the region below the web opening (Fig. 5.10b). This region is subjected to shear force V_b and a tension force N_t applied at the level of the bottom longitudinal reinforcement. Therefore, this region works under the same loading conditions as the beam in Fig. 5.8b, and its shear resistance is calculated according to the 2PKT approach with Eq. (5.4) as illustrated in Fig. 5.7. Fig. 5.7 shows that, if the regions above and below the web opening are identical in terms of geometry and reinforcement, the bottom region will resist less shear. This is because the bottom region is subjected to tension N_t while the top region experiences a compression force of the same magnitude.

Finally, even though the regions above and below the opening resemble almost exactly shear spans of deep beams, there is an important difference that needs to be taken into account. While in deep beams the load is introduced into the CLZ via a plate or a column of a known dimension, in beams with openings the CLZ occur at the corners of the opening without clear geometrical limits. This has an effect on the size of the critical loading zones, and therefore on DOF Δ_c and shear component V_{CLZ}. To resolve this issue, it is suggested to use an effective size of the CLZ proposed for short shear walls and short coupling beams[88, 89] :

$$l_{b1e} = 0.11\sqrt{a^2 + h^2} \leq 370mm \tag{5.5}$$

where the square root represents the length of the diagonal of the shear span. The calculations for the region above (below) the web opening are performed with a shear span a_t (a_b) and depth h_t (h_b) as depicted in Fig. 5.10. With these lb1e values, DOF Δ_c and shear component V_{CLZ} are evaluated from Mihaylov et al. [10]:

$$\Delta_c = 0.0105 l_{b1e} \cot\alpha \tag{5.6}$$

$$V_{CLZ} = 1.43 f_c'^{0.8} k b l_{b1e} \sin^2\alpha \tag{5.7}$$

where k is a crack shape coefficient.

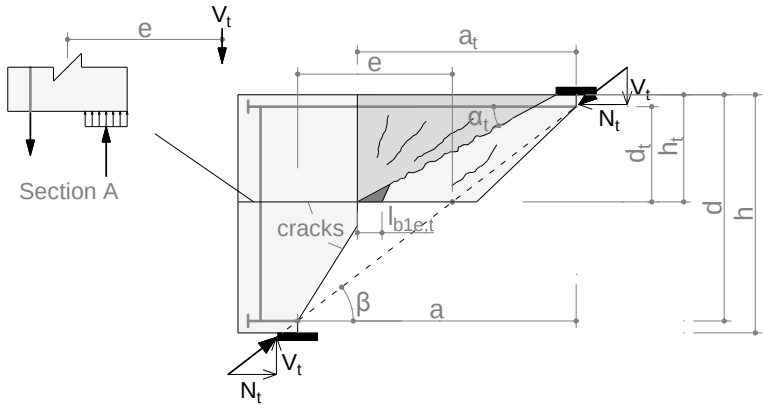

(a) Top L-shaped region

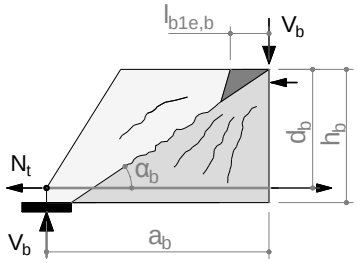

(b) Bottom region

Fig. 5.10 Equilibrium of forces in deep beams with openings

5.5.5. Calculation procedure

In summary, the calculation procedure of the proposed kinematics-based approach consists of five steps as illustrated in Fig. 5.11. The first step is to identify the two shear spans separated by the web opening and to calculate their geometry. The main geometrical properties include the shear span, the depth of the section, the position and amount of longitudinal tension reinforcement, as well as the stirrup ratio. In a second step, these properties are used to evaluate the shear capacity of the top shear span V_t following the 2PKT procedure in Fig. 5.7. The original demand curve of the 2PKT is replaced with the one given by Eq. (5.3) to account for the compression in the region above the opening. In a third step, the obtained shear resistance is compared to V_t associated with flexural failure of section A, and the minimum resistance is used to continue the calculations. The capacity of section A is calculated based on the classical approach for flexure combined with axial loading. In step 4, the shear strength of the region below the opening V_b is calculated based on the 2PKT method similarly to the calculations in step 2. However, as compared to the top region, the bottom region is subjected to a tension force $V_t.\cot\beta$ and the demand curve is given by Eq. (5.4). Finally, the shear capacity of the beam with an opening is obtained as the sum of the shear forces carried above and below the opening $V=V_t+V_b$.

5.5.6. Limits of applicability

Considering the simplifying assumptions made in the derivation of the proposed model, it is necessary to establish certain limits on its applicability. Firstly, as mentioned earlier, the model is developed for deep beams with rectangular web openings without heavy reinforcement around the opening. If the opening

features such reinforcement, the model will produce more conservative results. Furthermore, in order for the opening to cause sufficient disturbance of the flow of forces and to result in deformations consistent with the assumed kinematics, it must intersect the diagonal of the shear span and it must be sufficiently large. Based on comparisons with tests, the minimum horizontal and vertical dimensions of the opening are set at 0.2a and 0.1h, respectively. Finally, because the 2PKT is developed for deep beams and becomes very conservative for slender members, the shear-span-to-depth ratios of the regions above and below the opening a_t/h_t and a_b/h_b should not be larger than 4.

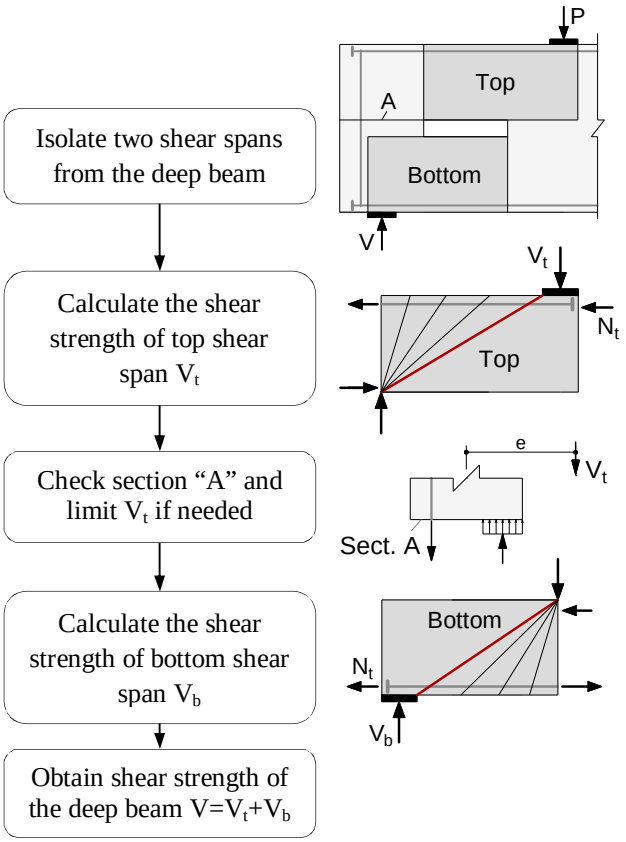

Fig. 5.11 Calculation procedure

5.6. Comparison with tests

Twenty seven deep beams satisfying the above criteria from two experimental programs [77, 81] are used to validate the proposed model. All beams were tested under symmetrical four-point bending and failed in shear. Fig. 5.12 shows a generic shear span with fully-defined properties while the data for each individual test is presented in an Appendix C. The shear-span-to-effective-depth ratio of the beams a/d varies from 0.5 to 1.6, beam depth h from 500 mm to 600 mm; the concrete compressive strength f_c from 21.0 MPa to 80.4 MPa, the bottom longitudinal reinforcement ratio ρ_l from 0.97% to 1.67%, and the stirrup ratio ρ_v from 0 to 0.47%. As shown in Fig. 5.12, the location of the centre of the opening is defined by k_1a and k_2h, where the former is measured from the centre of the support and the latter from the bottom edge of the beam. The size of the opening is $m_1a \times m_2h$. For the beams in the database, k_1 and k_2 keep constant as 0.5, while m_1 varies from 0.25 to 0.65 and m_2 from 0.1 to 0.5.

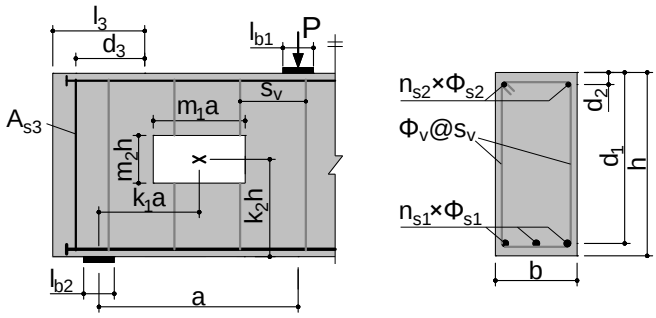

Fig. 5.12 A typical beam in this study

The shear capacity of each beam is calculated following the procedure outlined in Fig. 5.11 and the results are listed in the Appendix C. The obtained average ratio between the experimental and predicted shear capacity V_{exp}/V_{pred} for the twenty seven deep beams is 1.12 with a coefficient of variation (COV) of 7.6%. These results were obtained by neglecting the strain hardening of the reinforcement in section "A", even though the tensile strength of the bars fu used in Yang et al.[77] was 34% higher than the yield strength f_y. If this is taken into account, the average shear strength experimental-to-predicted ratio decreases to 1.03 and the COV increases slightly to 9.3%. Both sets of predictions are plotted in Fig. 5.13 as functions of the main test variables f_c, a/d, m_1 and m_2. As evident from the plot, the proposed model does not exhibit a clear bias with regards to any of the variables. In addition to generating this statistics, the proposed model is also used in the following to study the effect of the test variables on the shear strength of individual test series.

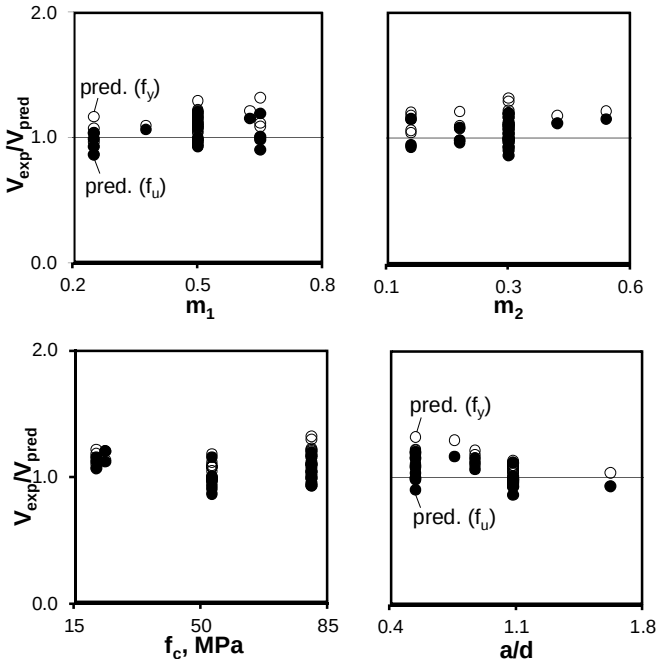

Fig. 5.13 Distribution of V_{exp}/V_{pred} with different parameters

5.6.1. Effect of opening size m_1 and m_2

The size of the web opening represents an important variable that significantly affects the shear strength. It is therefore first of interest to compare the predictions of the 2PKT approach to the shear strength of specimens NS-150-C and NS-250-C whose behaviour was studied in detail. According to the experimental points in Fig. 5.14, when the opening was enlarged from 30% to 50% of the section depth, the shear resistance decreased approximately two times. It can be seen that the 2PKT approach follows closely this trend, even though it produces slightly conservative predictions. It can also be seen that, according to the model, the bottom load path provided about 40% larger shear resistance than the top path. This result is counterintuitive because the opening was centred at the middle of the section and the region below the opening was subjected to shear and tension. However, the weakening effect of the tension force was offset by the bottom longitudinal reinforcement which was six time larger than the top reinforcement. In addition, for two of the three specimens, the capacity of the top region was limited by flexural failure in section A.

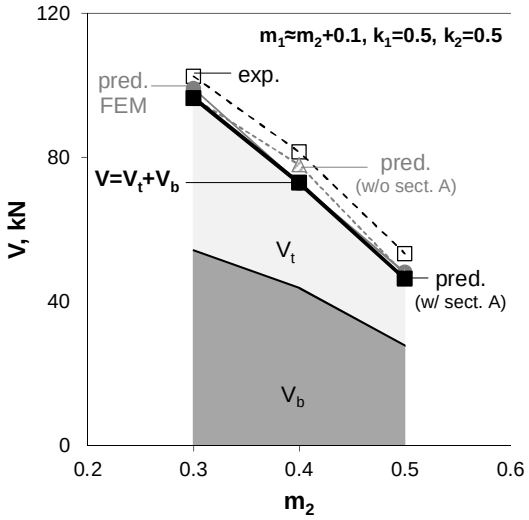

Fig. 5.14 Effect of opening size on the shear strength – specimens NS-C[81]

Similar observations are made in Fig. 5.15 which has been prepared for the tests by Yang et al. [77] where the horizontal and vertical size of the opening were varied separately. On average, the rate of decrease of the normalized shear strength $(\Delta V_{exp}/bhf_c)/\Delta m_1$ is about 0.11 and $(\Delta V_{exp}/bhf_c)/\Delta m_2$ is about 0.03. The reason for this difference is that, when the depth of the opening m_1h is increased, the regions above and below the opening become simultaneously shallower and more slender. On the other hand, when the width of the opening m_2a is increased, the depth of the regions remains the same and only the slenderness increases. In addition to m_1 and m_2, Fig. 5.15 also indicates the effect of the shear-span-to-effective-depth ratio a/d and concrete strength f_c.

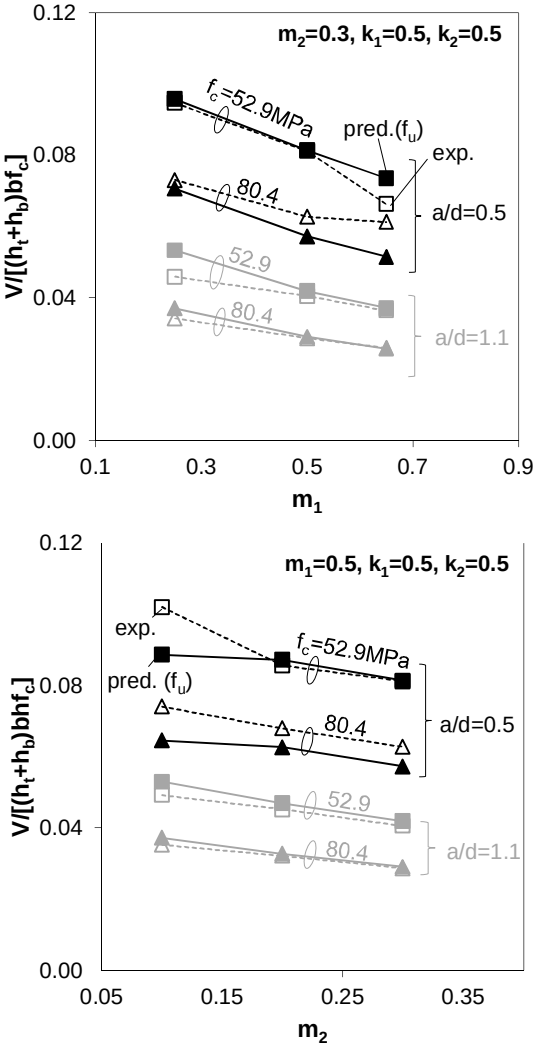

Fig. 5.15 Effect of opening size on the shear strength – tests by Yang et al.[77].

5.6.2. Effect of f_c

The effect of concrete strength is more clearly illustrated with the three tests in Fig. 5.16 where f_c is the only variable. Both experiments and predictions show an approximately linear increase of shear capacity with increasing f_c. As f_c was nearly quadrupled from 23.5 MPa to 80.4 MPa, the measured capacity increased by 45%. This shows that, even though in deep beams without stirrups the shear strength is typically proportional to ~ $f_c^{0.7-0.8}$, the test results scale approximately with $\sqrt{f_c}$ as in slender beams. The reason is that, while the a/d ratio of the tested beams was 0.5, the a/d of the regions above and below the web opening that govern the response was 2.12 and 1.0, respectively, and therefore these regions were closer to slender beams.

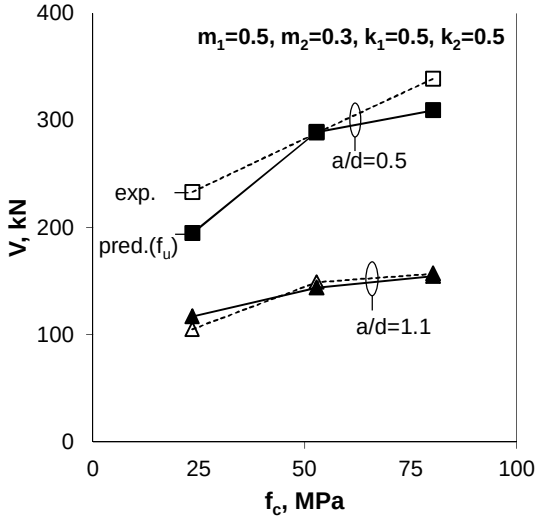

Fig. 5.16 Effect of concrete compressive strength on the shear strength – tests by Yang et al. [77]

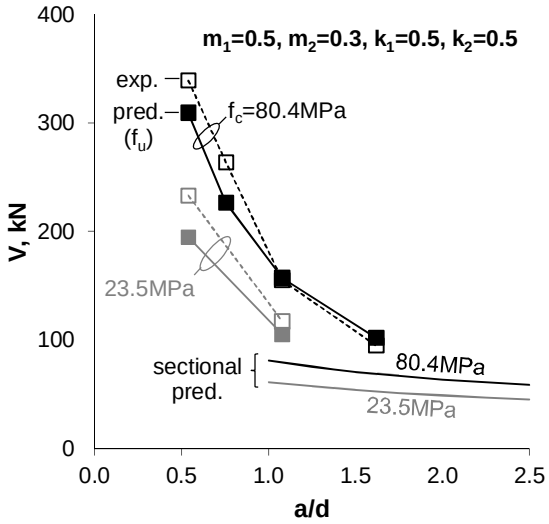

Fig. 5.17 Effect of shear-span-to-depth ratio on the shear strength – tests by Yang et al. [77]

5.6.3. Effect of a/d ratio

Finally, Fig. 5.17 shows the effect of the shear-span-to-depth ratio a/d of deep beams with web openings for two different concrete strengths. As in solid deep beams, the shear strength decreases significantly with increasing a/d ratio. For the beams with concrete strength of 80.4 MPa, the measured shear strength decreases approximately 3.6 times as a/d increases from 0.5 to 1.6. For both concrete strengths, the 2PKT approach produces slightly conservative predictions which become nearly equal to the experimental values at the maximum tested a/d ratios. It is important to note that, while in solid deep beams the transition to slender members typically occurs at a/d of about 2-2.5, in beams with web openings the transition occurs earlier. As explained earlier, the aspect ratios of the regions above and bellow the opening are typically larger than that of the entire shear span, and therefore those regions become slender before a/d reaches 2.5. It is expected that, if the a/d ratio of the beams with f_c=80.4 MPa was increased marginally; the shear strength would reach a lower bound and would decrease only slightly for larger a/d

ratios as in slender beams. To capture this transition, it is needed to combine the proposed 2PKT approach for deep shear spans with and appropriate sectional approach for slender members[53].

5.7. Conclusions

This paper studied the shear behaviour of deep beams with rectangular openings and proposed a kinematics-based approach for evaluating their shear strength. To develop the new approach, the failure modes of tests specimens were studied with the help of nonlinear finite element and strut-and-tie models. The main conclusions of the paper are as follows:

1) The complete failure mechanism of deep beams with rectangular openings can be approximated with a kinematic model with four degrees of freedom: the average strains along the top and bottom longitudinal reinforcement, as well as the transverse displacements along the critical shear cracks above and below the opening.

2) The load paths above and below the opening can be visualized with strut-and-tie models, and the shear resistance across the critical cracks can be evaluated based on the two-parameter kinematic theory for solid deep beams.

3) The proposed kinematics-based approach accounts for the interaction between the two load paths and produces adequate shear strength predictions. When applied to a database of 27 tests, the model resulted in an average shear strength experimental-to-predicted ratio of 1.03 and a COV of 9.3%.

4) The shear strength of deep beams with openings is affected more by the depth of the opening than by its horizontal dimension. Also, the transition from deep to slender beam behaviour in members with openings occurs at smaller a/d ratios than in solid members. These experimental observations were captured well by the 2PKT approach.

6.Conclusions and outlook

6.1. Summary and conclusions

This thesis consisted of four main parts: 1) a comparative study of models for shear capacity of reinforced concrete deep beams; 2) formulation and validation of a 1D macroelement for the full shear response of reinforced concrete deep beams; 3) mixed-type modelling framework for structures with both slender and deep beam elements; 4) a kinematic model for the shear capacity of deep beams with web openings. The summary and conclusions for each part are provided below.

6.1.1. A comparative study for shear capacity of RC deep beams

This study began with a comprehensive literature review on models for shear strength of RC deep beams. More than seventy models were collected from existing publications and classified into six categories according to their main features: 1) strut-and-tie models (36%); 2) numerical models (30%); 3) artificial intelligence models (18%); 4) upper-bound plasticity models (8%); 5) shear panel models (5%) and 6) other mechanical models (3%).

A comparative study was carried out for ten highly cited models with the help of a large database of 574 published tests of beams with $a/d \leq 3.0$. It was found that the semi-empirical strut-and-tie model proposed by Russo et al.[30] and the two-parameter kinematic theory (2PKT) by Mihaylov et al.[10] performed significantly better than the rest of the models in terms of shear strength experimental-to-predicted ratios V_{exp}/V_{pred}. Besides, it was shown that the 2PKT did not produce significant bias for any of the important parameters, i.e. a/d, ρ_v, ρ_l, and d, while the model proposed by Russo et al.[30] exhibited a trend of decreasing V_{exp}/V_{pred} ratios with increasing a/d.

Further comparisons were made between the two models through parametric studies. Individual series of deep beam tests were studied and used for this evaluation. The normalized shear capacity $V_{exp}/(bdf_c)$ was observed to decrease with a/d ratio and this trend becomes less significant when approaching the transition zone between deep and slender beams. Shear capacity of deep beams can be efficiently enhanced by stirrups but high stirrup ratios may cause sliding shear failures in deep beams. Increasing the longitudinal reinforcement is also beneficial for deep beams to resist shear. All these three effects were well captured by both models. However, in deep beams an important phenomenon is that the normalized shear capacity decreases with the beam size, i.e. size effect in shear, which was captured by 2PKT model while the model proposed by Russo et al.[30] does not account for this effect.

The contributions of this study are: 1) to summarize the numerous models on shear capacity of deep RC beams and make a clear classification based on their main characteristics; 2) to set a system of criteria for evaluating different models for shear capacity of RC deep beams; 3) to identify adequate models for shear strength of deep beams from both statistical and physical point of view.

6.1.2. Formulation and validation of a macroelement for RC deep beams

The original two-parameter kinematic theory (2PKT), which performed best in the comparisons in section 6.1.1, was extended by Mihaylov et al.[40] to continuous deep beams as a three parameter-kinematic theory (3PKT). Based on the 3PKT approach, a 1D macroelement for reinforced concrete deep beams was formulated in this study, aimed at providing the entire shear response, including both pre- and post-peak regime of either simply-supported or continuous reinforced concrete deep beams.

In the proposed macroelement, each shear span of a deep beam is represented by three nonlinear springs (two rotational and one transverse) and two rigid bars, and the stiffness of each spring is not required to be defined in advance. The behaviour of the transverse spring depends on the shear mechanisms along the shear crack and the response of the rotational springs is determined by either the bottom or the top longitudinal reinforcement and their surrounding concrete. The constitutive relationship of each spring prior to the formation of the diagonal shear crack was derived assuming the initial elastic stiffness generated from Timoshenko beam theory, and at the same time upon the formation of shear crack there is a sudden increase of displacement under the same load level.

Instead of discretising a shear span into a large number of 2D high-fidelity finite elements, the proposed macroelement uses only two nodes with two degrees of freedom at each node to represent a shear span of deep beam. Following a solution procedure based on secant stiffness, seven simply-supported deep beams and one continuous deep beam were modelled by using the macroelement. Satisfying results were obtained in terms of the entire shear response for all test specimens. It was observed in the experiments that continuous deep beams can redistribute shear forces from the critical shear spans to adjacent spans resulting in a more ductile behaviour, and this favourable effect was captured well by the macroelement model as well.

Furthermore, as the macroelement is based on kinematics, the width of the critical diagonal cracks is expressed with the kinematic parameters of the model which are predicted at each load step. Comparisons with tests showed that the predicted crack widths approximate well experimental results from simply supported and continuous deep beams up to the failure of the member.

With the ability of capturing well both the load-displacement response and crack widths, the macroelement can be used for the evaluation of existing deep beams in bridges and buildings for which measurements of crack widths and deflections are available. These measurements can be used together with the predicted load-deformation curves to evaluate the state and safety of the structure.

The contributions of this study are: 1) modelling of the initial behaviour of deep beams before the formation of diagonal shear cracks; 2) modelling the shear behaviour of a deep shear span with a novel 1D macroelement consisting of only three springs and two rigid bars; 3) to implement the 1D macroelement as a useful tool for the entire shear response of deep beams following a solution procedure proposed in this study; 4) to demonstrate the capability of the proposed 1D macroelement with the help of several tested deep beam specimens. The macroelement is able to provide satisfying predictions of full shear responses as well as crack widths.

6.1.3. Mixed-type modelling for structures with both slender and deep beam elements

With the simple 1D macroelement proposed in this thesis, it becomes possible to model an entire large frame structure including heavy transfer girders with only 1D elements, i.e. 1D slender beam elements for ordinary columns and beams, and the proposed 1D macroelements for deep beams. To realize this objective, a mixed-type modelling framework was therefore proposed in this study, which can be implemented in most of the existing finite element programmes. A representative finite element programme, i.e. VecTor5, developed in University of Toronto, was selected for the implementation of the proposed mixed-type modelling framework. The 1D macroelement for deep shear spans provides full compatibility with fibre-based 1D beam elements included in VecTor5 for slender members as it uses the

same nodal DOFs. The implementation was performed by adding a new subroutine to describe the 1D macroelement for deep beams without modifying the rest of the code of VecTor5.

Eighteen deep beams were used for the validation. For simply-supported deep beams, the proposed framework produced similarly adequate results as those obtained with 2D high-fidelity FEM and even improved the post-peak predictions. For continuous deep beams, the proposed 1D macroelement captured the increased ductility of shear-critical continuous deep beams resulting from force redistribution.

A twenty-storey large frame structure with heavy transfer girders was designed based on ACI 318. Following the proposed mixed-type framework, different schemes were adopted to model the large frame structure by considering whether modelling the entire structure or only the bottom two storeys, whether taking into account the lateral restraint or not. It was found that the 20-storey building carried nearly two times larger total load than the simplified 2-storey frame due to the extra shear resistance of the slender beams in the above floors. This leads to a concern on the simplified model focusing the analysis only on the bottom two floors, which was proven to be very conservative due to neglecting the interaction with the slender beams in the higher floors as in this case. It was also found that the lateral resisting could enhance the post-peak resistance of the frame and the structure became more resilient to overloading. Through those results the 1D mixed-type model was demonstrated capable of capturing the favourable effects that develop at the global structural level.

Furthermore, the proposed 1D mixed-type model exhibits high efficiency in terms of few elements and little computation time. To model the 20-story frame under imposed displacements, the proposed model required slightly less than six hours with forty load steps. While it is of great difficulty to establish the 2D finite element model for such a large structure, the analysis would take even much longer time to run. For all the structure types studied in this thesis, the analysis time required by the proposed 1D model was as little as a fraction of the time required by 2D high-fidelity finite element model. Taking into account the time on building the models, the advantage of the proposed 1D model will be even more pronounced.

Therefore, as the new framework is computationally efficient and captures well the complete pre- and post-peak behaviour of frames with slender and deep members, it represents a valuable tool for the analysis of complex structures under extreme loading.

The contributions of this study are: 1) to demonstrate the compatibility between the proposed 1D macroelement and the 1D slender beam element which is included in most of the finite element programs; 2) to propose a mixed-type modelling framework enabling the modelling of structures with both slender beams and deep beams; 3) to implement the mixed-type modelling into an existing finite element programme, i.e. VecTor5, by adding a subroutine without modification of the rest part of the programme; 4) to analyse different types of structures with the modified VecTor5 showing satisfying predictions on full shear responses; 5) to investigate resilience of the entire structure taking into account the interaction between deep beams and the rest of the structure; 6) to illustrate the efficiency of the proposed mixed-type modelling framework.

6.1.4. A kinematic model on shear capacity of simply-supported RC deep beams with web openings

While the previous works were focused on the development of a useful tool to predict the shear behaviour of RC deep beams, this work was aimed at extending the applicability of 3PKT to deep beams with web openings. Although the majority of research works were carried out for solid deep beams, in reality there

are web openings inevitably installed in large transfer girders to accommodate pipelines, electrify network etc. When the web opening intersects with the shear transfer path, the shear resistance of deep beams might be significantly reduced.

The behaviour of simply-supported deep beams with web openings was observed from both experiments and finite element analysis. When the usual diagonal load path as in solid deep beams is disturbed by web openings, loads are transferred through two load paths deviated by the web opening instead of going directly from loading point to the support. The failure mode of deep beams depends on the web opening size. When the size is not very large, the failure is mainly concentrated in the diagonal cracks above and below the web opening. With the opening size large enough, there is failure occurring as well in the top outer corner of the beam and a rotation between blocks separated by the cracks was observed. A strut-and-tie model was therefore proposed to account comprehensively for the two load paths as well as the possible failure modes.

Two sub deep shear spans were identified above and below the web openings based on the observations from both experiments and FEM analysis. Diagonal shear cracks in these sub deep shear spans exhibit similarity as in solid deep beams. Therefore, a kinematic model was proposed accommodating these two sub deep shears above and below the web opening as well as few other cracks emerged due to the deformation pattern imposed by four kinematic parameters. These four parameters are used to describe the entire deformation pattern of the shear span. Each sub shear span is associated to two kinematic parameters as in simply supported solid deep beams. The equilibrium condition of the top load path leads to an extra concern on a section containing a horizontal crack outside of the web opening. This section is under the combination of flexure and compression and its capacity limits the shear transfer capacity of the top load path. Therefore, a solution procedure was proposed taking into account both the two sub shear spans as well as the important horizontal section. The shear capacity of the two sub shear spans were calculated based on the existing 2PKT approach, but the shear capacity of the top shear span might be reduced due to the limited M-N capacity of the horizontal section outside of the web opening.

The proposed kinematic model was validated with twenty-seven simply-supported deep beams with rectangular web openings, and it was shown to be capable of providing satisfying predictions in terms of the experimental-to-predicted ratio on shear capacity, i.e. V_{exp}/V_{pred}. Those ratios did not exhibit significant bias to any of the important parameters, e.g. the size of the web openings, concrete strength etc. At the same time, parametric studies were conducted to examine if the proposed model was able to capture the effect of some important parameters. The prediction agreed well with the experimental results on the following observations: the shear strength of deep beams with openings is affected more by the depth of the opening than by its horizontal dimension. Also, the transition from deep to slender beam behaviour in members with openings occurs at smaller a/d ratios than in solid members. These experimental observations were captured well by the 2PKT approach.

The contributions of this study are: 1) to explore the shear mechanisms and failure modes of RC deep beams with web openings through experiments and finite element analysis; 2) to provide a strut-and-tie model indicating clear load paths deviated by the web opening in deep beams; 3) to propose a kinematic model for deep beams with web openings based on the existing 2PKT and to describe the entire deformation pattern by only four kinematic parameters; 4) to demonstrate the capability of the proposed model through accurately predicting the shear capacity of nearly thirty tested deep beam specimens.

6.2. Future work

One of the most important objectives of this thesis is to develop a useful 1D macroelement to predict shear behaviour of deep beams based on the existing three-parameter kinematic theory (3PKT). Fundamentally, the applicability of the proposed 1D macroelement is restricted by the limits of 3PKT. To extend the applicability of 3PKT to deep beams under various scenarios is essential to the improvement of the 1D macroelement.

The following are possible areas of research for the future:

1) The interaction between shear and flexure can be important when there is a large amount of stirrups in deep beams or the a/d ratio is close to the transition zone between deep beams and slender beams. Mihaylov and Franssen[90] attempted to address this problem when predicting the shear capacity of short coupling beams, and satisfying predictions were obtained though linking the principal compressive strains in the critical section to the longitudinal strains in the tension zone. It is also of interest to investigate the effect of this interaction along the entire response of deep beams. Back in 2015, Mihaylov et al.[88] assumed the strain distribution shape along the longitudinal reinforcement in reinforced concrete shear walls, and thereby established criteria for flexure failure of the base section of shear wall by calculating both the compressive and tensile stress in this section. Finally, the entire shear response of shear walls exhibiting shear-flexure failure was successfully captured. Therefore, based on these two works, the shear-flexure interaction can be taken into account as well for the entire response of deep beams.

2) Axial force is neglected in the formation of the macroelement. However, the interaction between deep beams and the rest of the structures might cause large axial forces in deep beams. Although it is intuitive to believe that the axial restraint accompanied by axial compression is beneficial to the shear behaviour of deep beams, it is necessary to investigate this effect and propose reasonable modifications to the macroelements.

3) When deep beams are connected with structural elements other than beams, e.g. short coupling beams connected with shear walls. It might be difficult to reach compatibility between the 1D macroelements with the 2D quadratic finite elements. One end section of deep shear span is represented by only one node in the 1D macroelement formulation; however, within the height of this end section, several quadratic elements are included in the 2D finite element model for shear walls. It will be thoughtless to connect the 1D macroelement with 2D quadratic finite elements through any common nodes directly.

4) It is of interest to improve the proposed kinematic model for reinforced concrete deep beams with web openings so that it can be used not only to predict the shear capacity but also to capture the entire shear response including both pre- and post-peak regime. Previous studies have shown that both the shear response as well as entire shear response of simply-supported solid deep beams can be successfully predicted by two kinematic parameters, while the existence of web openings significantly complicates the behaviour of deep beams. Double amount of kinematic parameters are required and at the same time there are more cracks accommodated in the shear span which cause difficulty to express the deformation pattern in a simple manner. Furthermore, it is assumed at shear failure that both the top and bottom shear spans fail simultaneously. However, the coordination between these two sub shear spans is not clear in the initial stage prior to shear failure.

5) As mentioned above, one most important measure to improve the macroelement is to extend the applicability of 3PKT. A number of topics remain to be investigated, e.g. non-rectangular beam cross sections; loading scenarios other than concentrated monotonic loads; various strengthening strategies to enhance the shear capacity of deep beams; reinforcement schemes different from non-prestressing steel rebars etc.

References

1. Kong, F. K. ed., “Reinforced Concrete Deep Beams,” CRC Press, 2006.
2. Kani, M. W., Huggins, M. W., and Wittkopp, R. R., “Kani on Shear in Reinforced Concrete,” University of Toronto Press, 1979.
3. Collins, M. P., and Mitchell, D., “Prestressed Concrete Structures,” Response Publications, 1997.
4. Yang, Y. “Shear Behaviour of Reinforced Concrete Members without Shear Reinforcement: a New Look at an Old Problem,” Doctoral thesis, Delft University of Technology, 2014.
5. AASHTO, “AASHTO LRFD Bridge Design Specifications, fourth edition,” American Association of State Highway Officials, Washington, DC, 2007.
6. CSA Committee A23.3, “Design of Concrete Structures for Buildings,” Canadian Standards Association, Rexdale, Canada, 1984.
7. CSA Committee A23.3, “Design of Concrete Structures,” Canadian Standards Association, Mississauga, Mississauga, Canada, 2004.
8. ACI Committee 318, “Building Code Requirements for Reinforced Concrete (ACI 318-08) and Commentary (318R-08),” American Concrete Institute, Farmington Hills, Mich., 2008.
9. European Committee for Standardization, “CEN, EN 1992-1-1 Eurocode 2: Design of Concrete Structures- Part 1-1: General Rules and Rules for Buildings,” Brussels, Belgium, 2004.
10. Mihaylov, B. I., Bentz, E. C., and Collins, M. P., “Two-Parameter Kinematic Theory for Shear Behavior of Deep Beams,” *ACI Structural Journal*, V. 110, No. 3, 2013, pp. 447-56.
11. Collins, M. P., Bentz, E. C., Quach, P. T., and Proestos, G. T., “The Challenge of Predicting the Shear Strength of Very Thick Slabs,” *Concrete International*, V.37, No.11, 2015, pp. 29-37.
12. Schlaich, J., Schäfer, K., and Jennewein, M., “Toward a Consistent Design of Structural Concrete,” *Journal of the Prestressed Concrete Institute*, V. 32, No. 3, 1987, pp. 74-150.
13. Wong, P. S., and Vecchio F. J., “VecTor2 and FormWorks User’s Manual,” University of Toronto, 2002.
14. Kam, W. Y., Pampanin, S., and Elwood, K., “Seismic Performance of Reinforced Concrete Buildings in the 22 February Christchurch (Lyttelton) Earthquake,” Bulletin of the New Zealand Society for Earthquake Engineering, V. 44, No. 4, 2011, pp. 239-78.
15. Cavagnis, F., Ruiz, M. F., and Muttoni, A., “An Analysis of the Shear-Transfer Actions in Reinforced Concrete Members without Transverse Reinforcement based on Refined Experimental Measurements,” *Structural Concrete*, V. 19, No.1, 2017, pp. 49-64.
16. Baumann, T., and Rusch, H., “Tests for the Analysis of Dowel Action of Flexural Reinforcement of Reinforced Concrete Beams (in German: Versuche zum Studium der Verdubelungswirkung der Biegezugbewehrung eines Stahlbetonbalkens),” Deutscher Ausschuss fur Stahlbeton, V. 210, 1970, pp. 43-83.

17. Huber, P., Huber, Y., and Kollegger, J., "Investigation of the Shear Behaviour of RC Beams on the Basis of Measured Crack Kinematics," *Engineering Structures*, V.113, 2016, pp. 41-58.

18. Mansur, M. A., Vinayagam, T., and Tan, K. H., "Shear Transfer across a Crack in Reinforced High-Strength Concrete," *Journal of Materials in Civil Engineering*, V. 20, No.4, 2008, pp. 294-302.

19. Walraven, J. C., "Fundamental Analysis of Aggregate Interlock," *Journal of the Structural Division*, V. 107, No. 11, 1981, pp. 2245-70

20. Li, B., Maekawa, K. and Okamura, H., "Contact Density Model for Stress Transfer across Cracks in Concrete," *Journal of the Faculty of Engineering*, University of Tokyo, V. 40, No. 1, 1989, pp. 9-52.

21. Bažant, Z. P., "Fracturing Truss Model: Size Effect in Shear Failure of Reinforced Concrete," *Journal of Engineering Mechanics*, V.123, No.12, 1997, pp.1276-88.

22. Mihaylov, B. I., Bentz, E. C. and Collins, M. P., "Behavior of Large Deep Beam Subjected to Monotonic and Reversed Cyclic Shear," *ACI Structural Journal*, V. 107, No. 6, 2010, pp. 726-34.

23. De Paiva, H. A. R, and Siess, C. P., "Strength and Behavior of Deep Beams in Shear," *Journal of Structural Engineering*, V. 91, No. 5, 1965, pp.19-41.

24. Mau, S. T., and Hsu, T. T. C., "Formula for the Shear Strength of Deep Beams," *ACI Structural Journal*, V.86, No.5, 1989, pp. 516-23.

25. Ashour, A. F., "Shear Capacity of Reinforced Concrete Deep Beams," *Journal of Structural Engineering*, V. 126, No. 9, 2000, pp. 1045-52.

26. Hwang, S. J, Lu, W. Y., and Lee, H. J., "Shear Strength Prediction for Deep Beams," *ACI Structural Journal*, V. 97, No. 3, 2000 , pp. 367-76.

27. Matamoros, A. B., and Wong, K. H., "Design of Simply Supported Deep Beams Using Strut-And-Tie Models," *ACI Structural Journal*, V.100, No.6, 2003, pp.704-12.

28. Zararis, P. D., "Shear Compression Failure in Reinforced Concrete Deep Beams," *Journal of Structural Engineering*, V. 129, No. 4, 2003, pp. 544-53.

29. Tang, C. Y., and Tan, K. H., "Interactive Mechanical Model for Shear Strength of Deep Beams," *Journal of Structural Engineering*, V. 130, No. 10, 2004, pp. 1534-44.

30. Russo, G., Venir, R., and Pauletta, M., "Reinforced Concrete Deep Beams - Shear Strength Model and Design Formula," *ACI Structural Journal*, V. 102, No. 3, 2005, pp. 429-37.

31. Tan, K. H., and Cheng, G. H., "Size Effect on Shear Strength of Deep Beams: Investigating with Strut-And-Tie Model," *Journal of Structural Engineering*, V. 132, No. 5, 2006, pp. 673-85.

32. Yang, K. H., and Ashour, A. F., "Strut-And-Tie Model Based on Crack Band Theory for Deep Beams," *Journal of Structural Engineering*, V. 137, No. 10, 2010, pp. 1030-8.

33. Senturk, A. E., and Higgins, C., "Evaluation of Reinforced Concrete Deck Girder Bridge Bent Caps with 1950s Vintage Details: Analytical Methods," *ACI Structural Journal*, V. 107, No. 5, 2010, pp. 544-53.

34. Nelsen, M. P., and Hoang, L. C., "Limit Analysis and Concrete Plasticity, third edition," New York: CRC, 2010.

35. Mau, S. T., Hsu, T. T. C., "Shear Strength Prediction for Deep Beams with Web Reinforcement," *ACI Structural Journal*, V. 84, No. 6, 1987, pp. 513-23.

36. Bakir, P. G., and Boduroğlu, H. M., "Mechanical Behavior and Non-Linear Analysis of Short Beams Using Softened Truss and Direct Strut & Tie Models," *Engineering Structures*, V. 27, No. 4, pp. 639-51.

37. Yu, H. W., Hwang, S. J., "Evaluation of Softened Truss Model for Strength Prediction of Reinforced Concrete Squat Walls," *Journal of Engineering Mechanics*, V.131, No. 8, 2005, pp. 839-46.

38. Muttoni, A., "Punching Shear Strength of Reinforced Concrete Slabs without Transverse Reinforcement," *ACI Structural Journal*, V. 105, No. 4, 2008, pp. 440-50.

39. Mihaylov, B. I., "Five-Spring Model for Complete Shear Behavior of Deep Beams," *fib Structural Concrete*, V. 16, No.1, 2015, pp. 71-83.

40. Mihaylov, B. I., Hunt, B., Bentz, E. C., and Collins, M. P., "Three-Parameter Kinematic Theory for Shear Behavior of Continuous Deep Beams," *ACI Structural Journal*, V. 112, No. 1, 2015, pp. 47-57.

41. Clark, A. P., "Diagonal Tension in Reinforced Concrete Beams," *ACI Structural Journal*, V. 48, No. 10, 195, pp.145-56.

42. Smith, K. N., and Vantsiotis, A. S., "Shear Strength of Deep Beams," *ACI Structural Journal*, V.79, No.3, 1982, pp. 201-13.

43. Lee, D., "An Experimental Investigation in the Effects of Detailing on the Shear Behavior of Deep Beams," Master Thesis, Department of Civil Engineering, University of Toronto, 1982, pp. 138.

44. Mathey, R. G., and Watstein, D., "Shear Strength of Beams without Web Reinforcement Containing Deformed Bars of Different Yield Strengths," *ACI Structural Journal*, V. 60, No. 2, 1963, pp.183-208.

45. Zhang, N., and Tan, K. H., "Size effect in RC deep beams: experimental investigation and STM verification," *Engineering Structures*, V. 29, No.12, 2007, pp.3241-54.

46. Birrcher, D. B., "Design of Reinforced Concrete Deep Beams for Strength and Serviceability," Doctoral Thesis, the University of Texas at Austin, 2009.

47. Liu, J., and Mihaylov, B. I., "A Comparative Study of Models for Shear Strength of Reinforced Concrete Deep Beams," *Engineering Structures*, V. 112, 2016, pp. 81-9.

48. Garber, D. B., Gallardo J. M., Huaco G. D., Samaras V. A., and Breen J. E., "Experimental Evaluation of Strut-and- Tie Model of Indeterminate Deep Beam," *ACI Structural Journal*, V. 111, No. 4, 2014, pp. 873-80.

49. Salem, H. M. and Maekawa K., "Computer-Aided Analysis of Reinforced Concrete Using a Refined Nonlinear Strut and Tie Model Approach," *Journal of Advanced Concrete Technology*, V. 4, No. 2, 2006, pp. 325-36.

50. Ashour, A. and Yang, K. H., "Application of Plasticity Theory to Reinforced Concrete Deep Beams: A Review," *Magazine of Concrete Research*, V. 60, No. 9, 2008, pp. 657-64.

51. Červenka, J., "ATENA Program Documentation Part 4-1: Tutorial for Program ATENA 2D," Červenka Consulting s.r.o., Prague, 2015.

52. Manie, J., "DIANA-9.5 User's Manual - Release 9.5," TNO DIANA BV, Delft, 2014.

53. Vecchio, F.J. and Collins, M.P., "The Modified Compression Field Theory for Reinforced Concrete Elements Subjected to Shear," *ACI Journal*, V. 83, No. 2, 1986, pp. 219-31.

54. Popovics, S., "A Review of Stress–strain Relationships for Concrete," *ACI Journal Proceedings*, V. 67, No. 3, 1970, pp. 243-8.

55. Vecchio, F.J., "Towards Cyclic Load Modelling of Reinforced Concrete," *ACI Journal*, V. 96, No. 2, 1999, pp. 193-202.

56. Goldsworthy, H. M., "Lessons on Building Design from the 22 February 2011 Christchurch Earthquake," *Australian Journal of Structural Engineering*, V.13, No. 2, 2012, pp.159-73.

57. Elwood, K. J., "Performance of Concrete Buildings in the 22 February 2011 Christchurch Earthquake and Implications for Canadian Codes," *Canadian Journal of Civil Engineering*, V. 40, No.3, 2013, pp.759-76.

58. Canterbury Earthquakes Royal Commission, Volume 4, Final Report Part Two, Earthquake-prone Buildings, 2012. Accessed 10/09/2014 from

    https://canterbury.royalcommission.govt.nz/Final-Report---Part-Two

59. Guner, S., "Performance Assessment of Shear-Critical Reinforced Concrete Plane Frames," Doctoral Thesis, University of Toronto, 2008

60. Rombach, G. A., "Finite Element Design of Concrete Structures: Practical Problems and Their Solution," Thomas Telford, 2004.

61. Sadeghian, V., Vecchio, F.J., and Kwon, O., "An Integrated Framework for Analysis of Mixed-type Reinforced Concrete Structures," CompDyn 2015 Conference, 2015.

62. Liu, J., and Mihaylov, B.I., "Macroelement for Complete Shear Behavior of Continuous Deep Girders," *ACI Structural Journal*, V. 115, No. 4, 2018, pp.1089-99.

63. Mazzoni, S., McKenna, F., Scott, M. H., and Fenves, G. L. "Open System for Earthquake Engineering Simulation: User Command-Language Manual," Pacific Earthquake Engineering Research Center, University of California, Berkeley, OpenSees version 2.0 users' manual, http://opensees.berkeley.edu/OpenSees/manuals/usermanual/index.html, May, 2009

64. Computers and Structures, Inc., "CSI Analysis Reference Manual for SAP2000®, ETABS®, SAFE® and CSiBridge®," Berkeley, USA, 2016.

65. Carr, A., "Ruaumoko Theory Manual," University of Canterbury, New Zealand, 2015.

66. Guner, S., and Vecchio, F. J. "User's Manual of VecTor5." Documentation, 2008, pp. 88.

67. Vecchio, F. J., "Disturbed Stress Field Model for Reinforced Concrete: Formulation," *Journal of Structural Engineering*, V. 126, No. 9, 2000, pp. 1070-7.

68. Guner, S., and Vecchio, F. J., "Pushover Analysis of Shear-Critical Frames: Verification and Application." *ACI Structural Journal*, V. 107, No. 1, 2010, pp. 72-81.

69. Guner, S., and Vecchio, F. J., "Pushover Analysis of Shear-Critical Frames: Formulation," *ACI Structural Journal*, V. 107, No. 1, 2010, pp. 63-71.

70. Tanimura, Y., and Sato, T., "Evaluation of Shear Strength of Deep Beams with Stirrups," *Quarterly Report of RTRI*, V. 46, No. 1, 2005, pp. 53-8.

71. Salamy, M. R., Kobayashi, H., and Unjoh, S., "Experimental and Analytical Study on RC Deep Beams," *Asian Journal of Civil Engineering (Building and Housing)*, V. 6, No. 5, 2005, pp. 409-21.

72. Leonhardt, F., and Walther, R., "The Stuttgart Shear Tests 1961," A translation of the articles that appeared in *Walther Beton und Stahlbetonbau*, V.56, No. 12, 1961 and V.57, No. 2,3,6,7 and 8, 1962, Cement and Concrete Association Library Translation No. 111, Wexham Springs, United Kingdom, Dec. 1964, 134 pp.

73. Kani, M.W., Huggins, M.W. and Wittkopp, R.R., "Kani on Shear in Reinforced Concrete," University of Toronto Press, Toronto, Canada, 1979, 225pp.

74. Rogowsky, D.M., and MacGregor, J.G., "Tests of Reinforced Concrete Deep Beams," *ACI Journal Proceedings*, V. 83, No. 4, July 1986, pp. 614-623.

75. Tan, K.H., Kong, F.K., Teng S., and Guan L.W., "High-Strength Concrete Deep Beams with Effective Span and Shear Span Variations," *ACI Structural Journal*, V. 92, No. 4, Jul. 1995, pp.1-11.

76. Kong, F.K., Robins, P.J., Singh, A., and Sharp, G. R., "Shear Analysis and Design of Reinforced Concrete Deep Beams," *The Structural Engineers*, V. 50, No. 10, 1972, pp. 405-9.

77. Yang, K. H., Eun, H. C., and Chung, H. S., "The Influence of Web Openings on the Structural Behaviour of Reinforced High-Strength Concrete Deep Beams," *Engineering Structures*, V.28, No.13, 2006, pp. 1825-34.

78. Yang K. H., and Ashour, F., "Effectiveness of Web Reinforcement around Openings in Continuous Concrete Deep Beams," ACI *Structural Journal*, Vol. 105, No. 4, 2008, pp.414-24.

79. Campione, G., and Minafo, G., "Behaviour of Concrete Deep Beams with Openings and Low Shear Span-to-depth Ratio," *Engineering Structures*, V.41, 2012, pp. 294-306.

80. Sahoo, D. R., Flores, C. A., and Chao, S. H., "Behavior of Steel Fiber Reinforcedconcrete Deep Beams with Large Opening," *ACI Structural Journal*, Vol. 109, No. 2, 2012, pp.193-203.

81. El-Maaddawy, T., and Sherif, S., "FRP Composites for Shear Strengthening of Reinforced Concrete Deep Beams with Openings," *Composite Structures*, V.89, No.1, 2009, pp. 60-9.

82. Hawileh, R. A., El-Maaddawy, T. A., and Naser, M. Z., "Nonlinear Finite Element Modelling of Concrete Deep Beams with Openings Strengthened with Externally-bonded Composites," *Materials and Design*, V.42, 2012, pp. 378-87.

83. Hussain, Q., and Pimanmas, A., "Shear Strengthening of RC Deep Beams with Openings Using Sprayed Glass Fibre Reinforced Polymer Composites (SGFRP): Part 1. Experimental Study," *KSCE Journal of Civil Engineering*, V.19, No.7, 2015, pp. 2121-33.

84. Lu, W. Y., Yu, H. W., Chen, C. L., Liu, S. L., and Chen, T. C., "High-strength Concrete Deep Beams with Web Openings Strengthened by Carbon Fibre Reinforced Plastics," Computers and Concrete, V.15, No.1, 2015, pp. 21-35.

85. Tan, K. H., Tong, K., and Tang, C. Y., "Consistent Strut-and-tie model of Deep Beams with Web Openings," *Magazine of Concrete Research*, V.55, No.1, 2003, pp. 65-75.

86. Kong, F. K., and Sharp, G. R., “Structural Idealization for Deep Beams with Web Openings,” Magazine of Concrete Research, V.29, No.99, 1977, pp. 81-91.

87. Tseng, C. C., Hwang, S. J., and Lu, W. Y., “Shear Strength Prediction of Reinforced Concrete Deep Beams with Web Openings,” *ACI Structural Journal*, V.114, No.6, 2017, pp.1569-79.

88. Mihaylov, B. I., Hannewald, P., and Beyer, K., “Three-parameter Kinematic Theory for Shear-dominated Reinforced Concrete Walls,” *Journal of Structural Engineering*, V. 142, No. 7, 2016, 04016041.

89. Mihaylov, B. I, and Franssen, R., “Macro-kinematic Approach for Shear Behaviour of Short Coupling Beams with Conventional Reinforcement,” High Tech Concrete: Where Technology and Engineering Meet. Springer, 2018.

90. Mihaylov, B. I, and Franssen, R., “Shear-flexure Interaction in the Critical Sections of Short Coupling Beams,” *Engineering Structures*, V.152, 2017, pp.370-80.

Appendices

A. Database of simply supported deep beams

Summary: This appendix provides data from 574 tests of beams with shear-span-to-depth ratios ≤ 3.0 which are used to compare models for shear strength of deep beams.

Columns in the database

Ref. #	Number of reference from the reference list at the end of the Appendix
a/d	Shear-span-to-depth ratio
b	Cross section width
d	Member effective depth
h	Member total depth
a: M/V	Length of shear span measured from the center of the support to the center of the loading plate
l_{b1}	Longitudinal length of loading plate
l_{b2}	Longitudinal length of support plate
V/P	Ratio of shear force to applied point load ≤1.0
$\rho_l=100A_s/(bd)$	Ratio of longitudinal reinforcement on flexural tension side of section
# bars	Number of longitudinal bars on flexural tension side of section
f_y	Yield strength of flexural tension reinforcement
a_g	Maximum specified size of course aggregate
f_c	Concrete cylinder strength at date of testing
ρ_v	Ratio of transverse reinforcement
d_{bv}	Stirrups bar diameter
s_v	Stirrups spacing
f_{yv}	Yield strength of stirrups
ρ_h	Ratio of longitudinal web reinforcement
d_{bh}	Bar diameter of longitudinal web reinforcement
s_h	Spacing of longitudinal web reinforcement
f_{yh}	Yield strength of longitudinal web reinforcement
Rep. mode	Reported mode of failure: “F” = flexure, “S” = shear (which includes diagonal tension, shear compression, etc.)
M_{max}/M_n	Ratio of maximum observed moment to nominal moment capacity according to ACI code
V_u	Maximum observed shear force
2PKT Exp/Pred	Ratio of observed shear strength to predicted shear strength for members that were reported to fail in shear and which failed with $M_{max}/M_n \leq 1.10$
Russo et al.,2005 Exp/Pred	Ratio of observed shear strength to predicted shear strength for members that were reported to fail in shear and which failed with $M_{max}/M_n \leq 1.10$

Note: Cells in the database that are shaded contain assumed values as the original values were not provided by the authors of the publication.

#	Ref. #	Year	Beam Name	a/d	b, mm	d, mm	h, mm	a: M/V mm	l_{b1}, mm	l_{b2}, mm	V/P	ρ_l, %	# bars	f_y, MPa	a_g, mm	f_c, MPa	ρ_v, %	d_{bv}, mm	s_v, mm	f_{yv}, MPa	ρ_h, %	d_{bh}, mm	s_h, mm	f_{yh}, MPa	Rep. mode	M_{max}/M_n	V_u, kN	2PKT [33] Exp/Pred	Russo et al. [34] Exp/Pred
1	1	1951	A1-1	2.35	203	389	457	914	89	89	0.5	3.10	3	321	10	24.6	0.38	9.5	183	331	0	9.5			S	0.87	222.5	0.95	0.82
2			A1-2	2.35	203	389	457	914	89	89	0.5	3.10	3	321	10	23.6	0.38	9.5	183	331	0	9.5			S	0.83	209.1	0.91	0.79
3			A1-3	2.35	203	389	457	914	89	89	0.5	3.10	3	321	10	23.4	0.38	9.5	183	331	0	9.5			S	0.89	222.5	0.97	0.84
4			A1-4	2.35	203	389	457	914	89	89	0.5	3.10	3	321	10	24.8	0.38	9.5	183	331	0	9.5			S	0.96	244.7	1.05	0.89
5			B1-1	1.96	203	389	457	762	89	89	1	3.10	3	321	10	23.4	0.37	9.5	191	331	0	9.5			S	0.93	278.8	1.08	0.97
6			B1-2	1.96	203	389	457	762	89	89	1	3.10	3	321	10	25.4	0.37	9.5	191	331	0	9.5			S	0.83	256.6	0.97	0.84
7			B1-3	1.96	203	389	457	762	89	89	1	3.10	3	321	10	23.7	0.37	9.5	191	331	0	9.5			S	0.94	284.8	1.10	0.98
8			B1-4	1.96	203	389	457	762	89	89	1	3.10	3	321	10	23.3	0.37	9.5	191	331	0	9.5			S	0.89	268.1	1.04	0.93
9			B1-5	1.96	203	389	457	762	89	89	1	3.10	3	321	10	24.6	0.37	9.5	191	331	0	9.5			S	0.79	241.4	0.92	0.81
10			B2-1	1.96	203	389	457	762	89	89	1	3.10	3	321	10	23.2	0.73	9.5	95	331	0	9.5			S	1.00	301.1	0.92	0.90
11			B2-2	1.96	203	389	457	762	89	89	1	3.10	3	321	10	26.3	0.73	9.5	95	331	0	9.5			S	1.03	322.2	0.95	0.90
12			B2-3	1.96	203	389	457	762	89	89	1	3.10	3	321	10	24.9	0.73	9.5	95	331	0	9.5			S	1.09	334.8	1.01	0.96
13			B6-1	1.96	203	389	457	762	89	89	1	3.10	3	321	10	42.1	0.37	9.5	191	331	0	9.5			S	1.10	379.3	1.21	0.91
14			C1-1	1.57	203	389	457	610	89	89	1	2.07	2	321	10	25.6	0.34	9.5	203	331	0	9.5			S	0.98	277.7	1.13	0.90
15			C1-2	1.57	203	389	457	610	89	89	1	2.07	2	321	10	26.3	0.34	9.5	203	331	0	9.5			S	1.09	311.1	1.25	0.99
16			C1-3	1.57	203	389	457	610	89	89	1	2.07	2	321	10	24.0	0.34	9.5	203	331	0	9.5			S	0.88	245.9	1.03	0.83
17			C1-4	1.57	203	389	457	610	89	89	1	2.07	2	321	10	29.0	0.34	9.5	203	331	0	9.5			S	0.99	285.9	1.10	0.85
18			C2-1	1.57	203	389	457	610	89	89	1	2.07	2	321	10	23.6	0.69	9.5	102	331	0	9.5			S	1.04	289.9		0.88
19			C2-2	1.57	203	389	457	610	89	89	1	2.07	2	321	10	25.0	0.69	9.5	102	331	0	9.5			S	1.07	301.1		0.88
20			C2-4	1.57	203	389	457	610	89	89	1	2.07	2	321	10	27.0	0.69	9.5	102	331	0	9.5			S	1.01	288.1		0.81
21			C3-1	1.57	203	389	457	610	89	89	1	2.07	2	321	10	14.1	0.34	9.5	203	331	0	9.5			S	0.93	223.6	1.17	1.09
22			C3-2	1.57	203	389	457	610	89	89	1	2.07	2	321	10	13.8	0.34	9.5	203	331	0	9.5			S	0.84	200.3	1.06	0.99
23			C3-3	1.57	203	389	457	610	89	89	1	2.07	2	321	10	13.9	0.34	9.5	203	331	0	9.5			S	0.79	188.1	0.99	0.93
24			C4-1	1.57	203	389	457	610	89	89	1	3.10	3	321	10	24.5	0.34	9.5	203	331	0	9.5			S	0.81	309.3	1.06	0.93
25			C6-2	1.57	203	389	457	610	89	89	1	3.10	3	321	10	45.2	0.34	9.5	203	331	0	9.5			S	0.97	423.8	1.14	0.85
26			C6-3	1.57	203	389	457	610	89	89	1	3.10	3	321	10	44.7	0.34	9.5	203	331	0	9.5			S	1.00	434.9	1.17	0.88
27			C6-4	1.57	203	389	457	610	89	89	1	3.10	3	321	10	47.6	0.34	9.5	203	331	0	9.5			S	0.98	428.6	1.12	0.84
28			D1-1	1.16	203	395	457	457	89	89	1	1.63	2	335	10	26.2	0.46	9.5	152	331	0	9.5			S	0.91	301.1	1.06	0.83
29			D1-3	1.16	203	395	457	457	89	89	1	1.63	2	335	10	24.5	0.46	9.5	152	331	0	9.5			S	0.78	256.6	0.94	0.74
30			D2-1	1.16	203	395	457	457	89	89	1	1.63	2	335	10	24.0	0.61	9.5	114	331	0	9.5			S	0.88	289.9	1.05	0.82
31			D2-2	1.16	203	395	457	457	89	89	1	1.63	2	335	10	25.9	0.61	9.5	114	331	0	9.5			S	0.94	312.2	1.08	0.84
32			D3-1	1.16	203	395	457	457	89	89	1	2.44	3	335	10	28.2	0.92	9.5	76	331	0	9.5			S	0.84	394.9	1.02	0.85
33			D4-1	1.16	203	395	457	457	89	89	1	1.63	2	335	10	23.1	1.22	9.5	57	331	0	9.5			S	0.96	312.2		0.80
34			D1-6	1.95	152	313	381	610	89	89	1	3.42	2	335	10	27.6	0.46	9.5	203	331	0	9.5			S	0.83	174.7	0.95	0.85
35			D1-7	1.95	152	313	381	610	89	89	1	3.42	2	335	10	28.0	0.46	9.5	203	331	0	9.5			S	0.84	179.2	0.97	0.86
36			D1-8	1.95	152	313	381	610	89	89	1	3.42	2	335	10	27.8	0.46	9.5	203	331	0	9.5			S	0.88	185.8	1.01	0.90

#	Ref. #	Year	Beam Name	a/d	b, mm	d, mm	h, mm	a: M/V mm	l_{b1}, mm	l_{b2}, mm	V/P	ρ_l, %	# bars	f_y, MPa	a_g, mm	f_c, MPa	ρ_v, %	d_{bv}, mm	s_v, mm	f_{yv}, MPa	ρ_h, %	d_{bh}, mm	s_h, mm	f_{yh}, MPa	Rep. mode	M_{max}/M_n	V_u, kN	2PKT [33] Exp/Pred	Russo et al.[34] Exp/Pred
37			E1-2	2.03	152	313	381	635	89	89	1	3.42	2	321	10	30.2	0.73	9.5	127	331	0	9.5			S	1.10	221.8	1.06	0.94
38			D2-6	2.43	152	313	381	762	89	89	1	3.42	2	321	10	29.5	0.61	9.5	152	331	0	9.5			S	1.00	168.4		0.81
39			D2-7	2.43	152	313	381	762	89	89	1	3.42	2	321	10	28.4	0.61	9.5	152	331	0	9.5			S	0.95	157.3		0.78
40			D2-8	2.43	152	313	381	762	89	89	1	3.42	2	321	10	26.1	0.61	9.5	152	331	0	9.5			S	1.04	168.4		0.87
41			D4-1	2.43	152	313	381	762	89	89	1	3.42	2	321	10	27.4	0.49	9.5	191	331	0	9.5			S	1.03	168.4		0.90
42			D4-2	2.43	152	313	381	762	89	89	1	3.42	2	321	10	25.6	0.49	9.5	191	331	0	9.5			S	0.98	157.3		0.87
43			D4-3	2.43	152	313	381	762	89	89	1	3.42	2	321	10	22.1	0.49	9.5	191	331	0	9.5			S	1.11	165.1		
44			D5-1	2.43	152	313	381	762	89	89	1	3.42	2	321	10	27.7	0.37	9.5	254	331	0	9.5			S	0.89	146.2	1.04	0.83
45			D5-2	2.43	152	313	381	762	89	89	1	3.42	2	321	10	29.0	0.37	9.5	254	331	0	9.5			S	0.94	157.3	1.11	0.87
46			D5-3	2.43	152	313	381	762	89	89	1	3.42	2	321	10	27.1	0.37	9.5	254	331	0	9.5			S	0.96	157.3	1.13	0.90
47			A0-1	2.35	203	389	457	914	89	89	0.5	0.98	2	370	10	21.5	0				0				S	0.81	89.0	1.09	0.66
48			A0-2	2.35	203	389	457	914	89	89	0.5	0.98	2	370	10	26.0	0				0				S	0.96	107.9	1.21	0.70
49			B0-1	1.96	203	389	457	762	89	89	1	0.98	2	370	10	23.6	0				0				S	0.91	121.0	0.99	0.72
50			B0-2	1.96	203	389	457	762	89	89	1	0.98	2	370	10	23.9	0				0				S	0.71	94.2	0.77	0.56
51			B0-3	1.96	203	389	457	762	89	89	1	0.98	2	370	10	23.5	0				0				S	0.96	128.0	1.05	0.76
52			C0-1	1.57	203	389	457	610	89	89	1	0.98	2	370	10	24.7	0				0				S	1.04	174.3	1.06	0.84
53			C0-3	1.57	203	389	457	610	89	89	1	0.98	2	370	10	23.6	0				0				S	1.01	166.9	1.05	0.83
54			D0-1	1.17	203	389	457	457	89	89	1	0.98	2	370	10	25.9	0				0				S	0.99	221.6	0.96	0.84
55			D0-3	1.17	203	389	457	457	89	89	1	0.98	2	370	10	26.0	0				0				S	1.00	223.2	0.96	0.85
56	2	1954	III-24a	1.52	178	533	609	813	203	203	1	2.72	4	315	25	17.8	0				0				S	0.78	296.5	1.09	1.09
57			III-24b	1.52	178	533	609	813	203	203	1	2.72	4	315	25	20.6	0				0				S	0.75	303.2	1.03	0.99
58			III-25a	1.52	178	533	609	813	203	203	1	3.46	4	313	25	24.3	0				0				S	0.54	267.6	0.76	0.71
59			III-25b	1.52	178	533	609	813	203	203	1	3.46	4	313	25	17.2	0				0				S	0.76	289.8	0.99	1.03
60			III-26a	1.52	178	533	609	813	203	203	1	4.25	4	302	25	21.7	0				0				S	0.88	421.1	1.18	1.17
61			III-26b	1.52	178	533	609	813	203	203	1	4.25	4	302	25	20.6	0				0				S	0.86	396.6	1.14	1.15
62			III-27a	1.52	178	533	609	813	203	203	1	2.72	4	315	25	21.4	0				0				S	0.85	347.7	1.16	1.10
63			III-27b	1.52	178	533	609	813	203	203	1	2.72	4	315	25	22.9	0				0				S	0.86	356.6	1.14	1.07
64			III-28a	1.52	178	533	609	813	203	203	1	3.46	4	313	25	23.3	0				0				S	0.62	303.2	0.89	0.84
65			III-28b	1.52	178	533	609	813	203	203	1	3.46	4	313	25	22.4	0				0				S	0.71	341.0	1.02	0.97
66			III-29a	1.52	178	533	609	813	203	203	1	4.25	4	302	25	21.7	0				0				S	0.81	389.9	1.09	1.08
67			III-29b	1.52	178	533	609	813	203	203	1	4.25	4	302	25	25.0	0				0				S	0.81	436.6	1.14	1.08
68			III-30	1.52	178	533	609	813	203	203	1	4.25	4	302	25	25.4	0.52	9.5	152	326	0				S	0.87	478.2	1.02	1.01
69			III-31	1.52	178	533	609	813	203	203	1	4.25	4	302	25	22.4	0.95	12.7	152	303	0				S	1.03	507.1	1.03	1.06
70			A2	3.00	178	267	305	800	102	102	0.5	2.15	2	380	25	31.0	0				0				S	0.61	66.7		
71			A3	2.99	178	268	305	800	102	102	0.5	2.22	3	380	25	31.0	0				0				S	0.67	75.6		
72			A4	2.96	178	270	305	800	102	102	0.5	2.37	4	380	25	31.5	0				0				S	0.59	71.2		

#	Ref. #	Year	Beam Name	a/d	b, mm	d, mm	h, mm	a: M/V mm	l_{b1}, mm	l_{b2}, mm	V/P	ρ_l, %	# bars	f_y, MPa	a_g, mm	f_c, MPa	ρ_v, %	d_{bv}, mm	s_v, mm	f_{yv}, MPa	ρ_h, %	d_{bh}, mm	s_h, mm	f_{yh}, MPa	Rep. mode	M_{max}/M_n	V_u, kN	2PKT [33] Exp/Pred	Russo et al.[34] Exp/Pred
73			B1	3.00	178	267	305	800	102	102	0.5	1.62	3	380	25	21.2	0				0				S	0.70	56.3		
74			B2	2.99	178	268	305	800	102	102	0.5	1.63	2	380	25	21.6	0				0				S	0.73	60.1		
75			B3	2.96	178	270	305	800	102	102	0.5	1.60	3	380	25	19.2	0				0				S	0.69	55.6		
76			B4	2.95	178	272	305	800	102	102	0.5	1.66	4	380	25	16.8	0				0				S	0.69	55.6		
77			C1	2.99	178	268	305	800	102	102	0.5	0.81	1	380	25	6.3	0				0				S	0.59	20.0		
78			C2	2.94	178	272	305	800	102	102	0.5	0.83	2	380	25	6.1	0				0				S	0.73	24.5		
79			C3	2.93	178	273	305	800	102	102	0.5	0.80	3	380	25	6.9	0				0				S	0.68	25.4		
80			C4	2.92	178	274	305	800	102	102	0.5	0.82	4	380	25	6.8	0				0				S	0.67	25.1		
81	3	1957	B14-E2	1.42	305	375	410	533	356	102	0.5	0.57	4	450	6	12.7	0				0				S	1.53	278.0		
82			B14-E4	1.45	305	368	406	533	356	102	0.5	1.24	5	450	6	28.9	0				0				S	1.33	511.5		
83			B14-B2	1.45	305	368	406	533	356	102	0.5	1.85	6	450	6	14.6	0				0				S	0.97	367.0	0.93	1.44
84			B14-B4	1.45	305	368	406	533	356	102	0.5	1.85	6	450	6	26.3	0				0				S	0.95	500.4	0.97	1.23
85			B14-B6	1.45	305	368	406	533	356	102	0.5	1.85	6	450	6	46.8	0				0				S	1.35	778.4		
86			B14-A4	1.47	305	362	406	533	356	102	0.5	2.50	6	450	6	22.6	0				0				S	0.93	511.5	0.97	1.32
87			B14-A6	1.50	305	356	406	533	356	102	0.5	3.83	7	450	6	45.4	0				0				S	0.97	900.7	1.03	1.29
88			B21-E2	1.90	305	375	406	711	356	102	0.5	0.57	4	450	6	11.3	0				0				S	1.58	211.7		
89			B21-F4	1.92	305	370	406	711	356	102	0.5	1.17	3	450	6	31.4	0				0				S	1.68	467.6		
90			B21-E4R	1.93	305	368	406	711	356	102	0.5	1.24	5	450	6	31.9	0				0				S	1.49	434.2		
91			B21-E4	1.95	305	365	406	711	356	102	0.5	1.24	5	450	6	24.2	0				0				S	1.53	423.0		
92			B21-B6	1.90	305	375	406	711	356	102	0.5	1.82	6	450	6	45.5	0				0				S	1.31	578.7		
93			B21-B4	1.93	305	368	406	711	356	102	0.5	1.85	6	450	6	27.1	0				0				S	1.00	396.4	1.07	1.19
94			B21-B2	1.94	305	367	406	711	356	102	0.5	1.86	6	450	6	13.9	0				0				S	0.89	238.5	0.90	1.23
95			B21-A4	1.93	305	368	406	711	356	102	0.5	2.46	6	450	6	29.8	0				0				S	1.04	523.1		
96			B21-A6	2.00	305	356	406	711	356	102	0.5	3.83	7	450	6	45.3	0				0				S	0.83	578.8	0.96	1.05
97			B28-E2	2.39	308	372	406	889	356	102	0.5	0.57	4	450	6	13.7	0				0				S	1.19	130.0		
98			B28-E4	2.41	305	368	406	889	356	102	0.5	1.24	5	450	6	33.1	0				0				S	1.15	267.9		
99			B28-B4	2.41	305	368	406	889	356	102	0.5	1.85	6	450	6	32.3	0				0				S	0.78	256.8	0.95	
100			B28-B6	2.41	305	368	406	889	356	102	0.5	1.85	6	450	6	43.9	0				0				S	0.94	323.5	1.00	
101			B28-B2	2.46	305	362	406	889	356	102	0.5	1.88	6	450	6	14.7	0				0				S	0.92	201.2	1.17	
102			B28-A4	2.41	305	368	406	889	356	102	0.5	2.46	6	450	6	27.5	0				0				S	0.82	323.5	1.30	
103			B28-A6	2.52	308	353	406	889	356	102	0.5	3.83	7	450	6	47.2	0				0				S	0.59	334.7	0.84	
104	4	1962	1	1.00	190	270	320	270	75	100	1	2.07	4	465	30	32.4	0				0				S	0.95	388.5	1.19	1.35
105			2	1.48	190	270	320	400	75	100	1	2.07	4	465	30	32.4	0				0				S	0.95	260.0	1.14	1.17
106			3	2.00	190	270	320	540	75	100	1	2.07	4	465	30	32.4	0				0				S	0.72	147.2	0.91	0.84
107	5	1963	I-1	1.51	203	403	457	610	89	89	1	3.05	3	267	25	25.4	0				0				S	0.88	312.9	1.24	0.96
108			I-2	1.51	203	403	457	610	89	89	1	3.05	3	267	25	23.0	0				0				S	0.89	310.7	1.28	1.03

#	Ref. #	Year	Beam Name	a/d	b, mm	d, mm	h, mm	a: M/V mm	l_{b1}, mm	l_{b2}, mm	V/P	ρ_l, %	# bars	f_y, MPa	a_g, mm	f_c, MPa	ρ_v, %	d_{bv}, mm	s_v, mm	f_{yv}, MPa	ρ_h, %	d_{bh}, mm	s_h, mm	f_{yh}, MPa	Rep. mode	M_{max}/M_n	V_u, kN	2PKT [33] Exp/Pred	Russo et al.[34] Exp/Pred
109			II-3	1.51	203	403	457	610	89	89	1	1.88	3	466	25	21.9	0				0				S	0.72	261.8	1.16	1.04
110			II-4	1.51	203	403	457	610	89	89	1	1.88	3	466	25	26.4	0				0				S	0.82	312.9	1.27	1.08
111			III-5	1.51	203	403	457	610	89	89	1	1.85	3	490	25	25.7	0				0				S	0.74	288.5	1.18	1.02
112			III-6	1.51	203	403	457	610	89	89	1	1.85	3	490	25	25.6	0				0				S	0.75	290.7	1.19	1.03
113			IV-7	1.51	203	403	457	610	89	89	1	1.86	3	443	25	24.1	0				0				S	0.82	290.8	1.26	1.08
114			IV-8	1.51	203	403	457	610	89	89	1	1.86	3	443	25	24.9	0				0				S	0.85	304.0	1.30	1.10
115			V-9	1.51	203	403	457	610	89	89	1	1.16	3	698	25	23.1	0				0				S	0.66	224.0	1.08	1.00
116			V-10	1.51	203	403	457	610	89	89	1	1.16	3	698	25	27.0	0				0				S	0.74	268.4	1.19	1.07
117			VI-11	1.51	203	403	457	610	89	89	1	1.17	3	698	25	25.4	0				0				S	0.63	224.0	1.02	0.93
118			VI-12	1.51	203	403	457	610	89	89	1	1.17	3	698	25	25.7	0				0				S	0.75	268.4	1.22	1.11
119			V-13	1.51	203	403	457	610	89	89	1	0.75	3	712	25	22.4	0				0				S	0.90	222.4	1.23	1.20
120			V-14	1.51	203	403	457	610	89	89	1	0.75	3	712	25	26.7	0				0				S	0.88	224.0	1.12	1.06
121			VI-15	1.51	203	403	457	610	89	89	1	0.75	3	712	25	25.5	0				0				S	0.71	179.5	0.92	0.88
122			VI-16	1.51	203	403	457	610	89	89	1	0.75	3	712	25	22.8	0				0				S	0.76	188.6	1.03	1.00
123			VIb-21	2.84	203	403	457	1143	89	89	1	0.84	3	707	25	26.1	0				0				S	0.48	71.4		
124			VIb-22	2.84	203	403	457	1143	89	89	1	0.84	3	707	25	25.8	0				0				S	0.42	62.4		
125			VIb-23	2.84	203	403	457	1143	89	89	1	0.84	3	707	25	30.6	0				0				S	0.49	75.1		
126	6	1979	69	1.00	155	542	610	543	229	229	1	2.67	5	373	19	27.4	0				0				S	0.89	585.0	1.15	1.29
127			67	1.03	157	528	610	543	152	152	1	2.75	5	407	19	30.3	0				0				S	0.78	548.0	1.26	1.15
128			72	1.98	152	549	610	1087	152	152	1	2.71	5	384	19	24.8	0				0				S	0.60	196.9	1.11	0.78
129			61	2.00	156	542	610	1085	64	76	1	2.75	5	349	19	26.8	0				0				S	0.51	163.3	1.06	0.60
130			65	2.46	150	552	610	1359	152	152	1	2.82	5	374	19	27.0	0				0				S	0.41	112.4		
131			76	2.62	152	518	610	1359	64	64	1	2.87	5	372	19	30.8	0				0				S	0.45	114.8		
132			71	2.99	155	544	610	1628	229	229	1	2.41	5	373	19	27.4	0				0				S	0.50	102.1		
133	7	1982	SD-1	1.56	200	900	1000	1400	300	200	0.5	1.89	12	498	19	33.5	0.50	11.3	200	529	0.33	11.3	300	529	S	1.06	967.5	1.18	1.00
134			SD-2	1.62	200	863	1000	1400	300	200	0.5	1.97	12	498	19	29.3	0.50	11.3	200	529	0.36	11.3	275	529	S	1.15	967.5		
135			SD-3	1.70	200	825	1000	1400	300	200	0.5	2.06	12	498	19	28.0	0.50	11.3	200	529	0.40	11.3	250	529	S	1.07	840.0		1.05
136			SD-4	1.78	200	788	1000	1400	300	200	0.5	2.16	12	498	19	27.4	0.50	11.3	200	529	0.50	11.3	200	529	S	1.14	840.0		
137	8	1982	0A0-44	1.00	102	305	356	305	102	102	1	1.94	3	422	13	20.5	0				0				S	0.72	139.5	1.02	1.15
138			0A0-48	1.00	102	305	356	305	102	102	1	1.94	3	422	13	20.9	0				0				S	0.69	136.1	0.98	1.11
139			1A1-10	1.00	102	305	356	305	102	102	1	1.94	3	422	13	18.7	0.28	6.4	229	460	0.23	6.4	140	460	S	0.87	161.2	1.21	1.26
140			1A2-11	1.00	102	305	356	305	102	102	1	1.94	3	422	13	18.0	0.28	6.4	229	460	0.45	6.4	70	460	S	0.82	148.3	1.13	1.15
141			1A3-12	1.00	102	305	356	305	102	102	1	1.94	3	422	13	16.1	0.28	6.4	229	460	0.68	6.4	94	460	S	0.86	141.2	1.16	1.13
142			1A4-51	1.00	102	305	356	305	102	102	1	1.94	3	422	13	20.5	0.28	6.4	229	460	0.68	6.4	94	460	S	0.88	170.9	1.21	1.17
143			1A6-37	1.00	102	305	356	305	102	102	1	1.94	3	422	13	21.1	0.28	6.4	229	460	0.91	6.4	70	460	S	0.94	184.1	1.28	1.19
144			2A1-38	1.00	102	305	356	305	102	102	1	1.94	3	422	13	21.7	0.63	6.4	102	460	0.23	6.4	140	460	S	0.88	174.5	1.18	1.13

#	Ref. #	Year	Beam Name	a/d	b, mm	d, mm	h, mm	a: M/V mm	l_{b1}, mm	l_{b2}, mm	V/P	ρ_l, %	# bars	f_y, MPa	a_g, mm	f_c, MPa	ρ_v, %	d_{bv}, mm	s_v, mm	f_{yv}, MPa	ρ_h, %	d_{bh}, mm	s_h, mm	f_{yh}, MPa	Rep. mode	M_{max}/M_n	V_u, kN	2PKT [33] Exp/Pred	Russo et al.[34] Exp/Pred
145			2A3-39	1.00	102	305	356	305	102	102	1	1.94	3	422	13	19.8	0.63	6.4	102	460	0.45	6.4	70	460	S	0.89	170.6	1.22	1.13
146			2A4-40	1.00	102	305	356	305	102	102	1	1.94	3	422	13	20.3	0.63	6.4	102	460	0.68	6.4	94	460	S	0.88	171.9	1.21	1.08
147			2A6-41	1.00	102	305	356	305	102	102	1	1.94	3	422	13	19.1	0.63	6.4	102	460	0.91	6.4	70	460	S	0.85	161.9	1.18	1.03
148			3A1-42	1.00	102	305	356	305	102	102	1	1.94	3	422	13	18.4	1.25	6.4	51	460	0.23	6.4	140	460	S	0.88	161.0	1.20	1.00
149			3A3-43	1.00	102	305	356	305	102	102	1	1.94	3	422	13	19.2	1.25	6.4	51	460	0.45	6.4	70	460	S	0.91	172.7	1.25	1.01
150			3A4-45	1.00	102	305	356	305	102	102	1	1.94	3	422	13	20.8	1.25	6.4	51	460	0.68	6.4	94	460	S	0.91	178.6	1.23	0.97
151			3A6-46	1.00	102	305	356	305	102	102	1	1.94	3	422	13	19.9	1.25	6.4	51	460	0.91	6.4	70	460	S	0.87	168.1	1.19	0.91
152			0B0-49	1.21	102	305	356	368	102	102	1	1.94	3	422	13	21.7	0				0				S	0.91	149.0	1.24	1.32
153			1B1-01	1.21	102	305	356	368	102	102	1	1.94	3	422	13	22.1	0.24	6.4	267	460	0.23	6.4	140	460	S	0.89	147.5	1.12	1.14
154			1B3-29	1.21	102	305	356	368	102	102	1	1.94	3	422	13	20.1	0.24	6.4	267	460	0.45	6.4	70	460	S	0.89	143.6	1.15	1.15
155			1B4-30	1.21	102	305	356	368	102	102	1	1.94	3	422	13	20.8	0.24	6.4	267	460	0.68	6.4	94	460	S	0.86	140.3	1.10	1.06
156			1B6-31	1.21	102	305	356	368	102	102	1	1.94	3	422	13	19.5	0.24	6.4	267	460	0.91	6.4	70	460	S	0.96	153.4	1.25	1.17
157			2B1-05	1.21	102	305	356	368	102	102	1	1.94	3	422	13	19.2	0.42	6.4	152	460	0.23	6.4	140	460	S	0.82	129.0	1.02	1.03
158			2B3-0.6	1.21	102	305	356	368	102	102	1	1.94	3	422	13	19.0	0.42	6.4	152	460	0.45	6.4	70	460	S	0.84	131.2	1.04	1.02
159			2B4-07	1.21	102	305	356	368	102	102	1	1.94	3	422	13	17.5	0.42	6.4	152	460	0.68	6.4	94	460	S	0.86	126.1	1.05	1.00
160			2B4-52	1.21	102	305	356	368	102	102	1	1.94	3	422	13	21.8	0.42	6.4	152	460	0.68	6.4	94	460	S	0.91	149.9	1.11	1.04
161			2B6-32	1.21	102	305	356	368	102	102	1	1.94	3	422	13	19.8	0.42	6.4	152	460	0.91	6.4	70	460	S	0.91	145.2	1.13	1.04
162			3B1-08	1.21	102	305	356	368	102	102	1	1.94	3	422	13	16.2	0.63	6.4	102	460	0.23	6.4	140	460	S	0.95	130.8	1.10	1.08
163			3B1-36	1.21	102	305	356	368	102	102	1	1.94	3	422	13	20.4	0.77	6.4	83	460	0.23	6.4	140	460	S	0.99	159.0	1.15	1.09
164			3B3-33	1.21	102	305	356	368	102	102	1	1.94	3	422	13	19.0	0.77	6.4	83	460	0.45	6.4	70	460	S	1.01	158.4	1.20	1.10
165			3B4-34	1.21	102	305	356	368	102	102	1	1.94	3	422	13	19.2	0.77	6.4	83	460	0.68	6.4	94	460	S	0.98	155.0	1.17	1.04
166			3B6-35	1.21	102	305	356	368	102	102	1	1.94	3	422	13	20.7	0.77	6.4	83	460	0.91	6.4	70	460	S	1.03	166.1	1.19	1.04
167			4B1-09	1.21	102	305	356	368	102	102	1	1.94	3	422	13	17.1	1.25	6.4	51	460	0.23	6.4	140	460	S	1.07	153.5	1.25	1.01
168			0C0-50	1.50	102	305	356	457	102	102	1	1.94	3	422	13	20.7	0				0				S	0.89	115.7	1.23	1.25
169			1C1-14	1.50	102	305	356	457	102	102	1	1.94	3	422	13	19.2	0.18	6.4	356	460	0.23	6.4	140	460	S	0.94	119.0	1.15	1.18
170			1C3-02	1.50	102	305	356	457	102	102	1	1.94	3	422	13	21.9	0.18	6.4	356	460	0.45	6.4	70	460	S	0.93	123.4	1.11	1.08
171			1C4-15	1.50	102	305	356	457	102	102	1	1.94	3	422	13	22.7	0.18	6.4	356	460	0.68	6.4	94	460	S	0.98	131.0	1.16	1.09
172			1C6-16	1.50	102	305	356	457	102	102	1	1.94	3	422	13	21.8	0.18	6.4	356	460	0.91	6.4	70	460	S	0.92	122.3	1.11	1.02
173			2C1-17	1.50	102	305	356	457	102	102	1	1.94	3	422	13	19.9	0.31	6.4	203	460	0.23	6.4	140	460	S	0.96	124.1	1.10	1.12
174			2C3-03	1.50	102	305	356	457	102	102	1	1.94	3	422	13	19.2	0.31	6.4	203	460	0.45	6.4	70	460	S	0.81	103.6	0.93	0.93
175			2C3-27	1.50	102	305	356	457	102	102	1	1.94	3	422	13	19.3	0.31	6.4	203	460	0.45	6.4	70	460	S	0.90	115.3	1.03	1.03
176			2C4-18	1.50	102	305	356	457	102	102	1	1.94	3	422	13	20.4	0.31	6.4	203	460	0.68	6.4	94	460	S	0.96	124.6	1.09	1.05
177			2C6-19	1.50	102	305	356	457	102	102	1	1.94	3	422	13	20.8	0.31	6.4	203	460	0.91	6.4	70	460	S	0.95	124.1	1.07	1.00
178			3C1-20	1.50	102	305	356	457	102	102	1	1.94	3	422	13	21.0	0.56	6.4	114	460	0.23	6.4	140	460	S	1.08	141.5	1.08	1.10
179			3C3-21	1.50	102	305	356	457	102	102	1	1.94	3	422	13	16.5	0.56	6.4	114	460	0.45	6.4	70	460	S	1.11	125.0		
180			3C4-22	1.50	102	305	356	457	102	102	1	1.94	3	422	13	18.3	0.56	6.4	114	460	0.68	6.4	94	460	S	1.05	127.7	1.03	1.02

#	Ref. #	Year	Beam Name	a/d	b, mm	d, mm	h, mm	a: M/V mm	l_{b1}, mm	l_{b2}, mm	V/P	ρ_l, %	# bars	f_y, MPa	a_g, mm	f_c, MPa	ρ_v, %	d_{bv}, mm	s_v, mm	f_{yv}, MPa	ρ_h, %	d_{bh}, mm	s_h, mm	f_{yh}, MPa	Rep. mode	M_{max}/M_n	V_u, kN	2PKT [33] Exp/Pred	Russo et al.[34] Exp/Pred
181			3C6-23	1.50	102	305	356	457	102	102	1	1.94	3	422	13	19.0	0.56	6.4	114	460	0.91	6.4	70	460	S	1.09	137.2	1.09	1.05
182			4C1-24	1.50	102	305	356	457	102	102	1	1.94	3	422	13	19.6	0.77	6.4	83	460	0.23	6.4	140	460	S	1.14	146.6		
183			4C3-04	1.50	102	305	356	457	102	102	1	1.94	3	422	13	18.5	0.63	6.4	102	460	0.45	6.4	70	460	S	1.04	128.6	1.01	1.02
184			4C3-28	1.50	102	305	356	457	102	102	1	1.94	3	422	13	19.2	0.77	6.4	83	460	0.45	6.4	70	460	S	1.20	152.4		
185			4C4-25	1.50	102	305	356	457	102	102	1	1.94	3	422	13	18.5	0.77	6.4	83	460	0.68	6.4	94	460	S	1.24	152.6		
186			4C6-26	1.50	102	305	356	457	102	102	1	1.94	3	422	13	21.2	0.77	6.4	83	460	0.91	6.4	70	460	S	1.21	159.5		
187			0D0-47	2.08	102	305	356	635	102	102	1	1.94	3	422	13	19.5	0				0				S	0.80	73.4	1.22	1.08
188			4D1-13	2.08	102	305	356	635	102	102	1	1.94	3	422	13	16.1	0.42	6.4	152	460	0.23	6.4	140	460	S	1.11	87.4		
189	9	1986	BM1/1.0 T1	1.05	200	950	1000	1000	300	200	0.5	0.95	6	380	10	26.1	0.15	6.0	188	570	0				S	1.01	602.0	1.06	0.84
190			BM1/1.0 T2	1.05	200	950	1000	1000	300	200	0.5	0.95	6	380	10	26.1	0				0				F	1.17	699.0		
191			BM2/1.0 T1	1.05	200	950	1000	1000	300	200	0.5	0.95	6	380	10	26.8	0				0.09	6.0	300	573	S	1.17	700		
192			BM2/1.0	1.05	200	950	1000	1000	300	200	0.5	0.95	6	380	10	26.8	0.15	6.0	188	570	0.09	6.0	300	573	F	1.17	700		
193			BM1/1.5 T1	1.87	200	535	600	1000	300	200	0.5	1.12	6	380	10	42.4	0				0				S	1.32	303.0		
194			BM1/1.5 T2	1.87	200	535	600	1000	300	200	0.5	1.12	6	455	10	42.4	0.19	6.0	150	570	0				F	1.30	354.0		
195			BM2/1.5 T1	1.87	200	535	600	1000	300	200	0.5	1.12	6	455	10	42.4	0				0.18	6.0	157	573	S	0.83	226.0	0.72	0.59
196			BM2/1.5 T2	1.87	200	535	600	1000	300	200	0.5	1.12	6	455	10	42.4	0.19	6.0	150	570	0.18	6.0	157	573	F	1.28	348.0		
197			BM1/2.0 T1	2.20	200	455	500	1000	200	200	0.5	0.88	4	455	10	43.2	0				0				F	1.13	177.0		
198			BM1/2.0 T2	2.20	200	455	500	1000	200	200	0.5	0.88	4	455	10	43.2	0.14	6.0	200	570	0				F	1.27	199.0		
199			BM2/2.0 T1	2.20	200	455	500	1000	200	200	0.5	0.88	4	455	10	43.2	0				0.21	6.0	137	573	S	1.18	185.0		
200			BM2/2.0 T2	2.20	200	455	500	1000	200	200	0.5	0.88	4	455	10	43.2	0.14	6.0	200	570	0.21	6.0	137	573	F	1.30	204.0		
201	10	1988	N220-l	2.99	400	190	220	569	100	100	1	1.20	3	433	20	34.2	0				0				S	0.86	103.6		
202			N350-l	2.81	400	313	350	880	100	100	1	1.20	3	436	20	34.2	0				0				S	0.75	158.0		
203			N485-l	2.72	400	440	485	1195	100	100	1	1.20	3	385	20	34.2	0				0				S	0.68	187.5		
204			N960-l	2.57	400	889	960	2289	100	100	1	1.20	6	385	20	34.2	0				0				S	0.62	366.6		
205			N220-h	2.99	400	190	220	569	100	100	1	2.00	5	433	20	34.2	0				0				S	0.66	122.7		
206			N350-h	2.81	400	313	350	880	100	100	1	2.00	5	436	20	34.2	0				0				S	0.54	178.6		
207			N485-h	2.72	400	440	485	1195	100	100	1	2.00	5	385	20	34.2	0				0				S	0.50	215.4		
208			N960-h	2.57	400	889	960	2289	100	100	1	2.00	10	385	20	34.2	0				0				S	0.42	386.1		
209			H220-l	2.99	400	190	220	569	100	100	1	1.20	3	433	10	58.6	0				0				S	0.85	105.9		
210			H350-l	2.81	400	313	350	880	100	100	1	1.20	3	436	10	58.6	0				0				S	0.71	157.3		
211			H485-l	2.72	400	440	485	1195	100	100	1	1.20	3	385	10	58.6	0				0				S	0.70	198.5		
212			H960-l	2.57	400	889	960	2289	100	100	1	1.20	6	385	10	58.6	0				0				S	0.52	316.7		
213			H220-h	2.99	400	190	220	569	100	100	1	2.00	5	433	10	58.6	0				0				S	0.67	135.3		
214			H350-h	2.81	400	313	350	880	100	100	1	2.00	5	436	10	58.6	0				0				S	0.54	189.6		
215			H485-h	2.72	400	440	485	1195	100	100	1	2.00	5	385	10	58.6	0				0				S	0.43	199.0		
216			H960-h	2.57	400	889	960	2289	100	100	1	2.00	10	385	10	58.6	0				0				S	0.34	337.4		

#	Ref. #	Year	Beam Name	a/d	b, mm	d, mm	h, mm	a: M/V mm	l_{b1}, mm	l_{b2}, mm	V/P	ρ_l, %	# bars	f_y, MPa	a_g, mm	f_c, MPa	ρ_v, %	d_{bv}, mm	s_v, mm	f_{yv}, MPa	ρ_h, %	d_{bh}, mm	s_h, mm	f_{yh}, MPa	Rep. mode	M_{max}/M_n	V_u, kN	2PKT [33] Exp/Pred	Russo et al. [34] Exp/Pred
217	11	1994	V011	1.00	250	360	400	360	90	90	0.5	1.13	4	420	8	16.1	0				0				S	0.64	226.0	1.06	0.94
218			V012	1.00	250	360	400	360	90	90	0.5	1.13	4	420	8	21.8	0				0				S	0.86	322.0	1.29	1.05
219			V013	1.00	250	360	400	360	90	90	0.5	1.13	4	420	8	22.1	0				0				S	0.92	344.0	1.37	1.11
220			V014	1.00	250	360	400	360	90	90	0.5	1.13	4	420	8	24.3	0				0				S	1.12	425.0		
221			V021	1.00	250	360	400	360	90	90	0.5	1.13	4	420	16	13.9	0				0				S	0.64	220.0	1.04	1.03
222			V023	1.00	250	360	400	360	90	90	0.5	1.13	4	420	16	20.1	0				0				S	0.94	347.0	1.35	1.21
223			V024	1.00	250	360	400	360	90	90	0.5	1.13	4	420	16	25.2	0				0				S	1.04	396.0	1.37	1.16
224			V031	1.00	250	360	400	360	90	90	0.5	1.13	4	420	32	20.0	0				0				S	0.88	323.0	1.02	1.13
225			V032	1.00	250	360	400	360	90	90	0.5	1.13	4	420	32	18.2	0				0				S	0.88	318.0	1.06	1.20
226			V033	1.00	250	360	400	360	90	90	0.5	1.13	4	420	32	19.8	0				0				S	0.67	246.0	0.78	0.87
227			V034	1.00	250	360	400	360	90	90	0.5	1.13	4	420	32	26.4	0				0				S	1.14	437.0		
228			V711	1.00	250	160	200	160	40	40	0.5	1.52	3	420	16	18.1	0				0				S	0.82	165.0	1.07	1.27
229			V022	1.00	250	360	400	360	90	90	0.5	1.13	4	420	16	19.9	0				0				S	0.73	270.0	1.06	0.95
230			V511	1.00	250	560	600	560	140	140	0.5	1.12	5	420	16	19.8	0				0				S	0.62	350.0	0.94	0.80
231			V411	1.00	250	740	800	740	185	185	0.5	1.10	8	420	16	19.4	0				0				S	0.50	365.0	0.79	0.64
232			V211	1.00	250	930	1000	930	233	233	0.5	1.08	8	420	16	20.0	0				0				S	0.55	505.0	0.90	0.70
233			V711/4	1.00	250	160	200	160	40	40	0.5	1.50	3	420	16	19.6	0.13	4.0	45	420	0				S	1.01	207.0	1.24	1.44
234			V711/4	1.00	250	360	400	360	90	90	0.5	1.13	4	420	16	18.2	0.13	6.0	100	420	0				S	0.87	317.0	1.22	1.14
235			V511/4	1.01	250	560	600	565	140	140	0.5	1.12	5	420	16	18.7	0.14	8.0	150	420	0				S	0.84	465.0	1.17	1.06
236			V411/4	0.97	250	760	800	740	190	190	0.5	0.78	8	420	16	17.0	0.17	10.0	190	420	0				S	0.82	467.0	0.98	0.93
237			V711/4	1.00	250	160	200	160	40	40	0.5	1.50	3	420	16	18.3	0.28	6.0	45	420	0				S	1.03	207.0	1.30	1.45
238			V022/3	1.00	250	360	400	360	90	90	0.5	1.13	4	420	16	19.6	0.35	10.0	100	420	0				S	1.03	380.0	1.34	1.21
239			V511/3	1.01	250	560	600	565	140	140	0.5	1.12	5	420	16	21.3	0.33	10.0	150	420	0				S	1.02	580.0	1.26	1.13
240			V411/3	0.97	250	760	800	740	190	190	0.5	0.78	8	420	16	19.8	0.33	14.0	190	420	0				S	1.15	665.0		
241	12	1995	A-0.27-2.15	0.29	110	438	500	125	150	150	1	1.23	2	505	10	58.8	0	10.0	300	375	0				S	0.69	675	0.94	1.48
242			A-0.27-3.23	0.29	110	438	500	125	150	150	1	1.23	2	505	10	51.6	0	10.0	300	375	0				S	0.65	630	0.96	1.46
243			A-0.27-4.30	0.29	110	438	500	125	150	150	1	1.23	2	505	10	53.9	0	10.0	300	375	0				S	0.65	640	0.94	1.46
244			A-0.27-5.38	0.29	110	438	500	125	150	150	1	1.23	2	505	10	57.3	0	10.0	300	375	0				S	0.64	630	0.89	1.40
245			B-0.54-2.15	0.57	110	438	500	250	150	150	1	1.23	2	505	10	56.0	0	10.0	300	375	0				S	0.96	468	0.84	1.16
246			B-0.54-3.23	0.57	110	438	500	250	150	150	1	1.23	2	505	10	45.7	0	10.0	300	375	0				S	0.92	445	0.92	1.22
247			B-0.54-4.30	0.57	110	438	500	250	150	150	1	1.23	2	505	10	53.9	0	10.0	300	375	0				S	1.02	500	0.92	1.26
248			B-0.54-5.38	0.57	110	438	500	250	150	150	1	1.23	2	505	10	53.0	0	10.0	300	375	0				S	0.98	480	0.90	1.22
249			C-0.81-2.15	0.86	110	438	500	375	150	150	1	1.23	2	505	10	51.2	0	10.0	300	375	0				S	1.24	403		
250			C-0.81-3.23	0.86	110	438	500	375	150	150	1	1.23	2	505	10	44.0	0	10.0	300	375	0				S	1.25	400		
251			D-1.08-2.15	1.14	110	438	500	500	150	150	1	1.23	2	505	10	48.2	0	10.0	300	375	0				S	1.11	270		
252			D-1.08-3.23	1.14	110	438	500	500	150	150	1	1.23	2	505	10	44.1	0	10.0	300	375	0				F	1.16	280		

#	Ref. #	Year	Beam Name	a/d	b, mm	d, mm	h, mm	a: M/V mm	l_{b1}, mm	l_{b2}, mm	V/P	ρ_l, %	# bars	f_y, MPa	a_g, mm	f_c, MPa	ρ_v, %	d_{bv}, mm	s_v, mm	f_{yv}, MPa	ρ_h, %	d_{bh}, mm	s_h, mm	f_{yh}, MPa	Rep. mode	M_{max}/M_n	V_u, kN	2PKT [33] Exp/Pred	Russo et al.[34] Exp/Pred
253			D-1.08-4.30	1.14	110	438	500	500	150	150	1	1.23	2	505	10	46.8	0	10.0	300	375	0				F	1.2	290		
254			D-1.08-5.38	1.14	110	438	500	500	150	150	1	1.23	2	505	10	48.0	0	10.0	300	375	0				F	1.2	290		
255			E-1.62-3.23	1.71	110	438	500	750	150	150	1	1.23	2	505	10	50.6	0	10.0	300	375	0				S	1.36	220		
256			E-1.62-4.30	1.71	110	438	500	750	150	150	1	1.23	2	505	10	44.6	0	10.0	300	375	0				F	1.18	190		
257			E-1.62-5.38	1.71	110	438	500	750	150	150	1	1.23	2	505	10	45.3	0	10.0	300	375	0				F	1.08	173		
258			F-2.16-4.30	2.28	110	438	500	1000	150	150	1	1.23	2	505	10	41.1	0	10.0	300	375	0				F	1.26	150		
259			G-2.70-5.38	2.85	110	438	500	1250	150	150	1	1.23	2	505	10	42.8	0	10.0	300	375	0				F	1.1	105		
260	13	1998	B1.2-3	0.76	125	1124	1200	850	250	250	1	1.34	6	440	10	88.0	0.67	6.3	75	590	0.29	6.30	170	590	F	1.23	1300		
261			B2.0A-4	0.88	125	624	700	550	100	250	1	2.42	6	440	10	89.0	0.67	6.3	75	590	0.37	6.30	135	590	F	1.09	950		
262			B3.0A-4	1.28	125	624	700	800	100	250	1	2.42	6	440	10	80.0	0.67	6.3	75	590	0.37	6.30	135	590	F	1.3	775		
263			B2.0-1	1.32	125	624	700	825	250	250	1	2.42	6	440	10	120.0	0.67	6.3	75	590	0.37	6.30	135	590	S	1.34	795		
264			B2.0-2	1.32	125	624	700	825	250	250	1	2.42	6	440	10	78.0	0.67	6.3	75	590	0.37	6.30	135	590	F	1.43	825		
265			B2.0-3	1.32	125	624	700	825	250	250	1	2.42	6	440	10	86.0	0.67	6.3	75	590	0.37	6.30	135	590	F	1.2	700		
266			B2.0B-5	1.32	125	624	700	825	250	250	1	2.42	6	440	10	93.0	0				0				F	1	585		
267			B2.0C-6	1.32	125	624	700	825	250	250	1	2.42	6	440	10	104.0	1.00	6.3	50	590	0				F	1.24	730		
268			B2.0D-7	1.32	125	624	700	825	250	250	1	2.42	6	440	10	80.0	0.67	6.3	75	590	0				F	1.25	720		
269			B3.0-1	1.88	125	624	700	1175	250	250	1	2.42	6	440	10	91.0	0.67	6.3	75	590	0.37	6.30	135	590	F	1.24	510		
270			B3.0-2	1.88	125	624	700	1175	250	250	1	2.42	6	440	10	96.0	0.67	6.3	75	590	0.37	6.30	135	590	F	1.27	525		
271			B3.0-3	1.88	125	624	700	1175	250	250	1	2.42	6	440	10	80.0	0.67	6.3	75	590	0.37	6.30	135	590	F	1.29	525		
272			B3.0B-4	1.88	125	624	700	1175	250	250	1	2.42	6	440	10	83.0	0				0				F	1.07	435		
273	14	1998	S1-1	2.50	250	292	350	730	100	100	1	2.80	2	452	7	63.6	0.16	5.0	100	569	0				S	0.70	228.3	0.87	
274			S1-2	2.50	250	292	350	730	100	100	1	2.80	2	452	7	63.6	0.16	5.0	100	569	0				S	0.64	208.3	0.80	
275			S1-3	2.50	250	292	350	730	100	100	1	2.80	2	452	7	63.6	0.16	5.0	100	569	0				S	0.63	206.1	0.79	
276			S1-4	2.50	250	292	350	730	100	100	1	2.80	2	452	7	63.6	0.16	5.0	100	569	0				S	0.85	277.9	1.06	
277			S1-5	2.50	250	292	350	730	100	100	1	2.80	2	452	7	63.6	0.16	5.0	100	569	0				S	0.78	253.3	0.97	
278			S1-6	2.50	250	292	350	730	100	100	1	2.80	2	452	7	63.6	0.16	5.0	100	569	0				S	0.69	224.1	0.86	
279			S2-1	2.50	250	292	350	730	100	100	1	2.80	2	452	7	72.5	0.11	5.0	150	569	0				S	0.78	260.3	1.00	
280			S2-2	2.50	250	292	350	730	100	100	1	2.80	2	452	7	72.5	0.13	5.0	125	569	0				S	0.70	232.5	0.88	
281			S2-3	2.50	250	292	350	730	100	100	1	2.80	2	452	7	72.5	0.16	5.0	100	569	0				S	0.76	253.3	0.93	
282			S2-4	2.50	250	292	350	730	100	100	1	2.80	2	452	7	72.5	0.16	5.0	100	569	0				S	0.66	219.4	0.81	
283			S2-5	2.50	250	292	350	730	100	100	1	2.80	2	452	7	72.5	0.21	5.0	75	569	0				S	0.85	282.1	1.00	
284			S2-6	2.50	250	292	350	730	100	100	1	2.80	2	452	7	72.5	0.26	5.0	60	569	0				F	1.08	359.0		
285			S3-1	2.49	250	297	350	740	100	100	1	1.66	2	450	7	67.4	0.10	4.0	100	632	0				S	1.01	209.2	1.00	
286			S3-2	2.49	250	297	350	740	100	100	1	1.66	2	450	7	67.4	0.10	4.0	100	632	0				S	0.86	178.0	0.85	
287			S3-3	2.49	250	293	350	730	100	100	1	2.79	2	452	7	67.4	0.10	4.0	100	632	0				S	0.69	228.6	0.89	
288			S3-4	2.49	250	293	350	730	100	100	1	2.79	2	452	7	67.4	0.10	4.0	100	632	0				S	0.53	174.9	0.68	

#	Ref. #	Year	Beam Name	a/d	b, mm	d, mm	h, mm	a: M/V mm	l_{b1}, mm	l_{b2}, mm	V/P	ρ_l, %	# bars	f_y, MPa	a_g, mm	f_c, MPa	ρ_v, %	d_{bv}, mm	s_v, mm	f_{yv}, MPa	ρ_h, %	d_{bh}, mm	s_h, mm	f_{yh}, MPa	Rep. mode	M_{max}/M_n	V_u, kN	2PKT [33] Exp/Pred	Russo et al.[34] Exp/Pred
289			S3-5	2.51	250	287	350	720	100	100	1	3.85	6	442	7	67.4	0.10	4.0	100	632	0				S	0.72	296.6	1.07	
290			S3-6	2.51	250	287	350	720	100	100	1	3.85	6	442	7	67.4	0.10	4.0	100	632	0				S	0.68	282.9	1.02	
291			S4-1	2.48	250	524	600	1300	100	100	1	3.12	4	452	7	87.3	0.16	5.0	100	569	0				S	0.52	354.0	0.92	
292			S4-2	2.50	250	428	500	1070	100	100	1	3.07	4	433	7	87.3	0.16	5.0	100	569	0				F	1.11	572.8		
293			S4-3	2.50	250	332	400	830	100	100	1	2.97	4	450	7	87.3	0.16	5.0	100	569	0				S	0.60	243.4	0.75	
294			S4-4	2.50	250	292	350	730	100	100	1	2.80	2	452	7	87.3	0.16	5.0	100	569	0				S	0.76	258.1	0.87	
295			S4-5	2.50	250	236	300	590	100	100	1	3.12	4	442	7	87.3	0.16	5.0	100	569	0				F	1.09	321.1		
296			S4-6	2.53	250	198	250	500	100	100	1	2.79	3	442	7	87.3	0.16	5.0	100	569	0				S	0.92	202.9	0.71	0.74
297			S5-2	2.74	250	292	350	800	100	100	1	2.80	2	452	7	89.4	0.16	5.0	100	569	0				S	0.84	259.9		
298			S5-3	2.50	250	292	350	730	100	100	1	2.80	2	452	7	89.4	0.16	5.0	100	569	0				S	0.72	243.8	0.81	
299			S5-4	1.99	250	292	350	580	100	100	1	2.80	2	452	7	89.4	0.16	5.0	100	569	0				S	1.12	476.7		
300			S5-5	1.75	250	292	350	510	100	100	1	2.80	2	452	7	89.4	0.16	5.0	100	569	0				S	1.18	573.4		
301			S5-6	1.51	250	292	350	440	100	100	1	2.80	2	452	7	89.4	0.16	5.0	100	569	0				F	1.15	647.7		
302			S8-1	2.50	250	292	350	730	100	100	1	2.80	2	452	7	74.6	0.11	5.0	150	569	0				S	0.82	272.1	1.03	
303			S8-2	2.50	250	292	350	730	100	100	1	2.80	2	452	7	74.6	0.13	5.0	125	569	0				S	0.75	250.9	0.93	
304			S8-3	2.50	250	292	350	730	100	100	1	2.80	2	452	7	74.6	0.16	5.0	100	569	0				S	0.93	309.6	1.12	
305			S8-4	2.50	250	292	350	730	100	100	1	2.80	2	452	7	74.6	0.16	5.0	100	569	0				S	0.80	265.8	0.97	
306			S8-5	2.50	250	292	350	730	100	100	1	2.80	2	452	7	74.6	0.20	5.0	80	569	0				S	0.87	289.2	1.02	
307			S8-6	2.50	250	292	350	730	100	100	1	2.80	2	452	7	74.6	0.22	5.0	70	569	0				S	0.85	283.9	0.98	
308	15	1998	BN100	2.92	300	925	1000	2700	152	152	0.5	0.76	4	550	10	37.2	0				0				S	0.52	192.0		
309			BN50	3.00	300	450	500	1350	152	152	0.5	0.81	4	490	10	37.2	0				0				S	0.78	132.0		
310			BN25	3.00	300	225	250	675	76	76	0.5	0.89	4	437	10	37.2	0				0				S	0.89	73.0		
311	16	1999	1-500/0.50	0.60	140	419	500	250	250	250	1	2.60	4	520	10	49.1	0				0				S	0.76	850	0.85	1.46
312			2-1000/0.50	0.58	140	859	1000	500	250	250	1	2.60	8	520	10	31.2	0.12	6.0	350	520	0.12	6.00	350	520	S	0.45	875	0.97	0.94
313			4-1750/0.50	0.57	140	1534	1750	880	250	250	1	2.60	12	520	10	42.6	0.12	6.0	350	520	0.12	6.00	350	520	S	0.4	1636	1.29	0.80
314			3-1400/0.50	0.58	140	1226	1400	705	250	250	1	2.60	10	520	10	32.8	0.12	6.0	350	520	0.12	6.00	350	520	S	0.4	1175	1.15	0.85
315			2-1000/0.75	0.86	140	859	1000	740	250	250	1	2.60	8	520	10	32.7	0.12	6.0	350	520	0.12	6.00	350	520	S	0.48	650	0.92	0.79
316			1-500/0.75	0.89	140	419	500	375	250	250	1	2.60	4	520	10	42.5	0				0				S	0.97	700	1.00	1.55
317			3-1400/0.75	0.86	140	1226	1400	1050	250	250	1	2.60	10	520	10	36.2	0.12	6.0	350	520	0.12	6.00	350	520	S	0.46	950	1.15	0.75
318			4-1750/0.75	0.86	140	1534	1750	1320	250	250	1	2.60	12	520	10	40.4	0.12	6.0	350	520	0.12	6.00	350	520	S	0.46	1240	1.34	0.74
319			1-500/1.00	1.19	140	419	500	500	250	250	1	2.60	4	520	10	37.4	0				0				S	1.1	570	1.14	1.63
320			2-1000/1.00	1.16	140	859	1000	1000	250	250	1	2.60	8	520	10	30.8	0.12	6.0	350	520	0.12	6.00	350	520	S	0.45	435	0.82	0.65
321			4-1750/1.00	1.15	140	1534	1750	1760	250	250	1	2.60	12	520	10	44.8	0.12	6.0	350	520	0.12	6.00	350	520	S	0.48	1000	1.27	0.65
322			3-1400/1.00	1.16	140	1226	1400	1420	250	250	1	2.60	10	520	10	35.3	0.12	6.0	350	520	0.12	6.00	350	520	S	0.53	800	1.24	0.76
323	17	2000	YB2000/0	2.86	300	1890	2000	5400	292	150	0.5	0.74	6	457	10	33.6	0				0				S	0.40	255.0		
324			YB2000/4	2.86	300	1890	2000	5400	292	150	0.5	0.74	6	457	10	36.4	0.07	12.7	590	468	0				S	1.06	674.0		

#	Ref. #	Year	Beam Name	a/d	b, mm	d, mm	h, mm	a: M/V mm	l_{b1}, mm	l_{b2}, mm	V/P	ρ_l, %	# bars	f_y, MPa	a_g, mm	f_c, MPa	ρ_v, %	d_{bv}, mm	s_v, mm	f_{yv}, MPa	ρ_h, %	d_{bh}, mm	s_h, mm	f_{yh}, MPa	Rep. mode	M_{max}/M_n	V_u, kN	2PKT [33] Exp/Pred	Russo et al.[34] Exp/Pred
325	18	2000	DF-1	2.33	500	1000	1090	2325	200	150	0.5	0.42	3	600	20	21.0	0				0				S	0.85	429.0	1.39	
326			DF-2	2.33	500	1000	1090	2325	200	150	0.5	0.42	3	600	20	18.4	0				0				S	0.63	315.0	1.09	
327			DF-2R	2.33	500	1000	1090	2325	200	150	0.5	0.42	3	600	20	18.4	0				0				S	0.76	378.0	1.30	
328			DF-3	2.33	500	1000	1090	2325	200	150	0.5	0.42	3	600	20	18.4	0				0				S	0.66	329.0	1.13	
329			DF-4	2.33	500	1000	1090	2325	200	150	0.5	0.60	10	600	20	25.5	0				0				S	0.55	387.0	1.01	
330			DF-5	2.33	500	996	1090	2325	200	150	0.5	0.66	12	600	20	25.5	0				0				S	0.50	381.0	0.98	
331			DF-6	2.20	500	1000	1090	2200	300	200	0.5	0.98	7	600	20	21.0	0				0				S	0.69	771.0	1.54	
332			DF-7	2.33	500	1000	1090	2325	200	150	0.5	0.98	7	600	20	20.6	0				0				S	0.41	435.0	1.10	
333			DF-8	2.33	500	1000	1090	2325	600	150	0.5	0.98	7	600	20	22.4	0				0				S	0.50	531.0	0.93	
334			DF-8R	2.33	500	1000	1090	2325	600	150	0.5	0.98	7	600	20	22.4	0				0				S	0.54	579.0	1.02	
335			DF-9	2.33	500	1000	1090	2325	200	150	0.5	0.98	7	600	20	31.7	0				0				S	0.47	532.0	1.09	
336			DF-10	2.33	500	1000	1090	2325	200	150	0.5	0.98	7	600	20	31.7	0				0				S	0.47	524.0	1.07	
337			DF-10R	2.33	500	1000	1090	2325	200	150	0.5	0.98	7	600	20	31.7	0				0				S	0.54	605.0	1.24	
338			DF-11	2.00	250	1000	1090	2000	200	150	0.5	0.84	3	600	20	19.5	0				0				S	0.62	330.0	1.26	0.77
339			DF-13	1.50	250	1000	1090	1500	200	150	0.5	0.84	3	600	20	20.3	0				0				S	0.77	550.0	1.49	0.99
340			DF-14	1.75	250	1000	1090	1750	200	150	0.5	0.84	3	600	20	19.5	0				0				S	0.67	409.0	1.32	0.86
341			DF-15	1.82	250	962	1090	1750	200	150	0.5	1.75	6	600	20	20.3	0				0				S	0.40	330.0	0.94	0.56
342			DF-16	1.43	250	1000	1090	1425	200	150	0.5	0.84	3	600	20	20.3	0				0				S	0.50	380.0	0.98	0.66
343	19	2003	L5-100	0.53	160	935	1000	500	100	100	1	0.90	4	804	19	31.4	0				0				S	0.33	582.1	0.93	0.74
344			L5-75	0.55	160	685	750	375	100	100	1	1.05	4	804	19	31.4	0				0				S	0.42	596.8	1.12	0.98
345			L5-60	0.54	160	555	600	300	100	100	1	0.97	3	804	19	31.4	0				0				S	0.49	535.1	1.10	1.12
346			L5-60R	0.54	160	555	600	300	100	100	1	0.97	3	804	19	31.4	0				0				S	0.44	479.2	0.99	1.00
347			L5-40	0.56	160	355	400	200	100	100	1	1.01	2	804	19	31.4	0				0				S	0.64	446.9	1.13	1.46
348			L10-100	1.07	160	935	1000	1000	100	100	1	0.90	4	804	19	31.4	0				0				S	0.62	543.9	1.36	0.93
349			L10-75	1.09	160	685	750	750	100	100	1	1.05	4	804	19	31.4	0				0				S	0.38	271.5	0.80	0.60
350			L10-75R	1.09	160	685	750	750	100	100	1	1.05	4	804	19	31.4	0				0				S	0.47	330.3	0.98	0.74
351			L10-60	1.08	160	555	600	600	100	100	1	0.97	3	804	19	31.4	0				0				S	0.69	375.3	1.22	1.05
352			L10-40	1.13	160	355	400	400	100	100	1	1.01	2	804	19	31.4	0				0				S	0.55	192.1	0.78	0.85
353			L10-40R	1.13	160	355	400	400	100	100	1	1.01	2	804	19	31.4	0				0				S	0.90	311.6	1.26	1.38
354			UH5-100	0.53	160	935	1000	500	100	100	1	0.90	4	804	19	78.5	0				0				S	0.54	1029.0	1.10	0.85
355			UH5-75	0.55	160	685	750	375	100	100	1	1.05	4	804	19	78.5	0				0				S	0.64	1010.4	1.21	1.07
356			UH5-60	0.54	160	555	600	300	100	100	1	0.97	3	804	19	78.5	0				0				S	0.68	823.2	1.05	1.11
357			UH5-40	0.56	160	355	400	200	100	100	1	1.01	2	804	19	78.5	0				0				S	0.95	733.0	1.08	1.54
358			UH10-100	1.07	160	935	1000	1000	100	100	1	0.90	4	804	19	78.5	0				0				S	0.80	769.3	1.36	0.84
359			UH10-75	1.09	160	685	750	750	100	100	1	1.05	4	804	19	78.5	0				0				S	0.43	338.1	0.67	0.48
360			UH10-75R	1.09	160	685	750	750	100	100	1	1.05	4	804	19	78.5	0				0				S	0.46	360.6	0.71	0.51

#	Ref. #	Year	Beam Name	a/d	b, mm	d, mm	h, mm	a: M/V mm	l_{b1}, mm	l_{b2}, mm	V/P	ρ_l, %	# bars	f_y, MPa	a_g, mm	f_c, MPa	ρ_v, %	d_{bv}, mm	s_v, mm	f_{yv}, MPa	ρ_h, %	d_{bh}, mm	s_h, mm	f_{yh}, MPa	Rep. mode	M_{max}/M_n	V_u, kN	2PKT [33] Exp/Pred	Russo et al. [34] Exp/Pred
361			UH10-60	1.08	160	555	600	600	100	100	1	0.97	3	804	19	78.5	0				0				S	0.95	573.3	1.22	1.03
362			UH10-40	1.06	160	355	400	375	100	100	1	1.01	2	804	19	78.5	0				0				S	1.22	498.8		
363			UH10-40R	1.06	160	355	400	375	100	100	1	1.01	2	804	19	78.5	0				0				S	0.94	385.1	0.87	1.05
364	20	2005	1	0.50	300	400	450	200	100	100	1	2.14	4	458	10	23.2	0				0				S	0.49	853.0	1.14	1.21
365			2	0.50	300	400	450	200	100	100	1	2.14	4	458	10	23.2	0.21	6.0	100	370	0				S	0.47	821.0	1.08	1.14
366			3	0.50	300	400	450	200	100	100	1	2.14	4	458	10	23.2	0.48	10.0	100	388	0				S	0.48	833.0	1.10	1.13
367			4	0.50	300	400	450	200	100	100	1	2.14	4	458	10	23.2	0.84	13.0	100	368	0				S	0.50	869.0	1.15	1.15
368			5	1.00	300	400	450	400	100	100	1	2.14	4	458	10	29.0	0				0				S	0.67	632.0	1.12	1.01
369			6	1.00	300	400	450	400	100	100	1	2.14	4	458	10	29.1	0.21	6.0	100	370	0				S	0.78	731.0	1.22	1.12
370			7	1.00	300	400	450	400	100	100	1	2.14	4	458	10	29.2	0.48	10.0	100	388	0				S	0.79	750.0	1.20	1.09
371			8	1.00	300	400	450	400	100	100	1	2.14	4	458	10	29.3	0.84	13.0	100	368	0				S	0.85	804.0	1.22	1.10
372			9	1.50	300	400	450	600	100	100	1	2.14	4	458	10	22.9	0				0				S	0.49	284.0	0.81	0.71
373			10	1.50	300	400	450	600	100	100	1	2.14	4	458	10	22.5	0.21	6.0	100	370	0				S	0.82	464.0	1.11	1.08
374			11	1.50	300	400	450	600	100	100	1	2.14	4	458	10	23.0	0.48	10.0	100	388	0				S	0.85	491.0	0.98	1.01
375			12	1.50	300	400	450	600	100	100	1	2.14	4	458	10	23.5	0.84	13.0	100	368	0				S	0.97	570.0	0.97	1.04
376			13	1.00	300	400	450	400	100	100	1	2.14	4	458	10	32.0	0				0				S	0.69	661.0	1.11	0.98
377			14	1.00	300	400	450	400	100	100	1	2.14	4	458	10	32.0	0.21	6.0	100	370	0				S	0.78	751.0	1.19	1.08
378			15	1.00	300	400	450	400	100	100	1	2.14	4	458	10	32.0	0.48	10.0	100	388	0				S	0.80	774.0	1.18	1.06
379			16	1.00	300	400	450	400	100	100	1	2.14	4	458	10	32.0	0.84	13.0	100	368	0				S	0.88	849.0	1.24	1.10
380			17	1.00	300	400	450	400	100	100	1	2.14	4	458	10	31.3	0.21	6.0	100	370	0				S	0.59	570.0	0.91	0.83
381			18	1.00	300	400	450	400	100	100	1	2.14	4	458	10	31.5	0.48	10.0	100	388	0				S	0.80	773.0	1.19	1.07
382			19	1.00	300	400	450	400	100	100	1	2.14	4	458	10	31.8	0.84	13.0	100	368	0				S	0.79	756.0	1.10	0.99
383			20	1.00	300	400	450	400	100	100	1	2.14	4	702	10	24.3	0.48	10.0	100	952	0				S	0.74	665.0	1.09	0.96
384			21	1.00	300	400	450	400	100	100	1	2.14	4	702	10	26.9	0.84	13.0	100	1051	0				S	0.68	661.0	1.03	0.76
385			22	1.50	300	400	450	600	100	100	1	2.14	4	702	10	26.2	0.48	10.0	100	952	0				S	0.84	537.0	0.73	0.82
386			23	1.50	300	400	450	600	100	100	1	2.14	4	702	10	26.3	0.84	13.0	100	1051	0				S	0.88	566.0	0.78	0.67
387			24	0.50	300	400	450	200	100	100	1	2.14	4	702	10	79.9	0				0				S	0.61	1958.0	1.24	1.39
388			25	1.00	300	400	450	400	100	100	1	2.14	4	702	10	76.4	0				0				S	0.88	1403.0	1.39	1.33
389			26	1.50	300	400	450	600	100	100	1	2.14	4	702	10	78.3	0				0				S	0.85	904.0	1.30	1.11
390			27	2.00	300	400	450	800	100	100	1	2.14	4	702	10	77.8	0				0				S	0.94	752.0	1.54	1.17
391			28	0.75	300	400	450	300	100	100	1	2.14	4	458	10	25.5	0.48	10.0	100	388	0				S	0.53	647.0	0.99	0.92
392			29	0.75	300	400	450	300	100	100	1	2.14	4	458	10	26.2	0.84	13.0	100	368	0				S	0.54	666.0	1.00	0.89
393			30	0.75	300	400	450	300	100	100	1	2.14	4	458	10	26.4	0.88	16.0	150	389	0				S	0.57	701.0	1.05	0.93
394			31	2.00	300	400	450	800	100	100	1	2.14	4	702	10	26.6	0.48	10.0	100	388	0				S	0.86	416.0	0.78	0.88
395			32	2.00	300	400	450	800	100	100	1	2.14	4	702	10	27.4	0.84	13.0	100	368	0				S	0.89	440.0	0.65	0.80
396			33	1.00	300	400	450	400	100	100	1	2.14	4	458	10	24.7	0.95	10.0	50	388	0				S	0.72	647.0	1.04	0.97

#	Ref. #	Year	Beam Name	a/d	b, mm	d, mm	h, mm	a: M/V mm	l_{b1}, mm	l_{b2}, mm	V/P	ρ_l, %	# bars	f_y, MPa	a_g, mm	f_c, MPa	ρ_v, %	d_{bv}, mm	s_v, mm	f_{yv}, MPa	ρ_h, %	d_{bh}, mm	s_h, mm	f_{yh}, MPa	Rep. mode	M_{max}/M_n	V_u, kN	2PKT [33] Exp/Pred	Russo et al. [34] Exp/Pred
397			34	1.00	300	400	450	400	100	100	1	2.14	4	458	10	24.8	0.95	19.0	200	375	0				S	0.66	598.0	0.96	0.90
398			35	0.50	300	400	450	200	100	100	1	0.42	4	1330	10	25.3	0				0				S	0.50	588.0	0.98	1.46
399			36	0.50	300	400	450	200	100	100	1	0.42	4	1330	10	24.5	0.48	10.0	100	388	0				S	0.47	539.0	0.90	1.28
400			37	0.50	300	400	450	200	100	100	1	0.42	4	1330	10	25.8	0.84	13.0	100	368	0				S	0.47	554.0	0.89	1.22
401			38	1.00	300	400	450	400	100	100	1	0.42	4	1330	10	25.2	0				0				S	0.61	358.0	0.92	1.16
402			39	1.00	300	400	450	400	100	100	1	0.42	4	1330	10	25.4	0.48	10.0	100	388	0				S	0.81	470.0	1.17	1.28
403			40	1.00	300	400	450	400	100	100	1	0.42	4	1330	10	25.9	0.84	13.0	100	368	0				S	0.80	470.0	1.16	1.15
404			41	2.50	300	400	450	1000	100	100	1	2.14	4	750	10	20.6	0.48	10.0	100	388	0				S	1.02	324.0		
405			42	2.50	300	400	450	1000	100	100	1	2.14	4	750	10	21.4	0.84	13.0	100	368	0				S	1.15	376.0		
406			45	2.50	300	400	450	1000	100	100	1	2.14	4	750	10	97.2	0				0				S	0.50	345.0	1.34	
407			46	1.00	300	400	450	400	100	100	1	2.14	4	750	10	97.5	0.21	6.0	100	957	0				S	0.71	1243.0	0.99	1.04
408			47	1.00	300	400	450	400	100	100	1	2.14	4	750	10	96.3	0.48	10.0	100	953	0				S	0.75	1300.0	1.01	1.02
409			48	1.50	300	400	450	600	100	100	1	2.14	4	750	10	94.5	0.21	6.0	100	957	0				S	0.81	932.0	0.97	0.98
410			49	1.50	300	400	450	600	100	100	1	2.14	4	750	10	94.2	0.48	10.0	100	953	0				S	0.85	980.0	0.86	0.92
411			L6	1.00	200	1000	1050	1000	200	200	1	0.40	4	1016	10	31.2	0.29	10.0	250	389	0				S	0.89	665.0	0.94	1.04
412			L7	1.00	400	2000	2100	2000	400	400	1	0.40	4	1016	10	30.5	0.29	19.0	500	375	0				S	0.86	2584.0	0.99	1.02
413	21	2005	B-2	0.50	240	400	475	200	100	100	1	2.02	5	376	20	36.2	0				0				S	0.61	775.0	1.02	1.02
414			B-3	0.50	240	400	475	200	100	100	1	2.02	5	376	20	36.2	0.40	6.0	65	376	0	6.0		376	S	0.60	768.0	0.99	0.98
415			B-4	0.50	240	400	475	200	100	100	1	2.02	5	376	20	31.3	0.80	10.0	75	376	0	10.0		376	S	0.78	975.5	1.38	1.34
416			B-6	1.00	240	400	475	400	100	100	1	2.02	5	376	20	31.3	0				0				S	0.84	525.0	1.13	1.01
417			B-7	1.00	240	400	475	400	100	100	1	2.02	5	376	20	31.3	0.40	6.0	65	376	0	6.0		376	S	0.94	590.5	1.20	1.06
418			B-8	1.00	240	400	475	400	100	100	1	2.02	5	376	20	37.8	0.80	10.0	75	376	0	10.0		376	S	1.17	750.5		
419			B-10-1	1.50	240	400	475	600	100	100	1	2.02	5	376	20	29.2	0				0				S	0.75	308.0	1.01	0.81
420			B-10-2	1.50	240	400	475	600	100	100	1	2.02	5	376	20	23.0	0				0				S	0.90	351.5	1.31	1.12
421			B-11	1.50	240	400	475	600	100	100	1	2.02	5	376	20	29.2	0.40	6.0	65	376	0	6.0		376	S	1.24	512.5		
422			B-12	1.50	240	400	475	600	100	100	1	2.02	5	376	20	31.3	0.80	10.0	75	376	0	10.0		376	S	1.39	580.5		
423			B-10.3-1	1.50	360	600	675	900	150	150	1	2.11	9	388	20	37.8	0				0				S	0.95	980.0	1.34	0.95
424			B-10.3-2	1.50	360	600	675	900	150	150	1	2.11	9	372	20	31.2	0				0				S	0.93	893.5	1.38	0.99
425			B-13-1	1.50	480	800	905	1200	200	200	1	2.07	10	398	20	31.6	0				0				S	0.84	1492.5	1.33	0.92
426			B-13-2	1.50	480	800	905	1200	200	200	1	2.07	10	398	20	24.0	0				0				S	0.67	1128.5	1.17	0.86
427			B-14	1.50	600	1000	1105	1500	250	250	1	2.04	14	398	20	31.0	0				0				S	0.72	1984.5	1.20	0.80
428			B-17	1.50	600	1000	1105	1500	250	250	1	2.04	14	398	20	28.7	0.40	13.0	100	398	0	13.0		398	S	0.96	2607.0	1.14	0.96
429			B15	1.50	720	1200	1305	1800	300	300	1	1.99	18	402	20	27.0	0				0				S	0.71	2695.0	1.27	0.84
430			B-16	1.50	840	1400	1505	2100	350	350	1	2.05	18	394	20	27.3	0				0				S	0.57	2987.5	1.03	0.68
431			B-18	1.50	840	1400	1505	2100	350	350	1	2.05	18	398	20	23.5	0.40	16.0	120	398	0	16.0		398	S	0.83	4198.0	0.99	0.90
432	22	2007	1DB35bw	1.10	80	313	350	344	53	53	1	1.25	4	455	10	25.9	0.40	6.0	150	426	0				S	0.88	99.5	0.99	0.93

#	Ref. #	Year	Beam Name	a/d	b, mm	d, mm	h, mm	a: M/V mm	l_{b1}, mm	l_{b2}, mm	V/P	ρ_l, %	# bars	f_y, MPa	a_g, mm	f_c, MPa	ρ_v, %	d_{bv}, mm	s_v, mm	f_{yv}, MPa	ρ_h, %	d_{bh}, mm	s_h, mm	f_{yh}, MPa	Rep. mode	M_{max}/M_n	V_u, kN	2PKT [33] Exp/Pred	Russo et al. [34] Exp/Pred
433			1DB50bw	1.10	115	454	500	499	75	75	1	1.28	4	520	10	27.4	0.39	6.0	150	426	0				S	0.69	186.5	0.89	0.80
434			1DB70bw	1.10	160	642	700	706	105	105	1	1.22	4	522	10	28.3	0.45	8.0	150	426	0				S	0.83	427.0	1.03	0.91
435			1DB100bw	1.10	230	904	1000	994	150	150	1	1.20	6	555	10	28.7	0.41	10.0	150	426	0				S	0.71	775.0	0.99	0.83
436			2DB35	1.10	80	314	350	345	53	53	1	1.25	4	469	10	27.4	0				0				S	0.73	85.0	1.05	0.86
437			2DB50	1.10	80	459	500	505	75	75	1	1.18	4	520	10	32.4	0				0				S	0.75	135.5	1.12	0.85
438			2DB70	1.10	80	650	700	715	105	105	1	1.33	4	520	10	24.8	0				0				S	0.57	155.5	1.10	0.80
439			2DB100	1.10	80	926	1000	1019	150	150	1	1.30	6	520	10	30.6	0				0				S	0.61	241.5	1.20	0.75
440			3DB35b	1.10	80	314	350	345	53	53	1	1.25	4	469	10	27.4	0				0				S	0.73	85.0	1.05	0.86
441			3DB50b	1.10	115	454	500	499	75	75	1	1.28	4	520	10	28.3	0				0				S	0.61	167.0	1.02	0.78
442			3DB70b	1.10	160	642	700	706	105	105	1	1.22	4	522	10	28.7	0				0				S	0.70	360.5	1.21	0.87
443			3DB100b	1.10	230	904	1000	994	150	150	1	1.20	6	555	10	29.3	0				0				S	0.61	672.0	1.16	0.79
444	23	2007	L-10N1	2.89	300	1400	1510	4050	150	150	0.5	0.83	5	452	10	38.4	0				0				S	0.52	265.0		
445			L-10N2	2.89	300	1400	1510	4050	150	150	0.5	0.83	5	452	10	40.3	0				0				S	0.47	242.0		
446			L-10H	2.89	300	1400	1510	4050	150	150	0.5	0.83	5	452	10	73.6	0				0				S	0.45	240.0		
447			L-10HS	2.89	300	1400	1510	4050	150	150	0.5	1.33	8	452	10	71.2	0.10	9.5	235	494	0				S	0.86	710.0		
448			L-20N1	2.89	300	1400	1510	4050	150	150	0.5	0.83	5	452	19	31.4	0				0				S	0.52	265.0		
449			L-20N2	2.89	300	1400	1510	4050	150	150	0.5	0.83	5	452	19	33.2	0				0				S	0.52	266.0		
450			L-40N1	2.89	300	1400	1510	4050	150	150	0.5	0.83	5	452	38	28.1	0				0				S	0.48	242.0		
451			L-40N2	2.89	300	1400	1510	4050	150	150	0.5	0.83	5	452	38	28.5	0				0				S	0.57	288.0		
452			L-50N1	2.89	300	1400	1510	4050	150	150	0.5	0.83	5	452	51	41.0	0				0				S	0.53	272.0		
453			L-50N2	2.89	300	1400	1510	4050	150	150	0.5	0.83	5	452	51	40.1	0				0				S	0.58	298.0		
454			L-50N2R	2.89	300	1400	1510	4050	150	150	0.5	0.83	5	452	51	40.1	0				0				S	0.63	323.0		
455			S-10N1	2.89	122	280	330	810	30	30	0.5	0.83	4	494	10	41.9	0				0				S	0.80	36.6		
456			S-10N2	2.89	122	280	330	810	30	30	0.5	0.83	4	494	10	41.9	0				0				S	0.84	38.3		
457			S-10H	2.89	122	280	330	810	30	30	0.5	0.83	4	494	10	77.3	0				0				S	0.80	37.7		
458			S-10HS	2.89	122	280	330	810	30	30	0.5	1.34	5	506	10	77.3	0.10	5.0	160	496	0				S	0.87	66.3		
459			S-20N1	2.89	122	280	330	810	30	30	0.5	0.83	4	494	19	39.2	0				0				S	0.86	39.1		
460			S-20N2	2.89	122	280	330	810	30	30	0.5	0.83	4	494	19	38.1	0				0				S	0.84	38.2		
461			S-40N1	2.89	122	280	330	810	30	30	0.5	0.83	4	494	38	29.1	0				0				S	0.94	41.8		
462			S-40N2	2.89	122	280	330	810	30	30	0.5	0.83	4	494	38	29.1	0				0				S	0.79	34.9		
463			S-50N1	2.89	122	280	330	810	30	30	0.5	0.83	4	494	51	43.5	0				0				S	0.84	38.5		
464			S-50N2	2.89	122	280	330	810	30	30	0.5	0.83	4	494	51	43.5	0				0				S	0.89	40.6		
465	24	2008	MS1-1	1.20	300	501	607	600	200	200	1	0.52	6	838	10	46.0	0.33	11.3	200	400	0.25	9.5	190	400	F	1.21	626.0		
466			MS1-2	1.19	300	503	607	600	200	200	1	1.13	6	870	10	44.0	0.33	11.3	200	400	0.45	12.7	190	400	F	0.99	1071.0		
467			MS1-3	1.19	300	506	607	600	200	200	1	2.29	9	880	10	44.0	0.33	11.3	200	400	0.45	12.7	190	400	S	0.96	1373.5	1.22	1.29
468			MS2-2	1.79	300	503	607	900	200	200	1	1.13	6	870	10	47.0	0.33	11.3	200	400	0.45	12.7	190	400	F	0.98	716.0		

#	Ref. #	Year	Beam Name	a/d	b, mm	d, mm	h, mm	a: M/V mm	l_{b1}, mm	l_{b2}, mm	V/P	ρ_l, %	# bars	f_y, MPa	a_g, mm	f_c, MPa	ρ_v, %	d_{bv}, mm	s_v, mm	f_{yv}, MPa	ρ_h, %	d_{bh}, mm	s_h, mm	f_{yh}, MPa	Rep. mode	M_{max}/M_n	V_u, kN	2PKT [33] Exp/Pred	Russo et al.[34] Exp/Pred
469			MS2-3	1.78	300	506	607	900	200	200	1	2.29	9	880	10	43.0	0.33	11.3	200	400	0.45	12.7	190	400	S	1.09	1027.5	1.34	1.25
470			MS3-2	2.39	300	503	607	1200	200	200	1	1.13	6	870	10	48.0	0.44	11.3	150	400	0.45	12.7	190	400	F	1.06	577.0		
471	25	2009	0.60/0.60/P	1.40	150	428	500	600	150	150	1	1.24	6	484	10	41.2	0.35	10.0	300	328	0				S	1.00	250.1	0.77	0.81
472			0.60/0.60/2P	1.40	150	428	500	600	150	150	0.83	1.24	6	484	10	41.2	0.35	10.0	300	328	0				S	1.22	305.6		
473			0.60/0.60/5P	1.40	150	428	500	600	150	150	0.73	1.24	6	484	10	41.2	0.35	10.0	300	328	0				S	1.02	256.8	0.87	0.83
474			0.45/0.75/P	1.75	150	428	500	750	150	150	0.83	1.24	6	484	10	41.2	0.35	10.0	300	328	0				S	1.19	240.1		
475			0.30/0.90/P	2.10	150	428	500	900	150	150	0.67	1.24	6	484	10	41.2	0.35	10.0	300	328	0				S	1.24	207.3		
476			0.30/0.90/5P	0.70	150	428	500	300	150	150	0.93	1.24	6	484	10	41.2	0.35	10.0	300	328	0				S	0.91	458.1	0.86	1.07
477			0.75/0.75/P	1.42	160	527	600	750	150	150	0.98	1.43	6	495	10	38.3	0.42	8.0	150	369	0				S	1.14	424.5		
478			0.75/0.75/2P	1.42	160	527	600	750	150	150	0.83	1.43	6	495	10	38.3	0.42	8.0	150	369	0				S	1.06	396.6	1.08	0.95
479			0.75/0.75/4P	1.42	160	527	600	750	150	150	0.75	1.43	6	495	10	38.3	0.42	8.0	150	369	0				S	1.18	440.1		
480			0.75/0.75/6P	1.42	160	527	600	750	150	150	0.71	1.43	6	495	10	38.3	0.42	8.0	150	369	0				S	0.82	307.2	0.87	0.74
481			0.45/1.05/P	1.99	160	527	600	1050	150	150	0.73	1.43	6	495	10	38.3	0.42	8.0	150	369	0				S	1.09	291.8	0.96	0.83
482			0.45/1.05/2P	0.85	160	527	600	450	150	150	1.02	1.43	6	495	10	38.3	0.42	8.0	150	369	0				S	0.89	552.7	1.03	1.04
483			0.30/1.20/P	2.28	160	527	600	1200	150	150	0.59	1.43	6	495	10	38.3	0.42	8.0	150	369	0				S	1.14	266.5		
484			0.30/1.20/2P	0.57	160	527	600	300	150	150	1	1.43	6	495	10	38.3	0.42	8.0	150	369	0				S	0.71	665.4	1.00	1.09
485	26	2009	DB1.0-1.00	1.05	165	581	635	610	203	114	1	0	2	414	10	33.3	0.31	5.7	102	605	0.21	5.70	152	605	F	2.21	338.5		
486			DB1.0-0.75	1.05	173	581	635	610	203	114	1	0	2	414	10	31.7	0.29	5.7	102	605	0.20	5.70	152	605	F	2.43	371.5		
487			DB1.0-0.50	1.05	157	581	635	610	203	114	1	0	2	414	10	30.6	0.32	5.7	102	605	0.22	5.70	152	605	F	2.39	364.5		
488			DB1.0-0.32	1.05	152	581	635	610	203	114	1	0	2	414	10	27.0	0.33	5.7	102	605	0.22	5.70	152	605	F	2.2	333.5		
489			DB1.0-0.75L	1.05	155	581	635	610	203	114	1	0.63	2	414	10	29.9	0.33	5.7	102	605	0.22	5.70	152	605	F	1.74	370.5		
490			DB1.0-0.28L	1.05	155	581	635	610	203	114	1	0.63	2	414	10	29.4	0.33	5.7	102	605	0.22	5.70	152	605	F	1.51	321		
491			DB1.5-0.75	1.51	152	405	457	610	203	114	1	0.65	2	414	10	32.7	0.33	5.7	102	605	0.22	5.70	152	605	F	2.19	229.5		
492			DB1.5-0.50	1.51	152	405	457	610	203	114	1	0.65	2	414	10	34.1	0.33	5.7	102	605	0.22	5.70	152	605	F	2.02	211.5		
493			DB1.5-0.38	1.51	152	405	457	610	203	114	1	0.65	2	414	10	33.8	0.33	5.7	102	605	0.22	5.70	152	605	F	2.04	213.5		
494			DB2.0-0.75	2.01	155	303	356	610	203	114	1	0.85	2	414	10	34.7	0.33	5.7	102	605	0.22	5.70	152	605	F	2.02	156.5		
495			DB2.0-0.50	2.01	155	303	356	610	203	114	1	0.85	2	414	10	33.0	0.33	5.7	102	605	0.22	5.70	152	605	F	1.93	148.5		
496			DB2.0-0.43	2.01	155	303	356	610	203	114	1	0.85	2	414	10	35.6	0.33	5.7	102	605	0.22	5.70	152	605	F	1.72	133		
497	27	2009	I-03-2	1.84	533	978	1118	1799	508	406	0.72	2.29	42	503	19	36.1	0.29	12.7	165	462	0.33	12.7	146	462	S	0.95	2531.0	1.17	1.01
498			I-03-4	1.84	533	978	1118	1799	508	406	0.72	2.29	42	503	19	36.8	0.30	9.5	178	503	0.33	12.7	146	462	S	1.10	2922.5	1.30	1.13
499			I-02-2	1.84	533	978	1118	1799	508	406	0.72	2.29	42	503	19	27.2	0.20	12.7	241	462	0.20	12.7	241	462	S	0.85	2019.5	1.17	1.01
500			I-02-4	1.84	533	978	1118	1799	508	406	0.72	2.29	42	503	19	28.7	0.21	9.5	254	503	0.20	12.7	241	462	S	0.96	2348.7	1.29	1.12
501			II-03-CCC2021	1.84	533	980	1067	1804	508	254	0.72	2.31	12	441	19	22.7	0.31	15.9	241	448	0.45	15.9	168	448	S	1.08	2224.1	1.17	1.15
502			II-02-CCC1021	1.84	533	980	1067	1804	254	254	0.72	2.31	12	476	19	31.9	0.20	15.9	381	462	0.19	12.7	257	427	S	0.59	1463.5	0.85	0.66
503			II-03-CCT1021	1.84	533	980	1067	1804	914	254	0.72	2.31	12	455	19	30.4	0.31	15.9	241	490	0.45	15.9	168	490	S	1.19	2829.1		
504			II-03-CCT0507	1.84	533	980	1067	1804	914	127	0.72	2.31	12	455	19	29.0	0.31	15.9	241	490	0.45	15.9	168	490	S	1.13	2660.0		

#	Ref. #	Year	Beam Name	a/d	b, mm	d, mm	h, mm	a: M/V mm	l_{b1}, mm	l_{b2}, mm	V/P	ρ_l, %	# bars	f_y, MPa	a_g, mm	f_c, MPa	ρ_v, %	d_{bv}, mm	s_v, mm	f_{yv}, MPa	ρ_h, %	d_{bh}, mm	s_h, mm	f_{yh}, MPa	Rep. mode	M_{max}/M_n	V_u, kN	2PKT [33] Exp/Pred	Russo et al.[34] Exp/Pred
505			II-02-CCT0507	1.84	533	980	1067	1804	914	127	0.72	2.31	12	476	19	21.5	0.20	15.9	381	441	0.19	12.7	254	434	S	0.90	1783.7	0.96	1.05
506			II-02-CCT0521	1.84	533	980	1067	1804	508	127	0.72	2.31	12	476	19	32.7	0.20	15.9	381	462	0.19	12.7	257	427	S	1.01	2526.6	1.27	1.13
507			III-1.85-00	1.84	533	980	1067	1804	508	406	0.72	2.31	12	455	19	21.9	0				0				S	0.81	1623.6	1.22	1.11
508			III-2.5-00	2.47	533	980	1067	2422	508	406	0.63	2.31	12	455	19	22.1	0				0				S	0.24	364.8	0.62	
509			III-1.85-02	1.84	533	980	1067	1804	508	406	0.72	2.31	12	476	19	28.3	0.20	15.9	368	441	0.19	12.7	257	427	S	0.90	2170.7	1.12	1.07
510			III-1.85-025	1.84	533	980	1067	1804	508	406	0.72	2.31	12	476	19	28.3	0.24	15.9	305	441	0.14	9.5	193	503	S	0.95	2295.3	1.14	1.11
511			III-1.85-03	1.84	533	980	1067	1804	508	406	0.72	2.31	12	476	19	34.4	0.29	15.9	254	441	0.29	15.9	257	434	S	0.72	1832.7	0.80	0.76
512			III-1.85-01	1.84	533	980	1067	1804	508	406	0.72	2.31	12	476	19	34.5	0.10	12.7	457	434	0.14	9.5	193	503	S	0.48	1214.4	0.62	0.55
513			III-1.85-03b	1.84	533	980	1067	1804	508	406	0.72	2.31	12	476	19	22.8	0.31	12.7	152	427	0.29	15.9	257	462	S	1.02	2095.1	1.08	1.11
514			III-1.85-02b	1.84	533	980	1067	1804	508	406	0.72	2.31	12	476	19	22.8	0.20	12.7	241	427	0.19	12.7	257	427	S	1.01	2081.8	1.18	1.19
515			III-1.2-02	1.20	533	980	1067	1177	508	406	0.82	2.31	12	455	19	28.3	0.20	12.7	241	414	0.19	12.7	257	414	S	1.05	3763.2	1.30	1.42
516			III-1.2-03	1.20	533	980	1067	1177	508	406	0.82	2.31	12	455	19	29.1	0.31	15.9	241	469	0.29	15.9	257	469	S	1.02	3687.6	1.22	1.30
517			III-2.5-02	2.49	533	980	1067	2441	508	406	0.62	2.31	12	455	19	31.9	0.20	12.7	241	427	0.19	12.7	257	427	S	0.74	1325.6		
518			III-2.5-03	2.49	533	980	1067	2441	508	406	0.62	2.31	12	455	19	34.7	0.31	15.9	241	448	0.29	15.9	257	448	S	1.27	2295.3		
519			IV-2175-1.85-02	1.85	533	1750	1905	3238	737	406	0.50	2.37	22	469	19	34.0	0.21	12.7	241	455	0.19	12.7	257	455	S	0.75	3394.0	1.18	0.82
520			IV-2175-1.85-03	1.85	533	1750	1905	3238	737	406	0.50	2.37	22	469	19	34.0	0.31	15.9	241	455	0.29	15.9	257	455	S	0.83	3745.4	1.14	0.86
521			IV-2175-2.5-02	2.50	533	1750	1905	4375	610	406	0.33	2.37	22	469	19	34.5	0.21	15.9	362	441	0.21	15.9	362	441	S	0.67	2268.6		
522			IV-2175-1.2-02	1.20	533	1750	1905	2100	610	406	0.68	2.37	22	469	19	34.5	0.21	15.9	362	441	0.21	15.9	362	441	S	0.78	5440.2	1.38	0.99
523			IV-2123-1.85-03	1.85	533	495	584	916	419	406	0.86	2.32	12	455	19	28.7	0.30	12.7	133	455	0.30	9.5	159	441	S	1.24	1463.5		
524			IV-2123-1.85-02	1.85	533	495	584	916	419	406	0.86	2.32	12	455	19	29.1	0.20	9.5	159	558	0.17	12.7	159	455	S	1.30	1543.5		
525			IV-2123-2.5-02	2.50	533	495	584	1238	394	406	0.81	2.32	12	448	19	31.5	0.20	9.5	133	400	0.17	9.5	159	558	S	0.81	716.2	0.76	
526			IV-2123-1.2-02	1.20	533	495	584	594	457	406	0.91	2.32	12	448	19	31.9	0.20	9.5	133	400	0.17	9.5	159	441	F	1.42	2633.3		
527			M-03-4-CCC2436	1.85	914	1016	1219	1880	610	406	0.71	2.93	27	462	19	28.3	0.31	15.9	279	421	0.27	15.9	165	421	S	1.11	5017.6		
528			M-03-4-CCC0812	1.85	914	1016	1219	1880	203	406	0.71	2.93	27	448	19	20.7	0.31	15.9	279	434	0.27	15.9	165	434	S	1.18	4136.8		
529			M-09-4-CCC2436	1.85	914	1016	1219	1880	610	406	0.71	2.93	27	462	19	28.3	0.86	15.9	102	421	0.27	15.9	165	421	F	1.39	6294.2		
530			M-02-4-CCC2436	1.85	914	1016	1219	1880	610	406	0.71	2.93	27	448	19	19.3	0.22	12.7	254	434	0.22	15.9	203	434	S	1.48	4901.9		
531			M-03-2-CCC2436	1.85	914	1016	1219	1880	610	406	0.71	2.93	27	469	19	33.8	0.31	22.2	279	427	0.27	15.9	165	427	F	0.95	4875.3		
532	28	2010	BML-0-0	0.50	100	400	450	200	100	100	0.8	1.13	4	400	10	45.2	0				0				S	1.09	371.2	1.22	1.27
533			BML-85-85	0.50	100	400	450	200	100	100	0.8	1.13	4	400	10	40.8	0.20	3.3	85	260	0.20	3.3	85	260	S	1.06	359.2	1.23	1.26
534			BML-68-83	0.50	100	400	450	200	100	100	0.8	1.13	4	400	10	43.2	0.25	3.3	68	260	0.21	3.3	83	260	S	1.09	371.2	1.22	1.26
535			BML-57-57	0.50	100	400	450	200	100	100	0.8	1.13	4	400	10	37.7	0.30	3.3	57	260	0.30	3.3	57	260	S	1.04	348.8	1.26	1.26
536			BML-57-0	0.50	100	400	450	200	100	100	0.8	1.13	4	400	10	40.5	0.30	3.3	57	260	0				S	0.98	331.2	1.14	1.19
537			BML-0-57	0.50	100	400	450	200	100	100	0.8	1.13	4	400	10	39.3	0				0.30	3.3	57	260	S	1.03	348.8	1.25	1.25
538			BML-0-36	0.50	100	400	450	200	100	100	0.8	1.13	4	400	10	38.9	0				0.48	3.3	36	260	S	1.07	360.0	1.30	1.27
539			BML-26-0	0.50	100	400	450	200	100	100	0.8	1.13	4	400	10	43.2	0.66	3.3	26	260	0				S	0.89	303.2	1.00	1.03
540			BML-0-50	0.50	100	400	450	200	100	100	0.8	1.13	4	400	10	44.8	0				0.34	3.3	50	260	S	1.06	360.0	1.19	1.19

#	Ref. #	Year	Beam Name	a/d	b, mm	d, mm	h, mm	a: M/V mm	l_{b1}, mm	l_{b2}, mm	V/P	ρ_l, %	# bars	f_y, MPa	a_g, mm	f_c, MPa	ρ_v, %	d_{bv}, mm	s_v, mm	f_{yv}, MPa	ρ_h, %	d_{bh}, mm	s_h, mm	f_{yh}, MPa	Rep. mode	M_{max}/M_n	V_u, kN	2PKT [33] Exp/Pred	Russo et al.[34] Exp/Pred
541			BML-53-100	0.50	100	400	450	200	100	100	0.8	1.13	4	400	10	44.9	0.32	3.3	53	260	0.17	3.3	100	260	S	1.04	354.4	1.14	1.18
542			BMM-125-125	0.50	100	400	450	200	100	100	0.8	1.13	4	400	10	36.3	0.20	4.0	125	440	0.20	4.0	125	440	S	1.09	365.6	1.35	1.34
543	29	2010	D6.A4.G60#5S	1.37	406	1778	1829	2438	203*	610	1	0.56**	4	490	25	26.7	0.44	16.0	222	429	0				S	0.74†	2253.0		
544			D6.A4.G40#4S	1.37	406	1778	1829	2438	203	610	1	0.56	4	470	25	26.2	0.29	13.0	222	348	0				S	0.61	1809.0		
545			D6.A2.G60#5S	1.37	406	1778	1829	2438	203	610	1	0.28	2	470	25	27.5	0.44	16.0	222	429	0				F	0.59	1754.0		
546			D6.A2.G40#4S	1.37	406	1778	1829	2438	203	610	1	0.28	2	478	25	24.4	0.29	13.0	222	346	0				S	0.44	1307.0		
547			D4.A2.G40#4S	2.09	406	1168	1219	2438	203	610	1	0.42	2	469	25	25.2	0.29	13.0	222	349	0				S	0.63	922.0		
548	30	2010	TCDB-2-3	1.46	180	687	750	1000	200	200	0.5	1.86	4	515	10	38.5	0.28	8	150	526	0.36	8	125	526	s	0.66	460	0.87	0.68
549	31	2010	S0M	1.55	400	1095	1200	1700	300	150	0.5	0.70	6	652	20	34.2	0				0				S	0.61	721.0	0.88	0.56
550			S0C	1.55	400	1095	1200	1700	300	150	0.5	0.70	6	652	20	34.2	0				0				S	0.98	1162.0	1.42	0.90
551			L0M	2.28	400	1095	1200	2500	300	150	0.5	0.70	6	652	20	29.1	0				0				S	0.52	416.0	1.00	
552			L0C	2.28	400	1095	1200	2500	300	150	0.5	0.70	6	652	20	29.1	0				0				S	0.62	492.0	1.18	
553			S1M	1.55	400	1095	1200	1700	300	150	0.5	0.70	6	652	20	33.0	0.10	9.5	10	490	0				S	0.80	941.0	0.93	0.70
554			S1C	1.55	400	1095	1200	1700	300	150	0.5	0.70	6	652	20	33.0	0.10	9.5	10	490	0				S	0.80	943.0	0.93	0.70
555			L1M	2.28	400	1095	1200	2500	300	150	0.5	0.70	6	652	20	37.8	0.10	9.5	10	490	0				S	0.82	663.0	0.88	
556			L1C	2.28	400	1095	1200	2500	300	150	0.5	0.70	6	652	20	37.8	0.10	9.5	10	490	0				S	0.79	642.0	0.86	
557			SB	1.59	400	1070	1200	1700	300	150	0.5	0.60	1	652	20	30.5	0				0				S	0.74	727.0	1.09	0.68
558			MB	1.59	400	1070	1200	1700	300	150	0.5	0.61	4	475	20	30.5	0				0				S	1.19	877.0		
559	32	2013	B3	0.61	170	900	1000	550	300	200	1	2.00	6	439	20	58.5	0				0				S	0.77	1546	1.23	1.04
560			B4	0.61	170	900	1000	550	300	200	1	2.00	6	439	20	58.5	0				0.42	9.53	200	463	S	0.84	1678	1.34	1.07
561			B5	0.61	170	900	1000	550	300	200	1	2.00	6	439	20	58.5	0				0.84	9.53	100	463	S	0.93	1870	1.49	1.14
562			C3	0.61	170	900	1000	550	300	200	1	2.00	6	439	20	58.5	0				0				S	0.77	1542	1.23	1.04
563			C4	0.61	170	900	1000	550	300	200	0.5	2.00	6	439	20	58.5	0				0.42	9.5	200	463	S	0.93	1859	1.48	1.19
564			C5	0.61	170	900	1000	550	300	200	0.5	2.00	6	439	20	58.5	0				0.84	9.5	100	463	S	1.01	2018	1.61	1.23
565			B1	0.83	200	900	1000	750	300	200	0.5	1.70	6	439	20	34.6	0				0				S	0.81	1141	1.34	1.05
566			B2	0.83	200	900	1000	750	300	200	0.5	1.70	6	439	20	34.6	0.26	9.53	270	463	0.71	9.5	100	463	S	0.95	1337	1.47	1.07
567			B6	0.83	200	900	1000	750	300	200	0.5	1.70	6.00	439	20	67.8	0				0				S	1.07	1606	1.38	1.04
568			B7	0.83	200	900	1000	750	300	200	0.5	1.70	6.00	439	20	67.8	0				0.71	9.5	100	463	S	1.17	1765		
569			B8	0.83	200	900	1000	750	300	200	0.5	1.70	6.00	439	20	67.8	0.26	9.53	270	463	0				S	1.14	1722		
570			C1	0.83	200	900	1000	750	300	200	0.5	1.70	6	439	20	34.6	0				0				S	0.82	1156	1.36	1.06
571			C2	0.83	200	900	1000	750	300	200	0.5	1.70	6	439	20	34.6	0.26	9.53	270	463	0.71	9.5	100	463	S	0.98	1375	1.51	1.10
572			C6	0.83	200	900	1000	750	300	200	0.5	1.70	6	439	20	67.8	0				0				S	0.98	1474	1.27	0.96
573			C7	0.83	200	900	1000	750	300	200	0.5	1.70	6	439	20	67.8	0				0.71	9.5	100	463	S	1.06	1600	1.37	0.97
574			C8	0.83	200	900	1000	750	300	200	0.5	1.70	6	439	20	67.8	0.26	9.53	270	463	0				S	1.04	1563	1.26	0.99
																										# of beams	392	350
																										Avg=	1.08	1.00

		COV=	15.4%	19.8%

For the specimens by Senturk and Higgins25 which had indirect loading and bar cut-offs:
*- Taken as the distance between the end bars of hanger reinforcement within the width of the transverse members loading the test specimen
**- Based on the bars anchored in the support zone
†- Considering the bottom longitudinal bars in the section with maximum bending moment

References

1. Clark, A. P., “Diagonal Tension in Reinforced Concrete Beams,” ACI Journal Proceedings, V. 48, No. 10, 1951, pp. 145-56.
2. Moody, K. G., Viest, I. M., Elstner, R. C., and Hognestad, E., “Shear Strength of Reinforced Concrete Beams Part 1 -Tests of Simple Beams,” ACI Journal Proceedings, V. 51, No. 12, 1954, pp. 317-32.
3. Morrow, J., and Viest, I. M., “Shear Strength of Reinforced Concrete Frame Members without Web Reinforcement,” ACI Journal Proceedings, V. 53, No. 3, 1957, pp. 833-69.
4. Leonhardt, F., and Walther, R., “The Stuttgart Shear Tests 1961,” A translation of the articles that appeared in Beton und Stahlbetonbau, V.56, No. 12, 1961 and V.57, No. 2,3,6,7 and 8, 1962, Cement and Concrete Association Library Translation No. 111, Wexham Springs, United Kingdom, Dec. 1964, 134 pp.
5. Mathey, R. G., and Watstein, D., “Shear Strength of Beams without Web Reinforcement Containing Deformed Bars of Different Yield Strengths,” ACI Journal Proceedings, V. 60, No. 2, 1963, pp. 183-208.
6. Kani, M. W., Huggins, M. W. and Wittkopp, R. R., “Kani on Shear in Reinforced Concrete,” University of Toronto Press, Toronto, Canada, 1979, pp. 225.
7. Lee, D., “An Experimental Investigation in the Effects of Detailing on the Shear Behavior of Deep Beams,” Master Thesis, Department of Civil Engineering, University of Toronto, 1982, pp. 138.
8. Smith, K. N., and Vantsiotis, A. S., “Shear Strength of Deep Beams,” ACI Journal Proceedings, V. 79, No. 3, 1982, pp. 201-13.
9. Rogowsky, D. M., and MacGregor, J. G., “Tests of Reinforced Concrete Deep Beams,” ACI Journal Proceedings, V. 83, No. 4, 1986, pp. 614-23.
10. Ghannoum, W. M., “Size Effect on Shear Strength of Reinforced Concrete Beams,” Master’s Thesis, Department of Civil Engineering and Applied Mechanics, McGill University, 1988, pp. 126.
11. Walraven, J., Lehwalter, N., “Size Effects in Short Beams Loaded in Shear,” ACI Structural Journal, V. 91, No. 5, 1994, pp. 585-93.
12. Tan, K. H., Kong, F. K., Teng S., and Guan L. W., “High-Strength Concrete Deep Beams with Effective Span and Shear Span Variations,” ACI Structural Journal, V. 92, No. 4, 1995, pp.1-11.
13. Foster, S. J. and Gilbert, R. I, “Experimental Studies on High-Strength Concrete Deep Beams,” ACI Structural Journal, V. 95, No. 4, 1998, pp. 382-90.
14. Kong, P. Y. L., and Rangan, B. V., “Shear Strength of High-Performance Concrete Beams,” ACI Structural Journal, V. 95, No. 6, 1998, pp. 677-88.
15. Podgórniak-Stanik, B., “The Influence of Concrete Strength, Distribution of Longitudinal Reinforcement, Amount of Transverse Reinforcement and Member Size on Shear Strength of Reinforced Concrete Members”, Master’s Thesis, Department of Civil Engineering, University of Toronto, 1998, pp. 711.

16. Tan, K. H. and Lu, H. Y., “Shear Behavior of Large Reinforced Concrete Deep Beams and Code Comparisons,” ACI Structural Journal, V. 96, No. 5, 1999, pp.836-46.

17. Yoshida, Y., “Shear Reinforcement for Large Lightly Reinforced Concrete Members,” Master’s Thesis, Department of Civil Engineering, University of Toronto, 2000, pp. 160.

18. Adebar, P., “One Way Shear Strength of Large Footings,” Canadian Journal of Civil Engineering, V. 27, No. 3, 2000, pp. 553-62.

19. Yang, K. H., Chung, H. S., Lee, E. T., and Eun, H. C., “Shear Characteristics of High-Strength Concrete Deep Beams without Shear Reinforcements,” Engineering Structures, V. 25, No. 10, 2003, pp. 1343-52.

20. Tanimura, Y., and Sato, T., “Evaluation of Shear Strength of Deep Beams with Stirrups,” Quarterly Report of RTRI, V. 46, No. 1, 2005, pp. 53-8.

21. Salamy M. R., Kobayashi H. and Unjoh S., “Experimental and Analytical Study on RC Deep Beams,” Asian Journal of Civil Engineering (AJCE), V.6, No.5, 2005, pp.409-22.

22. Zhang, N., and Tan, K. H., “Size Effect in RC Deep Beams: Experimental Investigation and STM Verification,” Engineering Structures, V. 29, No. 12, 2007, pp. 3241-54.

23. Sherwood, E. G., Bentz, E. C., and Collins, M. P., “Effect of Aggregate Size on Beam- Shear Strength of Thick Slabs,” ACI Structural Journal, V. 104, No. 2, 2007, pp. 180-90.

24. Garay, J. D., and Lubell, A. S., “Behavior of Concrete Deep Beams with High Strength Reinforcement,” 2008 Structures Congress - Crossing Borders, Vancouver, Canada, April 2008, pp.10.

25. Zhang, N., Tan, K. H., and Leong, C. L., “Single-Span Deep Beams Subjected to Unsymmetrical Loads,” ASCE Journal of Structural Engineering, V. 135, No. 3, 2009, pp. 239-52.

26. Breña, S.F. and Roy, N.C., “Evaluation of Load Transfer and Strut Strength of Deep Beams with Short Longitudinal Bar Anchorages,” ACI Structural Journal, V. 106, No. 5, 2009, pp.678-89.

27. Birrcher, D., Tuchscherer, R., Huizinga, M., Bayrak, O., Wood, S., and Jirsa, J., “Strength and Serviceability Design of Reinforced Concrete Deep Beams,” Report No. FHWA/TX-09/0-5253-1, Center for Transportation Research, the University of Texas at Austin, 2009.

28. Sahoo, D. K., Sagi, M. S. V., Singh, B., and Bhargava, B., “Effect Of Detailing of Web Reinforcement on the Behavior of Bottle-Shaped Struts,” Journal of Advanced Concrete Technology, V. 8, No. 3, 2010, pp. 303-14.

29. Senturk, A. E., and Higgins, C., “Evaluation of Reinforced Concrete Deck Girder Bridge Bent Caps with 1950s Vintage Details: Laboratory Tests,” ACI Structural Journal, V. 107, No. 5, 2010, pp. 534-43.

30. Zhang, N., and Tan, K. H., “Effects of Support Settlement on Continuous Deep Beams and STM Modeling,” Engineering Structures, V.32, No. 2, 2010, pp. 361-72.

31. Mihaylov, B. I., Bentz, E. C., Collins, M. P., “Behavior of Large Deep Beam Subjected to Monotonic and Reversed Cyclic Shear,” ACI Structural Journal, V. 107, No. 6, 2010, pp. 726-34.

32. Lu, W. Y., Lin, I. J., and Yu, H. W., “Shear Strength of Reinforced Concrete Deep Beams,” ACI Structural Journal, V. 110, No. 4, 2013, pp. 671-80.

33. Mihaylov, B. I., Bentz, E. C., and Collins, M. P., “Two-parameter kinematic theory for shear behavior of deep beams,” ACI Structural Journal, V. 110, No.3, pp. 447-56.

34. Russo, G., Venir, R., and Pauletta, M., “Reinforced Concrete Deep Beams - Shear Strength Model and Design Formula,” ACI Structural Journal, V.102, No.3, 2005, pp. 429-37.

B. Additional equations for macroelement formulation

This appendix contains additional equations which were not provided in the main body of the paper for the sake of brevity.

- **Calculation of strut strain** ε_d

$$\varepsilon_d = \frac{|C| - V_{CLZ}\cot\alpha}{E_c b c}$$

where |C| = T is the compression force in the section with maximum bending moment and $V_{CLZ}.\cot\alpha$ is the horizontal component of the compression force in the critical loading zone, see Fig. 3.6. The depth of the compression zone *c* is estimated as in the flexural theory for cracked sections:

$$c = \left(\sqrt{n^2\rho_l^2 + 2n\rho_l} - n\rho_l\right)d$$

where $\rho_l = A_s/bd$ is the ratio of flexural reinforcement and $n = E_s/E_c$ is the ratio of steel and concrete moduli of elasticity.

- **The M-θ relationship**

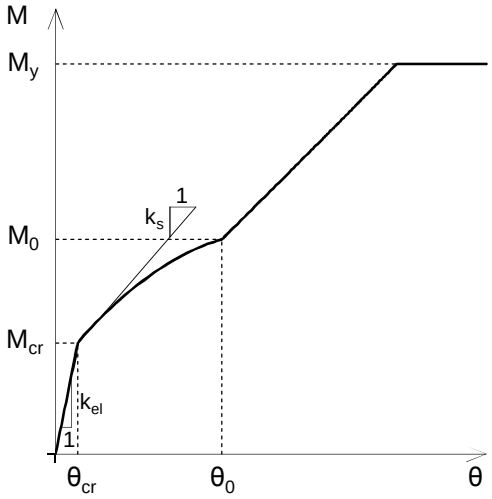

Fig. B.1 Behavior of rotational springs

If $0 \le \theta \le \theta_{cr}$: $M = k_{el}\theta$

If $\theta > \theta_{cr}$: $M = \min\begin{cases}\max\begin{cases}C_1\theta^2 + C_2\theta + C_3 \\ T(0.9d)\end{cases} \\ M_y\end{cases}$

Where

$\theta_{cr} = M_{cr}/k_{el}$

$M_{cr} = T_{cr}(0.9d)$

$$T_{cr} = \left[A_{c,eff} + (E_s / E_c - 1) A_s \right] 0.63 \sqrt{f_c^{'}}$$

$$A_{c,eff} = b \times \min\left[1.5(h-d), h/2 \right]$$

$$k_{el} = \frac{6kG_c A E_c I}{12E_c I + kG_c A a^2} \left(\frac{4E_c I}{kG_c A a} + \frac{a}{3} \right)$$

$$C_1 = \frac{(M_0 - M_{cr}) - k_s (\theta_0 - \theta_{cr})}{(\theta_0 + \theta_{cr})^2}$$

$$M_0 = T_0 (0.9d)$$

$$k_s = E_s A_s (0.9d)\, d / l_t$$

$$\theta_0 \approx M_0 / k_s$$

$$C_2 = k_s - 2C_1 \theta_{cr}$$

$$C_3 = M_0 - C_1 \theta_0^2 - C_2 \theta_0$$

$$T = \frac{E_s A_s d}{l_t} \theta + \frac{0.33 \sqrt{f_c^{'}}}{\sqrt{1 + 200(d/l_t)\theta}} A_{c,eff} \le A_s f_y$$

$$M_y = A_s f_y 0.9d$$

- **Aggregate interlock shear stress $v_{ci}(w,s)$ based on contact density model**

$$v_{ci} = \int_{-\frac{\pi}{2}}^{\frac{\pi}{2}} \sigma_{con} K A_t \Omega \sin\varphi d\varphi$$

This integral is evaluated numerically, where:

$$0 \le \sigma_{con} = f_{cy} \frac{w_\varphi}{w_{lim}} \le f_{cy} \text{ , MPa}$$

$w_{\lim} = 0.04\text{mm}$

$f_{cy} = 13.7 \sqrt[3]{f_c}$, MPa

$w_\varphi = s \sin\varphi - w \cos\varphi$

$$K = 1 - \exp\left(1 - \frac{a_g}{w} \right) \ge 0$$

$A_t = 4/\pi$

$\Omega = 0.5 \cos\varphi$

C. Database of deep beams with web openings

Ref.	No.	**Beam**	f_c, MPa	a_g, mm	**a/d**	**h**, mm	d_1, mm	d_2, m m	**b**, mm	**a**, mm	A_{s1}, mm^2	n_{s1}	Φ_{s1}, mm	ρ_{II}, %	f_{y1}, Mpa	n_{s2}	Φ_{s2}, mm	ρ_v, %	Φ_v, mm	s_v, mm
[1]	1	H5F1	52.9	25	0.5	600	556	39	160	300	861	3	19	0.97	420	2	10	0	-	-
	2	H5F2	52.9	25	0.5	600	556	39	160	300	861	3	19	0.97	420	2	10	0	-	-
	3	H5F3	52.9	25	0.5	600	556	39	160	300	861	3	19	0.97	420	2	10	0	-	-
	4	H5T3	52.9	25	0.5	600	556	39	160	300	861	3	19	0.97	420	2	10	0	-	-
	5	H5S3	52.9	25	0.5	600	556	39	160	300	861	3	19	0.97	420	2	10	0	-	-
	6	H10F1	52.9	25	1.1	600	556	39	160	600	861	3	19	0.97	420	2	10	0	-	-
	7	H10F2	52.9	25	1.1	600	556	39	160	600	861	3	19	0.97	420	2	10	0	-	-
	8	H10F3	52.9	25	1.1	600	556	39	160	600	861	3	19	0.97	420	2	10	0	-	-
	9	H10T3	52.9	25	1.1	600	556	39	160	600	861	3	19	0.97	420	2	10	0	-	-
	10	H10S3	52.9	25	1.1	600	556	39	160	600	861	3	19	0.97	420	2	10	0	-	-
	11	UH5F1	80.4	25	0.5	600	556	39	160	300	861	3	19	0.97	420	2	10	0	-	-
	12	UH5F2	80.4	25	0.5	600	556	39	160	300	861	3	19	0.97	420	2	10	0	-	-
	13	UH5F3	80.4	25	0.5	600	556	39	160	300	861	3	19	0.97	420	2	10	0	-	-
	14	UH5T3	80.4	25	0.5	600	556	39	160	300	861	3	19	0.97	420	2	10	0	-	-
	15	UH5S3	80.4	25	0.5	600	556	39	160	300	861	3	19	0.97	420	2	10	0	-	-
	16	UH7F3	80.4	25	0.8	600	556	39	160	420	861	3	19	0.97	420	2	10	0	-	-
	17	UH10F1	80.4	25	1.1	600	556	39	160	600	861	3	19	0.97	420	2	10	0	-	-
	18	UH10F2	80.4	25	1.1	600	556	39	160	600	861	3	19	0.97	420	2	10	0	-	-
	19	UH10F3	80.4	25	1.1	600	556	39	160	600	861	3	19	0.97	420	2	10	0	-	-
	20	UH10T3	80.4	25	1.1	600	556	39	160	600	861	3	19	0.97	420	2	10	0	-	-
	21	UH10S3	80.4	25	1.1	600	556	39	160	600	861	3	19	0.97	420	2	10	0	-	-
	22	UH15F3	80.4	25	1.6	600	556	39	160	900	861	3	19	0.97	420	2	10	0	-	-
	23	L5F3C	23.5	25	0.5	600	556	39	160	300	861	3	19	0.97	420	2	10	0	-	-
	24	L10F3C	23.5	25	1.1	600	556	39	160	600	861	3	19	0.97	420	2	10	0	-	-
[2]	25	NS-150-C	21.0	10	0.9	500	460	25	80	400	616	4	14	1.67	420	2	8	0.47	6	150
	26	NS-200-C	21.0	10	0.9	500	460	25	80	400	616	4	14	1.67	420	2	8	0.47	6	150
	27	NS-250-C	21.0	10	0.9	500	460	25	80	400	616	4	14	1.67	420	2	8	0.47	6	150

Continue

No.	f_{yv}, Mpa	l_{b1}, mm	l_{b2}, mm	**V/P**	m_1	m_2	k_1	k_2	l_3, mm	A_{s3}, mm^2	f_{y3}, MPa	d_3, mm	V_{pred}, kN	V_{exp}, kN	V_{exp} / V_{pred}
1		100	100	1.0	0.50	0.10	0.50	0.50	225	314	408	170	397 (405) *	466	1.18 (1.15)
2	-	100	100	1.0	0.50	0.20	0.50	0.50	225	314	408	170	323 (354)	348	1.08 (0.98)
3	-	100	100	1.0	0.50	0.30	0.50	0.50	225	314	408	170	260 (289)	289	1.11 (1.00)
4	-	100	100	1.0	0.25	0.30	0.50	0.50	263	314	408	208	314 (340)	337	1.07 (0.99)
5	-	100	100	1.0	0.65	0.30	0.50	0.50	203	314	408	148	236 (262)	236	1.00 (0.90)
6	-	100	100	1.0	0.50	0.10	0.50	0.50	300	314	408	245	216(242)	225	1.04 (0.93)
7	-	100	100	1.0	0.50	0.20	0.50	0.50	300	314	408	245	171(191)	184	1.07 (0.96)
8	-	100	100	1.0	0.50	0.30	0.50	0.50	300	314	408	245	134 (149)	144	1.07 (0.97)
9	-	100	100	1.0	0.25	0.30	0.50	0.50	375	314	408	320	170 (190)	163	0.96 (0.86)

10	-	100	100	1.0	0.65	0.30	0.50	0.50	255	314	408	200	119 (132)	130	1.09 (0.98)
11	-	100	100	1.0	0.50	0.10	0.50	0.50	225	314	408	170	428 (448)	515	1.20 (1.15)
12	-	100	100	1.0	0.50	0.20	0.50	0.50	225	314	408	170	347 (387)	419	1.21 (1.08)
13	-	100	100	1.0	0.50	0.30	0.50	0.50	225	314	408	170	278 (309)	339	1.22 (1.10)
14	-	100	100	1.0	0.25	0.30	0.50	0.50	263	314	408	208	339 (382)	395	1.16 (1.03)
15	-	100	100	1.0	0.65	0.30	0.50	0.50	203	314	408	148	252 (278)	331	1.32 (1.19)
16	-	100	100	1.0	0.50	0.30	0.50	0.50	255	314	408	200	204 (227)	264	1.29 (1.16)
17	-	100	100	1.0	0.50	0.10	0.50	0.50	300	314	408	245	231 (259)	245	1.06 (0.95)
18	-	100	100	1.0	0.50	0.20	0.50	0.50	300	314	408	245	181 (202)	199	1.10 (0.98)
19	-	100	100	1.0	0.50	0.30	0.50	0.50	300	314	408	245	141 (157)	155	1.10 (0.99)
20	-	100	100	1.0	0.25	0.30	0.50	0.50	375	314	408	320	179 (200)	185	1.04 (0.93)
21	-	100	100	1.0	0.65	0.30	0.50	0.50	255	314	408	200	126 (139)	140	1.11 (1.01)
22	-	100	100	1.0	0.50	0.30	0.50	0.50	375	314	408	320	91 (102)	95	1.04 (0.93)
23	-	100	100	1.0	0.50	0.30	0.50	0.50	225	314	408	170	195 (195)	233	1.20 (1.20)
24	-	100	100	1.0	0.50	0.30	0.50	0.50	300	314	408	245	104 (105)	117	1.13 (1.11)
25	300	100	100	1.0	0.38	0.30	0.50	0.50	225	616	420	185	94 (97)	103	1.09 (1.06)
26	300	100	100	1.0	0.50	0.40	0.50	0.50	200	616	420	160	69 (73)	82	1.18 (1.12)
27	300	100	100	1.0	0.63	0.50	0.50	0.50	175	616	420	135	44 (46)	53	1.21 (1.15)
													Avg.	**=**	**1.12(1.03)**
													COV	**=**	**7.6% (9.3%)**

Note: The values in brackets are obtained by considering the strain hardening of the reinforcement in section A.

References

1. Yang KH, Eun HC, Chung HS. The influence of web openings on the structural behaviour of reinforced high-strength concrete deep beams. Eng Struct 2006; 28:1825-34.
2. El-Maaddawy T, Sherif S. FRP composites for shear strengthening of reinforced concrete deep beams with openings. Compos Struct 2009; 89: 60-9